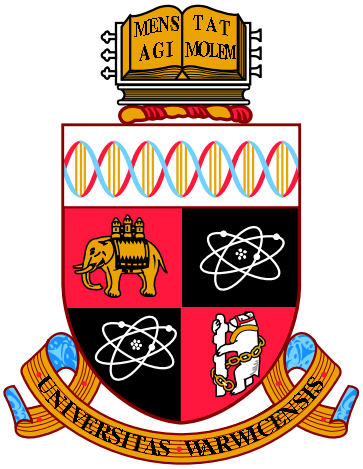

A measurement of the CKM angle γ from studies of $DK\pi$ Dalitz plots

by

Daniel Craik

Thesis

Submitted to the University of Warwick

for the degree of

Doctor of Philosophy

Department of Physics

September 2015

THE UNIVERSITY OF
WARWICK

Contents

List of Tables

List of Figures

Acknowledgments

Firstly I would like to thank my supervisor, Tim Gershon, who has consistently gone beyond the call of duty as a mentor and friend. Thank you for your constant guidance, for your inspiring wisdom and encouragement, and for giving me the chance to work on such a stimulating analysis.

I'm very grateful to Michal Kreps for his insightful help and enthusiastic support. Special thanks are reserved for Tom Latham and Mark Whitehead who have taught me a great deal over the past four years — I am certainly a better physicist for your contributions. Thanks to the rest of the Warwick LHCb gang, past and present: Anton, John, Tom, Christoph, Dave, Matt, Matt, Tom, Rafael (batata), Charlotte, Dan, Abhijit, Andrew and David, for entertaining and informative discussions (sometimes about physics but often regarding jellyfish). Thanks to all the people working on LHCb and the LHC who have made this work possible, and especially to the members of the B2OC working group — particularly Anton, Moritz, Sneha and Vava.

A heartfelt thanks to my family. Thanks to my grandparents, who have always inspired me; to my parents-in-law, who live on in our loving memories; and to my siblings, partners in fun and mischief, and life-long friends, Sam and Bethany. Special thanks to my amazing parents, Angela and Malcolm, for your infinite love and care, and your life-long support — I wouldn't be where I am today without you. Finally I thank my wonderful, loving and ever-supportive wife and best friend, Diana, I love you so very much.

Declarations

The work presented in this thesis is all my own, unless explicitly stated otherwise. Much of the software used in the presented analyses depends on external packages, which are identified in the text when used. The only exceptions to this are the ROOT framework, which is used extensively throughout this thesis, and the RooFit fitting package, which is used for all one-dimensional fits. My own contributions to these external packages, where applicable, are detailed in appendices. This thesis has not been submitted, in any form, to this or any other university for another qualification.

Daniel Craik

Abstract

Various measurements of quantities relating to $B^0_{(s)} \to DK^\pm\pi^\mp$ decays are reported from analyses building towards a measurement of the CKM angle γ. The first observation of the decay $B^0_s \to \overline{D}{}^0 K^-\pi^+$ is reported. Based on a data sample corresponding to an integrated luminosity of $1.0\,\text{fb}^{-1}$ of pp collision data recorded by the LHCb detector, the branching fraction relative to that of the topologically similar decay $B^0 \to \overline{D}{}^0\pi^+\pi^-$ is measured to be

$$\frac{\mathcal{B}\left(B^0_s \to \overline{D}{}^0 K^-\pi^+\right)}{\mathcal{B}\left(B^0 \to \overline{D}{}^0\pi^+\pi^-\right)} = 1.18 \pm 0.05\,(\text{stat.}) \pm 0.12\,(\text{syst.})\,.$$

In addition, the relative branching fraction of the decay $B^0 \to \overline{D}{}^0 K^+\pi^-$ is measured to be

$$\frac{\mathcal{B}\left(B^0 \to \overline{D}{}^0 K^+\pi^-\right)}{\mathcal{B}\left(B^0 \to \overline{D}{}^0\pi^+\pi^-\right)} = 0.106 \pm 0.007\,(\text{stat.}) \pm 0.008\,(\text{syst.})\,.$$

The resonant substructures of $B^0_s \to \overline{D}{}^0 K^-\pi^+$ and $B^0 \to \overline{D}{}^0 K^+\pi^-$ decays are studied using a data sample corresponding to an integrated luminosity of $3.0\,\text{fb}^{-1}$ of pp collision data recorded by the LHCb detector. In $B^0_s \to \overline{D}{}^0 K^-\pi^+$ decays, an excess at $m(\overline{D}{}^0 K^-) \approx 2.86\,\text{GeV}/c^2$ is found to be an admixture of spin-1 and spin-3 resonances. This is the first observation of a heavy flavoured spin-3 resonance, and the first time that any spin-3 particle has been seen to be produced in B decays. The masses and widths of the new states and of the $D^*_{s2}(2573)^-$ meson are measured as part of this analysis, giving the most precise determinations to date, while the masses and widths of the $D^*_0(2400)^-$ and $D^*_2(2460)^-$ resonances are measured from the analysis of $B^0 \to \overline{D}{}^0 K^+\pi^-$ decays. The complex amplitudes and fit fractions for all components included in the two amplitude models are also measured.

Finally, a first determination of γ from an amplitude analysis of $B^0 \to DK^+\pi^-$ decays is reported based on measurements of the Cartesian parameters

$$\begin{aligned} x_\pm &= r_B \cos\left(\delta_B \pm \gamma\right)\,, \\ y_\pm &= r_B \sin\left(\delta_B \pm \gamma\right)\,. \end{aligned}$$

Chapter 1

Introduction

The principle goal of physics is the determination of a complete predictive mathematical description of the world around us — a so far unknown theory of everything. While most recent improvements in the field have been incremental steps based on established theories, there is precedent for precision measurements to transform our understanding of physics.

At the turn of the 20th century, in an address to the British Association for the Advancement of Science, Lord Kelvin is famously (albeit apocryphally) purported to have announced "There is nothing new to be discovered in physics now. All that remains is more and more precise measurement". As is often the case in anecdotes of such hubris, this was swiftly followed by Max Planck's eponymous postulate. Presented to the German Physical Society that same year, this simple idea based on his studies of black-body radiation laid the foundations for quantum mechanics. Within five years Albert Einstein had revolutionised the field with the publication of his "Annus Mirabilis" papers.

A century later, the Standard Model of particle physics represents our most complete understanding of the fundamental workings of the universe to date and has survived many years of experimental tests, but even this is known to be incomplete. The clearest evidence of the need for new physics is in our own existence. We live in a matter dominated universe, yet, in the early universe, matter and antimatter would have been present in equal amounts. If the laws of physics were symmetric with respect to the exchange of matter and antimatter, we would expect this early matter and antimatter to annihilate leaving only light. Our very existence, therefore, demands a small asymmetry in the fundamental laws of physics. While the Standard Model allows for a matter-antimatter asymmetry of one part in 10^{-17}, an asymmetry ten million times larger is required to allow for the existence of the universe we

see today. A series of precise measurements of the parameters that quantify this asymmetry (strictly speaking the asymmetry under the inversion of all quantum numbers and spatial coordinates — denoted *CP* asymmetry) could therefore give us our first glimpse of the world beyond the Standard Model. The search for the source(s) of this asymmetry is the main topic of this thesis.

CP asymmetry in the weak decays of quarks is parameterised within the Standard Model by a single parameter but this can be related to a wide range of measurable quantities allowing the model to be over-constrained. Of particular interest is a comparison between measurements from so-called loop processes, where Feynman diagrams containing closed loops dominate, and so-called tree processes, where the effects of closed loops are negligible. While new heavy particles may contribute significantly to loop processes, tree processes are expected to be dominated by Standard Model contributions. Key among these quantities is the unitarity triangle angle $\gamma \equiv \arg\left[-V_{ud}V_{ub}^{*}/(V_{cd}V_{cb}^{*})\right]$, where V_{xy} are elements of the Cabibbo–Kobayashi–Maskawa quark mixing matrix, as this parameter can be determined entirely from tree processes.

This thesis presents a series of analyses of the decays of B^0 and B_s^0 mesons to $DK\pi$ final states. Note that the inclusion of charge-conjugate processes is implied throughout this work unless otherwise stated. While the decay $B^0 \to \overline{D}{}^0 K^+\pi^-$ has been observed prior to the work described in this thesis, the B_s^0 decay to the $\overline{D}{}^0 K^-\pi^+$ final state has not. Crucially, this also marks the first investigation of the three-body kinematics of these decays. It is just such an analysis of these decays, specifically the decays $B^0 \to \overline{D}{}^0 K^+\pi^-$ and $B^0 \to D_{CP}K^+\pi^-$, where D_{CP} represents a neutral D meson decaying to an eigenstate of the *CP* transformation, which can be used to extract a measurement of γ.

The structure of this thesis is as follows. Chapter 2 presents a general introduction to the Standard Model and *CP* violation, and details a method for the determination of γ from $B^0 \to D_{CP}K^+\pi^-$ decays while Chapter 3 describes the Large Hadron Collider and the LHCb detector. Elements common to all of the analyses discussed in later chapters, such as data selection, and background and efficiency modelling, are detailed in Chapter 4. Chapter 5 covers the measurement of the branching fractions for $B^0_{(s)} \to \overline{D}{}^0 K^{\pm}\pi^{\mp}$ decays, while Dalitz plot analyses of $B_s^0 \to \overline{D}{}^0 K^-\pi^+$ and $B^0 \to \overline{D}{}^0 K^+\pi^-$ are described in Chapters 6 and 7. The extraction of γ is detailed in Chapter 8 and Chapter 9 provides a summary and conclusion. A list of alternative equations used to describe resonances is given in Appendix A, while Appendices B and C detail contributions made to the EvtGen and Laura^{++} software packages.

Chapter 2

Theory

2.1 The Standard Model of particle physics

The Standard Model (SM) of particle physics is a quantum field theory that describes the interactions of particles via the electro-magnetic (EM), strong and weak forces. The theory incorporates the three generations of fermions, each composed of two quarks and two leptons, listed in Table 2.1 and the force-mediating bosons, which are listed in Table 2.2. With the discovery of the Higgs boson in 2012 [1, 2], the fundamental constituents of the SM have now all been observed experimentally.

Table 2.1: The fundamental fermions of the Standard Model. Masses are taken from the PDG [3]. Limits on the neutrino masses are the limit set on the sum of the neutrino masses by cosmological constraints.

Generation	Particle	Symbol	Electric charge ($e/3$)	Mass (MeV/c^2)
I	down quark	d	-1	$4.8^{+0.5}_{-0.3}$
	up quark	u	2	$2.3^{+0.7}_{-0.5}$
	electron	e^-	-3	0.510998928(11)
	electron neutrino	ν_e	0	< 0.0000003
II	strange quark	s	-1	95 ± 5
	charm quark	c	2	1275 ± 25
	muon	μ^-	-3	105.6583715(35)
	muon neutrino	ν_μ	0	< 0.0000003
III	bottom quark	b	-1	4180 ± 30
	top quark	t	2	$173\,070^{+520}_{-720}$
	tau	τ^-	-3	1776.82 ± 0.16
	tau neutrino	ν_τ	0	< 0.0000003

While the weak force interacts with all of the fermions and the EM force affects all but the neutrinos, the strong force only acts on the quarks, which carry a strong colour charge. Quarks carry a red, green or blue colour charge, with anti-quarks

Table 2.2: The fundamental bosons of the Standard Model. Masses are taken from the PDG [3]. Note that while gluons are theoretically massless, a mass as large as a few MeV cannot be excluded experimentally.

Particle	Symbol	Force	Mass (MeV/c^2)
photon	γ	EM	$< 1 \times 10^{-24}$
gluon	g	Strong	0*
W boson	$W^{\pm}$	Weak	$80\,385 \pm 15$
Z boson	Z^0	Weak	$91\,187.6 \pm 2.1$
Higgs boson	H^0	Mass	$125\,900 \pm 400$

carrying an anti-red, anti-green or anti-blue charge. Due to colour confinement, only colour neutral states can exist freely so quarks always combine into hadrons[1] — either mesons (a quark and an anti-quark) such as pions ($u\bar{d}$, $\frac{u\bar{u}-d\bar{d}}{\sqrt{2}}$) and kaons ($s\bar{u}$, $s\bar{d}$), or baryons (three quarks) such as protons (uud) and neutrons (udd).

While the naming conventions for baryons and unflavoured mesons are somewhat complicated, the simple naming convention for flavoured mesons is shown in Table 2.3, along with the lightest meson (a pseudoscalar) in each flavour family. Excited states in these families are identified according to spin, parity and mass (in MeV/c^2). States with natural spin parity ($J^P = 0^+$, 1^-, 2^+, 3^-, ...) are labelled with a *, while a collection of both natural and unnatural states is labelled **. States are also labelled with their spin as a subscript (*e.g.* $K_0^*(1430)$ — a scalar) although this is often omitted for pseudoscalars and vectors. These states can be compared to the orbitally and radially excited states of the $q\bar{q}'$ pair predicted by the quark model, which are shown in Fig. 2.1 for the D_s system. Observed states that do not conform to this structure are candidates for exotic states such as hybrids, tetraquarks and meson molecules. Recent studies have confirmed the existence of multiple exotic states: the $Z(4430)^+$ tetraquark [4–6], and two pentaquarks, $P_c(4380)^+$ and $P_c(4450)^+$ [7].

The SM has been verified by experimental observations to high degrees of precision. Elements of the theory were used to predict the existence of the charm [9], bottom and top quarks [10], the W and Z bosons [11, 12], the gluon [13] and the Higgs boson [14–16] before these particles were experimentally observed. Despite these successes there are several known phenomena which are not explained by the SM such as gravity, dark matter, neutrino mixing and the matter-antimatter asymmetry of the universe. This final puzzle relates to the topic of this thesis.

To produce a matter-antimatter asymmetry, three conditions [17] must be met. There must be a departure from thermal equilibrium to allow an excess of matter

[1]Except for the top quark which, due to its short lifetime, decays before it can hadronise into a colour neutral state.

Table 2.3: The flavoured meson families and their pseudoscalar ground-state particles. Masses are taken from the PDG [3].

Flavour	Symbol	Quark content	Ground state	Mass (MeV/c^2)
Strange	K	$s\bar{d}$	K^0	497.614 ± 0.024
		$s\bar{u}$	K^-	493.677 ± 0.016
Charm	D	$c\bar{d}$	D^+	1869.62 ± 0.15
		$c\bar{u}$	D^0	1864.86 ± 0.13
Charm-strange	D_s	$c\bar{s}$	D_s^+	1968.50 ± 0.32
Bottom	B	$b\bar{d}$	B^0	5279.58 ± 0.17
		$b\bar{u}$	B^-	5279.26 ± 0.17
Bottom-strange	B_s	$b\bar{s}$	B_s^0	5366.77 ± 0.24
Bottom-charm	B_c	$b\bar{c}$	B_c^-	6274.5 ± 1.8

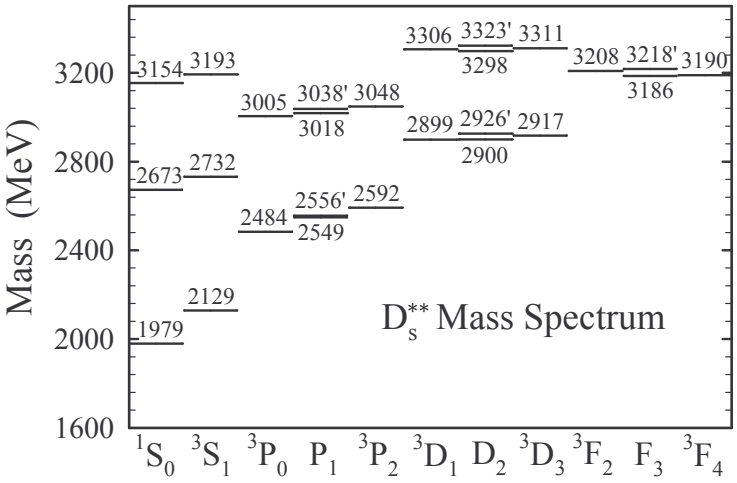

Figure 2.1: Predicted states of the D_s^{**} mass spectrum [8]. The $^1S_0$ and $^3S_1$ columns correspond to pseudoscalars and vectors. The $^3P_0$, P_1 and $^3P_2$ columns correspond to orbitally excited scalars, axial-vectors and tensors, while further columns contain higher orbital excitations. Higher-mass states in each column are due to radial excitations.

to build up; a process that violates baryon number must exist to create the excess matter; and the process that produces antimatter must occur at a different rate to its analogous matter-producing counterpart — both Charge (C) and Charge-Parity (CP) symmetries must be violated.

2.2 *CP* violation

Symmetry under charge conjugation is the assumption that physics should not change if all positive and negative quantum numbers are exchanged, while parity

(P) symmetry would require physics to be invariant under the inversion of all spatial dimensions. Both C and P symmetries are independently conserved by the EM and strong forces but are both violated maximally by the weak force. Under the C and P transformations, a left-handed neutrino would become a left-handed anti-neutrino and a right-handed neutrino, respectively. As the weak force couples only to left-handed matter and right-handed anti-matter, both C and P symmetries are violated. The combined CP transformation transforms a left-handed neutrino into a right-handed anti-neutrino and was therefore a candidate to be an exact symmetry of nature. While CP symmetry is now known to be violated, its combination with time (T) symmetry, CPT symmetry, is observed to be an exact symmetry up to current precision. Indeed, the CPT theorem requires CPT to be conserved in any locally Lorentz invariant field theory [18–20].

The first observation of CP violation came in the neutral kaon system. The two neutral kaon flavour states (K^0 ($d\bar{s}$) and $\overline{K}^0$ ($s\bar{d}$)) mix to form the observed mass eigenstates $K^0_{\rm S}$ and $K^0_{\rm L}$. In the case of no CP violation these would correspond to the CP eigenstates, $K_1 = \frac{K^0+\overline{K}^0}{\sqrt{2}}$ and $K_2 = \frac{K^0-\overline{K}^0}{\sqrt{2}}$, and would decay via the weak interaction to the 2π (CP even) and 3π (CP odd) final states, respectively. The observation of the CP-suppressed $K^0_{\rm L} \to 2\pi$ decay [21] confirmed the existence of CP violation in the weak interaction. A brief summary of the different manifestations of CP violation in the quark sector is given below.

2.2.1 *CP* violation in decays

CP violation in decays arises when the rates at which two CP conjugate decays occur differ. The complex amplitude associated with the decay to the final state f can be written as

$$A_f = \sum_j A_j e^{i(\delta_j+\phi_j)} \ , \tag{2.1}$$

where the sum is over the different coherent contributions to the decay, and δ_j and ϕ_j are the CP conserving strong phase and the CP violating weak phase corresponding to process j. For direct CP violation to occur, the ratio of the CP conjugate amplitudes,

$$\left|\frac{\bar{A}_{\bar{f}}}{A_f}\right| = \left|\frac{\sum_j A_j e^{i(\delta_j-\phi_j)}}{\sum_j A_j e^{i(\delta_j+\phi_j)}}\right| , \tag{2.2}$$

must differ from unity. This requires at least two processes to contribute to the decay amplitude, A_f, with different strong and weak phases.

2.2.2 *CP* violation in mixing

CP violation can also arise due to mixing in the neutral flavoured mesons. This occurs when the mass eigenstates do not correspond to the *CP* eigenstates. As described further in Section 2.3, the weak force couples the different generations of up-type and down-type quarks. This allows neutral mesons to oscillate between flavour states via box diagrams such as those shown in Fig. 2.2 for the neutral B mesons.

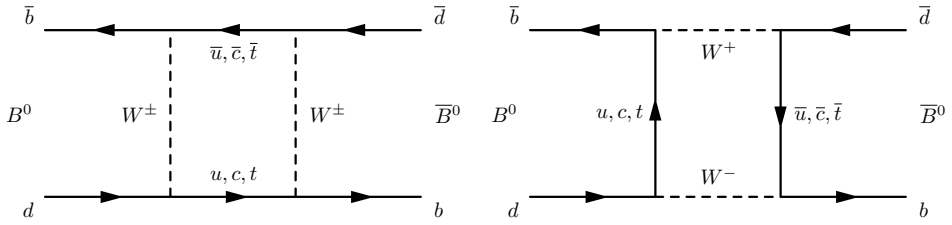

Figure 2.2: Box Feynman diagrams contributing to neutral B meson oscillation.

Through oscillations and decays, a population of B^0 and $\overline{B}^0$ mesons,

$$|\psi(0)\rangle = a(0)\left|B^0\right\rangle + b(0)\left|\overline{B}^0\right\rangle \ , \tag{2.3}$$

at time, $t = 0$, will evolve over time as

$$|\psi(t)\rangle = a(t)\left|B^0\right\rangle + b(t)\left|\overline{B}^0\right\rangle + c_1(t)\left|f_1\right\rangle + c_2(t)\left|f_2\right\rangle + ... \ , \tag{2.4}$$

where the coefficient $c_j(t)$ accounts for decays to the final state f_j. If only the $a(t)$ and $b(t)$ coefficients are of interest then, over timescales much larger than the typical strong interaction timescale, the additional decay terms can be neglected. This simplified time evolution may then be described by a 2×2 effective Hamiltonian, $\mathbf{H}$, which is non-Hermitian due to the presence of decays. This can be written in terms of Hermitian matrices:

$$\mathbf{H} = \mathbf{M} + \frac{i}{2}\mathbf{\Gamma} \, , \tag{2.5}$$

where $\mathbf{M}$ and $\mathbf{\Gamma}$ can be associated with oscillations via off-shell and on-shell intermediate states, respectively. As in the neutral kaon sector, mass states, which are eigenstates of this simplified time evolution, can be constructed from a linear combination of the neutral B flavour states:

$$|B_L\rangle = p\sqrt{1-z}\left|B^0\right\rangle + q\sqrt{1+z}\left|\overline{B}^0\right\rangle \ , \tag{2.6}$$

$$|B_H\rangle = p\sqrt{1+z}\left|B^0\right\rangle - q\sqrt{1-z}\left|\overline{B}^0\right\rangle \ , \tag{2.7}$$

where L and H label the light and heavy mass eigenstates respectively, and the flavour composition of each of the mass states is parameterised by three complex coefficients p, q and z. CPT conservation requires $z = 0$ and in the case where CP is also conserved, $|p|^2 - |q|^2 = 0$. CP violation in mixing occurs if the rate at which the B^0 meson oscillates into the $\overline{B}^0$ meson differs from the reverse rate and corresponds to $|p/q| \neq 1$.

2.2.3 *CP* violation from interference

Another form of CP violation can occur when a particle and its antiparticle can both decay to the same final state. This is due to interference between decays with and without mixing, *e.g.*, $B^0 \to f_{CP}$ and $B^0 \to \overline{B}^0 \to f_{CP}$, where f_{CP} is a CP eigenstate that, by definition, is accessible to both B^0 and $\overline{B}^0$ decays.

This type of CP violation is defined by

$$\Im(\lambda_{f_{CP}}) \neq 0 \ , \tag{2.8}$$

with

$$\lambda_{f_{CP}} \equiv \frac{q}{p}\frac{\bar{A}_{f_{CP}}}{A_{f_{CP}}} \ , \tag{2.9}$$

where $A_{f_{CP}}$ and $\bar{A}_{f_{CP}}$ are the amplitudes corresponding to the decays $B^0 \to f_{CP}$ and $\overline{B}^0 \to f_{CP}$, respectively. In the absence of the other forms of CP violation then $|\lambda_{f_{CP}}| = 1$, however, a phase difference between the mixing and decay amplitudes can still give $\lambda_{f_{CP}}$ a non-zero imaginary part, giving rise to CP violation.

2.2.4 Direct and indirect *CP* violation

Historically, CP violation has been categorised as either direct or indirect. Indirect CP violation may be entirely accounted for by a non-zero phase in the off-diagonal elements of $\mathbf{M}$, while direct CP violation requires additional CP violating phases. This categorisation was relevant to superweak models [22], which predicted only indirect CP violation. CP violation in mixing and CP violation in decays are sources of indirect and direct CP violation, respectively. A single observation of CP violation from interference is consistent with indirect CP violation, however, the observation of CP violation in two decays of the same meson requires direct CP violation unless

$$\eta_{f_1}\Im(\lambda_{f_1}) = \eta_{f_2}\Im(\lambda_{f_2}) \, , \tag{2.10}$$

where η_{f_i} is $+1$ (-1) for a CP-even (CP-odd) final state f_i.

2.3 Quark mixing and the CKM matrix

CP violation in the quark sector is introduced into the SM in the Cabibbo–Kobayashi–Maskawa (CKM) quark-mixing matrix [10,23], which describes the couplings between the various up-type and down-type quarks in flavour changing weak decays, and has the form:

$$V_{\mathrm{CKM}} = \begin{pmatrix} V_{ud} & V_{us} & V_{ub} \\ V_{cd} & V_{cs} & V_{cb} \\ V_{td} & V_{ts} & V_{tb} \end{pmatrix} . \tag{2.11}$$

While couplings between the quarks are governed by the components of the CKM matrix, anti-quarks couple according to the complex conjugates of these components, so *CP* violation appears when complex values are present. The presence of *CP* violation in the CKM matrix requires a non-zero phase difference between the elements. The CKM matrix is required to be unitary, and can therefore be parameterised by a set of angles and phase differences. The number of such parameters depends on the size of the matrix. For two generations of quarks, the CKM matrix is formed from a single mixing angle, so *CP* violation is not possible. With three generations, we have four non-trivial parameters, which can be expressed as three mixing angles and a single phase. The standard parameterisation [24] uses the angles θ_{12}, θ_{13}, θ_{23} and the phase δ_{13} giving

$$V_{\mathrm{CKM}} = \begin{pmatrix} c_{12}c_{13} & s_{12}c_{13} & s_{13}e^{-i\delta_{13}} \\ -s_{12}c_{23} - c_{12}s_{23}s_{13}e^{i\delta_{13}} & c_{12}c_{23} - s_{12}s_{23}s_{13}e^{i\delta_{13}} & s_{23}c_{13} \\ s_{12}s_{23} - c_{12}c_{23}s_{13}e^{i\delta_{13}} & -c_{12}s_{23} - s_{12}c_{23}s_{13}e^{i\delta_{13}} & c_{23}c_{13} \end{pmatrix} , \tag{2.12}$$

where s_{ij} and c_{ij} are the sine and cosine of the angle θ_{ij}, respectively.

2.3.1 The Wolfenstein parameterisation

From experiments, it is known that $s_{13} \ll s_{23} \ll s_{12} \ll 1$ [3]. For convenience, this hierarchy among the elements of the CKM matrix can be made explicit using the Wolfenstein parameters [25–27], λ, A, ρ and η, which are defined by

$$s_{12} = \lambda, \tag{2.13}$$

$$s_{23} = A\lambda^2, \tag{2.14}$$

$$s_{13}e^{i\delta_{13}} = A\lambda^3(\rho + i\eta). \tag{2.15}$$

This gives the CKM matrix to $\mathcal{O}(\lambda^3)$ as

$$V_{\rm CKM} = \begin{pmatrix} 1-\lambda^2/2 & \lambda & A\lambda^3(\rho - i\eta) \\ -\lambda & 1-\lambda^2/2 & A\lambda^2 \\ A\lambda^3(1-\rho-i\eta) & -A\lambda^2 & 1 \end{pmatrix} + \mathcal{O}(\lambda^4). \tag{2.16}$$

The improved Wolfenstein parameters, $\bar{\rho}$ and $\bar{\eta}$ are introduced to ensure that the CKM matrix is unitary to all orders in λ and are defined by

$$A\lambda^3(\rho + i\eta) \equiv \frac{A\lambda^3(\bar{\rho} + i\bar{\eta})\sqrt{1 - A^2\lambda^4}}{\sqrt{1-\lambda^2}\,(1 - A^2\lambda^4(\bar{\rho} + i\bar{\eta}))}\ . \tag{2.17}$$

2.3.2 The CKM Unitarity Triangle

The unitarity of the CKM matrix introduces the requirements $\sum_i V_{ij}V_{ik}^* = \delta_{jk}$ and $\sum_j V_{ij}V_{kj}^* = \delta_{ik}$. Each of the six vanishing sums can be represented as a closed triangle in the complex plane as illustrated in Fig. 2.3. The areas of these six triangles are the same and give a measure of the *CP* violation introduced into the SM by the CKM matrix, $J/2$, where J is known as the Jarlskog invariant [28]. The most commonly chosen triangle derives from $V_{ud}V_{ub}^* + V_{cd}V_{cb}^* + V_{td}V_{tb}^* = 0$. This is divided by the most well measured term $V_{cd}V_{cb}^*$ to give a triangle with vertices at (0,0), (1,0) and $(\bar{\rho},\bar{\eta})$. The angles of this triangle are labelled either (α, β, γ) or (ϕ_2, ϕ_1, ϕ_3), as shown in Fig. 2.3, and can be calculated from the elements of the CKM matrix as

$$\alpha \equiv \arg\left(-\frac{V_{td}V_{tb}^*}{V_{ud}V_{ub}^*}\right), \quad \beta \equiv \arg\left(-\frac{V_{cd}V_{cb}^*}{V_{td}V_{tb}^*}\right), \quad \gamma \equiv \arg\left(-\frac{V_{ud}V_{ub}^*}{V_{cd}V_{cb}^*}\right). \tag{2.18}$$

The current best measurements of these angles are given in Table 2.4.

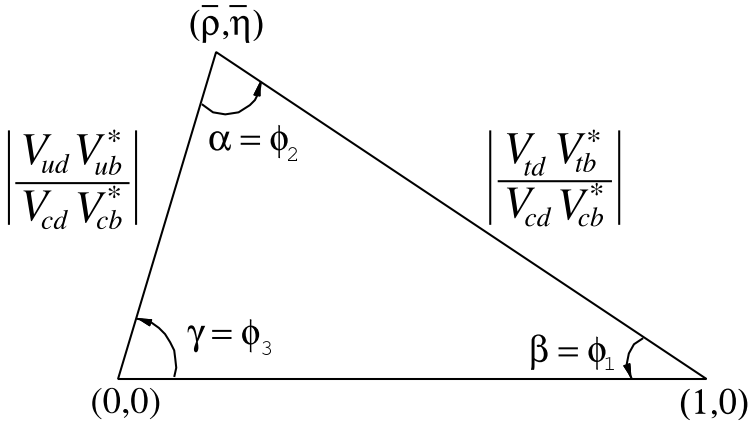

Figure 2.3: The most commonly used unitarity triangle, derived from the unitarity condition on the first and third columns of the CKM matrix [3].

Table 2.4: The current best experimental measurements of the angles of the unitarity triangle. Measurements of all three angles have a two-fold ambiguity, $\phi \to \phi + \pi$. *The measurement of $\sin 2\beta$ has an additional ambiguity, $\beta \to \pi/2 - \beta$, however, positive $\cos 2\beta$ solutions are preferred by other measurements and by the global fit [3].

Parameter	Value (°)
α	$85.4^{+3.9}_{-3.8}$
β	21.1 ± 0.9*
γ	$68.0^{+8.0}_{-8.5}$

A key goal of high energy physics is to use many independent measurements of CKM parameters to over constrain the CKM matrix. As has been shown, the CKM matrix only contains four independent parameters so measuring all of the elements and angles allows the consistency of the SM to be tested. Of particular interest among the three CKM angles is γ. This is the only angle that does not depend on the interactions of the top quark so it can be measured from tree-level processes, *i.e.* processes that proceed via diagrams that do not contain loops. Since "new physics" can enter into loop processes, a comparison of measurements from tree- and loop-level processes could reveal the first signs of physics beyond the SM. The current best experimental measurements of CKM parameters give good agreement with the SM. The non-vanishing unitarity conditions for the first and second rows and columns are all consistent with one and the sum of the three angles is consistent with 180°. These tests are summarised in Table 2.5.

Table 2.5: Quantities that test the unitarity of the CKM matrix [3].

Quantity	SM value	Experimental value
$\lvert V_{ud}\rvert^2 + \lvert V_{us}\rvert^2 + \lvert V_{ub}\rvert^2$	1	0.9999 ± 0.0006
$\lvert V_{cd}\rvert^2 + \lvert V_{cs}\rvert^2 + \lvert V_{cb}\rvert^2$	1	1.024 ± 0.032
$\lvert V_{ud}\rvert^2 + \lvert V_{cd}\rvert^2 + \lvert V_{td}\rvert^2$	1	1.000 ± 0.004
$\lvert V_{us}\rvert^2 + \lvert V_{cs}\rvert^2 + \lvert V_{ts}\rvert^2$	1	1.025 ± 0.032
$\alpha + \beta + \gamma$	180°	$(175 \pm 9)°$

A global fit is performed [27] incorporating all of the available measurements and assuming the SM for loop processes (unitarity in three generations). The constraints are shown in the $\bar{\rho} - \bar{\eta}$ plane in Fig. 2.4, the best fit values for the Wolfenstein parameters are given in Table 2.6 and the values obtained for the magnitudes of the nine CKM elements are

$$|V_{\rm CKM}| = \begin{pmatrix} 0.97427 \pm 0.00014 & 0.22536 \pm 0.00061 & 0.00355 \pm 0.00015 \\ 0.22522 \pm 0.00061 & 0.97343 \pm 0.00015 & 0.0414 \pm 0.0012 \\ 0.00886^{+0.00033}_{-0.00032} & 0.0405^{+0.0011}_{-0.0012} & 0.99914 \pm 0.00005 \end{pmatrix}. \quad (2.19)$$

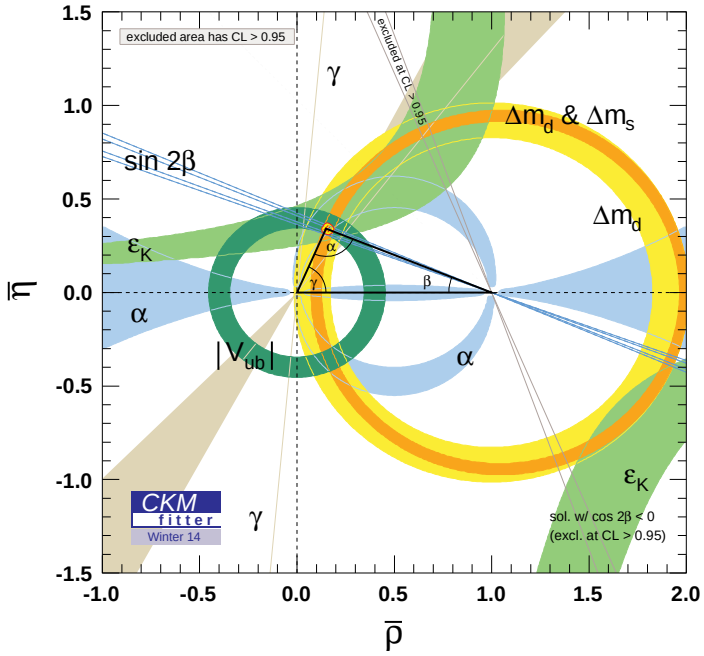

Figure 2.4: Current experimental constraints on the CKM unitarity triangle [27].

Table 2.6: Best fit values to the Wolfenstein parameters [27].

Parameter	Value
λ	0.22537 ± 0.00061
A	$0.814\,^{+0.023}_{-0.024}$
$\bar{\rho}$	0.117 ± 0.021
$\bar{\eta}$	0.353 ± 0.013

2.4 Measuring the CKM angle γ

Of the three angles in the CKM Unitarity Triangle, the angle γ has been measured with the least precision. As mentioned in Sec. 2.3.2, this angle is also of interest because it can be measured in tree-level processes. Processes that occur via loop diagrams can be affected by physics beyond the SM so, by comparing measurements from tree-level and loop-level processes, one can look for discrepancies that would indicate the presence of new physics. The respective constraints on the Unitarity Triangle from tree-level and loop-level processes are shown in Fig. 2.5.

Sensitivity to the CKM angle γ comes from the interference between diagrams containing V_{ub} and V_{cb} vertices in $B \to DX$ decays such as those shown in Sec. 2.4.3

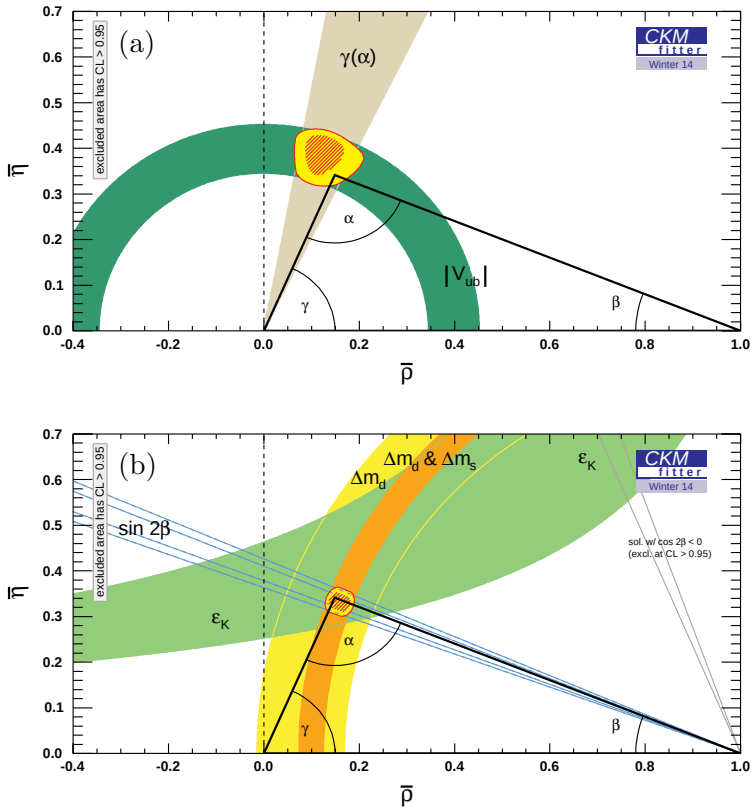

Figure 2.5: Constraints on the CKM Unitarity Triangle from measurements of (a) tree-level and (b) loop-level processes [27].

(Fig. 2.7) for $B^0 \to {}^{(}\overline{D}{}^{)0}K^+\pi^-$ decays. A selection of these decays are discussed below.

2.4.1 Counting analyses

Counting analyses involve measuring the yields observed for a decay and its charge conjugate, and relating the asymmetry of these yields to γ. This technique is used to study two-body or quasi-two-body decays such as $B^+ \to {}^{(}\overline{D}{}^{)0}K^+$ and $B^0 \to {}^{(}\overline{D}{}^{)0}K^*(892)^0$. Three methods used to extract γ-sensitive observables from these decays are described below (all named after their inventors): Gronau, London, Wyler (GLW) [29]; Atwood, Dunietz, Soni (ADS) [30]; Giri, Grossman, Soffer, Zupan (GGSZ) [31].

GLW

The GLW method uses $\overset{(}{D}\overset{)}{}^0$ decays to *CP* eigenstates such as K^+K^- and $\pi^+\pi^-$. The decays of D^0 and $\overline{D}^0$ mesons to these final states are indistinguishable when the initial flavour of the $\overset{(}{D}\overset{)}{}^0$ meson is not tagged. The different quark couplings in the weak decay of the B meson and the different rescattering effects in the B decay introduce phase differences of γ and δ_B, respectively, between these two pathways. The amplitudes due to the two pathways are related by

$$A_{b\to u} = r_B e^{i(\delta_B \pm \gamma)} A_{b\to c}\,, \tag{2.20}$$

where r_B parameterises the ratio of the magnitudes. The sign in front of the weak phase, γ, is positive for B^+ decays and negative for B^- decays.

Decays to *CP* eigenstates proceed via the *CP* eigenstates of the neutral D meson system, $D_{CP+} = \frac{D^0+\bar{D}^0}{\sqrt{2}}$ and $D_{CP-} = \frac{D^0-\bar{D}^0}{\sqrt{2}}$, where the phase convention has been defined by $CP\left|D^0\right\rangle = +\left|\overline{D}^0\right\rangle$ and the effects of D mixing and *CP* violation in the D decay have been neglected. The decay width, *e.g.* of $B^\pm \to D_{CP+}K^\pm$, can hence be written in terms of γ, δ_B and r_B as:

$$\Gamma\left(B^\pm \to D_{CP+}K^\pm\right) = |A_B|^2\,|A_D|^2\left|1 + r_B e^{i(\delta_B\pm\gamma)}\right|^2\,, \tag{2.21}$$

where A_B and A_D are the amplitudes of the $B^- \to \overline{D}^0 K^-$ decay and the subsequent D_{CP+} decay, respectively. These decay widths can then be related to observables such as the *CP* asymmetry:

$$A_{CP\pm} = \frac{\Gamma\left(B^- \to D_{CP\pm}K^-\right) - \Gamma\left(B^+ \to D_{CP\pm}K^+\right)}{\Gamma\left(B^- \to D_{CP\pm}K^-\right) + \Gamma\left(B^+ \to D_{CP\pm}K^+\right)} = \frac{\pm 2 r_B \sin\delta_B \sin\gamma}{1 + r_B^2 \pm 2 r_B \cos\delta_B \cos\gamma}\,. \tag{2.22}$$

ADS

The ADS method uses quasi-flavour-specific $\overset{(}{D}\overset{)}{}^0$ decays such as the decay to the $K^+\pi^-$ final state, which is CKM-favoured for the $\overline{D}^0$ state but CKM-suppressed for the D^0, and the π^+K^- state, which is favoured for the D^0 and suppressed for the $\overline{D}^0$. In addition to the different B decay amplitudes, this method must account for the different D^0 and $\overline{D}^0$ decay amplitudes present in the two pathways, which introduce an additional magnitude factor, r_D and an additional phase difference, δ_D. Including these factors, the amplitudes due to the two pathways are related by

$$A_{b\to u} = r_B r_D e^{i(\delta_B \pm \gamma + \delta_D)} A_{b\to c}\,, \tag{2.23}$$

for the favoured $K^+\pi^-$ final state and

$$A_{b\to u} = \frac{r_B}{r_D} e^{i(\delta_B \pm \gamma - \delta_D)} A_{b\to c}\,, \tag{2.24}$$

for the suppressed π^+K^- final state. As in the GLW case, the decay widths, *e.g.* of $B^\pm \to D_{K\pi}K^\pm$ and $B^\pm \to D_{\pi K}K^\pm$, can be written as:

$$\Gamma\left(B^\pm \to D_{K\pi}K^\pm\right) = |A_B|^2 |A_D|^2 \left|1 + r_D r_B e^{i(\delta_B+\delta_D\pm\gamma)}\right|^2, \tag{2.25}$$

$$\Gamma\left(B^\pm \to D_{\pi K}K^\pm\right) = |A_B|^2 |A_D|^2 \left|r_D + r_B e^{i(\delta_B-\delta_D\pm\gamma)}\right|^2, \tag{2.26}$$

where the subscripts, $K\pi$ and πK, denote the superpositions of flavour states that decay to the $K^+\pi^-$ and π^+K^- final states, respectively. The *CP* asymmetries, in this case, are given by

$$A_{K\pi} = \frac{r_B r_D \sin(\delta_B+\delta_D)\sin\gamma}{1 + (r_B r_D)^2 + 2 r_B r_D \cos(\delta_B+\delta_D)\cos\gamma}\,, \tag{2.27}$$

$$A_{\pi K} = \frac{r_B r_D \sin(\delta_B-\delta_D)\sin\gamma}{r_B^2 + r_D^2 + 2 r_B r_D \cos(\delta_B-\delta_D)\cos\gamma}\,, \tag{2.28}$$

where the effects of neutral D mixing have been neglected. Additional observables can be constructed by also considering the non-charge-averaged ratio of the suppressed π^+K^- decay mode to the favoured $K^+\pi^-$ mode:

$$R^\pm = \frac{\Gamma(B^\pm \to D_{\pi K}K^\pm)}{\Gamma(B^\pm \to D_{K\pi}K^\pm)} = \frac{r_B^2 + r_D^2 + 2 r_B r_D \cos(\delta_B - \delta_D \pm \gamma)}{1 + (r_B r_D)^2 + 2 r_B r_D \cos(\delta_B + \delta_D \pm \gamma)}\,. \tag{2.29}$$

GLW and ADS observables have been measured at LHCb with two-body ${}^{(}\overline{D}{}^{)}0$ decays for $B^\pm \to {}^{(}\overline{D}{}^{)}0 K^\pm$ and $B^\pm \to {}^{(}\overline{D}{}^{)}0 \pi^\pm$ decays [32], for $B^0_{(s)} \to {}^{(}\overline{D}{}^{)}0 {}^{(}\overline{K}{}^{)}*(892)^0$ decays [33], and also for $B^+ \to {}^{(}\overline{D}{}^{)}0 K^+\pi^+\pi^-$ and $B^+ \to {}^{(}\overline{D}{}^{)}0 \pi^+\pi^+\pi^-$ decays [34]. In addition, observables have been measured from $B^\pm \to {}^{(}\overline{D}{}^{)}0 K^\pm$ decays with four body ADS decays of the ${}^{(}\overline{D}{}^{)}0$ [35].

GGSZ

The GGSZ method uses the three-body self-conjugate decays ${}^{(}\overline{D}{}^{)}0 \to K^0_S\pi^+\pi^-$ and ${}^{(}\overline{D}{}^{)}0 \to K^0_S K^+K^-$. In these decays, the phase difference introduced by the ${}^{(}\overline{D}{}^{)}0$ decay, δ_D, and the ratio of amplitudes, r_D, vary across the Dalitz plot (DP). The

distribution of decays across the $\overline{(}D\overline{)}^0$ DP is given by the probability density function

$$S_{\pm}\left(m^2_{\pm}, m^2_{\mp}\right) = \left| f\left(m^2_{\pm}, m^2_{\mp}\right) + r_B e^{i(\delta_B \pm \gamma)} f\left(m^2_{\mp}, m^2_{\pm}\right) \right|^2 , \tag{2.30}$$

where f describes the complex amplitude associated with the D^0 decay across the DP and $m^2_{\pm}$ is the invariant mass squared of the neutral kaon with the $\pi^{\pm}$ meson. To improve the stability of fits to data, an alternative parameterisation is often used, defined by

$$x_{\pm} + iy_{\pm} = r_B e^{i(\delta_B \pm \gamma)} . \tag{2.31}$$

This parameterisation effectively allows r_B to take different values in the simultaneous fits to the *CP*-conjugate decays. The constraint $x^2_+ + y^2_+ = x^2_- + y^2_- = r^2_B$ is applied in a second step to determine γ from the observables.

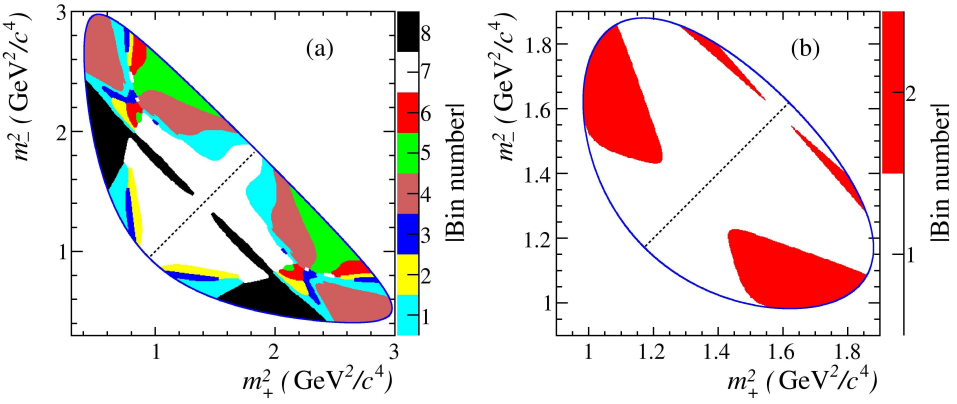

Figure 2.6: Binning schemes in the (a) $\overline{(}D\overline{)}^0 \to K^0_S\pi^+\pi^-$ and (b) $\overline{(}D\overline{)}^0 \to K^0_S K^+K^-$ DPs, chosen to maximise sensitivity to γ [36]. The diagonal line separates positive and negative bins, which are symmetric under the exchange of m^2_+ and m^2_-.

At LHCb two approaches have been taken to extract γ from $B^{\pm} \to D_{K^0_S hh}K^{\pm}$ decays. A model-independent approach [37] divides the $\overline{(}D\overline{)}^0$ DP into bins, as shown in Fig. 2.6 for the $K^0_S\pi^+\pi^-$ and $K^0_S K^+K^-$ DPs, and defines the yield in each bin, i, as

$$N^+_{\pm i} = h_+ \left(K_{\mp i} + (x^2_+ + y^2_+)K_{\pm i} + 2\sqrt{K_i K_{-i}}(x_+ c_{\pm i} \mp y_+ s_{\pm i}) \right) , \tag{2.32}$$

$$N^-_{\pm i} = h_- \left(K_{\pm i} + (x^2_- + y^2_-)K_{\mp i} + 2\sqrt{K_i K_{-i}}(x_- c_{\pm i} \mp y_- s_{\pm i}) \right) , \tag{2.33}$$

where the superscripts "+" and "−" label the *CP*-conjugate B decays, K_i is the yield in bin i from flavour-tagged D^0 decays as seen in DP models reported by BaBar [38, 39], and c_i and s_i are the average cosine and sine of the strong phase,

δ_D, in bin i as measured by CLEO-c [40]. The *CP*-parameters $x_\pm$ and $y_\pm$ and the normalisation factors $h_\pm$ are determined from a fit to data. The second approach is model-dependent [41] and involves using Eq. 2.30 to describe the distribution of decays observed across the $^{(}\overline{D}^{)}0$ DP, where f is obtained from the BaBar models [38, 39]. Unlike the model-independent approach, this method goes beyond a simple counting analysis and, therefore, offers improved statistical sensitivity to γ.

Compared to the GLW/ADS approach, the GGSZ method gives far greater sensitivity to γ. The main disadvantage of this method is the need to first understand the $^{(}\overline{D}^{)}0 \to K^0_S hh$ DP.

2.4.2 Time-dependent analyses

In decays such as $B^0_s \to D^\mp_s K^\pm$, the flavour of the D^+_s meson is tagged by its charge so amplitudes corresponding to the two flavours do not interfere. In these decays, sensitivity to γ arises via flavour oscillations of the decaying B meson, *e.g.* the $B^0_s \to D^-_s K^+$ and $B^0_s \to \overline{B}^0_s \to D^-_s K^+$ decay pathways interfere with a relative phase of $\gamma - 2\beta_s$, where $-2\beta_s$ is the phase difference due to B^0_s – $\overline{B}^0_s$ mixing. These measurements can be combined with an independent measurement of β_s to obtain a measurement of γ. Alternatively, combined with an independent measurement of γ this gives a measurement of $-2\beta_s$. At LHCb, a measurement of γ has been obtained from a time-dependent analysis of $B^0_s \to D^\mp_s K^\pm$ decays [42].

2.4.3 Dalitz plot analyses

A DP analysis of $B^0 \to {}^{(}\overline{D}^{)}0 K^+\pi^-$, where D^0 and $\overline{D}^0$ decay to the same final state, can be used to measure γ. Sensitivity to γ comes from interference between the diagrams shown in Fig. 2.7. While D^{**-} resonances and D^{**+}_s resonances are only produced via V_{cb} and V_{ub} diagrams, respectively, K^{**0} resonances are produced by both.

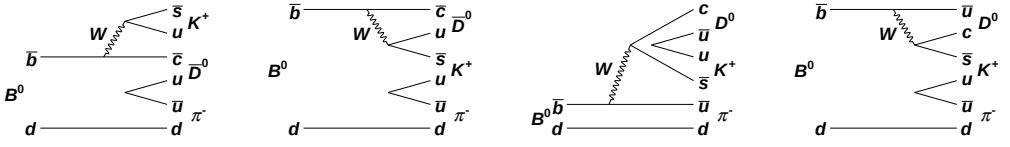

Figure 2.7: Decay diagrams for (left to right) CKM-favoured (V_{cb}) $B^0 \to \overline{D}^0 K^+\pi^-$ decays via D^{**-} and K^{**0} resonances, and CKM-suppressed (V_{ub}) $B^0 \to D^0 K^+\pi^-$ decays via D^{**+}_s and K^{**0} resonances.

When the $^{(}\overline{D}^{)}0$ meson decays to a *CP* eigenstate, D_{CP}, such that the flavour of the meson is unknown, all four of the diagrams in Fig. 2.7 can contribute to the

decay amplitude. Where these amplitudes contribute at the same point in phase space, they interfere giving sensitivity to γ. A method to determine γ, using the interference in the DP, was proposed in Ref. [43] and is illustrated in Fig. 2.8. The method utilises DP analyses of $B^0 \to \overline{D}^0 K^+\pi^-$ and $B^0 \to D_{CP} K^+\pi^-$ decays, where the second DP description includes *CP*-violating terms such that amplitudes may differ between the DPs of the B^0 and $\overline{B}^0$ decays. Because the D^{**-} resonances enter all three DPs with the same phases, a single resonance (*e.g.* the $D_2^*(2460)$ state) can be chosen to serve as a reference between the DPs. If a K^{**0} resonance has a phase, Δ, relative to the reference component in the $B^0 \to \overline{D}^0 K^+\pi^-$ DP, then the relative phases of the $b \to u$ amplitudes in the $B^0 \to D_{CP} K^+\pi^-$ and $\overline{B}^0 \to D_{CP} K^-\pi^+$ DPs are given by $\Delta + \delta_B + \gamma$ and $\Delta + \delta_B - \gamma$, respectively, where δ_B and γ are the strong and weak phases associated with the decay $B^0 \to \overline{D}^0 K^{*0}$. The complex amplitudes are related by the equations:

$$A(B^0 \to \overline{D}^0 K^{*0}) = \rho e^{i\Delta} A(B^0 \to D_2^{*-} K^+)\,, \tag{2.34}$$

$$A(\overline{B}^{(0)} \to D_{CP}\,\overline{K}^{(*0)}) = \rho e^{i\Delta}(1 + r_B e^{i(\delta_B \pm \gamma)}) A(B^0 \to D_2^{*-} K^+)\,. \tag{2.35}$$

As the complex amplitudes associated with the $K^*(892)^0$ in the three DPs are parameterised by only five quantities, ρ, Δ, r_B, δ_B and γ, a measurement of γ may be extracted using only the $D_2^*(2460)^-$ and $K^*(892)^0$ resonances. However, if other K^{**0} resonances (*e.g.* $K_0^*(1430)$ or $K_2^*(1430)$) make a significant contribution to the DP, and if the values of r_B corresponding to these decays are large, then they may improve the overall sensitivity to γ. Compared to the quasi-two-body GLW/ADS

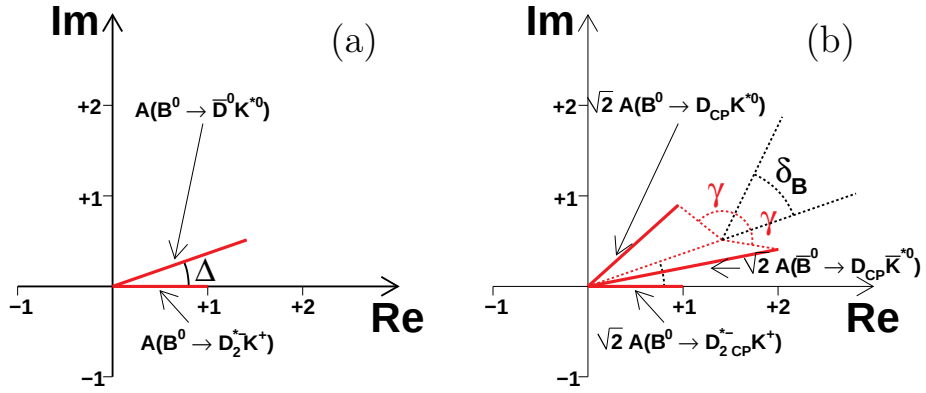

Figure 2.8: Argand diagrams demonstrating how DP analyses of (a) $B^0 \to \overline{D}^0 K^+\pi^-$ and (b) $B^0 \to D_{CP} K^+\pi^-$ decays can be utilised to extract a measurement of the CKM angle γ [43].

analysis of $B^0 \to \overline{D}^0 K^{*0}$ decays, the sensitivity to γ of a DP analysis is found to be significantly less dependent on the value of δ_B [44]. In addition, the eight-fold ambiguity in γ and δ_B inherent in the GLW two-body measurements is reduced to a two-fold ambiguity.

2.5 Dalitz plot formalism

In the decay of a pseudoscalar particle to three pseudoscalar daughters, the kinematics of the decay are uniquely defined by two variables [45]. These variables form the DP and are commonly chosen to be two of the three two-body invariant masses (see Fig. 2.9). The third two-body invariant mass is fixed by the relationship, $m_{12}^2 + m_{13}^2 + m_{23}^2 = m_B^2 + m_1^2 + m_2^2 + m_3^2$, where the three daughters are labelled 1, 2 and 3, and B labels the decaying mother particle.

The three-body decay can be due to multiple underlying channels. These channels may be resonant, where the mother first decays via a weak process into two particles and one of these particles (the resonance) quickly decays via a strong process into two daughters. As shown in Fig. 2.9, resonances in two of the two-body pairs form horizontal and vertical bands in the DP. Resonances in the third pair produce diagonal bands running from top-left to bottom-right with low-mass resonances appearing closer to the upper-right kinematic limit. The decay may also proceed via intermediate states that do not correspond to a resonance but that do correspond to a given spin in one of the daughter pairs. All of the resonant and nonresonant contributions with the same spin in the same pair of daughters can be grouped together as a "partial wave".

Due to conservation of angular momentum in the initial two-body decay, the spin of the resonance is polarised along its own direction of flight in the rest frame of the mother particle. As described further in Sec. 2.5.1, the angular probability distribution of the resonance decay, with respect to the resonance's spin axis, depends on the spin of the resonance. This information is extracted from the distribution of values taken by the helicity angle over many events. The helicity angle is defined as the angle between the momenta of one of the resonance daughters and the daughter produced directly from the mother decay (the bachelor) in the rest frame of the resonance. This angular distribution leads to the structure seen in Fig. 2.9, where the number of "dips" along the band produced by a resonance corresponds to the spin of that resonance.

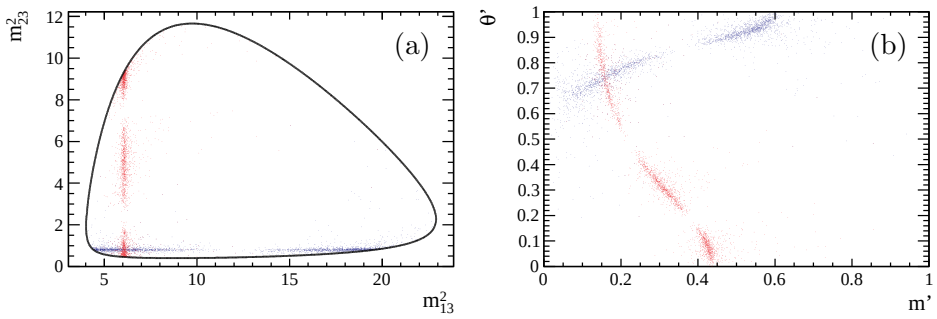

Figure 2.9: (a) Example of a DP ($B^0_s \to \overline{D}^0 K^- \pi^+$) with (red) a tensor resonance in m_{13} and (blue) a vector resonance in m_{23}. The black contour marks the kinematic boundary of the DP. Also shown, (b) are the same data mapped onto the square Dalitz plot phase space (Eq. 2.52).

2.5.1 The isobar model

The contents of the DP can be parameterised using the isobar model [46–48], which constructs the complex amplitude across the DP phase space from the coherent sum of multiple resonant and nonresonant terms:

$$\mathcal{A}(m^2_{13}, m^2_{23}) = \sum_{j=1}^{n} c_j F_j(m^2_{13}, m^2_{23}) \ , \tag{2.36}$$

where c_j is a complex coefficient associated with the contribution from the channel described by the dynamical amplitude F_j. The amplitude for each contribution is composed of invariant-mass and angular distributions, and is normalised such that the integral over the phase space is unity. For example, a resonance in m_{13} is given by

$$F(m^2_{13}, m^2_{23}) = R(m_{13}) \times X(|\vec{p}|\, r_{\rm BW}) \times X(|\vec{q}|\, r_{\rm BW}) \times T(\vec{p}, \vec{q}) \ , \tag{2.37}$$

where the functions R, X and T are the resonance mass term, the Blatt–Weisskopf barrier factor term [49] and the angular term, respectively, and $\vec{p}$ and $\vec{q}$ are the momenta of the bachelor particle and one of the resonance daughters. Both $\vec{p}$ and $\vec{q}$ are evaluated in the rest frame of the resonance.

The two Blatt–Weisskopf barrier factors [49] correspond to the decays of the mother particle and the resonance. These are dependent on the spin of the resonance,

L, and are given by

$$L = 0 \;:\; X(z) = 1\,, \tag{2.38}$$

$$L = 1 \;:\; X(z) = \sqrt{\frac{1+z_0^2}{1+z^2}}\,, \tag{2.39}$$

$$L = 2 \;:\; X(z) = \sqrt{\frac{z_0^4+3z_0^2+9}{z^4+3z^2+9}}\,, \tag{2.40}$$

$$L = 3 \;:\; X(z) = \sqrt{\frac{z_0^6+6z_0^4+45z_0^2+225}{z^6+6z^4+45z^2+225}}\,, \tag{2.41}$$

where $z = |\vec{p}|\, r_{\rm BW}$, $r_{\rm BW}$ is the radius of the barrier[2] and the subscript 0 denotes the value of a quantity evaluated at the pole mass, m_0, of the resonance.

The angular probability distribution term, $T(\vec{p},\vec{q})$, can either be described by the helicity formalism, which allows for a longitudinal component in the resonance propagator, or by the Zemach tensor formalism which enforces transversality. In B decays, the available phase space requires the description of the resonance amplitude to be well-behaved at masses significantly different from the pole mass. This is achieved by enforcing transversality, so the Zemach tensors are used giving [50, 51]

$$L = 0 \;:\; T(\vec{p},\vec{q}) = 1\,, \tag{2.42}$$

$$L = 1 \;:\; T(\vec{p},\vec{q}) = -2\,\vec{p}\cdot\vec{q}, \tag{2.43}$$

$$L = 2 \;:\; T(\vec{p},\vec{q}) = \frac{4}{3}\left[3(\vec{p}\cdot\vec{q})^2 - (|\vec{p}||\vec{q}|)^2\right]\,, \tag{2.44}$$

$$L = 3 \;:\; T(\vec{p},\vec{q}) = -\frac{24}{15}\left[5(\vec{p}\cdot\vec{q})^3 - 3(\vec{p}\cdot\vec{q})(|\vec{p}||\vec{q}|)^2\right]\,, \tag{2.45}$$

which are proportional to the Legendre polynomials, $P_L(x)$, where x is the cosine of the helicity angle (the angle between $\vec{p}$ and $\vec{q}$).

Various mass terms are used to describe different types of resonant and nonresonant contributions. The most common types are described below, but further shapes are discussed in App. A. The mass term for the majority of resonances can be described by the relativistic Breit–Wigner (RBW) function,

$$R(m) = \frac{1}{m_0^2 - m^2 - i m_0 \Gamma(m)}, \tag{2.46}$$

[2] In this thesis, the barrier radii are taken to be $4\,\mathrm{GeV}^{-1} \approx 0.8\,\mathrm{fm}$ for all resonances unless otherwise stated.

where the decay width, $\Gamma(m)$, is dependent on m and is given by

$$\Gamma(m) = \Gamma_0 \left(\frac{q}{q_0}\right)^{2L+1} \left(\frac{m_0}{m}\right) X^2(qr_{\rm BW}), \tag{2.47}$$

where $q = |\vec{q}|$ and, as before, the subscript 0 indicates parameters evaluated at the pole mass.

This shape can also be used to describe contributions from resonances whose pole masses lie outside the kinematically allowed phase space. These contributions are labelled virtual and, when calculating q_0 for these contributions, the pole mass, m_0, must be set to an effective mass, $m_0^{\rm eff}$, within the phase space. This is achieved using the formula

$$m_0^{\rm eff}(m_0) = m^{\rm min} + \frac{1}{2}\left(m^{\rm max} - m^{\rm min}\right)\left(1 + \tanh\left(\frac{m_0 - \frac{m^{\rm min}+m^{\rm max}}{2}}{m^{\rm max} - m^{\rm min}}\right)\right), \tag{2.48}$$

where $m^{\rm min}$ and $m^{\rm max}$ are the limits of the kinematically allowed mass range [52]. Only the tails of such virtual contributions enter the DP.

The DP can also contain slowly-varying contributions that are not associated with a resonance. These nonresonant components can be parameterised by an ad-hoc exponential form factor (EFF) [53],

$$R(m) = e^{-\alpha m^2}, \tag{2.49}$$

where α is a fit parameter to be determined from a fit to data.

While most resonances are described well by the RBW function, the presence of broad overlapping RBW resonances in the same partial wave violates unitarity. Such broad resonances are common in low-spin partial waves. In particular, the $K_0^*(1430)$ resonance interferes strongly with a nonresonant S-wave term and requires a different approach. The LASS lineshape [54] combines these two amplitudes:

$$R(m) = \frac{m}{q\cot\delta_B - iq} + e^{2i\delta_B}\frac{m_0\Gamma_0\frac{m_0}{q_0}}{m_0^2 - m^2 - im_0\Gamma_0\frac{q}{m}\frac{m_0}{q_0}}, \tag{2.50}$$

$$\text{where } \cot\delta_B = \frac{1}{aq} + \frac{1}{2}rq\,, \tag{2.51}$$

m_0 and Γ_0 are the pole mass and width of the $K_0^*(1430)$ state, respectively, and a and r are shape parameters. This parameterisation was originally introduced to model $K\pi$ scattering at invariant masses below $1.6\,\text{GeV}/c^2$ so the slow-varying part (the first term in Eq. 2.50) is not well described at high masses. A cutoff to this

term is introduced close to the charm hadron mass.[3]

2.5.2 The square Dalitz plot

Since, particularly in B decays, events tend to populate regions of the DP close to the kinematic boundaries, it is useful to define the square Dalitz plot (SDP), which uses the parameters

$$m' \equiv \frac{1}{\pi} \arccos\left(2\frac{m_{12} - m_{12}^{\min}}{m_{12}^{\max} - m_{12}^{\min}} - 1\right) \qquad \text{and} \qquad \theta' \equiv \frac{1}{\pi}\theta_{12}\,, \tag{2.52}$$

where $m_{12}^{\min} = m_1 + m_2$ and $m_{12}^{\max} = m_B - m_3$ are the minimum and maximum kinematically allowed values of m_{12}. In these parameters, the kinematically-allowed phase space is mapped to a unit square, as shown in Fig. 2.9 (b), and the interesting regions of the phase space are enlarged. The SDP is particularly useful for describing background contributions and efficiencies, which must be evaluated from simulated data and are generally described by histograms.

2.5.3 Fitting the Dalitz plot

The probability density for signal events across the DP, in the absence of any acceptance considerations, is given by

$$\mathcal{P}_{\text{phys}}\left(m_{13}^2, m_{23}^2\right) = \frac{|\mathcal{A}\left(m_{13}^2, m_{23}^2\right)|^2}{\iint_{\text{DP}} |\mathcal{A}\left(m_{13}^2, m_{23}^2\right)|^2 \, dm_{13}^2 \, dm_{23}^2}\,. \tag{2.53}$$

Once efficiency variations across the DP are considered this becomes

$$\mathcal{P}_{\text{sig}}\left(m_{13}^2, m_{23}^2\right) = \frac{\epsilon\left(m_{13}^2, m_{23}^2\right)|\mathcal{A}\left(m_{13}^2, m_{23}^2\right)|^2}{\iint_{\text{DP}} \epsilon\left(m_{13}^2, m_{23}^2\right)|\mathcal{A}\left(m_{13}^2, m_{23}^2\right)|^2 \, dm_{13}^2 \, dm_{23}^2}\,, \tag{2.54}$$

where the function, $\epsilon\left(m_{13}^2, m_{23}^2\right)$, parameterises the reconstruction and selection efficiency for signal events across the DP. This function can be obtained from a histogram produced using simulated data and corrected for known data-simulation differences.

The likelihood function that is maximised when fitting the DP is given by

$$\mathcal{L} = e^{-N} \prod_i^{N_e} \left[\sum_k N_k \mathcal{P}_k\left(m_{13,\,i}^2, m_{23,\,i}^2\right)\right], \tag{2.55}$$

[3] In the analyses described in this thesis, a cutoff at $1.7\,\text{GeV}/c^2$ is used unless otherwise stated.

where the indices i and k run over the N_e events and the signal and background categories, respectively. Here N_k is the number of events of category k in the data, N is equal to $\sum_k N_k$, and the probability densities for the background categories can be obtained from histograms.

As the amplitudes returned by a DP fit are convention-dependent, fit fractions are also reported, which provide a meaningful way to compare results between different fits. The fit fraction for a single fit component, j, is defined as

$$FF_j = \frac{\iint_{\mathrm{DP}} \left|c_j F_j\left(m_{13}^2, m_{23}^2\right)\right|^2 \, dm_{13}^2 \, dm_{23}^2}{\iint_{\mathrm{DP}} \left|\mathcal{A}\left(m_{13}^2, m_{23}^2\right)\right|^2 \, dm_{13}^2 \, dm_{23}^2} \,. \tag{2.56}$$

Due to interference effects, the sum of these fit fractions need not be unity. These interferences are given by the interference fit fractions, which are defined for $i < j$ as

$$FF_{ij} = \frac{\iint_{\mathrm{DP}} 2\,\mathrm{Re}\left[c_i c_j^* F_i\left(m_{13}^2, m_{23}^2\right) F_j\left(m_{13}^2, m_{23}^2\right)^*\right] \, dm_{13}^2 \, dm_{23}^2}{\iint_{\mathrm{DP}} \left|\mathcal{A}\left(m_{13}^2, m_{23}^2\right)\right|^2 \, dm_{13}^2 \, dm_{23}^2} \,. \tag{2.57}$$

Chapter 3

The LHC accelerator and the LHCb detector

3.1 The Large Hadron Collider

The Large Hadron Collider (LHC) [55], currently the world's highest-energy particle accelerator, is a proton–proton colliding synchrotron located at CERN. The machine is installed in the 27 km tunnel, spanning the Franco–Swiss border, that was formerly occupied by the Large Electron Positron collider.

The LHC is composed of repeating sequences of dipole and higher-order multipole magnets designed to bend, accelerate and compress the two beams of protons. These magnets comprise eight arcs connected by eight 528 m straight sections where detectors and utilities are inserted (identified as Points 1–8). Experiments are located at four of these points. The two general-purpose detectors, ATLAS [56] and CMS [57], are located diametrically opposite each other across the ring at points 1 and 5, respectively. The ALICE detector [58], designed to study heavy ion collisions during special lead–lead and proton–lead runs, is located at point 2 and the LHCb detector, which is described in detail in Sec. 3.2, is located at point 8. The layout of the LHC and the accelerator chain, used to inject protons into the beams, is shown in Fig. 3.1.

The LHC has a design energy of 7 TeV for each proton beam to give a collision centre-of-mass energy of 14 TeV. During the first data-taking run, the LHC collided protons at centre-of-mass energies of 7 TeV (2011) and 8 TeV (2012). The instantaneous luminosity of interactions is given by

$$\mathcal{L} = \frac{f N^2 n_b}{4\pi\sigma^2} F\,, \tag{3.1}$$

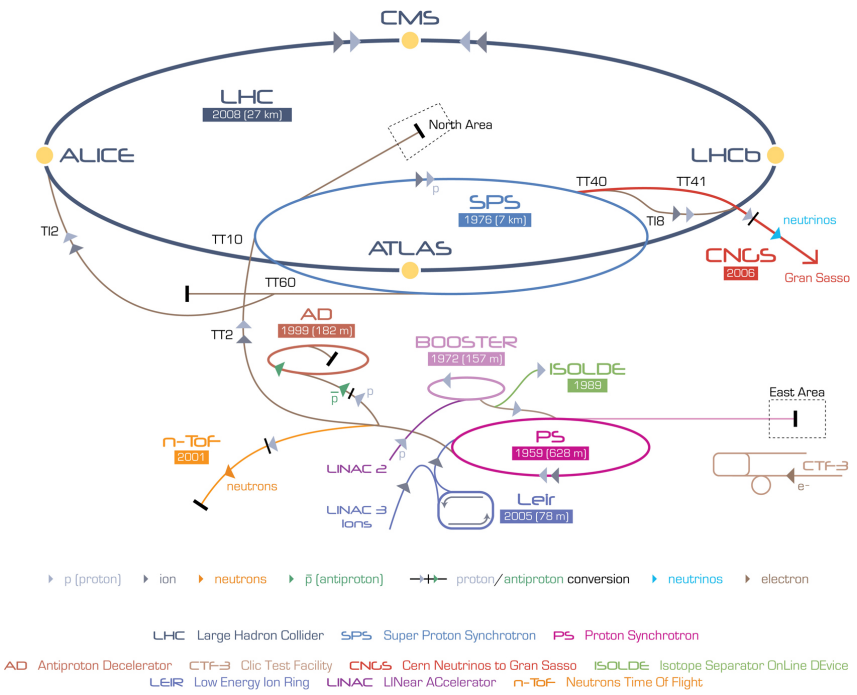

Figure 3.1: Layout of the CERN accelerator complex, reproduced from Ref. [59].

where f is the revolution frequency, N is the number of protons per bunch, n_b is the number of bunches in each beam, σ is the RMS radius of each beam and F is a geometrical reduction factor due to the beam crossing angle. The beam size is usually parameterised in terms of the normalised emittance, ϵ_n, and the beta function at the interaction point, β^*, giving

$$\mathcal{L} = \frac{fN^2 n_b \gamma}{4\pi\epsilon_n \beta^*} F\,, \tag{3.2}$$

where γ is the relativistic factor. During Run 1, the LHC achieved a peak luminosity of $7.7 \times 10^{33}\,\mathrm{cm}^{-2}\mathrm{s}^{-1}$ by colliding 1374 bunches of 1.7×10^{11} protons [60], and delivered integrated luminosities in excess of $28\,\mathrm{fb}^{-1}$ to the general-purpose detectors and $3\,\mathrm{fb}^{-1}$ to LHCb. In early 2013, the LHC entered into a long shutdown period to prepare the machine and the experiments to run at an increased energy. This second run started in early 2015.

3.2 The LHCb detector

The LHCb detector [61] is a single-arm spectrometer in the forward region covering an angular range from 10 mrad to 300 mrad (250 mrad) in the bending (non-bending)

planes of the dipole magnet. This angular coverage corresponds to a pseudorapidity range of approximately $2 < \eta < 5$, where pseudorapidity is defined in terms of the angle from the beamline, θ, as

$$\eta = -\ln\left(\tan\left(\theta/2\right)\right) , \tag{3.3}$$

or for a particle of momentum, p, and longitudinal momentum, p_{L}, as

$$\eta = \frac{1}{2}\ln\left(\frac{p + p_{\mathrm{L}}}{p - p_{\mathrm{L}}}\right) . \tag{3.4}$$

This range was chosen to maximise the acceptance for b- and c-hadrons which are predominantly produced in pairs in the forward and backward regions at the LHC. The layout of the LHCb detector is shown in Fig. 3.2 with the z-axis pointing along the beamline and the y-axis pointing vertically up.

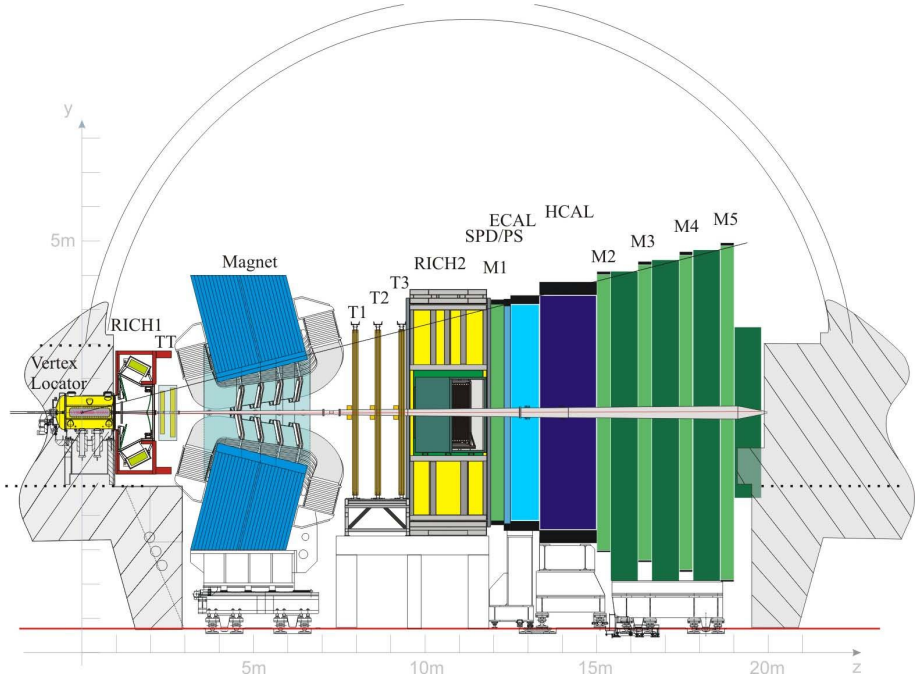

Figure 3.2: Side-view schematic of the LHCb detector with the subdetectors labelled. Figure reproduced from Ref. [61].

A key signature of b- and c-hadron decays is a displaced secondary vertex. The identification of these decays in the LHCb detector, therefore, requires precise tracking close to the interaction point and triggering based on fast vertex reconstruction. The LHCb detector was designed to run at a reduced instantaneous luminosity of $2 \times 10^{32}\,\mathrm{cm}^{-2}\mathrm{s}^{-1}$ to reduce the number of interactions per bunch crossing (hence

speeding up vertex reconstruction) and to reduce the radiation damage to the detector (allowing for instrumentation closer to the beam pipe). While the detector has been run at intensities up to $4 \times 10^{32}\,\mathrm{cm}^{-2}\mathrm{s}^{-1}$, this is still a factor of 20 below the peak luminosity of the LHC. This lower luminosity was achieved through beam displacement luminosity levelling — the beams are displaced at the interaction point and this displacement is varied throughout each fill to achieve a constant luminosity. The following sections will cover the main components of the LHCb detector: the dipole magnet is described in Sec. 3.2.1, the vertex locator (VELO) and the rest of the tracking system in Sec. 3.2.2 and Sec. 3.2.3, respectively, the ring imaging Cherenkov (RICH) detectors in Sec. 3.2.4, the calorimeters in Sec. 3.2.5 and the muon detectors in Sec. 3.2.6. In addition, the trigger, the online system and relevant software are covered in Sec. 3.2.7, Sec. 3.2.8, and Sec. 3.2.9, respectively.

3.2.1 The dipole magnet

The LHCb detector utilises a dipole magnet [62] to deflect charged particles allowing their momenta to be measured. The magnet is aligned to bend particle tracks in the horizontal plane and provides an integrated magnetic field of 4 Tm over a 10 m track length. A warm magnet was chosen over a super-conducting magnet due to economic and time constraints. The magnet consists of symmetric saddle-shaped coils in a large rectangular yoke with poles sloped to match the required acceptance as shown in Fig. 3.3. The polarity of the magnet is inverted periodically to allow the effects of any detector asymmetry to be understood.

3.2.2 The vertex locator

The VELO [63, 64] provides precise tracking close to the pp interaction point and is used to identify the displaced secondary vertices seen in b- and c- hadron decays. It consists of a series of modules positioned within and immediately after the interaction region, as shown in Fig. 3.4 (a), to track charged particles immediately after they are produced. Because of its proximity to the beams, the VELO is composed of two halves which can be separated as shown in Fig. 3.4 to provide the larger aperture required during beam injections. Once stable beams have been achieved, the VELO is closed again to collect data.

Each VELO module has two layers of silicon microstrip detectors orientated radially and azimuthally, used to reconstruct the tracks of charged particles close to the point of decay. This not only allows tracks to be traced back to the primary vertex (PV) but also enables reconstruction of secondary vertices, a common feature

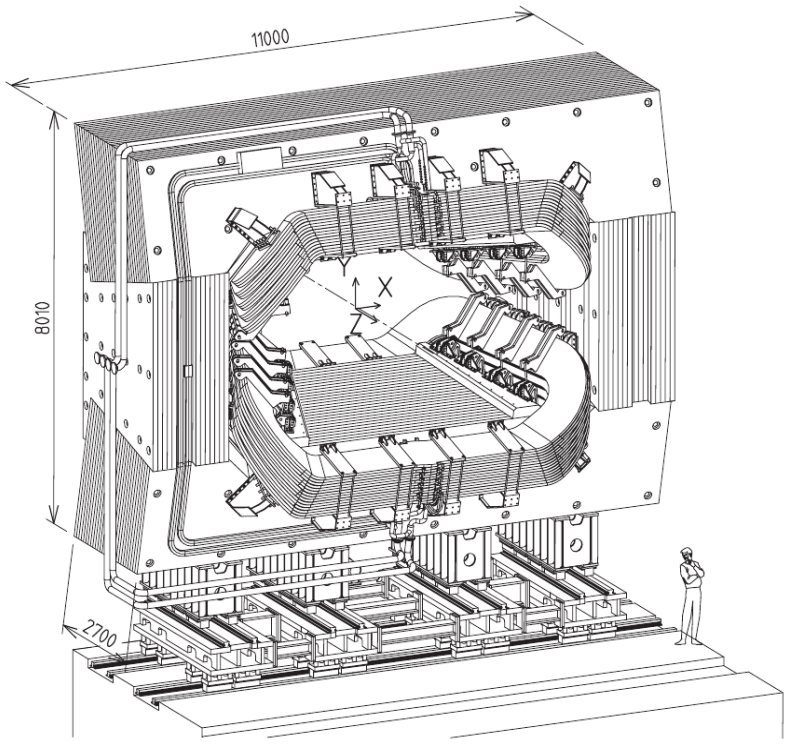

Figure 3.3: The LHCb dipole magnet. Figure reproduced from Ref. [61].

of b-hadron decays, which correspond to particles being formed at the PV, flying a short distance ($\mathcal{O}(1\,\text{cm})$) and decaying before exiting the VELO. The modules are positioned to ensure that tracks over a wide range of angles pass through at least four stations to allow reconstruction.[1] The pile-up veto system consists of two modules upstream of the VELO and was designed to distinguish between events with a single visible pp interaction and those with multiple PVs.

3.2.3 The tracking system

The tracking system consists of the Tracker Turicensis (TT), the Inner Tracker (IT) [65] and the Outer Tracker (OT) [66, 67], as shown in Fig. 3.5. Each of the stations T1 – T3 (labelled in Fig. 3.2) has a central region and a peripheral region, which collectively comprise the IT and OT, respectively. The TT and IT are collectively known as the Silicon Tracker (ST) since both consist of silicon microstrip detectors. Each of the stations of the ST has four layers of detectors with strips aligned vertically in the first and final layers and rotated by $+5^\circ$ and -5° respectively in the second and third layers. The OT is a drift-time detector for tracking charged

[1] Reconstruction of a VELO track requires a minimum of three radial and three azimuthal hits.

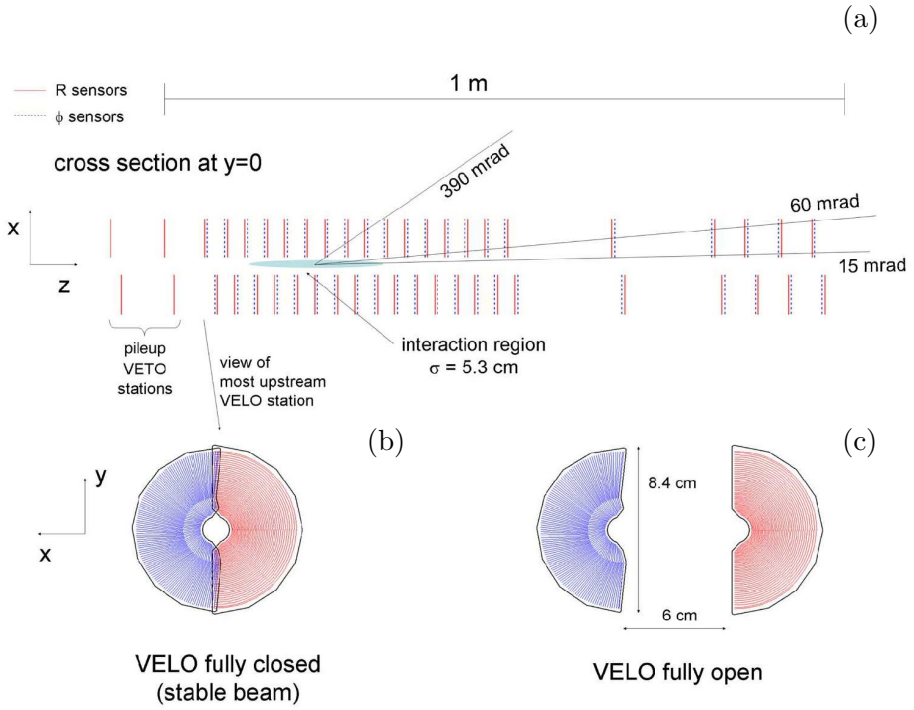

Figure 3.4: (a) Top view of the distribution of modules along the beamline within the VELO, and front views of a pair of modules in the (b) closed and (c) open positions. Figure reproduced from Ref. [61].

particles and measuring their momenta. It consists of straw tube modules filled with a mixture of Argon and CO_2. Inside these modules are drift tubes, which consist of two coaxial electrodes with a potential difference maintained between them. When a charged particle traverses the tube, the gas inside it is ionised, releasing electrons which drift to the positive electrode and produce a current. Each of the three stations of the OT is made up of four layers of modules orientated in the same way as in the ST.

3.2.4 The RICH detectors

The two RICH detectors (RICH1 upstream of the dipole magnet and RICH2 downstream) [68,69] provide particle identification (PID) information that allows different types of charged particles to be distinguished — particularly pions, kaons and protons. Particles pass through different radiator materials (aerogel and C_4F_{10} in RICH1, CF_4 in RICH2) at speeds exceeding the local speed of light. These particles emit Cherenkov radiation which is focussed by flat and spherical mirrors onto hybrid photon detectors outside the angular acceptance of the detector as shown in Fig. 3.6.

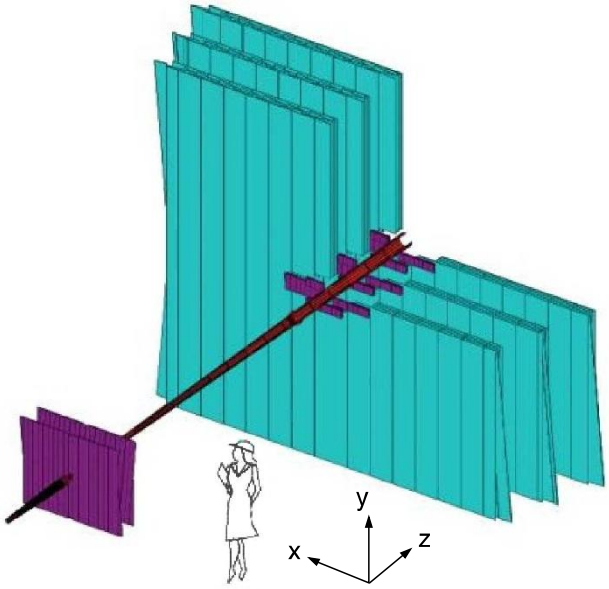

Figure 3.5: The layout of the (purple) ST and (cyan) OT around the beamline. The TT is to the left, while the T1 – T3 stations are on the right. Figure reproduced from Ref. [61].

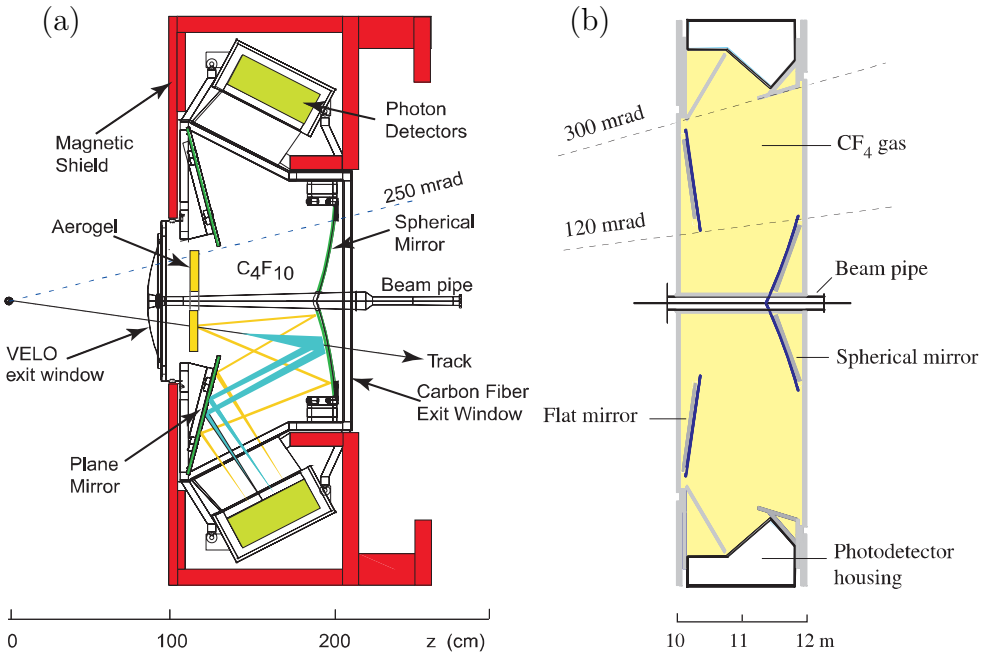

Figure 3.6: (a) A side-view schematic of the RICH1 detector and (b) a top-down schematic of the RICH2 detector. Figures reproduced from Refs. [61, 68].

Photons are radiated at an angle, θ_c, governed by the equation,

$$\cos\theta_c = \frac{1}{n\beta}\,, \tag{3.5}$$

where n is the refractive index of the medium and β is the velocity of the particle. This velocity, in combination with the momentum measured in the tracking system, allows particles of different masses to be distinguished. The incorporation of three different radiators was designed to give PID for particles with a wide range of momenta ($1 - 60\,\mathrm{GeV}/c$ in RICH1 and $15 - 100\,\mathrm{GeV}/c$ in RICH2) as is shown in Fig. 3.7.

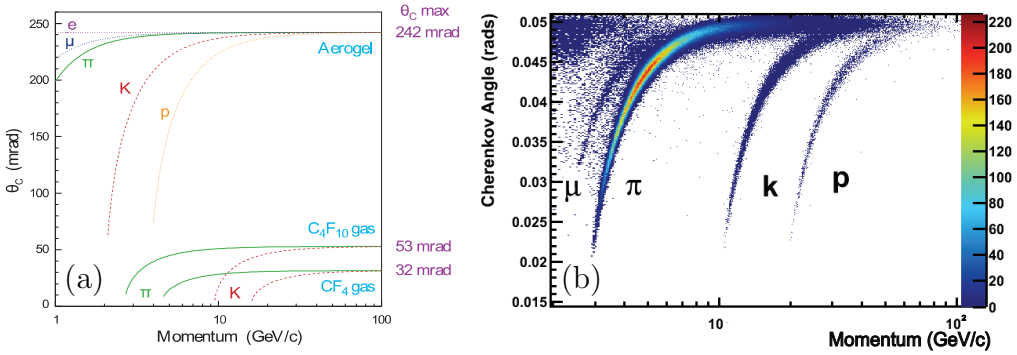

Figure 3.7: Cherenkov angle plotted against momentum for different particle species: (a) as designed for all three RICH radiators; and (b) as measured in the C_4F_{10} radiator. Figures reproduced from Refs. [61, 69].

3.2.5 The calorimeters

The LHCb calorimeter system [70, 71] is composed of the Scintillator Pad Detector (SPD), the preshower detector (PS), the Electromagnetic Calorimeter (ECAL) and the Hadronic Calorimeter (HCAL). The SPD, PS and ECAL are primarily used to identify electrons and photons, measure their energies and provide information to the hardware-level trigger. Only charged particles leave a signal in the SPD so this is used to identify clusters from photons and also to count the number of charged tracks per interaction. The PS is used to differentiate between charged pions and electrons. The ECAL measures the energies of electrons and photons and is used by the trigger to select particles with large transverse energies, E_{T}, where E_{T} is the energy of the particle perpendicular to the direction of the beam. The HCAL measures the transverse energies of hadrons and is also used by the trigger.

The calorimeter system uses variable lateral segmentation to provide higher

resolution closer to the beamline. The SPD, PS and ECAL use three regions and the HCAL uses two as shown in Fig. 3.8. The segmentation regions in the SPD and PS are chosen so that they project exactly onto the corresponding regions in the ECAL. All four subdetectors use wavelength-shifting fibres to transmit scintillation light to photomultipliers (PMTs). The ECAL and HCAL are shashlik calorimeters composed of alternating absorber and detector layers. To avoid significant energy loss due to punch through, the ECAL is 25 electromagnetic radiation lengths deep and the HCAL is 5.6 hadronic interaction lengths deep.

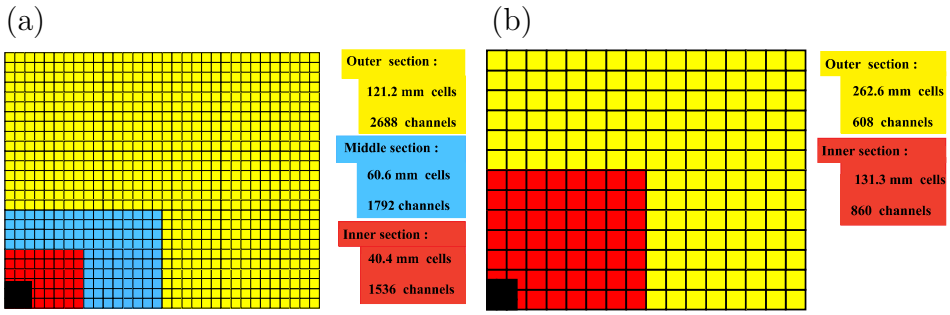

Figure 3.8: The lateral segmentation (a) of the SPD, PS and ECAL, and (b) of the HCAL. Note that the black regions are the gap around the beam pipe. Figure reproduced from Ref. [61].

3.2.6 The muon system

The muon system [72–74] consists of five stations positioned in front of (M1) and behind (M2 – M5) the calorimeters. Its role is to track muons as they leave the detector and measure their transverse momenta (p_{T}). The final two stations have a poorer spatial resolution and are only used to detect the presence of a track. As with the calorimeters, the muon stations are divided into zones of variable segmentation. These four zones increase in radial size across the five stations so that they project exactly between the stations. Along with the calorimeters, the muon system provides important information that is used in the hardware stage of the trigger.

3.2.7 Trigger

The LHCb trigger [75, 76] is composed of three levels: an initial hardware trigger (L0) and a two-stage software high level trigger (HLT1 and HLT2), which runs on a dedicated server farm consisting of 29 000 logical cores. The L0 trigger operates at the LHC bunch crossing rate (up to 40 MHz) and uses information from the ECAL, HCAL and muon system to trigger on electrons and photons, hadrons, and

muons, respectively. The purpose of the L0 trigger is to reduce the data rate to the 1 MHz rate at which the whole detector can be read out. The L0 trigger selects high p_{T} signatures in the muon system and high E_{T} deposits in both calorimeters. Information from the SPD is used to reject high multiplicity events, which would otherwise introduce large combinatorial backgrounds and increase the timing needs of the HLT due to the large number of charged tracks present.

The HLT1 stage uses information from the VELO and the tracking stations to further reduce the rate. At this level, the data rate is still too high to reconstruct all of the tracks through the whole detector. Track stubs are reconstructed in the VELO and PVs are identified. Tracks with a large impact parameter[2] (IP), indicating they were produced at a secondary vertex, are selected for reconstruction through the rest of the detector. Additionally, tracks that have been matched to hits in the muon system are reconstructed through the full detector at this stage. In HLT1 the rate is reduced from 1 MHz to approximately 40 kHz. At this rate it is possible to reconstruct all of the tracks detected in the VELO for use in HLT2, which, in 2011 (2012), further reduced the rate to approximately 3 (4) kHz before events were written to disk.

Various selections (known as trigger lines) are applied within HLT2. Of most relevance to the analyses presented in this thesis, are the topological trigger lines [76, 77] which were designed to select secondary vertices composed of two, three or four tracks. A two-body object is constructed from two good quality tracks with a distance of closest approach (DOCA) of less than 0.2 mm. In turn a 3 (4)-body object is constructed from a 2 (3)-body object and another track with a DOCA (in this case evaluated between the existing object and the new track) of less than 0.2 mm. An important feature of these lines is that a corrected B mass variable is used in the selection to account for missing tracks. This allows *e.g.* a 5-body B decay to pass the 4-body trigger without the need for a very loose B mass requirement. This corrected mass is given by

$$m_{\mathrm{corr}} = \sqrt{m^2 + p_{\mathrm{T}}^{\mathrm{miss}\,2}} + p_{\mathrm{T}}^{\mathrm{miss}} \tag{3.6}$$

where $p_{\mathrm{T}}^{\mathrm{miss}}$ is the missing momentum transverse to the direction of flight as determined from the PV and the n-body object.

In 2012, a deferred trigger was introduced in the HLT to make use of the online computing resources during machine downtime. While collisions were occurring, 20 % of the output from the L0 trigger was written to disk. These data were then

[2]The impact parameter of a reconstructed track is defined as its distance of closest approach to a PV.

processed during downtime, *e.g.* during proton injection. This deferral increased the effective output rate of the HLT to approximately 5 kHz.

During the offline selection, trigger decisions are divided into two categories based on the track that passes the hardware trigger. Events where one of the tracks in the signal decay has caused the trigger are labelled "Trigger On Signal" (TOS), while events where a track from the rest of the event has passed the trigger are labelled "Trigger Independent of Signal" (TIS). In addition to increasing the size of the recorded dataset, decays that have been selected by independent trigger pathways are useful to test for any systematic biases that may be introduced by a TOS trigger requirement. This classification is possible as the trigger decision can be accurately reproduced offline.

3.2.8 Online system

The LHCb online system [78] is responsible for ensuring the transfer of data from the front end electronics on the detector to storage for offline analysis. The system consists of three components: the Data Acquisition system, which transfers data identified by the trigger to storage; the Experiment Control System, which monitors and controls all aspects of the detector; and the Timing and Fast Control system, which distributes the beam synchronous clock and fast control commands to drive all stages of data readout.

3.2.9 Software

Various software packages are used within the LHCb collaboration for tasks such as data processing and the generation of simulated data. A brief summary of some relevant software packages is given below.

Gauss

The Gauss package is used to generate proton-proton collisions and the subsequent decays of particles produced therein, and then simulate the interaction of the decay products with the LHCb detector. The generation and decay phase makes use of a range of external packages such as Pythia [79] and EvtGen [80, 81] to model the underlying physics of particle production and decays based on experimental observations and theoretical models. In the simulation phase, Gauss uses the Geant4 toolkit [82] to simulate the interaction of the generated particles with the LHCb detector.

Pythia

Pythia 8 is the general purpose event generator used within Gauss to generate

proton-proton collision events. PYTHIA models the underlying hard process and the resulting parton showers up to hadronisation.

EvtGen

Once c- and b-hadrons have been produced in simulation, EVTGEN is used to describe their decays into final state particles. The inclusive decay chain for each particle and the model used to describe each decay are configured in a main "decay file", which is updated to match branching fractions reported by the PDG [3]. For simulating signal events, EVTGEN also supports "user decay files", which may specify exclusive decay chains for some particles. EVTGEN is actively developed and maintained within the Warwick LHCb group, and a record of my contributions to this development can be found in App. B.

Boole

BOOLE is the LHCb digitisation package and is responsible for modelling the response of the LHCb subdetectors to the particle hits simulated by GAUSS.

Moore

The MOORE package implements the LHCb HLT algorithms and is used to process both online data obtained from the LHCb detector and simulated data produced using GAUSS and BOOLE. To minimise differences between online and offline track reconstruction, the same algorithms are used both online and offline, however, some configuration differences exist to meet the time requirements of the online system. The most significant difference is that the p_{T} threshold above which a track is reconstructed is set to be higher for online reconstruction.

Brunel

The BRUNEL package is responsible for reconstructing data from the LHCb subdetectors including tracking, particle identification and calorimeter objects. As with MOORE, BRUNEL is used to reconstruct both real data and simulated events.

DaVinci

DAVINCI is the LHCb analysis package used to select events of interest to a particular analysis from the reconstructed data produced by BRUNEL and to perform some high-level reconstruction. For events that pass the specified requirements, parameters of interest relating to the reconstructed particles are recorded for further use offline.

PIDCalib

As particle identification variables are poorly modelled in simulated data, the PIDCalib package is used to model the effect of PID requirements as a function of kinematic variables such as the momentum or transverse momentum of the particle as well as detector occupancy. Calibration samples, where the species of a particle can be inferred without PID requirements, are used to measure the efficiency of a particular requirement in bins across the kinematic phase space. For example, in the decay chain $D^{*+} \to D^0(\to K^-\pi^+)\pi_s^+$, the charge of the slow pion, π_s^+, tags the flavours of the kaon and pion produced in the D^0 decay based on their charges. The efficiencies obtained from such samples can be used to weight simulated events based on the kinematics of the tracks in each event.

Laura^{++}

Laura^{++} [83] is a Dalitz plot fitting package, developed and maintained within the Warwick LHCb group. The package is used to perform unbinned maximum-likelihood fits to data. Signal models are described parametrically using the isobar formalism introduced in Sec. 2.5.1, while background components and efficiency effects can be described by histograms. A record of my contributions to the development of this package can be found in App. C.

Multivariate algorithms

A multivariate algorithm (MVA) converts information from multiple variables into a single classifier capable of distinguishing between two populations (here labelled signal and background) based on training performed using samples of both categories. Two types of MVA are used in the analyses reported in the following chapters: boosted decision trees (BDTs) are used to identify secondary vertices and to identify $\overline{D}^0$ candidates; neural networks (NNs) are used both to separate signal decays from combinatorial background and to separate pions, kaons and protons.

BDTs are trained by repeatedly constructing decision trees to separate the two training samples by placing requirements on the input variables. At each node in a tree the variable and requirement are chosen to maximise the separation between signal and background. Once a tree is constructed the events that have been sorted into the incorrect category are "boosted" to increase their importance in the next tree. The score for a given event is then given by a weighted sum of the scores returned by each of these decision trees.

Neural networks are based on a simplified model of the brain. The input

variables are transformed before being passed into a set of input "neurons". These signals then pass through one or more internal layers of neurons, where the signal received by any node in layer $i + 1$ is determined by a weighted sum of the signals at the neurons in layer i with weights determined from the training samples. The final layer consists of a single neuron that outputs the classifier.

Chapter 4

Common selection, backgrounds and efficiencies

4.1 Overview

The following chapters detail a series of analyses that build towards a measurement of the CKM angle γ from a DP analysis of $B^0 \to D_{CP}K^+\pi^-$ decays. The relevant decay diagrams are shown in Fig. 2.7. These analyses were all performed using data collected using the LHCb detector during Run 1 of the LHC.

In the first analysis [84], the branching fractions of $B^0 \to \overline{D}^0 K^+\pi^-$ and $B_s^0 \to \overline{D}^0 K^-\pi^+$ decays were measured relative to the control channel $B^0 \to \overline{D}^0\pi^+\pi^-$ using 1.0 fb^{-1} of data collected by LHCb during 2011. This was the first observation of the $B_s^0 \to \overline{D}^0 K^-\pi^+$ decay, although the resonant contribution $B_s^0 \to \overline{D}^0\overline{K}^{*0}$ had previously been observed [85]. The data selection, background studies and efficiencies for this analysis, including many elements common to the subsequent analyses, are discussed in the remainder of this chapter. The fit to the reconstructed B candidate mass distribution and the determination of the two branching fractions are presented in Chapter 5.

The remaining analyses were performed on a data sample comprised of 1.0 fb^{-1} of data collected during 2011 and 2.0 fb^{-1} collected in 2012 at centre-of-mass energies of 7 TeV and 8 TeV, respectively. Chapters 6 and 7 cover DP analyses of the $B_s^0 \to \overline{D}^0 K^-\pi^+$ [52, 86] and $B^0 \to \overline{D}^0 K^+\pi^-$ [87] decay modes, respectively, while Chapter 8 details the extraction of the CKM angle γ from a DP analysis of $B^0 \to D_{CP}K^+\pi^-$ decays.

Note that these analyses were performed over a three year period and, as such, various improvements to analysis techniques and new measurements of external

parameters were incorporated into the later analyses. The following chapters detail these analyses as they were originally performed and do not attempt to incorporate such improvements retroactively.

4.2 Selection

4.2.1 Trigger

Events are required to pass both the hardware L0 trigger and the software HLT triggers via specific paths. In the hardware trigger two distinct paths are included. Either a particle from the signal decay must register a large E_{T} in the HCAL to pass the TOS hadronic trigger or a particle from the rest of the event must pass a TIS global trigger by registering a large p_{T} (E_{T}) in one of the muon stations (calorimeters). In the software trigger a set of topological triggers are used as described in Sec. 3.2.7.

4.2.2 Initial selection

To reduce the volume of data that needs to be processed for each analysis, the raw dataset that passes the trigger selection is first separated into streams based on the type of event present. Each of these streams is produced by a set of related "stripping lines" that are designed to pick out specific types of decays. For the analyses presented in this thesis, the `B02D0KPiD2HHBeauty2CharmLine` stripping line is used. This line is designed to select three-body B meson decays, where the three decay daughters are a $\overline{D}^0$ meson, a charged kaon and a charged pion. The $\overline{D}^0$ meson is reconstructed from two charged hadrons: either $\pi^+\pi^-$, $K^\pm\pi^\mp$ or K^+K^-. Here and throughout this thesis the charged particles that are produced directly from the B decay are referred to as "bachelors". In addition, the `B02D0PiPiD2HHBeauty2CharmLine` stripping line is used to select $B^0 \to \overline{D}^0\pi^+\pi^-$ decays which are used as a normalisation channel for the branching fraction analysis and as a training sample for the NNs used in these analyses. The full requirements applied in the `B02D0KPiD2HHBeauty2CharmLine` and `B02D0PiPiD2HHBeauty2CharmLine` stripping lines are summarised in Table 4.1. For the B^0 candidate, requirements are made on: the reconstructed mass, $m^{\mathrm{reco}}_{B^0}$; the reconstructed decay time, $\tau_{\mathrm{reconstructed}}$; the minimum χ^2 of the impact parameter of the reconstructed B^0 candidate from any of the primary vertices, min χ^2_{IP}; the χ^2 per degree of freedom of the B^0 vertex fit, $\left(\chi^2/\mathrm{ndf}\right)_{\mathrm{vertex}}$; the cosine of the angle between the momentum of the B^0 candidate and the line between the B^0 decay vertex and the primary vertex, $\cos\theta_{\mathrm{dir}}$; the sum of the p_{T} of the four tracks, $\Sigma_{\mathrm{all}}p_{\mathrm{T}}$. In addition, a BDT is used to identify secondary vertices [88]. Similar requirements are also

made for the $\overline{D}^0$ candidate and the $K\pi$ combination reconstructed from the bachelor pair. Additional requirements are made on: the χ^2 of the distance between the reconstructed decay vertex and the primary vertex, χ^2_{flight}; the maximum distance of closest approach between the daughter tracks, max (DOCA). Further requirements are also placed on the p, p_{T}, min χ^2_{IP}, track quality (χ^2_{track}), and minimum impact parameter (min IP) of the charged tracks and on the total number of tracks in the event ($N_{\text{long tracks}}$).

Following the stripping, further selection requirements are made offline. The goal of these initial requirements is to reduce the background level in the $\overline{D}^0\pi^+\pi^-$ control sample enough that the signal peak is visible, so that a NN can be trained to further purify the data. This selection is similar to the selections used in analyses of the similar decays, $B^0_{(s)} \to \overline{D}^0\overline{K}^{*0}$ [85] and $B^0_{(s)} \to \overline{D}^0 K^+K^-$ [89].

A BDT is used to identify $\overline{D}^0 \to K^+\pi^-$ candidates, based on a large number of parameters relating to the $\overline{D}^0$ candidate and its daughters. This BDT is designed to identify $\overline{D}^0$ candidates produced in B decays and was previously used to identify $B^0_s \to D^0\overline{D}^0$ decays [90]. Requirements are placed on the so-called probNN variables. These provide PID information based on the output of a NN that incorporates PID-sensitive parameters from multiple subdetectors. The PID requirements are described further in Sec. 4.2.5. A summary of the requirements applied for the measurement of the branching fractions is shown in Table 4.2. Some improvements were made to the selection criteria for subsequent analyses and these are detailed in later chapters.

To improve the resolution of the reconstructed B mass, a vertex fit is performed with the mass of the $\overline{D}^0$ meson constrained to match the value reported by the PDG [3]. Where possible, variables calculated with this constraint are used in the selection. Events are also required to pass fits with the B candidate mass constrained to either the B^0 or B^0_s mass as these fits are used to calculate the DP variables.

4.2.3 Neural network selection

A NN package, `NeuroBayes` [91], is used to distinguish signal from combinatorial background. `NeuroBayes` is trained on $B^0 \to \overline{D}^0\pi^+\pi^-$ data using weights, extracted from a simple fit to $m(\overline{D}^0\pi^+\pi^-)$, to distinguish signal from background. The decision to train the NN on $B^0 \to \overline{D}^0\pi^+\pi^-$ data was based on the large yield compared to the signal decay modes and the almost identical topology of the control mode to the two signal decays. Since `NeuroBayes` is trained using only data, combinatorial background rejection is not dependent on simulation.

To simplify the fit, `NeuroBayes` is trained only on B candidates in the

Table 4.1: Selection requirements applied in the `B02D0KPiD2HHBeauty2CharmLine` and `B02D0PiPiD2HHBeauty2CharmLine` stripping lines.

Particle	Parameter	Requirement
B^0	$m^{\text{reco}}_{B^0}$	> 4.75 and $< 7.0\,\text{GeV}/c^2$
	$\tau_{\text{reconstructed}}$	$> 0.2\,\text{ps}$
	$\min \chi^2_{\text{IP}}$	< 25
	$\left(\chi^2/\text{ndf}\right)_{\text{vertex}}$	< 10
	$\cos\theta_{\text{dir}}$	> 0.999
	$\Sigma_{\text{all}} p_{\text{T}}$	$> 5.0\,\text{GeV}/c$
	BDT output	> 0.05
$\overline{D}^0$	$\lvert \text{m}^{\text{reco}}_{\overline{D}^0} - \text{m}^{\text{PDG}}_{\overline{D}^0} \rvert$	$< 100\,\text{MeV}/c^2$
	$\left(\chi^2/\text{ndf}\right)_{\text{vertex}}$	< 10
	χ^2_{flight}	> 36
	$\cos\theta_{\text{dir}}$	> 0.0
	$\max\left(\text{DOCA}\right)$	$< 0.5\,\text{mm}$
	$\Sigma_{\text{daughters}} p_{\text{T}}$	$> 1.8\,\text{GeV}/c$
Bachelor pair	m^{reco}	$< 5.2\,\text{GeV}/c^2$
	$\left(\chi^2/\text{ndf}\right)_{\text{vertex}}$	< 16
	χ^2_{flight}	> 16
	$\cos\theta_{\text{dir}}$	> 0.0
	$\max\left(\text{DOCA}\right)$	$< 0.5\,\text{mm}$
	$\Sigma_{\text{bachelors}} p_{\text{T}}$	$> 1.0\,\text{GeV}/c$
Charged tracks	p_{T}	$> 100\,\text{MeV}/c$
	$p_{\overline{D}^0\text{daughter}}$	$> 1.0\,\text{GeV}/c$
	p_{bachelor}	$> 2.0\,\text{GeV}/c$
	$\min \chi^2_{\text{IP}}$	> 4
	χ^2_{track}	< 4
One $\overline{D}^0$ daughter and one bachelor	p_{T}	$> 500\,\text{MeV}/c$
	p	$> 5.0\,\text{GeV}/c$
	χ^2_{track}	< 3
One track	p_{T}	$> 1.7\,\text{GeV}/c$
	p	$> 10.0\,\text{GeV}/c$
	χ^2_{track}	< 2.5
	$\min \chi^2_{\text{IP}}$	> 16
	$\min$ IP	$> 0.1\,\text{mm}$
Global	$N_{\text{long tracks}}$	< 500

mass range 5200 – 5600 MeV/c^2. This avoids the need to parameterise the signal-like partially reconstructed background that is present at lower masses. The fit model for the $\overline{D}^0\pi^+\pi^-$ mass spectrum includes a double Gaussian to describe the $B^0 \to \overline{D}^0\pi^+\pi^-$ peak and a linear component to describe the combinatorial background contribution. Smaller background contributions are neglected in this

Table 4.2: Offline selection requirements applied prior to the NN training. Requirements labelled * are only used for the bachelor kaon in the $B^0_{(s)} \to \overline{D}{}^0 K\pi$ decay modes, while those labelled ** are used for the $B^0 \to \overline{D}{}^0\pi^+\pi^-$ selection and the bachelor pion in $B^0_{(s)} \to \overline{D}{}^0 K\pi$. Parameters labelled † are calculated after a $\overline{D}{}^0$ mass constraint.

Particle	Parameter	Requirement
B^0	†M	> 5000 and < 5600 MeV/c^2
	$\left(\chi^2/\text{ndf}\right)_{\text{vertex}}$	< 4
	† $\cos\theta_{\text{dir}}$	> 0.99995 (angle $\lesssim 10$ mrad)
	†min χ^2_{IP}	< 9
$\overline{D}{}^0$	M	> 1844 and < 1884 MeV/c^2
	BDT output	> 0.5
	flight distance	> 1 mm
$\overline{D}{}^0(\pi)$	$\text{probNN}_\pi \times (1 - \text{probNN}_K)$	> 0.1
	p	< 100 GeV/c
$\overline{D}{}^0(K)$	$\text{probNN}_K \times (1 - \text{probNN}_\pi)$	> 0.1
	p	< 100 GeV/c
$^*K$	$\text{probNN}_K \times (1 - \text{probNN}_\pi)$	> 0.3
	p	< 100 GeV/c
$^{**}\pi$	$\text{probNN}_\pi \times (1 - \text{probNN}_K)$	> 0.2
	p	< 100 GeV/c

fit. This simplified fit model is sufficient to establish the properties of signal and background — imperfections may lead to a sub-optimally trained NN but will not cause a bias. Signal and background events are distinguished by using signal `sWeights`, determined using the `sPlot` [92] formalism, to weight the events. These take larger values for more signal-like events with the constraints that:

$$\sum_{i=1}^{N} {}_s\mathcal{P}_n(i) = N_n \ , \tag{4.1}$$

$$\sum_{l=1}^{N_s} {}_s\mathcal{P}_l(i) = 1 \ \forall \ i \ , \tag{4.2}$$

where ${}_s\mathcal{P}_n(i)$ is the `sWeight` for event i being in category n, the indices i and l run over the N events and the N_s categories, respectively, and N_n is the yield of category n. In this case, the two categories correspond to signal and background decays. Figure 4.1 shows the simple fit to $m(\overline{D}{}^0\pi^+\pi^-)$ and the signal `sWeight` as a function of the B candidate mass. An advantage of the simple fit model is the smooth behaviour of the signal `sWeight` as a function of $m(\overline{D}{}^0\pi^+\pi^-)$.

The variables used to train `NeuroBayes` are shown in Table 4.3. As with the

initial selection, variables calculated after the $\overline{D}^0$ mass constraint are used where possible. Information from the rest of the event is included through the "cone" variables that describe the $p_{\rm T}$ asymmetry, $A_{p_{\rm T}}$, and track multiplicity within a cone with half-angle of 1.5 units in the plane of pseudorapidity and azimuthal angle (measured in radians) [32] around the B candidate flight direction, with

$$A_{p_{\rm T}} = \frac{p_{\rm T}(B) - \sum_n p_{\rm T}(n)}{p_{\rm T}(B) + \sum_n p_{\rm T}(n)}\,, \tag{4.3}$$

where the sum is over the tracks contained within the cone excluding those associated with the B candidate. The output of the `NeuroBayes` training includes a ranking of the input variables based on how well they distinguish between signal and background. These ranks are also shown in Table 4.3.

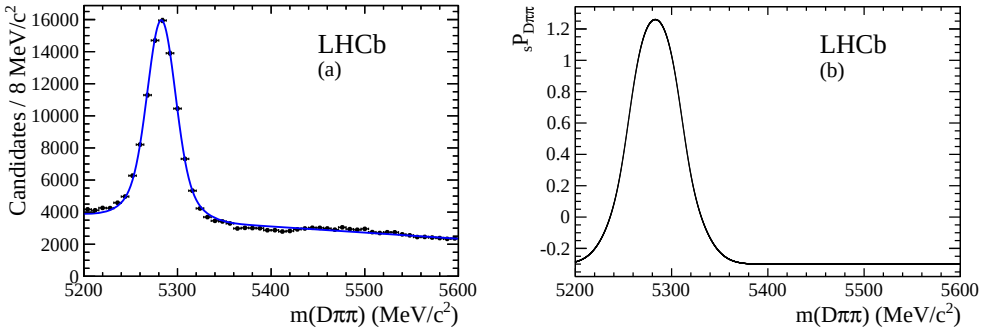

Figure 4.1: (a) Fit to the $B^0 \to \overline{D}^0\pi^+\pi^-$ data sample, used to obtain `sWeights` as input to `NeuroBayes` and (b) signal `sWeight` as a function of $m(\overline{D}^0\pi\pi)$.

Table 4.3: Variables used as inputs to train the `NeuroBayes` selection. Parameters labelled † are calculated after a $\overline{D}^0$ mass constraint. The "cone" variables contain information about the rest of the event in the region around the B candidate.

Particle	Variables	`NeuroBayes` ranking
B^0	$^\dagger p_{\rm T}$	6
	$\chi^2_{\rm vertex}$	4
	$^\dagger\chi^2_{\rm flight}$	8
	$^\dagger\cos\theta_{\rm dir}$	9
	†min $\chi^2_{\rm IP}$	3
	cone $A_{p_{\rm T}}$	7
	cone track multiplicity	10
$\overline{D}^0$	BDT output	2
$\pi^\pm$	†smaller min $\chi^2_{\rm IP}$	1
	†larger min $\chi^2_{\rm IP}$	5

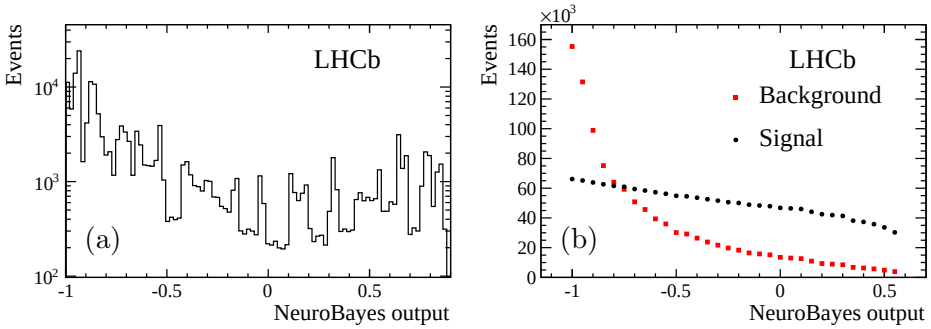

Figure 4.2: (a) `NeuroBayes` output variable plotted for all events and (b) yields of signal and background obtained by fitting $m(\overline{D}^0\pi\pi)$ with different requirements on the `NeuroBayes` output. Periodic structures seen in the output variable are a side effect of the way that `NeuroBayes` transforms the input variables into an output signal probability, and are not a sign of over-training or low statistics in the training sample.

The result of the `NeuroBayes` training is shown in Fig. 4.2. A more negative value of this variable suggests an event is background-like, while a more positive value identifies the event as signal-like. An appropriate requirement on the `NeuroBayes` output is selected as follows.

- The $B^0 \to \overline{D}^0 K^+\pi^-$ signal yield is expected to be suppressed by a factor of approximately 10 compared to $B^0 \to \overline{D}^0\pi^+\pi^-$, based on the relative branching fractions of the decays [3].

- The $B^0_s \to \overline{D}^0 K^+\pi^-$ and $B^0 \to \overline{D}^0\pi^+\pi^-$ branching fractions are assumed to be the same, as their respective Feynman diagrams differ only in the spectator quark.

- The $B^0_s \to \overline{D}^0 K^+\pi^-$ yield is expected to be suppressed as a b-quark is less likely to hadronise into a B^0_s meson than a B^0 meson. This relative rate is given by the ratio of fragmentation fractions, $f_s/f_d = 0.267\,^{+0.021}_{-0.020}$ [93].[1]

- Since most charged tracks are pions, the kaon identification requirement on the bachelor kaon reduces the level of combinatoric background. From the sidebands of the $\overline{D}^0 hh$ mass distributions, the background is estimated to be reduced by a factor of 4.

- From these factors, the expected significances for the B^0 and B^0_s decays to $\overline{D}^0 K^+\pi^-$ can be approximated as $S_{B^0\to\overline{D}^0K\pi}/\sqrt{S_{B^0\to\overline{D}^0K\pi} + B_{B^0\to\overline{D}^0K\pi}} \propto S_{\overline{D}^0\pi\pi}/\sqrt{S_{\overline{D}^0\pi\pi} + 2.5B_{\overline{D}^0\pi\pi}}$ and $S_{B^0_s\to\overline{D}^0K\pi}/\sqrt{S_{B^0_s\to\overline{D}^0K\pi} + B_{B^0_s\to\overline{D}^0K\pi}} \propto$

[1] Note that a more precise measurement of f_s/f_d [94], with a slightly different central value, has been published since this analysis was performed.

$S_{\overline{D}^0\pi\pi}/\sqrt{S_{\overline{D}^0\pi\pi}+B_{\overline{D}^0\pi\pi}}$, respectively, where S_i and B_i correspond to the number of signal and background events for channel i.

- The simple fit to the $\overline{D}^0\pi\pi$ mass distribution is repeated with different requirements made on the `NeuroBayes` output variable to obtain $S_{\overline{D}^0\pi\pi}$ and $B_{\overline{D}^0\pi\pi}$ as functions of the requirement as shown in Fig. 4.2 (right).

- The expected significances as functions of the requirement applied, shown in Fig. 4.3, peak near values of 0.4 and 0.1 for the B^0 and B_s^0 yields, respectively. An intermediate value of 0.3 is chosen as the requirement.

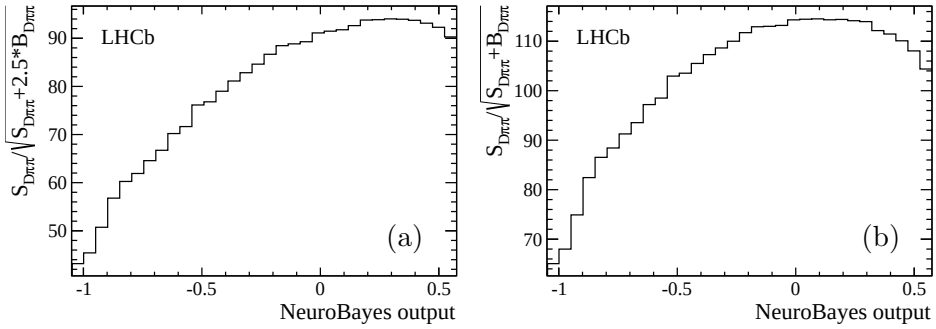

Figure 4.3: Optimisation of the requirement on the `NeuroBayes` output for (a) $B^0 \to \overline{D}^0 K^+\pi^-$ and (b) $B_s^0 \to \overline{D}^0 K^+\pi^-$ decays. Note that the y-axis scale is arbitrary.

4.2.4 Vetoes

Various decays, which result in a four track final state, can show up as peaking backgrounds in the two- and three-body invariant mass distributions. The backgrounds that lead to these peaks are discussed further in Sec. 4.3.2, while the invariant mass cuts (vetoes) applied to remove them are detailed here.

$D^*(2010)^-$ veto

The decay $B^0 \to D^*(2010)^-\pi^+$, with $D^*(2010)^- \to \overline{D}^0\pi^-$ occurs with the branching fractions,

$$\mathcal{B}\left(B^0 \to D^*(2010)^-\pi^+\right) = (2.76 \pm 0.13) \times 10^{-3}, \quad (4.4)$$

$$\mathcal{B}\left(D^*(2010)^- \to \overline{D}^0\pi^-\right) = (67.7 \pm 0.5) \times 10^{-2}. \quad (4.5)$$

This contribution to the $B^0 \to \overline{D}^0\pi^+\pi^-$ decay is larger than all of the other contributions combined and is not included in the three-body branching fraction

reported by the PDG [3]. A veto is applied to remove events with $m(\overline{D}^0\pi) - m(\overline{D}^0)$ within $2.5\,\mathrm{MeV}/c^2$ of the nominal $D^*(2010)^- - \overline{D}^0$ mass difference for either of the bachelor pions. This veto is also applied to the $\overline{D}^0 K\pi$ data both on $m(\overline{D}^0\pi) - m(\overline{D}^0)$ and $m(\overline{D}^0 K_\pi) - m(\overline{D}^0)$, where the subscript π indicates that the invariant mass is evaluated under the pion mass hypothesis for the bachelor kaon. Figure 4.4 shows the $m(\overline{D}^0\pi)$ distributions for $\overline{D}^0\pi\pi$ and $\overline{D}^0 K\pi$ data events.

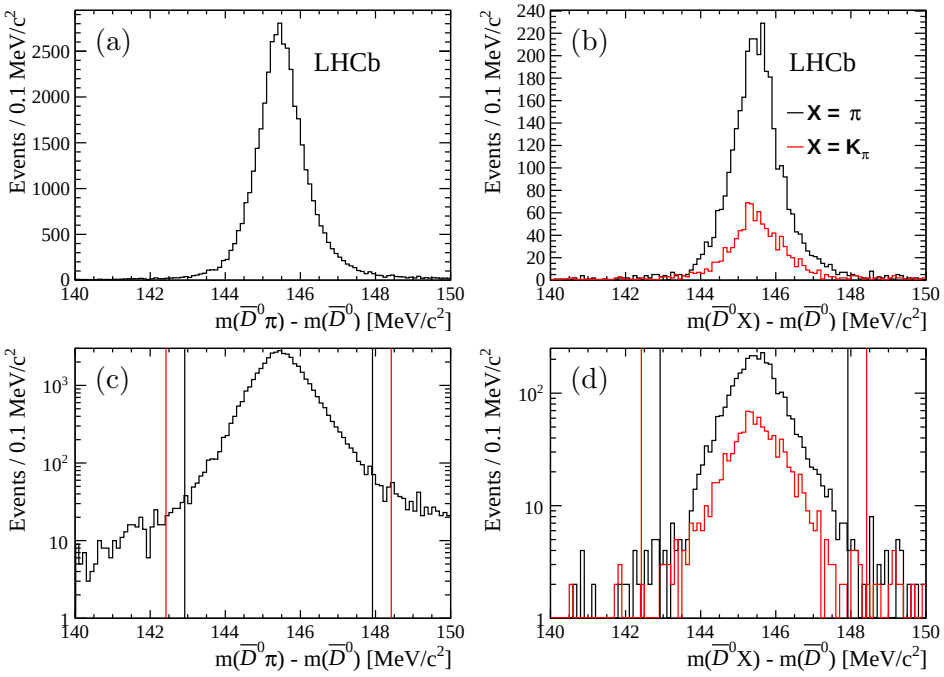

Figure 4.4: Plots of (a) $m(\overline{D}^0\pi)$ for $B^0 \to \overline{D}^0\pi^+\pi^-$ candidates, and (b) $m(\overline{D}^0\pi)$ and $m(\overline{D}^0 K_\pi)$ for $B^0_{(s)} \to \overline{D}^0 K^\pm\pi^\mp$ candidates (the K_π notation implies that the mass is recalculated with the pion mass hypothesis for the kaon track). The lack of background is due to the narrow x-axis range. The same data are shown in (c) and (d) on logarithmic scales. The vertical lines on the log plots show the range of (black) the nominal $\pm 2.5\,\mathrm{MeV}/c^2$ veto and (red) a $\pm 3.0\,\mathrm{MeV}/c^2$ range used to establish a systematic uncertainty due to the $D^*(2010)^-$ veto in Sec. 5.2.

$D_s^\pm$ and $D^\pm$ vetoes

Of the possible peaking backgrounds considered in Sec. 4.3.2, the decays $B^0_{(s)} \to D^\pm K^\mp$ and $B^0_{(s)} \to D_s^\pm\pi^\mp$ may contribute non-negligible backgrounds to the $\overline{D}^0 K\pi$ DPs. To remove these backgrounds, candidates are vetoed where the three-body invariant mass of the two bachelor tracks with the pion (kaon) from the $\overline{D}^0$ decay is consistent with the mass of the $D^\pm$ ($D_s^\pm$) meson. Veto ranges are chosen based on the distributions seen in simulated data (Fig. 4.5). The vetoes applied are

$1850 < m(\overline{D}^0(\pi)K\pi) < 1885\,\mathrm{MeV}/c^2$ and $1955 < m(\overline{D}^0(K)K\pi) < 1975\,\mathrm{MeV}/c^2$ for the $D^\pm$ and $D_s^\pm$ peaks, respectively, where the notation $\overline{D}^0(h)$ indicates a track that has been reconstructed as a $\overline{D}^0$ daughter. After the initial selection, 0.6 % of the remaining signal candidates are removed by the $D^\pm$ veto and 0.4 % are removed by the $D_s^\pm$ veto.

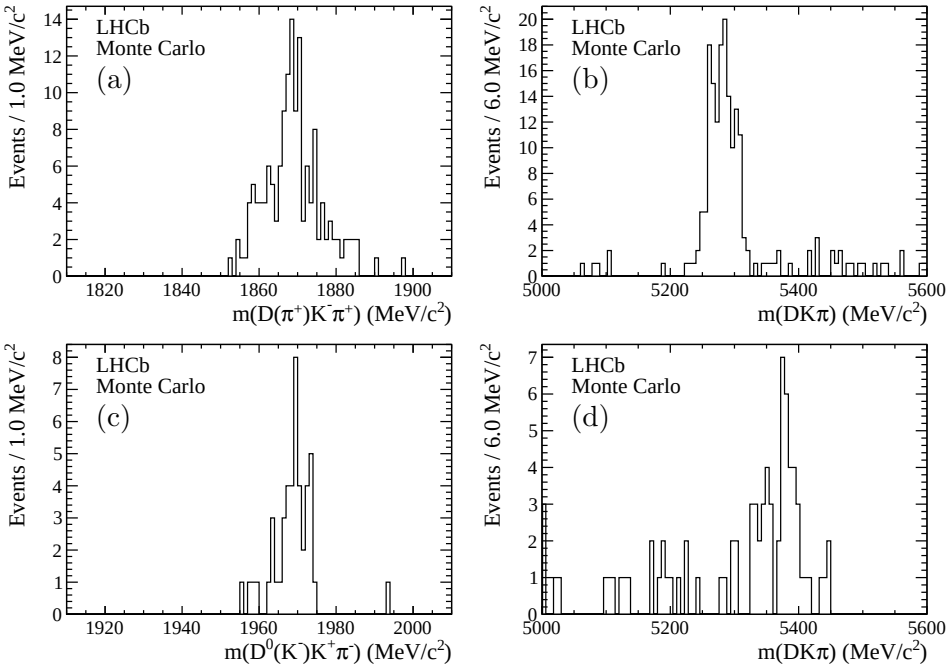

Figure 4.5: Invariant mass distribution of the particle reconstructed as the (a) pion and (c) kaon from the $\overline{D}^0$ decay with the pair of particles identified as bachelors following the application of the initial selection to simulated (a) $B^0 \to D^\mp\pi^\pm$ and (c) $B_s^0 \to D_s^\mp\pi^\pm$ decays. Also shown in (b) and (d) are the B candidate invariant mass distributions for the same events.

4.2.5 Particle identification requirements

To identify the species of particle that has produced a charged track in LHCb, measurements from multiple subdetectors must be combined. A momentum measurement from the tracking system can be combined with velocity information from the RICH detectors to give a measurement of the mass. Further information is also available from the calorimeters and the muon system.

The probNN$_i$ variables combine all of the relevant information into a single variable that takes values between 0 and 1. These parameters can be treated as the probability that a given particle is of a particular species, i. In the analyses described in this thesis, requirements are made on the products of these variables,

e.g. $\text{probNN}_K \times (1 - \text{probNN}_\pi)$.

The nominal requirements are $\text{probNN}_\pi \times (1 - \text{probNN}_K) > 0.2$ for the bachelor pion and $\text{probNN}_K \times (1 - \text{probNN}_\pi) > 0.3$ for the bachelor kaon. The $\overline{D}^0$ meson and its daughters are identified by the $\overline{D}^0$ BDT and a requirement for the reconstructed $\overline{D}^0$ decay vertex to be separated from the B decay vertex by at least 1 mm. In addition to these requirements, similar — but looser — PID requirements to those applied to the bachelor tracks are also applied to the $\overline{D}^0$ daughters. To check that the chosen requirements are appropriate, the reconstructed B mass distribution is investigated with looser and tighter requirements applied, as shown in Fig. 4.6 for the bachelor kaon. With a looser requirement on the kaon, a clear peak is seen between the two signal peaks corresponding to a peaking background from $B^0 \to \overline{D}^0\pi^+\pi^-$. Applying a tighter requirement doesn't significantly affect the level of background in the mass distribution. Although not strictly optimised these requirements appear to be reasonable.

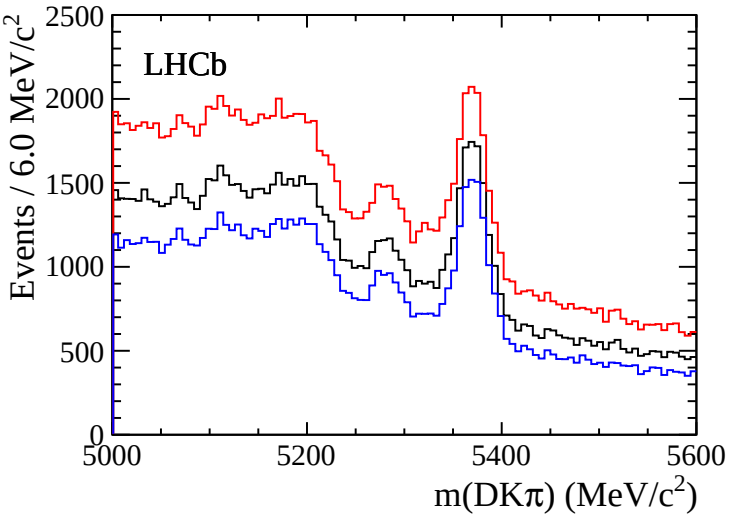

Figure 4.6: The $\overline{D}^0K^+\pi^-$ invariant mass distribution, after applying different bachelor kaon particle identification requirements. (Red) $\text{probNN}_K \times (1 - \text{probNN}_\pi) > 0.2$; (black) > 0.3 (nominal); (blue) > 0.4.

All four tracks are also required to not be identified as muons by the muon system. This requirement removes a potential background contribution from $B^0_{(s)} \to J/\psi\,(\mu^+\mu^-)K^{*0}$ decays. This background was found to produce a peak at the J/ψ mass in the invariant mass distribution of the bachelor pion with the kaon from the $\overline{D}^0$ decay as shown in Fig. 4.7. This veto removes 7.7 % of the $\overline{D}^0K\pi$ candidate decays that pass the initial selection.

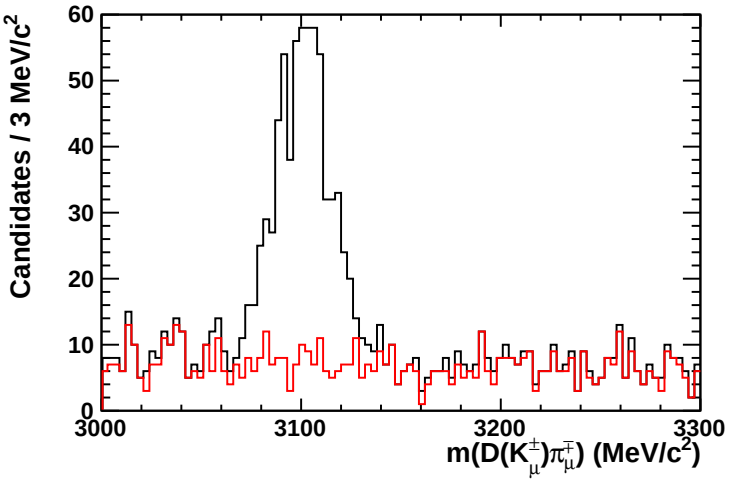

Figure 4.7: The invariant mass distribution, near the J/ψ mass, of the kaon from the $\overline{D}^0$ decay with the bachelor pion (black) before and (red) after the muon veto. The invariant mass has been calculated under the muon mass hypothesis for both tracks.

4.3 Background studies

This section details the potential backgrounds that were investigated for the $\overline{D}^0 K\pi$ final state. A similar study was performed for the $\overline{D}^0\pi\pi$ normalisation channel. By relaxing the requirements on the mass of the reconstructed $\overline{D}^0$ meson and comparing the levels of background in the reconstructed $B^0_{(s)}$ and $\overline{D}^0$ mass distributions (Fig. 4.8), it was determined that most of the background candidates in the data sample contain a real $\overline{D}^0$ candidate. In addition, the lack of other peaks in the $\overline{D}^0$ mass distribution indicates that there are no significant contributions from other $\overline{D}^0$ decays such as $\overline{D}^0 \to \pi^+\pi^-$ or $\overline{D}^0 \to K^+K^-$. This means that the flat "sideband" regions can be used to investigate charmless backgrounds, *i.e.* backgrounds from decays without a real $\overline{D}^0$ meson.

In the following sections, various categories of background are considered. In Sec. 4.3.1 combinatorial background, which consists of a real or fake $\overline{D}^0$ meson combined with random tracks, is investigated. Peaking backgrounds, where another decay mode results in a four track final state are discussed in Sec. 4.3.2 and Sec. 4.3.3 for decays involving a real $\overline{D}^0$ meson and those without, respectively. In Sec. 4.3.4, partially reconstructed backgrounds are considered, where all four tracks come from a B decay but additional final-state particles are missed, *e.g.* the decay $B^0_s \to \overline{D}^{*0}K^-\pi^+, \overline{D}^{*0} \to \overline{D}^0\pi^0$, where the neutral pion is missed.

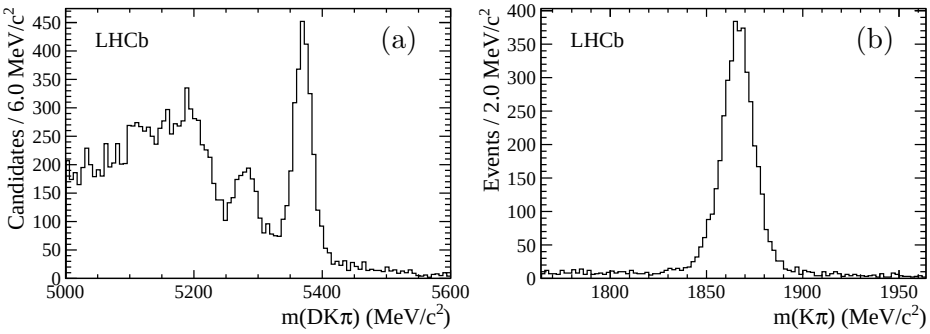

Figure 4.8: Distribution of events in (a) the reconstructed B mass and (b) the reconstructed $\overline{D}^0$ mass. The much lower background in the $\overline{D}^0$ mass distribution indicates that most background events contain a real $\overline{D}^0$ candidate.

4.3.1 Combinatorial background

Random combinations of tracks produce the largest single background to the $\overline{D}^0 K\pi$ signal peaks. This background is present across the whole mass range shown in Fig. 4.8 and is smoothly varying. In the analyses described in this thesis this background is described by either a first-order polynomial or an exponential function.

4.3.2 Peaking background

Due to particle misidentification, it is possible for a range of peaking backgrounds to enter the $\overline{D}^0 K\pi$ dataset from other decays to a $\overline{D}^0$ meson plus two charged hadrons. The decay modes that can contribute due to a single pion, kaon or proton being misidentified as a pion or kaon are listed in Table 4.4 and their distributions in the reconstructed B mass, as determined from simulation, are shown in Fig. 4.9. The expected level of peaking background, $N_{\rm peak}$, due to each of these contributions relative to the $B^0 \to \overline{D}^0 K^+\pi^-$ yield was calculated as,

$$\frac{N_{\rm peak}}{N_{\overline{D}^0 K\pi}} = \frac{f_x}{f_d} \times \frac{\mathcal{B}(\text{peak})}{\mathcal{B}(B^0 \to \overline{D}^0 K^+\pi^-)} \times \frac{\epsilon_{\rm peak}}{\epsilon_{\overline{D}^0 K\pi}}, \tag{4.6}$$

where f_x is the fragmentation fraction for the decaying b-hadron, $\mathcal{B}(\text{peak})$ is the branching fraction of the decay mode and $\epsilon_{\rm peak}$ is the efficiency with which the peaking background is reconstructed and selected. As the value of $\frac{f_{\Lambda_b^0}}{f_d}$ is seen to vary as a function of $p_{\rm T}$ [93, 95], a value is chosen that corresponds to the average $p_{\rm T}$ of events in the $\overline{D}^0\pi^+\pi^-$ data sample.

Peaking backgrounds can also arise from two-body $B^0_{(s)}$ decays, such as $B^0_{(s)} \to D^\pm_{(s)} h^\mp$ with $D^\pm_{(s)} \to 3h$ or $B^0_{(s)} \to D^0\overline{D}^0$. As these backgrounds form peaks in the invariant mass distributions of specific combinations of the final state particles,

Table 4.4: Estimates of the contributions from various peaking background sources to the $\overline{D}^0 K\pi$ dataset. Measurements of the branching fractions and fragmentation fractions were taken from Refs. [3, 89, 93, 94, 96, 97]. Efficiencies were estimated from the fraction of simulated events that were reconstructed and passed the initial selection requirements. The values used for $\mathcal{B}(B^0 \to \overline{D}^0 K^+\pi^-)$ and $\epsilon_{\overline{D}^0 K\pi}$ when calculating $N_{\rm peak}/N_{B^0\to\overline{D}^0 K\pi}$ were 9×10^{-4} and 2.5 %, respectively.

Mode	$\overline{\Lambda}_b^0 \to \overline{D}^0\overline{p}\pi^+$	$\overline{\Lambda}_b^0 \to \overline{D}^0\overline{p}K^+$	$B^0 \to \overline{D}^0\pi^+\pi^-$
Branching fraction	10^{-3}	10^{-4}	8.4×10^{-4}
f_x/f_d	0.55 [93]	0.55 [93]	1
Efficiency	7.0×10^{-3}	4.4×10^{-3}	1.1×10^{-3}
$N_{\rm peak}/N_{B^0\to\overline{D}^0 K\pi}$	1.75	0.11	0.42
Mode	$B^0 \to \overline{D}^0 K^+K^-$	$B_s^0 \to \overline{D}^0 K^+K^-$	
Branching fraction	4.7×10^{-5}	4.2×10^{-5}	
f_x/f_d	1	0.267 [94]	
Efficiency	5.5×10^{-3}	6.0×10^{-3}	
$N_{\rm peak}/N_{B^0\to\overline{D}^0 K\pi}$	0.12	0.03	

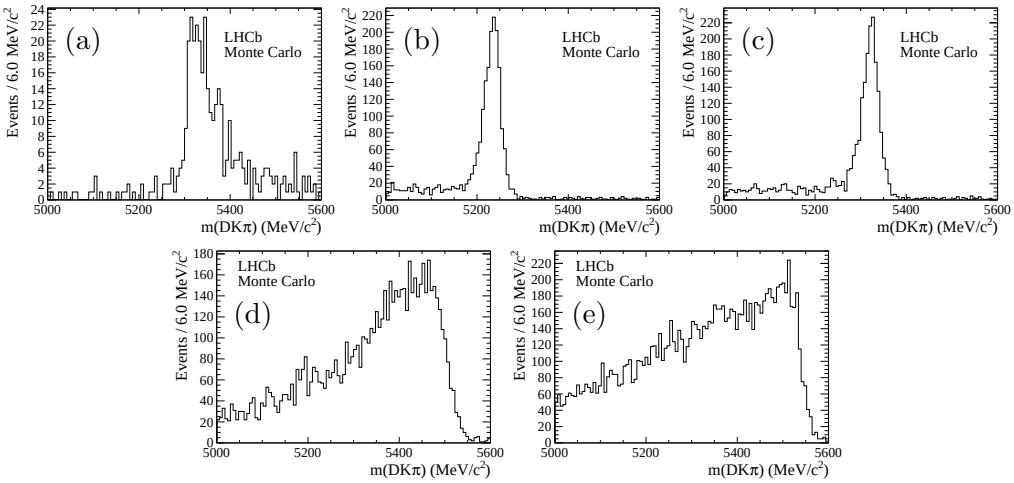

Figure 4.9: Reconstructed $m(\overline{D}^0 K\pi)$ distributions obtained from simulated events that pass the selection requirements: (a) $B^0 \to \overline{D}^0\pi^+\pi^-$, (b) $B^0 \to \overline{D}^0 K^+K^-$, (c) $B_s^0 \to \overline{D}^0 K^+K^-$, (d) $\overline{\Lambda}_b^0 \to \overline{D}^0\overline{p}K^+$ and (e) $\overline{\Lambda}_b^0 \to \overline{D}^0\overline{p}\pi^+$. Events were generated uniformly across the three-body phase space.

they were investigated using data. Figure 4.10 shows the two- and three-body combinations that contain exactly one of the tracks assigned to the $\overline{D}^0$ meson. For correctly reconstructed signal events, these mass distributions should not contain any resonant peaks. Doubly charged combinations, *e.g.* $\pi^+\pi^+$, were excluded. Small peaks were seen at the $\overline{D}^0$ mass in the $\overline{D}^0(\pi^-)K^+$ and $\overline{D}^0(K^+)\pi^-$ combinations, due to signal events where the $\overline{D}^0$ was reconstructed from the wrong pair of tracks. As these peaks were small compared to the number of correctly reconstructed signal events in the same region of the phase space, no vetoes were applied. Peaks were also seen at the $D^\pm$ and $D_s^\pm$ masses in the $\overline{D}^0(\pi^-)K^\pm\pi^\mp$ and $\overline{D}^0(K^+)K^\pm\pi^\mp$ combinations, respectively. These backgrounds were removed by the vetoes described in Sec. 4.2.4.

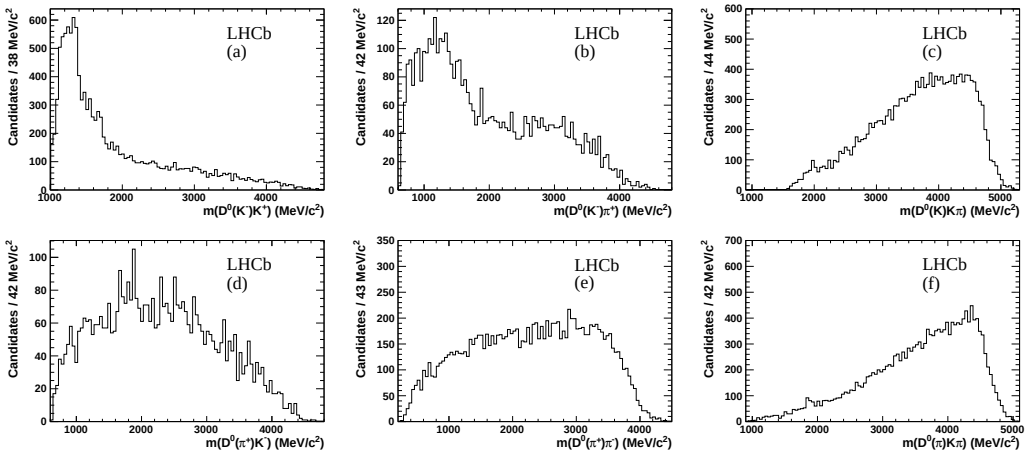

Figure 4.10: Combinations of particles in the $B^0_{(s)} \to \overline{D}^0 K\pi$ dataset, (a) K from $\overline{D}^0$ with bachelor K, (b) K from $\overline{D}^0$ with bachelor π, (c) K from $\overline{D}^0$ with bachelors K and π, (d) π from $\overline{D}^0$ with bachelor K, (e) π from $\overline{D}^0$ with bachelor π and (f) π from $\overline{D}^0$ with bachelors K and π. The PID requirements on the $\overline{D}^0$ daughters, and the vetoes described in Sec. 4.2.4 are not applied to the data in these plots.

4.3.3 Charmless peaking background

The level of charmless background passing the selection is shown to be low in Fig. 4.8. To check for any backgrounds that peak in the B mass, the B mass distribution was investigated for events in the "sideband" regions ($1764 \to 1784\,\mathrm{MeV}/c^2$ and $1944 \to 1964\,\mathrm{MeV}/c^2$) of the reconstructed $\overline{D}^0$ mass distribution as shown in Fig. 4.11. No peaks were seen in this distribution, therefore, it can be absorbed into the combinatorial component.

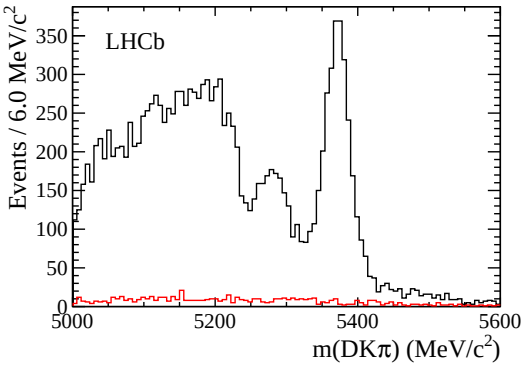

Figure 4.11: Reconstructed $B^0_{(s)}$ mass distribution obtained from (red) charmless background events underneath the $\overline{D}^0$ mass peak, estimated from events that fail the $\overline{D}^0$ mass requirement. For comparison this is overlaid on (black) the mass distribution from events that pass the $\overline{D}^0$ mass requirement.

4.3.4 Partially reconstructed background

Partially reconstructed backgrounds, where some tracks are missing from the reconstructed B candidate, populate the low mass region below 5200 (5300) MeV/c^2 for $B^0_{(s)}$ decays. These backgrounds are very signal-like so they are not removed by the NN requirement. The dominant partially reconstructed backgrounds to $B^0_{(s)} \to \overline{D}^0 K\pi$ decays are due to $B^0_{(s)} \to \overline{D}^{*0} K\pi$ decays where the $\overline{D}^{*0}$ meson decays to either $\overline{D}^0\pi^0$ or $\overline{D}^0\gamma$, and the soft neutral particle is not reconstructed. In addition, partially reconstructed backgrounds with mis-identified particles, *e.g.* $B^0 \to \overline{D}^{*0}\pi\pi$, can also contribute. The reconstructed $\overline{D}^0 K\pi$ mass distributions from simulated samples of $B^0_s \to \overline{D}^{*0} K\pi$ and $B^0 \to \overline{D}^{*0}\pi\pi$ are shown in Fig. 4.12.

4.4 Efficiencies

As the kinematics of the decay vary across the DP phase space, the efficiency with which an event can be reconstructed and selected also varies. To account for this variation, the efficiency must be calculated as a function of the DP variables. In the analyses described in this thesis, the efficiency is broken down into multiple contributions that are multiplied together to give the total efficiency.

In the branching fraction analysis the total efficiency, ϵ^{tot}, is given by

$$\epsilon^{\text{tot}} = \epsilon^{\text{geom}}\epsilon^{\text{sel|geom}}\epsilon^{\text{PID|geom\&sel}}\epsilon^{\text{trig|geom\&sel\&PID}}, \tag{4.7}$$

where ϵ^{geom} is the probability that all of the tracks in the final state are within

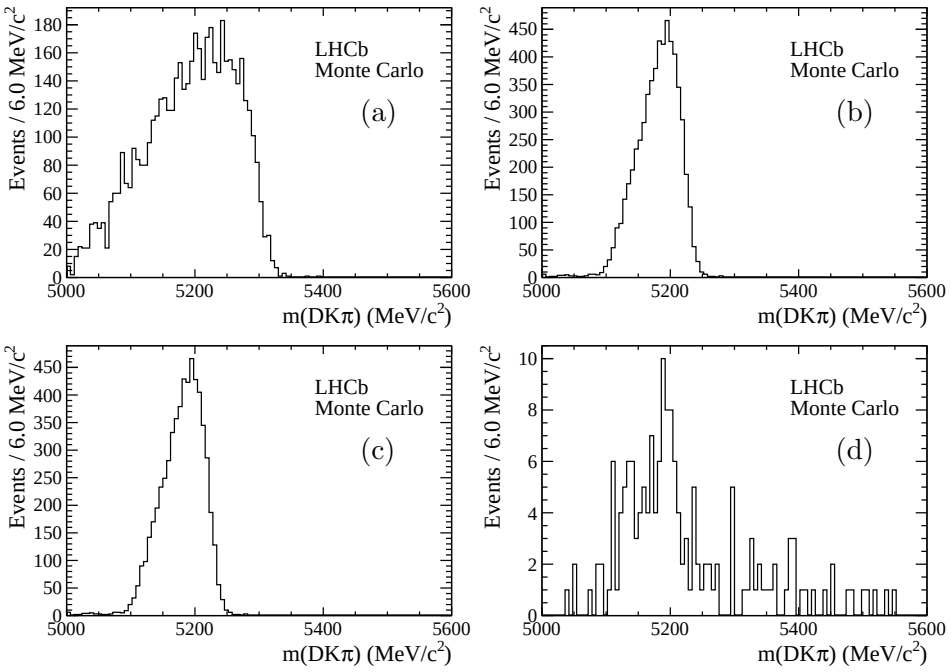

Figure 4.12: Reconstructed $m(\overline{D}^0 K\pi)$ distributions obtained from simulated samples of $B \to \overline{D}^{*0} hh'$ decay modes: (a) $B_s^0 \to \overline{D}^{*0} K\pi$ with $\overline{D}^{*0} \to \overline{D}^0\gamma$, (b) $B_s^0 \to \overline{D}^{*0} K\pi$ with $\overline{D}^{*0} \to \overline{D}^0\pi^0$, (c) $B^0 \to \overline{D}^{*0}\pi\pi$ with $\overline{D}^{*0} \to \overline{D}^0\gamma$, (d) $B^0 \to \overline{D}^{*0}\pi\pi$ with $\overline{D}^{*0} \to \overline{D}^0\pi^0$.

the detector acceptance, $\epsilon^{\text{sel|geom}}$ is the probability that the decay is accepted by the selection requirements (excluding PID), $\epsilon^{\text{PID|geom\&sel}}$ is the probability that the decay passes the PID requirements and $\epsilon^{\text{trig|geom\&sel\&PID}}$ is the probability that the decay passes the trigger requirements. Each efficiency is conditional on the preceding terms. As the selection requires each candidate to pass one of a small number of related software trigger lines, the conditional probability with which these events pass the required triggers is very high. For the DP analyses the efficiency is broken down as

$$\epsilon^{\text{tot}} = \epsilon^{\text{geom}} \epsilon^{\text{sel\&trig|geom}} \epsilon^{\text{PID|geom\&sel\&trig}}, \tag{4.8}$$

where the requirement to pass the trigger has been included explicitly in the selection efficiency.

As previously stated, each contribution to the efficiency was evaluated as a function of the DP variables. To evaluate the geometrical efficiency, simulated events were generated without any reconstruction effects. Each event was generated

with the B meson within the detector acceptance[2] ($2 < \eta < 5$) and the fraction of events where all four tracks fell within the detector acceptance was evaluated in bins in the DP phase space. The efficiencies for the $B^0 \to \overline{D}^0\pi\pi$ control mode and the $B^0_{(s)} \to \overline{D}^0 K\pi$ signal decays in bins across the DP are shown in Fig. 4.13.

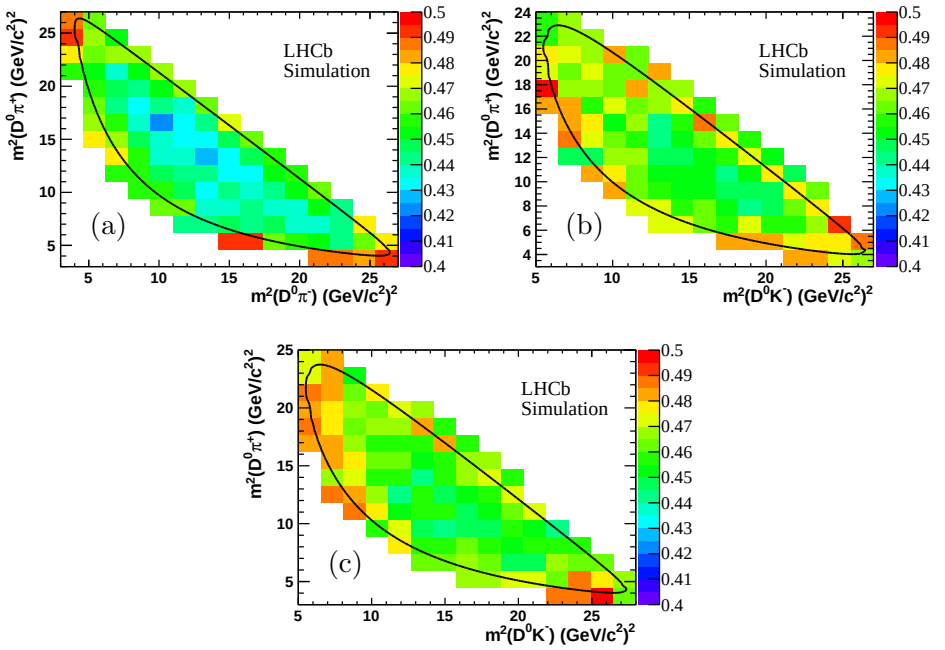

Figure 4.13: ϵ^{geom} across the $B \to \overline{D}^0 hh'$ DPs, obtained from simulated data. (a) $B^0 \to \overline{D}^0\pi^+\pi^-$, (b) $B^0 \to \overline{D}^0 K^+\pi^-$, (c) $B^0_s \to \overline{D}^0 K^-\pi^+$. The black lines correspond to the kinematic boundaries of the DPs.

For the selection efficiency, events were generated with the $B^0_{(s)}$ meson decay products within the detector's acceptance and passed through the full GEANT4 simulation and reconstruction. The efficiency was evaluated in each bin in the phase space as the ratio of the number of reconstructed events that passed the selection to the number of events generated. The selection efficiencies across the phase space are shown in Fig. 4.14.

As PID variables are difficult to simulate accurately, the PIDCALIB package, introduced in Sec. 3.2.9, was used to model the effect of PID requirements on the efficiency. The calibration samples were used to produce efficiency profiles for the

[2]The kinematics of the subsequent decay are independent of the B meson's direction of flight and only B mesons within the acceptance can possibly produce four daughters within the acceptance, so it is more efficient to only generate events where the B meson is produced within the detector's acceptance.

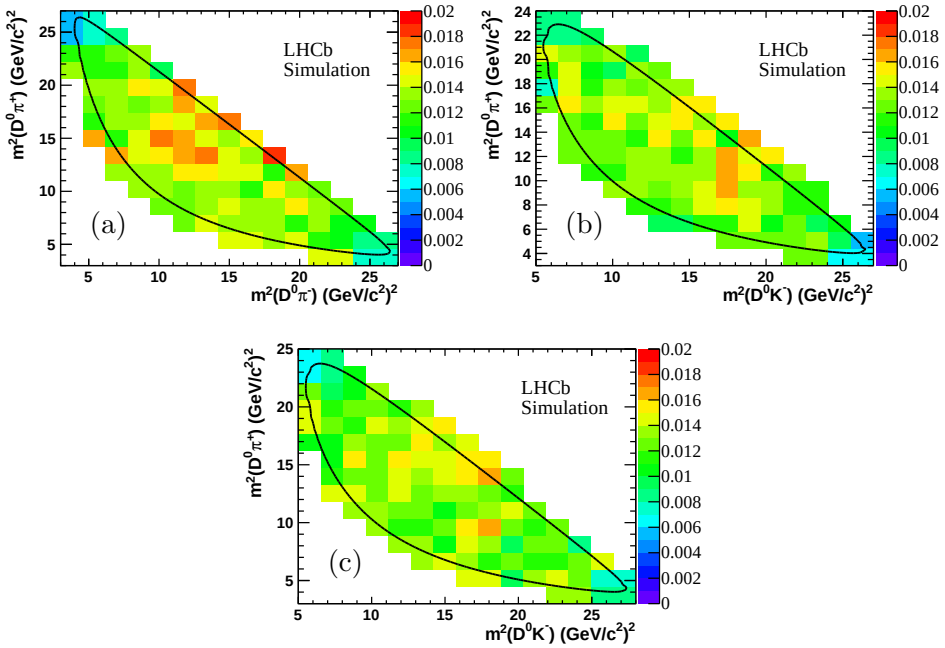

Figure 4.14: $\epsilon^{\text{sel|geom}}$ across the $B \to \overline{D}^0 hh'$ DPs, obtained from simulated data. (a) $B^0 \to \overline{D}^0\pi^+\pi^-$, (b) $B^0 \to \overline{D}^0 K^+\pi^-$, (c) $B_s^0 \to \overline{D}^0 K^-\pi^+$. The black lines correspond to the kinematic boundaries of the DPs.

PID requirements applied to pions and kaons as a function of p and p_{T}.[3] For each simulated event that passed the selection requirements, the event was weighted to account for the PID response. The efficiency in each bin was then evaluated as the ratio of the weighted sum to the unweighted sum of events in that bin. The PID efficiencies across the phase space are shown in Fig. 4.15.

The trigger efficiency was evaluated from simulated data with all selection requirements applied (including PID requirements) but without the explicit trigger requirements applied. The efficiency in each bin was evaluated as the fraction of events that passed the trigger requirements within that bin. The trigger efficiencies across the phase space are shown in Fig. 4.16. A summary of all of the efficiency contributions, averaged across the DP, for the three $B^0_{(s)} \to \overline{D}^0 hh$ decay modes is given in Table 4.5.

[3] In the later analyses, the PID response was also taken as a function of the track multiplicity of the event.

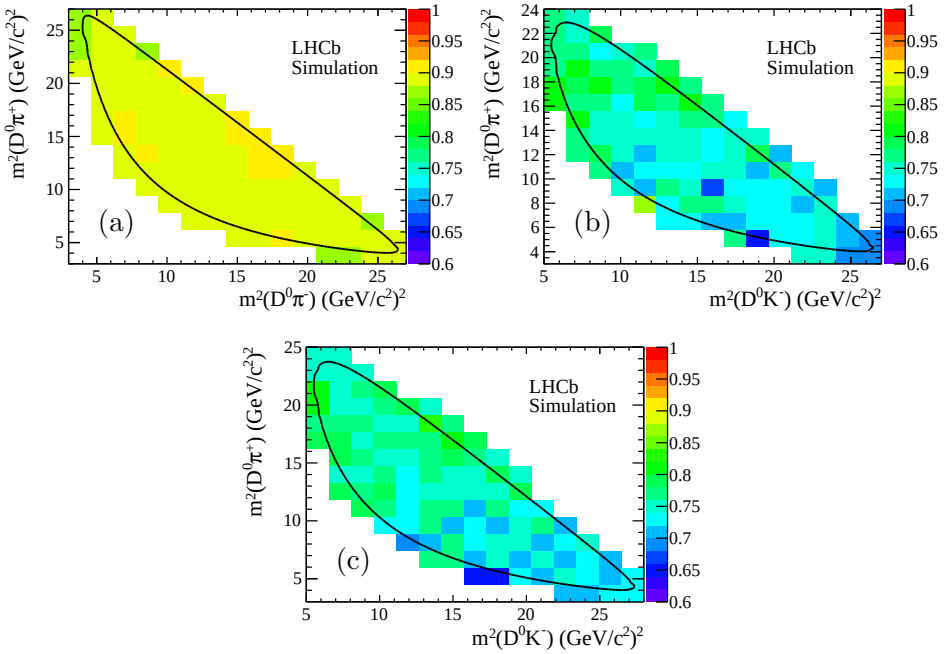

Figure 4.15: $\epsilon^{\text{PID|sel\&geom}}$ across the $B \to \overline{D}^0 hh'$ DPs, obtained from simulated data. (a) $B^0 \to \overline{D}^0 \pi^+ \pi^-$, (b) $B^0 \to \overline{D}^0 K^+ \pi^-$, (c) $B_s^0 \to \overline{D}^0 K^- \pi^+$. The black lines correspond to the kinematic boundaries of the DPs.

Table 4.5: Summary of the efficiencies found for $\overline{D}^0 \pi\pi$ and $\overline{D}^0 K\pi$ decays in simulated data. Values given are in percent.

	$B^0 \to \overline{D}^0 \pi\pi$	$B^0 \to \overline{D}^0 K\pi$	$B_s^0 \to \overline{D}^0 K\pi$
ϵ^{geom}	44.7%	46.6%	46.5%
$\epsilon^{\text{sel\|geom}}$	1.35%	1.29%	1.28%
$\epsilon^{\text{PID\|sel\&geom}}$	89.3%	74.8%	75.0%
$\epsilon^{\text{trig\|PID\&sel\&geom}}$	97.7%	97.1%	97.6%
ϵ^{tot}	0.53%	0.44%	0.44%

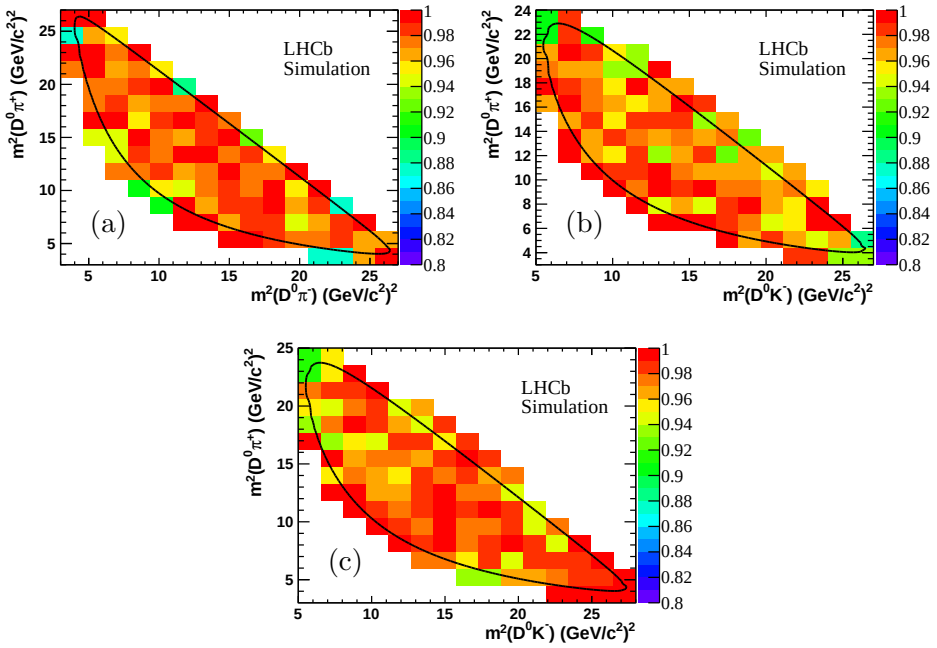

Figure 4.16: $\epsilon^{\text{trig|PID\&sel\&geom}}$ across the $B \to \overline{D}^0 hh'$ DPs, obtained from simulated data. a) $B^0 \to \overline{D}^0 \pi^+ \pi^-$, (b) $B^0 \to \overline{D}^0 K^+ \pi^-$, (c) $B_s^0 \to \overline{D}^0 K^- \pi^+$. The black lines correspond to the kinematic boundaries of the DPs.

Chapter 5

Branching fraction measurements

This chapter decribes the measurement of the branching fractions of $B^0 \to \overline{D}^0 K^+\pi^-$ and $B_s^0 \to \overline{D}^0 K^-\pi^+$ decays relative to the control channel, $B^0 \to \overline{D}^0\pi^+\pi^-$. These measurements are made using 1.0 fb^{-1} of data collected by LHCb during 2011.

5.1 Fits to the B mass distributions

Unbinned extended maximum likelihood fits are performed to obtain the yields of the signal components from the $\overline{D}^0 K\pi$ and $\overline{D}^0\pi\pi$ datasets. In practice, the values of the likelihood, $\mathcal{L}$, obtained by varying the fit parameters may span many orders of magnitude. It is, therefore, more convenient to minimise the negative log likelihood, $\text{NLL} = -\ln\mathcal{L}$.

Based on the background study detailed in Sec. 4.3, the following components are included in the models used to describe the $\overline{D}^0 K\pi$ and $\overline{D}^0\pi\pi$ mass distributions.

- $\overline{D}^0 K\pi$
  - B^0 signal
  - B_s^0 signal
  - combinatorial background
  - partially reconstructed background from $B_s^0 \to \overline{D}^{*0} K^-\pi^+$
  - peaking background from $B^0 \to \overline{D}^0\pi^+\pi^-$

- $\overline{D}^0\pi\pi$
  - B^0 signal
  - combinatorial background
  - partially reconstructed background from $B^0 \to \overline{D}^{*0}\pi^+\pi^-$
  - peaking background from $\overline{\Lambda}_b^0 \to \overline{D}^0\overline{p}\pi^+$

While a significant contribution from $\overline{\Lambda}_b^0 \to \overline{D}^0\overline{p}\pi^+$ decays is expected in the $m(\overline{D}^0 K\pi)$ distribution, the yield for this component is found to be strongly correlated to the combinatorial background which has a similar shape. To stabilise the fit this contribution is removed from the model and the background absorbed into the combinatorial background component. The fit to the $\overline{D}^0 K\pi$ ($\overline{D}^0\pi\pi$) mass distribution is performed in the range 5200 (5150) – 5600 MeV/c^2. These ranges allow for simplified descriptions of the partially reconstructed background contributions to both datasets.

5.1.1 Signal and background PDFs

Signal

Each signal peak is parameterised as a pair of Gaussian functions with a common mean,

$$\mathcal{P}_{\text{sig}}(m) = f\,G(m;\mu_B,\sigma_1) + (1-f)\,G(m;\mu_B,\sigma_2)\,, \tag{5.1}$$

where f parameterises the relative normalisation of the two Gaussians, and the parameters μ_B, σ_1, f and the ratio σ_2/σ_1[1] are determined from fits to data or simulated data. This parameterisation is validated using simulated decays and is found to give a reasonable description of the signal shape. Fits to simulated samples of the three signal decay modes are shown in Fig. 5.1 and the results of the fits are tabulated in Table 5.1. In the fit to $m(\overline{D}^0\pi\pi)$ data, μ_B, σ_1, f and σ_2/σ_1 are all left as free parameters of the fit. In the fit to $m(\overline{D}^0 K\pi)$, f and σ_2/σ_1 are constrained to the values obtained from simulated $B_s^0 \to \overline{D}^0 K^-\pi^+$ decays. These constraints enter the fit as Gaussian penalty terms in the likelihood equation. In addition, the value of σ_1 is shared between the B^0 and B_s^0 signal peaks and the difference between the means of the two shapes, μ_B and μ_{B_s}, is fixed to the mass difference reported by the PDG [3].

[1] Varying σ_1 and the ratio σ_2/σ_1 is found to produce more stable fits than varying σ_1 and σ_2 independently as the two widths are highly correlated.

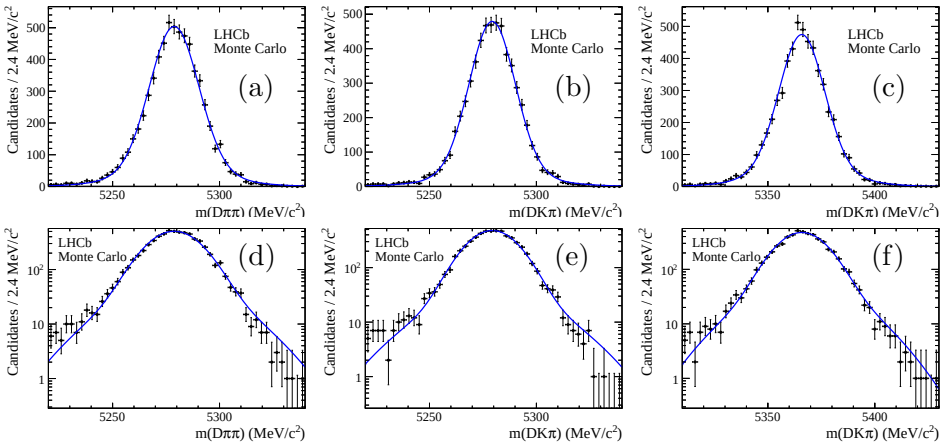

Figure 5.1: Fit to the B candidate invariant mass distribution for (a) $B^0 \to \overline{D}^0\pi\pi$, (b) $B^0 \to \overline{D}^0 K\pi$ and (c) $B_s^0 \to \overline{D}^0 K\pi$ simulated data. The same data are shown in (d), (e) and (f) on logarithmic scales. The asymmetry between the low-mass and high-mass tails of the distributions is due to "radiative decays" where photons are emitted by final state particles and not included in the reconstructed candidate decay. This discrepancy in the fit model is treated as a source of systematic uncertainty in Sec. 5.2.1.

Table 5.1: Parameters of the signal double Gaussian shape (Eq. 5.1) obtained from fits to simulated data.

Parameter	$B^0 \to \overline{D}^0\pi\pi$	$B^0 \to \overline{D}^0 K\pi$	$B_s^0 \to \overline{D}^0 K\pi$
μ_B (MeV/c^2)	5278.80 ± 0.16	5279.32 ± 0.16	5365.89 ± 0.16
σ_1 (MeV/c^2)	11.5 ± 0.3	10.8 ± 0.2	10.6 ± 0.3
σ_2 (MeV/c^2)	23.8 ± 1.7	24.7 ± 1.8	21.8 ± 1.3
f	0.84 ± 0.04	0.86 ± 0.03	0.82 ± 0.04
χ^2/n.d.o.f.	1.32	0.97	0.95

Combinatorial background

In the fits to both mass distributions, the combinatorial background is parameterised as a first order polynomial with the yield and slope as free parameters. In the $\overline{D}^0 K\pi$ fit, the larger number of fit components makes it necessary to constrain the gradient of the combinatorial background. This constraint is extracted from a fit to the doubly charged $\overline{D}^0 K^\pm\pi^\pm$ data sample.

Candidates with a reconstructed B mass significantly different from the true B^0 and B_s^0 masses are more likely to fail the mass constrained vertex fits introduced in Sec. 4.2. To account for this effect, the combinatorial background shape is multiplied

by the function,

$$f(m) = \begin{cases} 1 & \text{if } m \leq m_0 \\ 1 - k(m - m_0) & \text{if } m > m_0, \end{cases} \tag{5.2}$$

where the threshold mass, m_0, and the parameter, k, are obtained separately for the $\overline{D}^0\pi\pi$ and $\overline{D}^0 K\pi$ samples from fits to the B mass distributions of candidates that fail the vertex fits.[2] The results from these fits are summarised in Table 5.2. It is sufficient to only apply this correction to the combinatorial background component, as no other components contribute significantly at high masses.

Table 5.2: Parameters of the linear shape obtained from fits to events that failed the mass constrained vertex fits. Parameters are defined in Eq. 5.2.

Parameter	$\overline{D}^0\pi\pi$	$\overline{D}^0 K\pi$
k	$(0.0029 \pm 0.0004)(\text{MeV}/c^2)^{-1}$	$(0.0031 \pm 0.0005)(\text{MeV}/c^2)^{-1}$
m_0	$(5450 \pm 4)\,\text{MeV}/c^2$	$(5437 \pm 9)\,\text{MeV}/c^2$

Partially reconstructed background

In the fit to $m(\overline{D}^0\pi\pi)$, the dominant partially reconstructed background is due to $B^0 \to \overline{D}^{*0}\pi^+\pi^-$ decays which peaks below $5150\,\text{MeV}/c^2$. It is sufficient to model the residual partially reconstructed candidates with an exponential component where both the yield and the exponential coefficient are free parameters in the fit to data.

The dominant partially reconstructed background in the $\overline{D}^0 K\pi$ fit is due to B_s^0 decays. As these backgrounds are found at higher masses it is not possible to employ a simple exponential model. Instead, a smoothed non-parametric PDF derived from simulated $B_s^0 \to \overline{D}^{*0}K^-\pi^+$ decays is used with the yield as a free parameter in the fit. As the slope depends on the underlying phasespace distribution of these decays, an additional shape describing the resonant contribution $B_s^0 \to \overline{D}^{*0}\overline{K}^{*0}$ is included as a systematic variation of the fit. The relative proportions of the three helicity amplitudes for this decay are fixed to those seen for $B^0 \to \overline{D}^{*0}\rho^0$ decays [98], while the combined yield is a free parameter in the fit. The PDFs for these backgrounds are shown in Fig. 5.2.

[2] Due to improvements in the vertex fitting algorithm, this correction factor is not needed in the subsequent analyses.

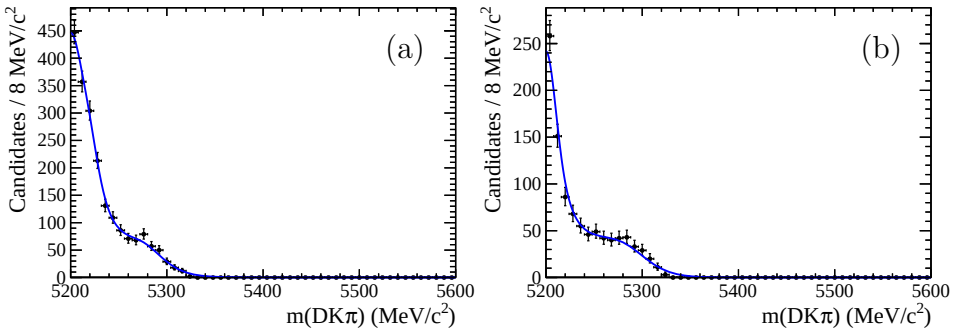

Figure 5.2: Reconstructed B mass distributions of (a) $B^0_s \to \overline{D}^{*0}K\pi$ and (b) $B^0_s \to \overline{D}^{*0}K^{*0}$ background PDFs.

Peaking background

One peaking background component is included in each of the mass fits: due to $B^0 \to \overline{D}^0\pi^+\pi^-$ decays in $m(\overline{D}^0K\pi)$ and due to $\overline{\Lambda}^0_b \to \overline{D}^0\overline{p}\pi^+$ decays in $m(\overline{D}^0\pi\pi)$. As previously mentioned, a $\overline{\Lambda}^0_b \to \overline{D}^0\overline{p}\pi^+$ background component in $m(\overline{D}^0K\pi)$ is absorbed into the combinatorial background to avoid large correlations between the fit parameters. All of these components are described by smoothed non-parametric PDFs derived from simulated data.

The simulated data used to describe each of these backgrounds are generated uniformly across the relevant DP phase space but in reality these DPs include resonant structures. To better describe these background contributions, the simulated datasets are reweighted to match data [89, 97] in the invariant mass distribution of the pair of correctly identified daughter particles. The reweighting procedure is illustrated in Fig. 5.3 and the PDFs are shown in Fig. 5.4.

5.1.2 Fit to data

The fits to $m(\overline{D}^0\pi\pi)$ and $m(\overline{D}^0K\pi)$ are shown in Figs 5.5 and 5.6, respectively, and the fitted parameters are listed in Table 5.3. The signal yields obtained from these fits are used to calculate the branching fraction ratios,

$$R_{B^0_{(s)}} \equiv \frac{\mathcal{B}\left(B^0_{(s)} \to \overline{D}^0K\pi\right)}{\mathcal{B}\left(B^0 \to \overline{D}^0\pi\pi\right)}\,, \tag{5.3}$$

as described in Sec. 5.1.3. To ensure each fit is stable and unbiased, 1000 mass distributions are generated based on the total fit PDF with the number of events in each distribution varied around the true number according to Poisson statistics. The fit model is used to fit each of the generated samples to obtain the pulls on all

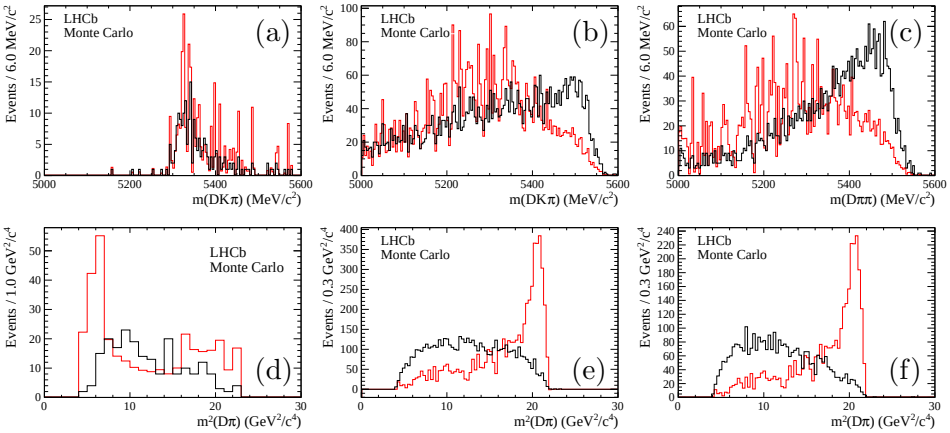

Figure 5.3: B candidate mass distributions of (a) $B^0 \to \overline{D}^0\pi^+\pi^-$ and (b) $\overline{\Lambda}_b^0 \to \overline{D}^0\overline{p}\pi^+$ backgrounds to the $\overline{D}^0 K\pi$ channel, and (c) $\overline{\Lambda}_b^0 \to \overline{D}^0\overline{p}\pi^+$ background to the $\overline{D}^0\pi\pi$ channel. Distributions are shown both (black) before and (red) after reweighting. Note that in each case the reweighted shape is used to obtain the background PDF. The corresponding unweighted and weighted $m(\overline{D}^0\pi)$ distributions are shown in (d), (e) and (f).

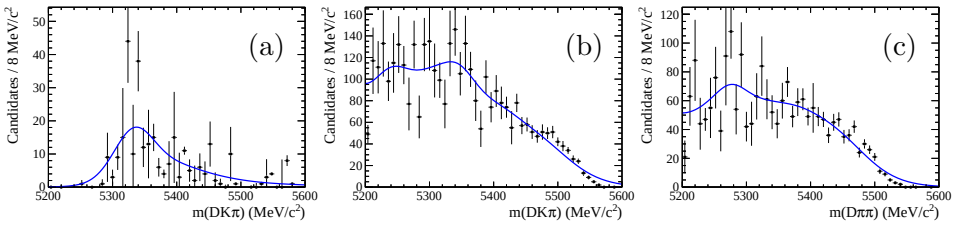

Figure 5.4: PDFs for (a) $B^0 \to \overline{D}^0\pi^+\pi^-$ and (b) $\overline{\Lambda}_b^0 \to \overline{D}^0\overline{p}\pi^+$ backgrounds to the $\overline{D}^0 K\pi$ channel, and (c) $\overline{\Lambda}_b^0 \to \overline{D}^0\overline{p}\pi^+$ background to the $\overline{D}^0\pi\pi$ channel.

of the parameters of the fit.[3] A Gaussian fit is performed to the distribution of pulls obtained for each parameter. For all of the parameters, the fitted Gaussian mean and width are consistent with zero and one, respectively, indicating that the fits to the mass distributions are unbiased and that the statistical uncertainties obtained from the fit are accurate.

[3]The pull is defined as the difference between the generated and fitted values divided by their combined uncertainties.

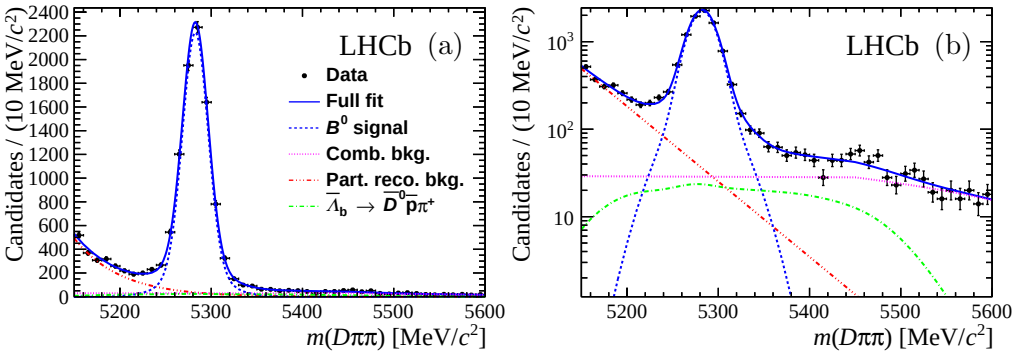

Figure 5.5: Fit to the B candidate invariant mass distribution for $\overline{D}^0\pi\pi$ candidates on (a) linear and (b) logarithmic y-axis scales. Data points are shown in black, the full fitted PDF as a solid blue line and the component PDFs as detailed in the legend.

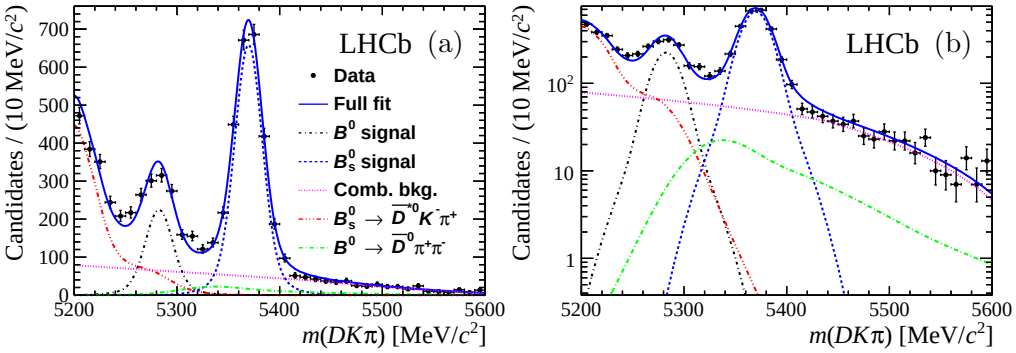

Figure 5.6: Fit to the B candidate invariant mass distribution for $\overline{D}^0K\pi$ candidates on (a) linear and (b) logarithmic y-axis scales. Data points are shown in black, the full fitted PDF as a solid blue line and the component PDFs as detailed in the legend.

5.1.3 Calculation of branching fraction ratios

The ratios of branching fractions are determined as

$$R_{B^0} \equiv \frac{\mathcal{B}\left(B^0 \to \overline{D}^0 K^+\pi^-\right)}{\mathcal{B}\left(B^0 \to \overline{D}^0\pi^+\pi^-\right)} = \frac{N^{\rm corr}(B^0 \to \overline{D}^0 K^+\pi^-)}{N^{\rm corr}(B^0 \to \overline{D}^0\pi^+\pi^-)}\,, \tag{5.4}$$

$$R_{B^0_s} \equiv \frac{\mathcal{B}\left(B^0_s \to \overline{D}^0 K^-\pi^+\right)}{\mathcal{B}\left(B^0 \to \overline{D}^0\pi^+\pi^-\right)} = \left(\frac{f_s}{f_d}\right)^{-1} \frac{N^{\rm corr}(B^0_s \to \overline{D}^0 K^-\pi^+)}{N^{\rm corr}(B^0 \to \overline{D}^0\pi^+\pi^-)}\,, \tag{5.5}$$

where the efficiency-corrected yield is $N^{\rm corr} = \sum_i W_i/\epsilon_i^{\rm tot}$. Here the index i runs over all candidates in the fit range, W_i is the signal `sWeight` [92] for candidate i, determined from the fits shown in Figs 5.5 and 5.6, and $\epsilon_i^{\rm tot}$ is the efficiency for candidate i determined as a function of its DP position. The ratio of fragmentation fractions, f_s/f_d, is taken to be 0.256 ± 0.020 [94].

Table 5.3: Parameters from the fits to $\overline{D}^0\pi\pi$ and $\overline{D}^0K\pi$ datasets.

Parameter	$\overline{D}^0\pi\pi$	$\overline{D}^0K\pi$
μ_{B^0}	$5282.6 \pm 0.2\,\text{MeV}/c^2$	$5282.5 \pm 0.4\,\text{MeV}/c^2$
σ_1	$13.9 \pm 0.4\,\text{MeV}/c^2$	$13.0 \pm 0.5\,\text{MeV}/c^2$
σ_2	$\sigma_1 \times 2.20 \pm 0.24$	$\sigma_1 \times 2.06 \pm 0.10$
Relative fraction (f)	0.83 ± 0.04	0.80 ± 0.04
Linear slope	-0.000066 ± 0.000018	-0.0001769 ± 0.0000006
Exponential slope	-0.0198 ± 0.0014	—
$N(B^0 \to \overline{D}^0K^+\pi^-)$	—	815 ± 55 events
$N(B_s^0 \to \overline{D}^0K^-\pi^+)$	—	2391 ± 81 events
$N(B^0 \to \overline{D}^0\pi^+\pi^-)$	8558 ± 134 events	282 ± 159 events
N(part. reco. bkg)	2479 ± 118 events	—
N(comb. bkg)	1184 ± 102 events	1683 ± 207 events
$N(\overline{\Lambda}_b^0 \to \overline{D}^0\overline{p}\pi^-)$	613 ± 146 events	—
$N(B_s^0 \to \overline{D}^{*0}K^-\pi^+)$	—	1625 ± 84 events

5.2 Systematic uncertainties

Various sources of systematic uncertainty are considered for the two branching fraction ratios. These sources are summarised in Table 5.4 and described in more detail below.

Table 5.4: Summary of systematic uncertainties on the $B^0_{(s)} \to \overline{D}^0K\pi/B^0 \to \overline{D}^0\pi\pi$ branching fraction ratios. The total is obtained from the sum in quadrature of all contributions.

Source	Uncertainty (B^0)	Uncertainty (B_s^0)
Fit model	6.3 %	4.3 %
Efficiency model	3.4 %	3.1 %
Simulation statistics	2.0 %	2.0 %
Vetoes	2.0 %	1.1 %
Particle identification	1.0 %	1.0 %
Trigger	1.0 %	1.0 %
f_s/f_d	—	7.8 %
Total	7.8 %	9.8 %

5.2.1 Fit model

The $\overline{D}^0K\pi$ fit model is varied by replacing the double Gaussian signal component with a double Crystal Ball function [99], scaling the width of the signal PDF to account for the different masses of the B^0 and B_s^0 mesons, replacing each of the background PDFs with an unsmoothed version, and adding components for back-

grounds due to $B_s^0 \to \overline{D}^{*0}\overline{K}^{*0}$ and $\overline{\Lambda}_b^0 \to \overline{D}^0\overline{p}\pi^+$ decays. For the $\overline{D}^0\pi\pi$ model, the PDF of the $\overline{\Lambda}_b^0 \to \overline{D}^0\overline{p}\pi^+$ component is replaced with an unsmoothed version, the slope of the combinatorial background is varied and the exponential partially reconstructed background PDF is replaced with a non-parametric PDF from simulated $B^0 \to \overline{D}^{*0}\pi^+\pi^-$ decays. Combined in quadrature, these variations contribute a 6.3 % (4.3 %) relative uncertainty to R_{B^0} ($R_{B_s^0}$). No evidence of fit bias is seen so the corresponding systematic uncertainty is considered to be negligible.

5.2.2 Efficiency variation across the Dalitz plot

Variation of the efficiency across the DP may not be modelled correctly in simulation. To evaluate the uncertainty due to this source, a two-dimensional polynomial function is used to fit each of the efficiency components and these functions are used to generate alternative efficiency histograms, varying the fit parameters within their uncertainties. The efficiency-corrected yields are calculated from each set of histograms and the uncertainties are calculated from a Gaussian fit to the distribution of values obtained. This leads to a systematic uncertainty of 3.4 % (3.1 %) for R_{B^0} ($R_{B_s^0}$). In addition, the limited number of events in the simulated data used to evaluate the efficiencies contributes a 2.0 % relative uncertainty in both R_{B^0} and $R_{B_s^0}$.

5.2.3 Event selection

As most of the selection requirements applied to the $\overline{D}^0K\pi$ and $\overline{D}^0\pi\pi$ datasets are identical, any systematic effects due to these requirements should cancel in the ratio of branching fractions. The invariant mass vetoes described in Sec. 4.2.4 do, however, contribute a systematic uncertainty to the branching fraction ratios. The range of each veto is varied, yielding a combined uncertainty of 2.0 % (1.1 %) to R_{B^0} ($R_{B_s^0}$).

The main difference between the selection requirements made for the $\overline{D}^0K\pi$ and $\overline{D}^0\pi\pi$ data samples is in the bachelor track PID requirements. A systematic uncertainty of 0.5 % is assigned for both the pion and kaon identification requirements. This value is consistent with uncertainties assigned in similar analyses [32, 100]. To cover any correlations between these uncertainties they are combined linearly to give a total uncertainty of 1.0 %.

5.2.4 Trigger

The response of the hadronic trigger in simulation does not perfectly reproduce the response in data and this effect may not cancel exactly in the ratio of branching fractions. Previous studies of the effect on kaons and pions have limited the systematic

uncertainty to less than 2 % [101]. Since the hadronic L0 trigger only provides approximately half of the data, an uncertainty of 1 % is assigned.

5.2.5 Ratio of fragmentation fractions

The ratio, f_s/f_d was previously measured by LHCb to be 0.256 ± 0.020 [93]. This enters into the calculation of $R_{B^0_s}$, contributing a 7.8 % relative uncertainty.

5.2.6 Crosschecks

Various crosschecks are performed to test the stability of the results. The datasets are divided by L0 trigger category and magnet polarity. In addition, the PID selection and the requirement on the output of the NN are varied, and the requirement for events to pass the B-mass constrained vertex fit is removed. In all cases, the fit results are found to be consistent with the nominal fit result.

5.3 Results

Table 5.5: Raw yields and event-by-event efficiency-corrected numbers of events for the $\overline{D}^0 K\pi$ and $\overline{D}^0\pi\pi$ datasets.

	$B^0 \to \overline{D}^0 K\pi$	$B^0_s \to \overline{D}^0 K\pi$	$B^0 \to \overline{D}^0\pi\pi$
N	815 ± 55	$2\,391 \pm 81$	$8\,558 \pm 134$
N^{corr}	$213\,000 \pm 12\,000$	$607\,000 \pm 16\,000$	$2\,008\,000 \pm 25\,000$

The ratios of the branching fractions, $R_{B^0_{(s)}}$, are determined from efficiency-corrected `sWeighted` yields as described in Sec. 5.1.3. The fitted and corrected yields for the three signal components are shown in Table 5.5. The statistical uncertainties on the corrected yields are determined as

$$\sigma(N^{\text{corr}}) = \sqrt{\sum_i \left(\frac{W_i}{\epsilon_i^{\text{tot}}}\right)^2}, \tag{5.6}$$

where, as in Sec. 5.1.3, W_i and ϵ_i^{tot} are the signal `sWeight` and total efficiency for event i, and the sum runs over all candidate decays in the fitted mass range. This calculation does not include the uncertainty on the efficiency, ϵ^{tot}, which is included as a systematic uncertainty as discussed in Sec. 5.2.2. Additionally, the uncertainties on N^{corr} in Table 5.5 do not include the uncertainty due to variation of the shape parameters floated in the fit, as these parameters must be fixed for the `sWeight` extraction. These contributions are reintroduced as follows:

- The uncertainty on the fitted yields due to the shape parameters, σ^{shape}, is determined by subtracting in quadrature the uncertainty obtained with these parameters fixed in the fit, $\sigma^{\text{yields only}}$, from the uncertainty with them floated, σ^{fit}.

- These uncertainties are then scaled by the ratio N^{corr}/N and summed in quadrature with the uncertainties on the corrected yields, $\sigma(N^{\text{corr}})$, to obtain the corrected uncertainty, $\sigma^{\text{corr}}(N^{\text{corr}})$.

The values of the various uncertainties defined above are shown for all three signal yields in Table 5.6.

Table 5.6: Summary of uncertainties on the fitted and corrected yields used to calculate the statistical uncertainty on the ratio of branching fractions.

	$B^0 \to \overline{D}^0 K\pi$	$B_s^0 \to \overline{D}^0 K\pi$	$B^0 \to \overline{D}^0 \pi\pi$
$\sigma^{\text{fit}}(N)$	55	81	134
$\sigma^{\text{yields only}}(N)$	44	61	100
$\sigma^{\text{shape}}(N)$	33	53	89
$\sigma(N^{\text{corr}})$	12 000	16 000	25 000
$\sigma^{\text{corr}}(N^{\text{corr}})$	15 000	21 000	33 000

Substituting the values for N^{corr} and σ^{corr}, listed in Tables 5.5 and 5.6, into Eq. 5.4 yields the branching fraction ratios,

$$\frac{\mathcal{B}\left(B^0 \to \overline{D}^0 K^+\pi^-\right)}{\mathcal{B}\left(B^0 \to \overline{D}^0 \pi^+\pi^-\right)} = 0.106 \pm 0.007 \pm 0.008\,, \tag{5.7}$$

$$\frac{\mathcal{B}\left(B_s^0 \to \overline{D}^0 K^-\pi^+\right)}{\mathcal{B}\left(B^0 \to \overline{D}^0 \pi^+\pi^-\right)} = 1.18 \pm 0.05 \pm 0.12\,, \tag{5.8}$$

where the first uncertainty is statistical, calculated as described above, and the second is systematic, from the sources described in Sec. 5.2. Absolute branching fractions are determined by multiplying these ratios by the branching fraction of the $B^0 \to \overline{D}^0\pi^+\pi^-$ decay, which was previously measured to be $\mathcal{B}\left(B^0 \to \overline{D}^0\pi^+\pi^-\right) = (8.4 \pm 0.4 \pm 0.8) \times 10^{-4}$ [102].[4] Two corrections are applied to this branching fraction. The measurement assumed equal production of B^+B^- and $B^0\overline{B}^0$ pairs at the $\Upsilon(4S)$ resonance and used $\mathcal{B}\left(D^0 \to K^-\pi^+\right) = (3.80 \pm 0.07)\,\%$. Using updated measurements of $\Gamma(\Upsilon(4S) \to B^+B^-)/\Gamma(\Upsilon(4S) \to B^0\overline{B}^0) = 1.055 \pm 0.025$ [3] and $\mathcal{B}\left(D^0 \to K^-\pi^+\right) = (3.88 \pm 0.05)\,\%$ [3] yields a corrected branching fraction of

[4] Note that a more precise measurement of $\mathcal{B}\left(B^0 \to \overline{D}^0\pi^+\pi^-\right)$ [103] has been published since this analysis was performed.

$\mathcal{B}\left(B^0 \to \overline{D}^0\pi^+\pi^-\right) = (8.5 \pm 0.4 \pm 0.8) \times 10^{-4}$. Multiplying the previously determined ratios by this corrected value gives the branching fractions,

$$\mathcal{B}\left(B^0 \to \overline{D}^0 K^+\pi^-\right) = (9.0 \pm 0.6 \pm 0.7 \pm 0.9) \times 10^{-5}\,, \tag{5.9}$$

$$\mathcal{B}\left(B_s^0 \to \overline{D}^0 K^-\pi^+\right) = (1.00 \pm 0.04 \pm 0.10 \pm 0.10) \times 10^{-3}\,, \tag{5.10}$$

where the first uncertainty is statistical, the second systematic and the third from the uncertainty on the corrected $B^0 \to \overline{D}^0\pi^+\pi^-$ branching fraction.

To evaluate the statistical significance of each of the signal peaks, the likelihood is determined as a function of the relevant signal yield. The statistical significance is obtained as $\sqrt{2\Delta\text{NLL}}$, where ΔNLL is the change in the negative log likelihood when the signal yield is reduced to zero. Figure 5.7 shows how twice the negative log likelihood varies as each of the signal yields is varied.

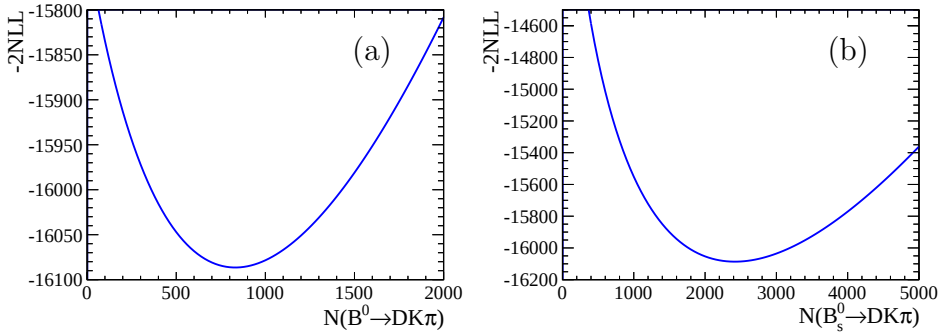

Figure 5.7: Negative log likelihood of the fit to $\overline{D}^0 K\pi$ data, -2NLL, plotted against the signal yield of (a) $B^0 \to \overline{D}^0 K\pi$ and (b) $B_s^0 \to \overline{D}^0 K\pi$ decays.

Systematic effects are incorporated into the significance calculation to give the total significance,

$$s_{\text{tot}} = \frac{s_{\text{stat}}}{\sqrt{1 + \left(\frac{\sigma_{\text{syst}}}{\sigma_{\text{stat}}}\right)^2}}\,, \tag{5.11}$$

where s_{stat} is the statistical significance obtained from the change in -2NLL, σ_{stat} is the statistical uncertainty and σ_{syst} includes all systematics that can affect the signal yield. The $B^0_{(s)}$ decay is found to have a significance of 12 (28) standard deviations. As both decays are clearly present, these significances are not discussed further.

Chapter 6

Dalitz plot analysis of $B_s^0 \to \overline{D}^0 K^- \pi^+$ decays

This chapter details the DP analysis of B_s^0 decays to the $\overline{D}^0 K^- \pi^+$ final state using the full $3\,\text{fb}^{-1}$ dataset recorded by LHCb during run 1 of the LHC. Results are reported for the masses, widths and spins of some D_s^{**} resonances, and for the branching fractions of the quasi-two-body decays that contribute to the DP.

6.1 Selection modifications

As the following DP analyses are performed on the full $3\,\text{fb}^{-1}$ dataset, they make use of refined versions of the stripping lines which incorporate slight modifications to some of the selection requirements compared to the datasets used for the branching fraction analysis. The maximum χ^2_{track} requirement on all four charged tracks is reduced from 4 to 3 while the stricter requirement on one $\overline{D}^0$ daughter and one bachelor track is reduced from 3 to 2.5. In addition, the maximum number of long tracks allowed in each accepted event is reduced from 500 to 250.

In the subsequent offline selection, the initial requirements on the $\overline{D}^0$ candidate are less stringent to allow more of the selection to be performed by the NN. The minimum accepted value of the $\overline{D}^0$ BDT output is reduced from 0.5 to 0.3 and the accepted range of reconstructed $\overline{D}^0$ masses is expanded to $1814 < m(K^+\pi^-) < 1914\,\text{MeV}/c^2$.

A new NN is trained on the full dataset, incorporating additional variables relating to the $\overline{D}^0$ candidate and its daughters. While these variables were already used as inputs to the $\overline{D}^0$ BDT, it has been found that including some of these variables in the NN as well improves the discrimination between signal and background

categories. The full list of variables included in the updated NN is given in Table 6.1.

Table 6.1: Variables used as inputs to train the `NeuroBayes` selection. Parameters labelled † are calculated after a $\overline{D}^0$ mass constraint.

Particle	Variables	`NeuroBayes` ranking
B_s^0	$^\dagger p_{\rm T}$	5
	$\chi^2_{\rm vertex}$	3
	$^\dagger\chi^2_{\rm flight}$	12
	$^\dagger\cos\theta_{\rm dir}$	16 (worst)
	†min $\chi^2_{\rm IP}$	6
	cone $A_{p_{\rm T}}$	7
	cone track multiplicity	13
$\overline{D}^0$	BDT output	2
	$^\dagger\chi^2_{\rm vertex}$	14
	$^\dagger\chi^2_{\rm flight}$	15
	$^\dagger\cos\theta_{\rm dir}$	8
	†min $\chi^2_{\rm IP}$	11
$\overline{D}^0_K$	†min $\chi^2_{\rm IP}$	10
$\overline{D}^0_\pi$	†min $\chi^2_{\rm IP}$	9
π	†smaller min $\chi^2_{\rm IP}$	1 (best)
	†larger min $\chi^2_{\rm IP}$	4

The requirement on the NN output is optimised using the same procedure introduced in Sec. 4.2.3, however, the requirement is optimised to maximise the product of the signal significance and the signal purity rather than simply maximising the significance. This quantity peaks at a slightly higher value of the network output, as shown in Fig. 6.1, giving a cleaner signal. This allows better determination of relative phases so is more appropriate for a DP analysis. Candidates are selected with a network output greater than -0.8.

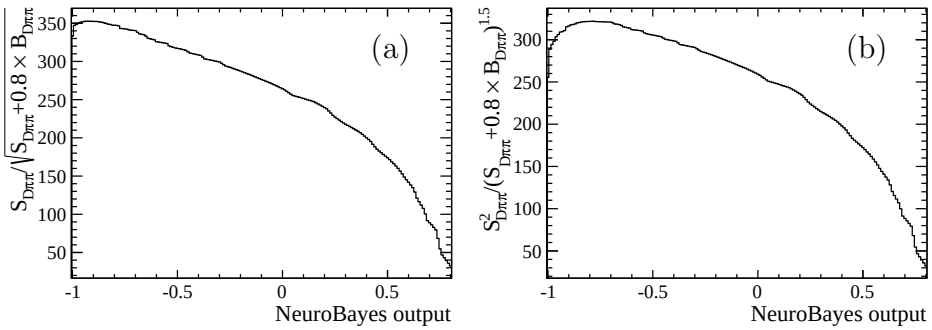

Figure 6.1: Optimisation of the requirement on the `NeuroBayes` output for $B_s^0 \to \overline{D}^0 K^-\pi^+$ candidates using (a) the significance and (b) the significance times the purity. Note that the y-axis scale is arbitrary.

As the dominant B_s^0 decays are to $\overline{D}^0 K^- \pi^+$ with $\overline{D}^0 \to K^+ \pi^-$, the two kaons in the final state are required to have opposite charges. This requirement halves the number of combinatorial background decays selected and also removes $B^0 \to \overline{D}^0 K^+ \pi^-$ decays. The suppressed $B^0 \to D^0 K^+ \pi^-$ decay is not removed by this requirement so a small B^0 signal peak may still feature in the mass distribution. In addition, the extremely suppressed $B_s^0 \to D^0 K^- \pi^+$ decay is also removed. This requirement also removes peaking background from $B^0_{(s)} \to D^\pm K^\mp$ decays so the $D^\pm$ veto introduced in Sec. 4.2.4 is not needed for this analysis. A peaking background is seen at the $\overline{D}^0$ mass in $m(K\pi)$ that was not removed in the previous analysis. This background is either due to $B_s^0 \to D^0 \overline{D}^0$ decays [90] or signal decays where the $\overline{D}^0$ candidate has been reconstructed from the wrong pair of tracks. This background is removed by vetoing candidates in the range $1835 < m(K^-\pi^+) < 1880\,\text{MeV}/c^2$.

6.2 Mass fit

A one dimensional fit to the reconstructed B_s^0 candidate mass distribution is performed to select an appropriate mass range to include in the B_s^0 DP fit and to obtain the signal and background yields within that range. The fit model used to describe the data contains the following components.

- B_s^0 signal;
- B^0 signal;
- combinatorial background;
- partially reconstructed background from $B_s^0 \to \overline{D}^{*0} K^- \pi^+$;
- peaking (and partially reconstructed) background from $B^0 \to \overline{D}^{(*)0} \pi^+ \pi^-$;
- peaking (and partially reconstructed) background from $\overline{\Lambda}_b^0 \to \overline{D}^{(*)0} \overline{p} \pi^+$;

The fit is performed to candidates within the mass range 5200 – 5900 MeV/c^2. This range provides a sufficient region below the signal peak to understand the partially reconstructed background and a large region above the mass peak to understand the combinatorial background. In this section a brief description is given of each of the signal and background PDFs used in this fit and the results of the fit are presented. The combinatorial and partially reconstructed backgrounds included in this fit model use the same functional forms as described previously in Sec. 5.1 so these are not described further. One small change to the combinatorial background shape is that, due to improvements in the mass-constrained vertex fitting procedure, the correction at high masses, introduced in Sec. 5.1.1, is no longer needed.

6.2.1 Signal and background PDFs

Signal

The B_s^0 signal peak is parameterised as a pair of Crystal Ball functions [99] with a common mean,

$$\mathcal{P}_{\text{sig}}(m) = f\,CB(m;\mu_B,\sigma_1,\alpha_1,n_1) + (1-f)\,CB(m;\mu_B,\sigma_2,\alpha_2,n_2)\,. \tag{6.1}$$

The Crystal Ball function, CB, consists of a core Gaussian region and a one-sided tail parameterised by the tail parameters α_i and n_i. The signal PDF is constructed such that the two tails lie on opposite sides of the peak. In the fit to data the values of μ_B and σ_1 are floated, the four tail parameters are fixed to values obtained from a fit to simulated signal decays, and f and σ_2/σ_1 are constrained to values obtained from a fit to a $\overline{D}^0\pi^+\pi^-$ data sample. The results of the fit to simulated decays are given in Table 6.2, while the constraints from $\overline{D}^0\pi^+\pi^-$ data are given in Table 6.3. The parameters of the B^0 signal component are fixed to those of the B_s^0 signal except that the PDF is shifted by the mass difference, $\mu_{B_s^0} - \mu_{B^0}$, reported by the PDG [3].

Table 6.2: Parameters obtained from a fit to the candidate B_s^0 mass distribution of simulated $B_s^0 \to \overline{D}^0 K^-\pi^+$ decays.

Parameter	Value
α_1	1.73 ± 0.13
n_1	1.48 ± 0.08
α_2	-2.35 ± 0.16
n_2	2.21 ± 0.27

Table 6.3: Parameters obtained from a fit to $B^0 \to \overline{D}^0\pi^+\pi^-$ data.

Parameter	Value
Width ratio (σ_2/σ_1)	1.756 ± 0.048
Relative fraction (f)	0.796 ± 0.018

Peaking background

Two components of peaking background are included in the fit: $B^0 \to \overline{D}^{(*)0}\pi^+\pi^-$ and $\overline{\Lambda}_b^0 \to \overline{D}^{(*)0}\overline{p}\pi^+$. Each shape is described by a smoothed non-parametric PDF as in Sec. 5.1, however, an improved weighting procedure is applied to the samples of simulated decays to ensure that they more closely resemble data. The shapes are reweighted to match the PID response of calibration data and also to match the

resonant structures of the $B^0 \to \overline{D}^0\pi^+\pi^-$ and $\overline{\Lambda}_b^0 \to \overline{D}^0\overline{p}\pi^+$ DPs [84, 97]. As the resonant structures of the partially reconstructed decays are unknown,[1] these are each reweighted to match the relevant $\overline{D}^0hh'$ DP. The $B^0 \to \overline{D}^0\pi^+\pi^-$ and $B^0 \to \overline{D}^{*0}\pi^+\pi^-$ components are combined according to their PDG branching fractions [3], while the ratio of the $\overline{\Lambda}_b^0 \to \overline{D}^0\overline{p}\pi^+$ and $\overline{\Lambda}_b^0 \to \overline{D}^{*0}\overline{p}\pi^+$ components assumes equal branching fractions, as the branching fraction of the $\overline{\Lambda}_b^0 \to \overline{D}^{*0}\overline{p}\pi^+$ decay is unmeasured.

The effects of this reweighting on the B candidate mass and DP distributions are shown for simulated $B^0 \to \overline{D}^0\pi^+\pi^-$ and $\overline{\Lambda}_b^0 \to \overline{D}^0\overline{p}\pi^+$ decays in Fig. 6.2 and the shapes used in the fit are shown in Fig. 6.3. The yields of these two fit components are free parameters in the fit to data.

6.2.2 Fit to data

The fit to $m(\overline{D}^0K^-\pi^+)$ is shown in Fig. 6.4 and the values of the free parameters are shown in Table 6.4. The fit yields a χ^2/ndf of 1.12. The fit is found to be stable and unbiased following a study identical to the one described in Sec. 5.1.2.

Candidates within a window around the signal peak corresponding to $\mu_{B_s^0} \pm 2.5\,\sigma_1$ are retained for the fit to the DP. This window corresponds to a mass range of 5333.7 – 5397.2 MeV/c^2. A zoom of this region of the mass distribution is shown in Fig. 6.5. Table 6.5 lists the signal and background yields within this window and within two alternative windows, which are used for systematic crosschecks.

Table 6.4: Parameters from the fit to the $\overline{D}^0K^-\pi^+$ mass distribution.

Parameter	Value
$\mu_{B_s^0}$	5365.5 ± 0.2 MeV/c^2
σ_1	12.7 ± 0.2 MeV/c^2
σ_2	$\sigma_1 \times 1.76 \pm 0.05$
Relative fraction (f)	0.797 ± 0.017
Linear slope	-0.000144 ± 0.000006
$N(B_s^0 \to \overline{D}^0K^-\pi^+)$	$12\,449 \pm 175$ events
$N(B^0 \to D^0K^+\pi^-)$	547 ± 81 events
N(comb. bkg)	9232 ± 579 events
$N(B_s^0 \to \overline{D}^{*0}K^-\pi^+)$	7594 ± 144 events
$N(B^0 \to \overline{D}^{(*)0}\pi^+\pi^-)$	1671 ± 614 events
$N(\overline{\Lambda}_b^0 \to \overline{D}^{(*)0}\overline{p}\pi^+)$	1270 ± 349 events

[1] An unpublished amplitude analysis of the $B^0 \to \overline{D}^{*0}\pi^+\pi^-$ decay exists [98] however, for consistency, this is treated in the same way as the $\overline{\Lambda}_b^0 \to \overline{D}^{*0}\overline{p}\pi^+$ background.

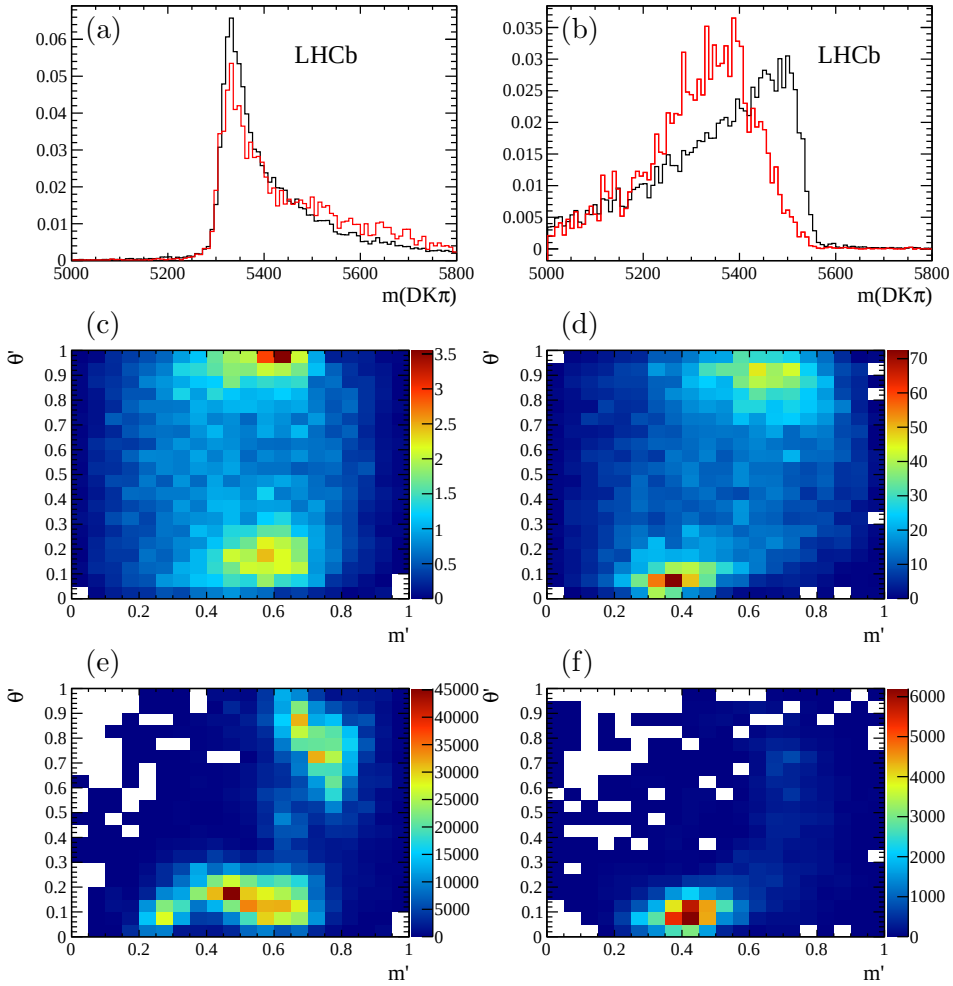

Figure 6.2: B^0_s candidate mass of (a) $B^0 \to \overline{D}{}^0\pi^+\pi^-$ and (b) $\overline{\Lambda}{}^0_b \to \overline{D}{}^0\overline{p}\pi^+$ backgrounds shown both (black) before and (red) after reweighting to match data in the SDP. Also shown are the unweighted SDP distributions in (c) and (d), and the reweighted SDP distributions in (e) and (f). In both backgrounds, the SDP variables have been calculated using the true mass hypothesis for the mis-identified daughter. Note that in each case the reweighted shape is used for the background PDF.

6.3 Signal efficiency variation across the Dalitz plot

The fit to the DP must account for efficiency variations across the phase space. The efficiency is factorised into contributions due to geometry, selection and PID as described in Sec. 4.4. Each efficiency contribution is determined as a function of the SDP variables, m' and θ'. The geometrical, selection and PID efficiencies are determined in the same way as described in Sec. 4.4. In addition, corrections are applied to account for the following known differences between data and simulation.

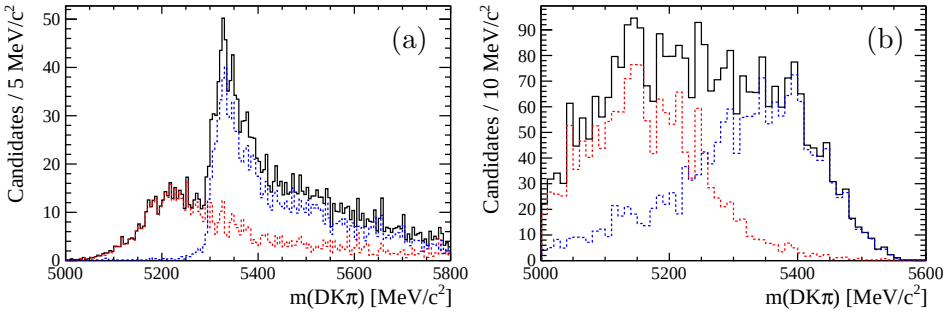

Figure 6.3: PDFs for (a) $B^0 \to \overline{D}^{(*)0}\pi^+\pi^-$ and (b) $\overline{\Lambda}_b^0 \to \overline{D}^{(*)0}\overline{p}\pi^+$ backgrounds, including (red) the $\overline{D}^{*0}hh'$ contribution and (blue) the $\overline{D}^0hh'$ contribution.

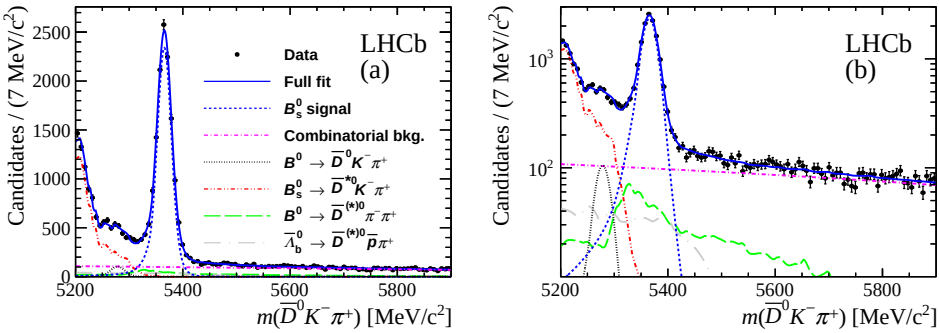

Figure 6.4: Fit to the B_s^0 candidate invariant mass distribution on (a) linear and (b) logarithmic scales. The components are as described in the legend.

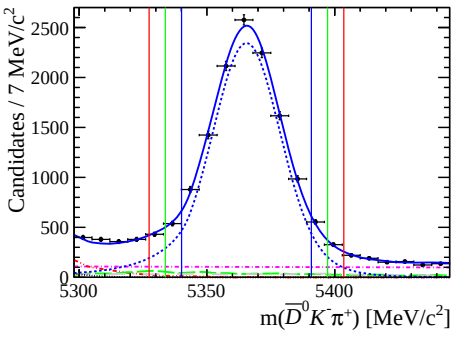

Figure 6.5: The signal region of the fit to the B_s^0 candidate invariant mass distribution showing the (blue) $\pm 2\sigma$, (green) $\pm 2.5\sigma$ and (red) $\pm 3\sigma$ regions.

- The selection efficiency is determined separately for events where the signal decay has passed the trigger (TOS) and events triggered only by the rest of the event (!TOS);
- The ratio of these two trigger pathways is weighted to match the ratio seen in

Table 6.5: Yields of the fit components within $\pm 2\sigma$, $\pm 2.5\sigma$ and $\pm 3\sigma$ of the fitted B_s^0 candidate mass distribution.

Component	Yield		
	$\pm 2\sigma$	$\pm 2.5\sigma$	$\pm 3\sigma$
$B_s^0 \to \overline{D}^0 K^- \pi^+$	10 688	11 302	11 646
$B^0 \to D^0 K^+ \pi^-$	1	2	2
comb. bkg	759	948	1138
$B_s^0 \to \overline{D}^{*0} K^- \pi^+$	28	40	58
$B^0 \to \overline{D}^{(*)0} \pi^+ \pi^-$	291	363	443
$\overline{\Lambda}_b^0 \to \overline{D}^{(*)0} \overline{p} \pi^+$	237	300	361

data;

- Each trigger pathway is corrected for a known discrepancy in the simulation of the L0 hadronic trigger;
- The selection efficiency is corrected for a known small discrepancy in the simulation of tracking;

6.3.1 Trigger correction

To account for differences in the L0 hadronic TOS trigger response between data and simulation, corrections are applied to the selection efficiency maps for both events that pass this trigger and events that do not. The stripping line used to select signal candidates includes a requirement on the HLT trigger decision, which biases the post-stripping sample towards passing the L0 hadronic TOS trigger. To obtain an unbiased sample, only candidates that are triggered by the rest of the event (regardless of the TOS trigger response) are used to evaluate this correction. Standard tables [104] are used to obtain the probability that each charged track would have fired the trigger based on its kinematics and the region of the HCAL that the track passes through. Naively, the total trigger efficiency for a candidate would be the probability that at least one track passes the trigger independently, however, if two tracks leave overlapping deposits in the calorimeter, this combined deposit is more likely to pass the trigger. To account for such an effect, the pair of tracks that passes through the HCAL with the smallest separation is considered together. Tracks that pass within half a calorimeter cell width of each other in both the vertical and horizontal directions are treated as a single combined deposit, while tracks with a larger separation are deemed to have deposited a fraction of their deposited charge in shared HCAL cells, boosting the trigger efficiencies of both tracks.

The true trigger efficiency variation across the SDP is obtained by calculating the average efficiency in each bin in the phase space. To convert this into a data/simulation correction for the TOS trigger pathway, the simulated efficiency in each bin is obtained by taking the ratio of the number of events that pass both the L0 TOS and L0 TIS triggers to all those that pass the TIS trigger. The correction for the !TOS trigger pathway is evaluated as the probability that no tracks pass the trigger divided by the ratio of the number of candidates that pass L0 TIS but not L0 TOS to all those that pass L0 TIS.

6.3.2 Tracking correction

Further corrections are applied to account for differences in the tracking efficiency between data and simulation for each of the four tracks. The simulated data is first reweighted to match the distribution of real data in the momentum (p) and pseudorapidity (η) of the track and in the multiplicity of the event. A standard table [105], containing the correction factor as a function of p and η, is used to obtain the efficiency correction for each candidate and these corrections are averaged in bins in the SDP to obtain the corrections for each of the four tracks across the SDP phase space. These corrections, shown in Fig. 6.6, are then multiplied to obtain the total efficiency correction due to tracking.

6.3.3 Spline interpolation

To obtain a smoothly varying efficiency profile across the phase space, the histogram describing each efficiency contribution is interpolated using a two dimensional cubic spline. At the centre of each bin, the efficiency, ϵ, and its derivatives $\frac{d\epsilon}{dm'}$, $\frac{d\epsilon}{d\theta'}$ and $\frac{d^2\epsilon}{dm'd\theta'}$ are fixed. In the cell between four bin centres, the 16 constraints from the corners of the cell are used to determine the coefficients, c_{ij}, of the polynomial, $\sum_{i,j=0}^{3} c_{ij}x^i y^j$ with $x = \frac{m'-m'_{\rm min}}{m'_{\rm max}-m'_{\rm min}}$ and $y = \frac{\theta'-\theta'_{\rm min}}{\theta'_{\rm max}-\theta'_{\rm min}}$ running between 0 and 1 within each cell. The splines for geometrical, selection and PID efficiencies and for the trigger and tracking corrections are multiplied to give the total efficiency profiles for each of the two trigger pathways, shown in Fig. 6.7.

6.4 Background Dalitz plot distributions

As was shown in Table 6.5, non-negligible contributions enter the signal region due to combinatorial ($\sim 7.4\,\%$), $B^0 \to \overline{D}^{(*)0}\pi^+\pi^-$ ($\sim 2.8\,\%$) and $\overline{\Lambda}_b^0 \to \overline{D}^{(*)0}\overline{p}\pi^+$ ($\sim 2.3\,\%$) backgrounds. A fit to the DP distribution, therefore, requires a description

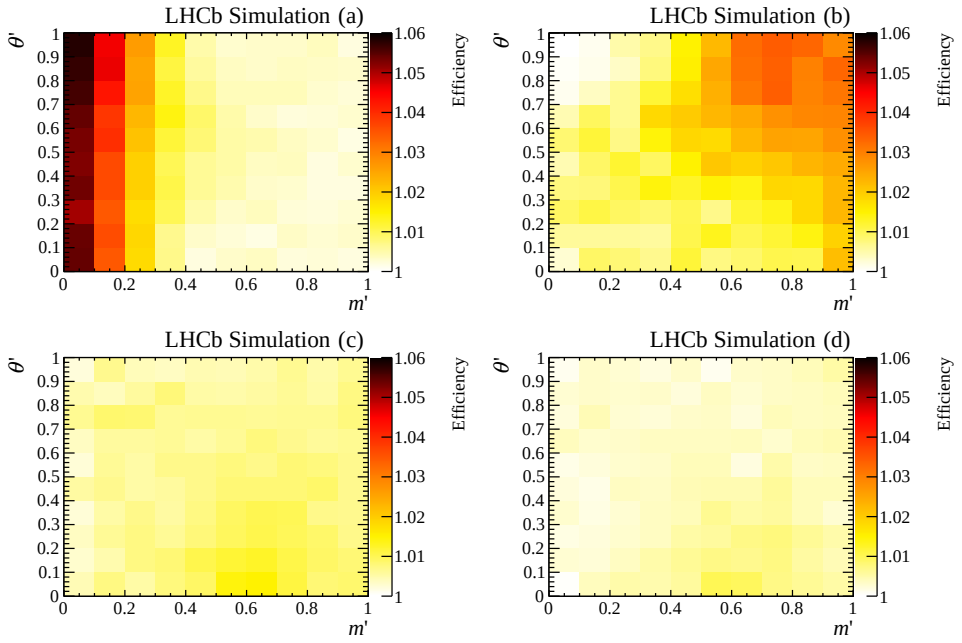

Figure 6.6: Efficiency correction across the $\overline{D}^0 K^- \pi^+$ SDP due to data-simulation discrepancies in the tracking of the (a) bachelor pion, (b) bachelor kaon, (c) $\overline{D}^0$ daughter pion and (d) $\overline{D}^0$ daughter kaon.

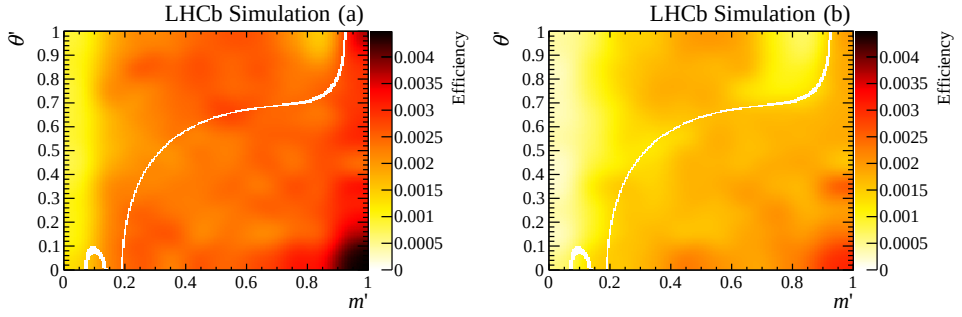

Figure 6.7: Efficiency variation across the SDP for (a) TOS and (b) !TOS candidates. The effect of the D^0 veto can be seen as a curved band running across the SDP, while the D^* veto appears in the bottom left corner of the SDP.

of the distribution of each of these backgrounds.[2] The methods used to obtain these distributions are detailed below.

6.4.1 Combinatorial background

As shown in Fig. 6.4, the region of the $\overline{D}^0 K^- \pi^+$ mass distribution above 5500 MeV/c^2 is dominated by combinatorial background with a small contribution due to $B^0 \to$

[2] The $\sim 0.3\,\%$ contribution from $B_s^0 \to \overline{D}^{*0} K^- \pi^+$ decays is neglected.

$\overline{D}^{(*)0}\pi^+\pi^-$ decays. Candidate decays with B masses in this range are used to determine the SDP distribution of the combinatorial background. The $B^0 \to \overline{D}^{(*)0}\pi^+\pi^-$ contribution to be subtracted is determined using weighted simulated decays as described below in Sec. 6.4.2. The distribution of events in the SDP phase space after the subtraction is shown in Fig. 6.9 (left).

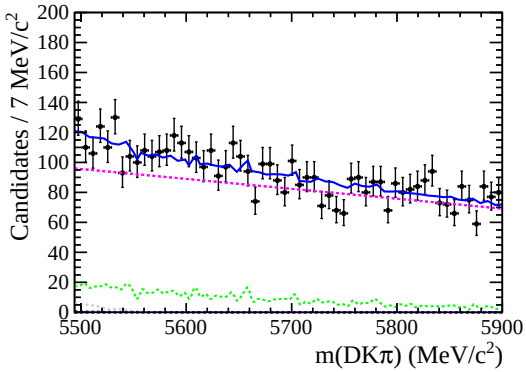

Figure 6.8: The fit to the region of the B_s^0 candidate invariant mass distribution used to obtain the combinatorial background DP distribution. The significant components are (magenta) the combinatorial background and (green) $B^0 \to \overline{D}^{(*)0}\pi^+\pi^-$ background. The data points are shown as black points.

6.4.2 $B^0 \to \overline{D}^{(*)0}\pi^+\pi^-$ and $\overline{\Lambda}_b^0 \to \overline{D}^{(*)0}\overline{p}\pi^+$ backgrounds

The backgrounds due to $\overline{\Lambda}_b^0 \to \overline{D}^{(*)0}\overline{p}\pi^+$ and $B^0 \to \overline{D}^{(*)0}\pi^+\pi^-$ decays are determined from simulated decays, reweighted to match data in both PID response and DP distribution. The efficiency-corrected DP distributions for $\overline{\Lambda}_b^0 \to \overline{D}^0\overline{p}\pi^+$ and $B^0 \to \overline{D}^0\pi^+\pi^-$ decays were obtained during previous analyses [84, 97]. As in Sec. 6.2.1, the decays to final states containing $\overline{D}^{*0}$ mesons are reweighted according to the DP distributions of the decays to the related $\overline{D}^0$ final states. The background DP distributions (shown in Fig. 6.9) are then obtained from the reweighted simulated events that fall within the signal region from the $m(\overline{D}^0K^-\pi^+)$ fit.

6.5 Dalitz plot fitting

The signal model in the B_s^0 DP fit is described using the isobar formalism, introduced in Sec. 2.5.1, and the components included in the nominal model are listed in Table 6.6. A state labelled $D_{sJ}^*(2860)^-$ has been previously observed by BaBar [106] and LHCb [107] to decay to both $\overline{D}^0K^-$ and $\overline{D}^{*0}K^-$. For both these decays to be allowed, this state must have natural spin-parity and non-zero spin. While previous

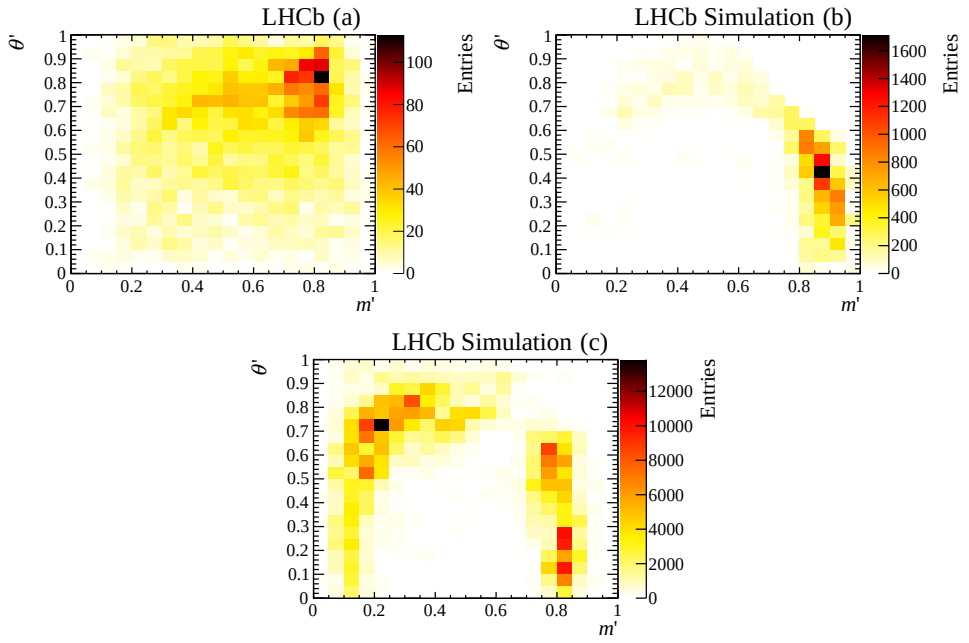

Figure 6.9: Distribution of the (a) combinatorial, (b) $\overline{\Lambda}_b^0 \to \overline{D}^{(*)0}\overline{p}\pi^+$ and (c) $B^0 \to \overline{D}^{(*)0}\pi^+\pi^-$ backgrounds in the SDP variables.

analyses assumed this to be a single resonance a significant improvement is seen in the likelihood when two resonances are included at this mass — one spin-1 and the other spin-3, as discussed further in Sec. 6.7.

The mass terms of the included components are described by the RBW, EFF and LASS shapes, introduced in Sec. 2.5.1, which are each parameterised by one or more shape parameters. For most of these components, the shape parameters are fixed to the values given by the PDG [3]. The masses and widths of the $D_{s2}^*(2573)^-$, $D_{s1}^*(2860)^-$ and $D_{s3}^*(2860)^-$ resonances are floated in the fit since it is possible to make world-leading measurements of these parameters. In addition, the shape parameters of the $K^-\pi^+$ and $\overline{D}^0K^-$ S-waves (described by the LASS and EFF models, respectively) are free parameters of the fit. The real and imaginary parts of the complex coefficient for each fit component and the floated shape parameters are determined from an unbinned maximum likelihood fit to data, performed using the Laura^{++} DP fitting package [83]. The complex coefficient of the $D_{s2}^*(2573)^-$ resonance is fixed to unity as a reference amplitude.

Blatt–Weisskopf barrier radius

As noted in Sec. 2.5.1, the radius parameters of the Blatt–Weisskopf barrier form factors are fixed to $4.0\,\text{GeV}^{-1}$ for all resonances in the baseline model. To validate this

Table 6.6: Resonances included in the signal DP model. Resonances labelled with subscript v are virtual. Parameters (and uncertainties) are taken from the PDG [3] unless stated otherwise.

Resonance	Spin	DP axis	Model	Parameters
$\overline{K}^*(892)^0$	1	$m^2(K^-\pi^+)$	RBW	$m = 895.81 \pm 0.19\,\text{MeV}/c^2$, $\Gamma = 47.4 \pm 0.6\,\text{MeV}$
$\overline{K}^*(1410)^0$	1	$m^2(K^-\pi^+)$	RBW	$m = 1414 \pm 15\,\text{MeV}/c^2$, $\Gamma = 232 \pm 21\,\text{MeV}$
$\overline{K}^*_0(1430)^0$	0	$m^2(K^-\pi^+)$	LASS	Floated
$\overline{K}^*_2(1430)^0$	2	$m^2(K^-\pi^+)$	RBW	$m = 1432.4 \pm 1.3\,\text{MeV}/c^2$, $\Gamma = 109 \pm 5\,\text{MeV}$
$\overline{K}^*(1680)^0$	1	$m^2(K^-\pi^+)$	RBW	$m = 1717 \pm 27\,\text{MeV}/c^2$, $\Gamma = 322 \pm 110\,\text{MeV}$
$\overline{K}^*_0(1950)^0$	0	$m^2(K^-\pi^+)$	RBW	$m = 1945 \pm 22\,\text{MeV}/c^2$, $\Gamma = 201 \pm 90\,\text{MeV}$
$D^*_{s2}(2573)^-$	2	$m^2(\overline{D}^0K^-)$	RBW	Floated
$D^*_{s1}(2700)^-$	1	$m^2(\overline{D}^0K^-)$	RBW	$m = 2709 \pm 4\,\text{MeV}/c^2$, $\Gamma = 117 \pm 13\,\text{MeV}$
$D^*_{s1}(2860)^-$	1	$m^2(\overline{D}^0K^-)$	RBW	Floated
$D^*_{s3}(2860)^-$	3	$m^2(\overline{D}^0K^-)$	RBW	Floated
$\overline{D}^0K^-$ S-wave		$m^2(\overline{D}^0K^-)$	EFF	Floated
D^{*-}_{sv}	1	$m^2(\overline{D}^0K^-)$	RBW	$m = 2112.3 \pm 0.5\,\text{MeV}/c^2$
$D^*_{s0\,v}(2317)^-$	0	$m^2(\overline{D}^0K^-)$	RBW	$m = 2317.8 \pm 0.6\,\text{MeV}/c^2$
B^{*+}_v	1	$m^2(\overline{D}^0\pi^+)$	RBW	$m = 5325.2 \pm 0.4\,\text{MeV}/c^2$

assumption, the radius parameters of the resonance barrier form factors corresponding to $K^-\pi^+$ and $\overline{D}^0K^-$ resonances are varied independently. The fit to data is found to have little sensitivity to the radius parameter of the parent barrier form factor so this is not varied. Figure 6.10 shows the 2D likelihood profile obtained from this study with a paraboloid fit superposed. This fit gives values of $r_{\text{BW}}(K^-\pi^+) = \left(3.6\,^{+1.1}_{-0.7}\right)\,\text{GeV}^{-1}$ and $r_{\text{BW}}(\overline{D}^0K^-) = \left(4.1\,^{+0.8}_{-0.5}\right)\,\text{GeV}^{-1}$. As a conservative systematic variation, the radius parameters for the parent and resonance barrier form factors are varied in the range 3.0–5.0 GeV^{-1}.

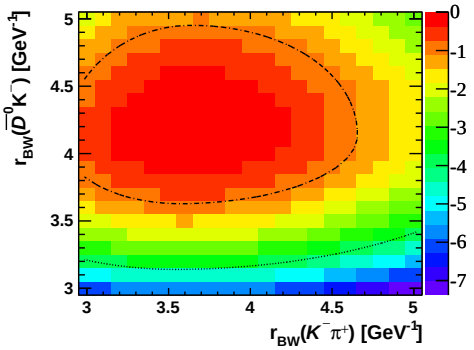

Figure 6.10: Variation of $-2 \times \Delta\text{NLL}$ as a function of the radius parameters of the $K^-\pi^+$ and $\overline{D}^0K^-$ resonance Blatt–Weisskopf barrier form factors. The dashed and dotted contours are from a paraboloid fit to the histogram and correspond to $-2 \times \Delta\text{NLL}$ values of 1 and 4, respectively.

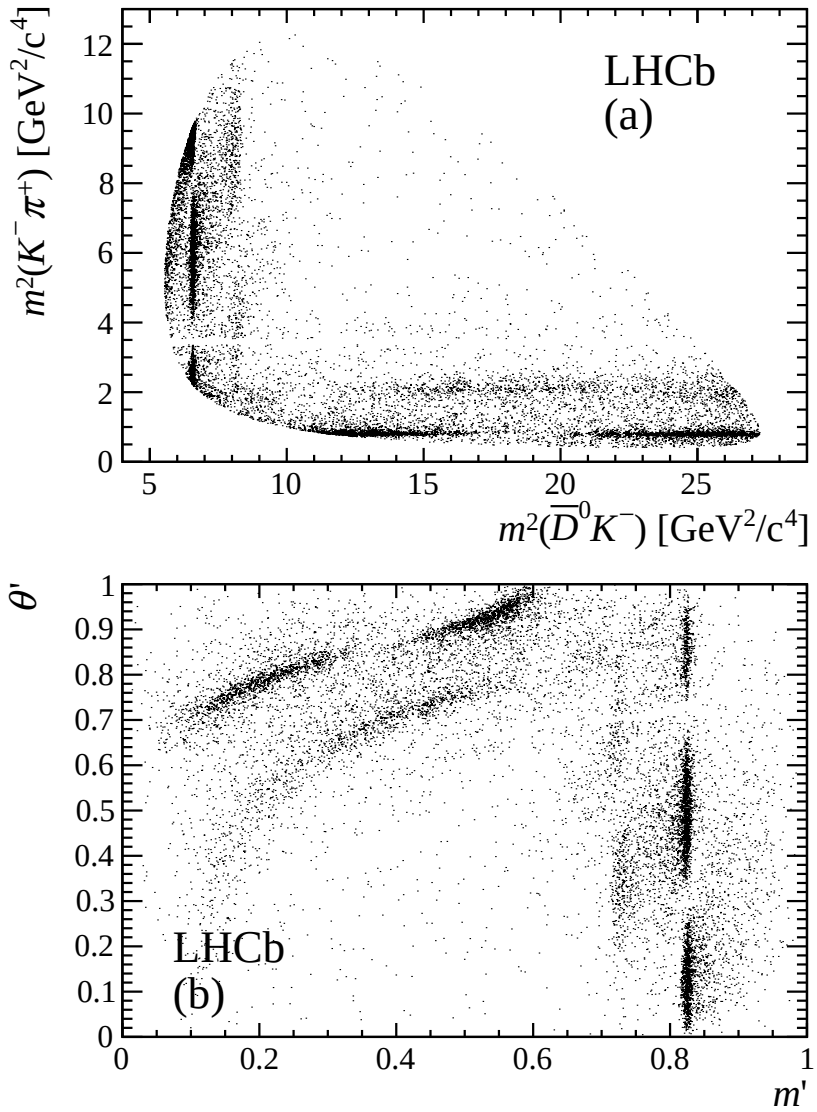

Figure 6.11: The distribution of data candidates in the (a) DP and (b) SDP variables.

6.5.1 The fit to data

The distributions across the DP and SDP, for candidates within the 5333.7 – 5397.2 MeV/c^2 mass range introduced in Sec. 6.2.2, are shown in Fig. 6.11. The complex amplitudes (c_j in Eq. 2.36) and fit fractions (Eq. 2.56) obtained from the fit to these data are given in Table 6.7, while the floated masses and widths, and the other floated shape parameters are given in Tables 6.8 and 6.9, respectively. The statistical uncertainties on the real and imaginary parts of the coefficients are taken from the parabolic uncertainties returned by the fit. The statistical uncertainties on

the fit fractions and other derived quantities are non-trivial to calculate so these are determined from an ensemble of independent pseudoexperiments generated using the fit model. The fit is performed to each of these datasets and, for each quantity, a Gaussian function is used to fit the distribution of values returned by the ensemble. The width of this Gaussian is taken as the statistical uncertainty on that quantity. As the parabolic uncertainties on the masses and widths are found to under-cover, this method is also used to obtain uncertainties on these parameters.

In addition to the individual fit fractions for the resonant and nonresonant parts of the LASS shape, the total LASS fit fraction is also reported, which includes the interference between these two components. The interference within the LASS shape accounts for most of the interference in the fit model.

Table 6.7: Fit fractions and complex coefficients determined from the B_s^0 DP fit. Uncertainties are statistical only and are determined as described in the text. Note that the sum of the fit fractions need not be 100% due to interference effects.

		Isobar model coefficients			
Resonance	Fit fraction (%)	Real part	Imaginary part	Magnitude	Phase
$\overline{K}^*(892)^0$	28.6 ± 0.6	-0.75 ± 0.08	0.74 ± 0.08	1.06 ± 0.02	2.36 ± 0.13
$\overline{K}^*(1410)^0$	1.7 ± 0.5	-0.25 ± 0.03	-0.04 ± 0.05	0.25 ± 0.04	-2.96 ± 0.21
LASS Non. Res.	13.7 ± 2.5	-0.43 ± 0.09	0.59 ± 0.06	0.73 ± 0.06	2.19 ± 0.16
$\overline{K}_0^*(1430)^0$	20.0 ± 1.6	-0.49 ± 0.10	0.73 ± 0.07	0.88 ± 0.04	2.16 ± 0.20
LASS total	21.4 ± 1.4				
$\overline{K}_2^*(1430)^0$	3.7 ± 0.6	0.09 ± 0.05	-0.37 ± 0.03	0.38 ± 0.03	-1.34 ± 0.10
$\overline{K}^*(1680)^0$	0.5 ± 0.4	-0.08 ± 0.04	0.12 ± 0.04	0.14 ± 0.06	2.16 ± 0.26
$\overline{K}_0^*(1950)^0$	0.3 ± 0.2	0.11 ± 0.03	-0.01 ± 0.04	0.11 ± 0.04	-0.09 ± 0.41
$D_{s2}^*(2573)^-$	25.7 ± 0.7	1.00	0.00	1.00	0.00
$D_{s1}^*(2700)^-$	1.6 ± 0.4	-0.22 ± 0.04	-0.13 ± 0.04	0.25 ± 0.04	-2.61 ± 0.17
$D_{s1}^*(2860)^-$	5.0 ± 1.2	-0.41 ± 0.05	0.16 ± 0.06	0.44 ± 0.05	2.78 ± 0.20
$D_{s3}^*(2860)^-$	2.2 ± 0.1	0.27 ± 0.02	-0.12 ± 0.03	0.29 ± 0.02	-0.42 ± 0.07
$\overline{D}^0 K^-$ S-wave	12.4 ± 2.7	0.58 ± 0.07	-0.39 ± 0.06	0.70 ± 0.08	-0.59 ± 0.10
$D_{s\,v}^{*-}$	4.7 ± 1.4	0.36 ± 0.04	0.23 ± 0.05	0.43 ± 0.05	0.57 ± 0.12
$D_{s0\,v}^*(2317)^-$	2.3 ± 1.1	0.18 ± 0.08	0.24 ± 0.04	0.30 ± 0.06	0.91 ± 0.21
B_v^{*+}	1.9 ± 1.2	-0.09 ± 0.10	-0.26 ± 0.05	0.27 ± 0.09	-1.90 ± 0.40
Total fit fraction	124.3				

Table 6.8: Parameters of the $D_{s2}^*(2573)^-$, $D_{s1}^*(2860)^-$ and $D_{s3}^*(2860)^-$ resonances from the B_s^0 DP fit. Uncertainties are statistical only.

Resonance	Mass (MeV/c^2)	Width (MeV/c^2)
$D_{s2}^*(2573)^-$	2568.39 ± 0.29	16.9 ± 0.5
$D_{s1}^*(2860)^-$	2859 ± 12	159 ± 23
$D_{s3}^*(2860)^-$	2860.5 ± 2.6	53 ± 7

The distributions of data and the fit model across the SDP phase space are shown in Fig. 6.12 (top). Comparing these distributions in 576 equally populated

Table 6.9: Floated shape parameters from the LASS and EFF shapes in the fit to data (statistical uncertainties only).

Parameter	value
a	$4.9 \pm 0.6\,\mathrm{GeV}/c^2$
r	$0.0 \pm 0.2\,\mathrm{GeV}/c^2$
m_0	$1551.9 \pm 9.5\,\mathrm{MeV}/c^2$
Γ_0	$195 \pm 12\,\mathrm{MeV}/c^2$
α	$0.412 \pm 0.024\ (\mathrm{GeV}/c^2)^{-2}$

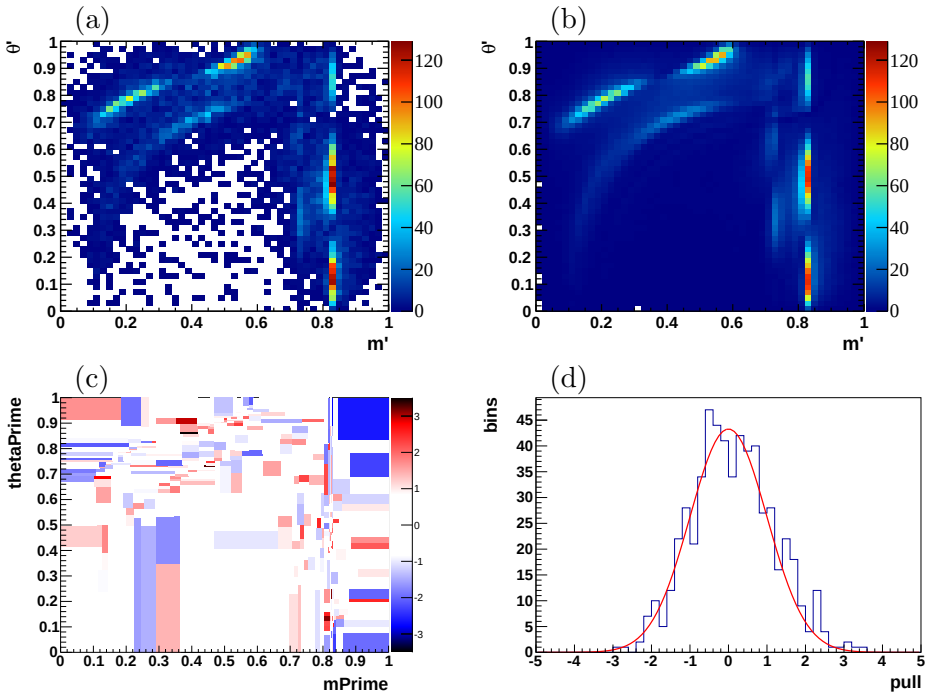

Figure 6.12: The distribution across the SDP of (a) data and (b) the fit model, and (c) the pull between the two distributions in equally populated bins. Also shown (d) is the distribution of these pulls — a Gaussian of mean zero and width one is superimposed.

bins yields a χ^2/ndf between $648.6/536 = 1.21$ and $648.6/575 = 1.13$, where the value of ndf is bounded by $n_{\mathrm{bins}} - n_{\mathrm{par}} - 1$ and $n_{\mathrm{bins}} - 1$ and the number of free parameters in the fit, n_{par}, is 39. This corresponds to a minimum bin content of 21 entries. While, given the large number of degrees of freedom, the determined χ^2 corresponds to a tiny p-value, such a situation is not uncommon for high statistics DP analyses, see *e.g.* Refs. [108, 109]. Moreover, this χ^2 is evaluated accounting only for statistical uncertainties. As shown below in Sec. 6.6, in the regions of the largest data-fit discrepancies, the systematic uncertainties on the parameters of the dominant components are comparable in size to the statistical uncertainties. The

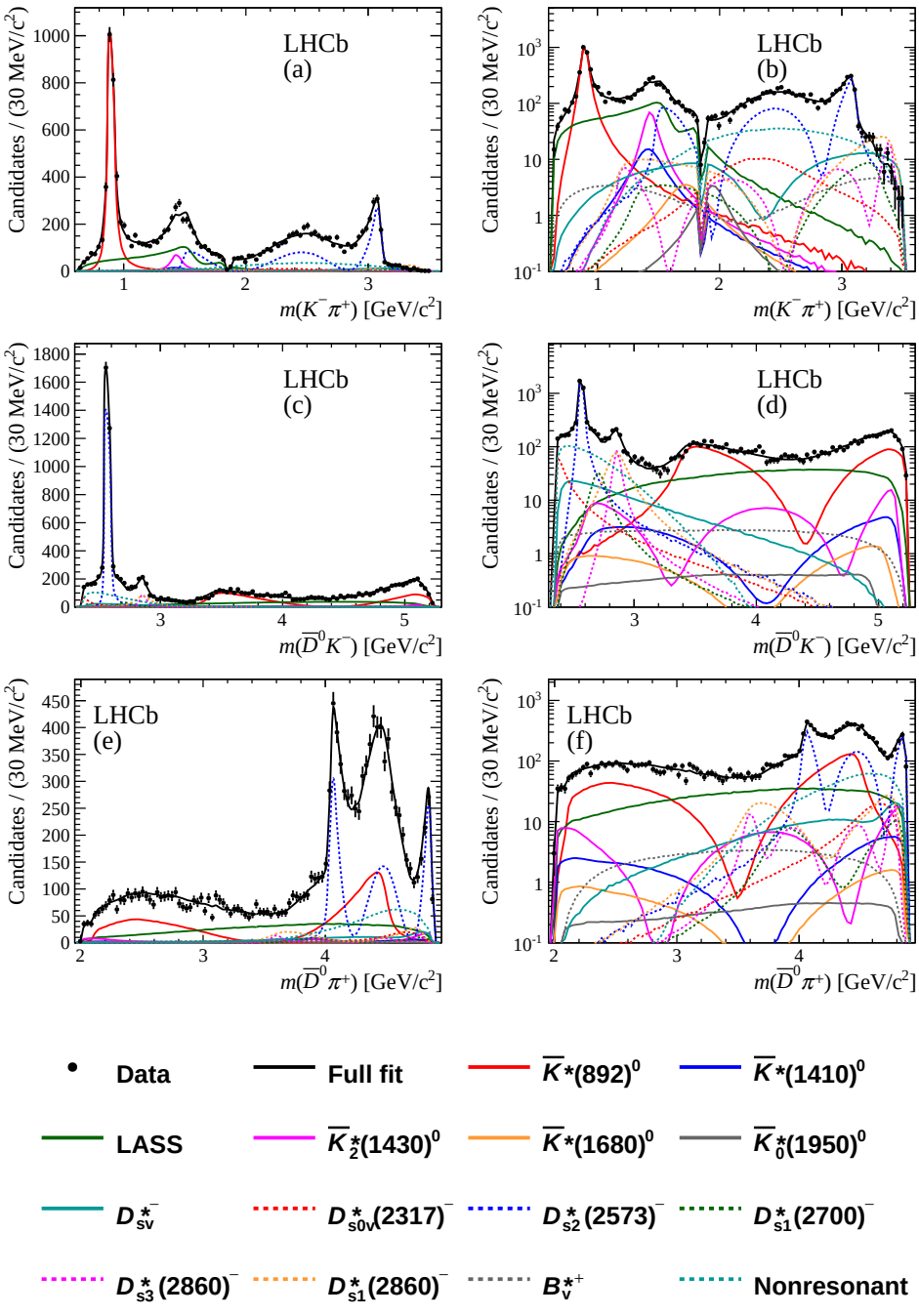

Figure 6.13: Invariant mass projections of the data and the DP fit result onto (a) $m(K^-\pi^+)$, (c) $m(\overline{D}^0K^-)$ and (e) $m(\overline{D}^0\pi^+)$. The same projections are shown on a logarithmic y-scale in (b), (d) and (f). The fit components are shown as described in the legend. Small background contributions are not shown.

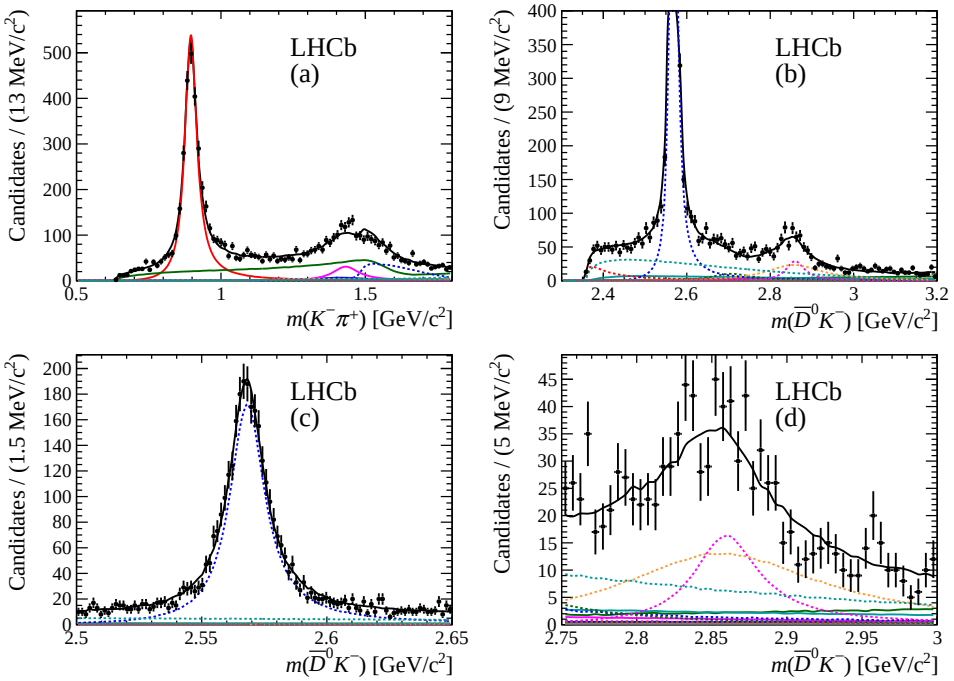

Figure 6.14: Invariant mass projections of the data and the DP fit result onto (a) $m(K^-\pi^+)$ in the range 0.5–1.8 GeV/c^2, (b) $m(\overline{D}^0K^-)$ in the range 2.2–3.2 GeV/c^2, (c) $m(\overline{D}^0K^-)$ around the $D^*_{s2}(2573)^-$ resonance and (d) $m(\overline{D}^0K^-)$ in the $D^*_{sJ}(2860)^-$ region. The components are as described in the legend for Fig. 6.13.

pulls between data and the fit model in these bins are shown in Fig. 6.12 (bottom) and are seen to follow a Gaussian distribution with a mean of 0.16 ± 0.05 and a width of 1.01 ± 0.04.

Alternative unbinned goodness of fit tests are also performed, namely, the mixed sample and point-to-point dissimilarity tests [110]. These give results consistent with a good but not perfect fit. Figure 6.13 shows the three invariant mass projections of the data with the fit model superimposed, while Fig. 6.14 shows zooms of these projections in the low $m(K^-\pi^+)$ and $m(\overline{D}^0K^-)$ regions and around the $D^*_{s2}(2573)^-$ and $D^*_{s1,3}(2860)^-$ resonances. The angular distributions in slices of $m(K^-\pi^+)$ and $m(\overline{D}^0K^-)$ are also shown in Figs 6.15 and 6.16. The good agreement between data and the fit model in these projections suggests that the fit model contains the correct set of resonances and that the spin composition of those resonances is correct. Some discrepancies are visible between the data and the fit model in the angular projections of the $\overline{K}^*(892)^0$ (Fig. 6.15(b)) and the $D^*_{s2}(2573)^-$ (Fig. 6.16(b)) resonances.

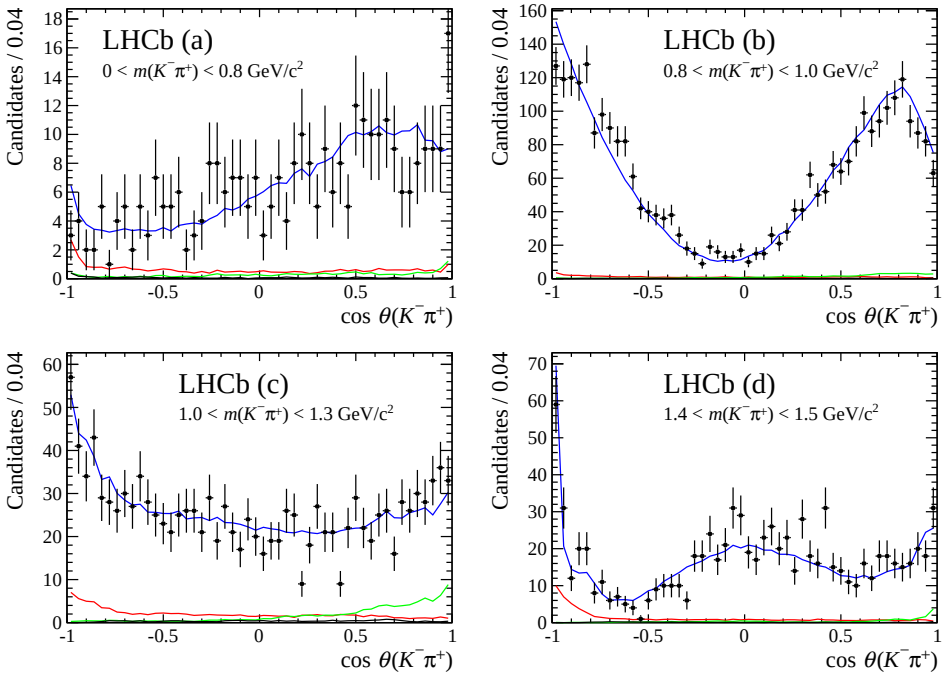

Figure 6.15: Projections of the data and DP fit results onto the cosine of the $K^-\pi^+$ helicity angle, $\cos\theta(K^-\pi^+)$, for slices in $m(K^-\pi^+)$ of (a) 0–0.8 GeV/c^2, (b) 0.8–1.0 GeV/c^2, (c) 1.0–1.3 GeV/c^2 and (d) 1.4–1.5 GeV/c^2. The full fit result is shown as a blue line, and the contributions from combinatorial background, $B^0 \to \overline{D}{}^0\pi^+\pi^-$ and $\overline{\Lambda}{}_b^0 \to \overline{D}{}^0\overline{p}\pi^+$ as red, green and black lines respectively. The data are shown as black points.

Secondary minima

Due to the large number of free parameters in a DP fit, it is common to see multiple solutions. In this analysis, each fit is performed 100 times with randomised starting values to ensure that the global minimum is found. The reported results correspond to the minimum with the smallest negative log likelihood, however, secondary minima are also observed with 2ΔNLL values of 21.8, 87.2, 91.4, 377.2, 377.3 and 472.8 units from the global minimum. Since the global minimum gives a significantly improved likelihood, these other minima are not considered further.

6.5.2 Testing the baseline model

To test if any resonances are missing from the signal model, a series of fits are performed including arbitrary additional resonances. All values of mass, width and spin (up to 3) and all combinations of daughter pair are considered. Figure 6.17 shows the results in terms of the change in 2ΔNLL.

The largest improvement in likelihood occurs for the addition of a broad spin-2

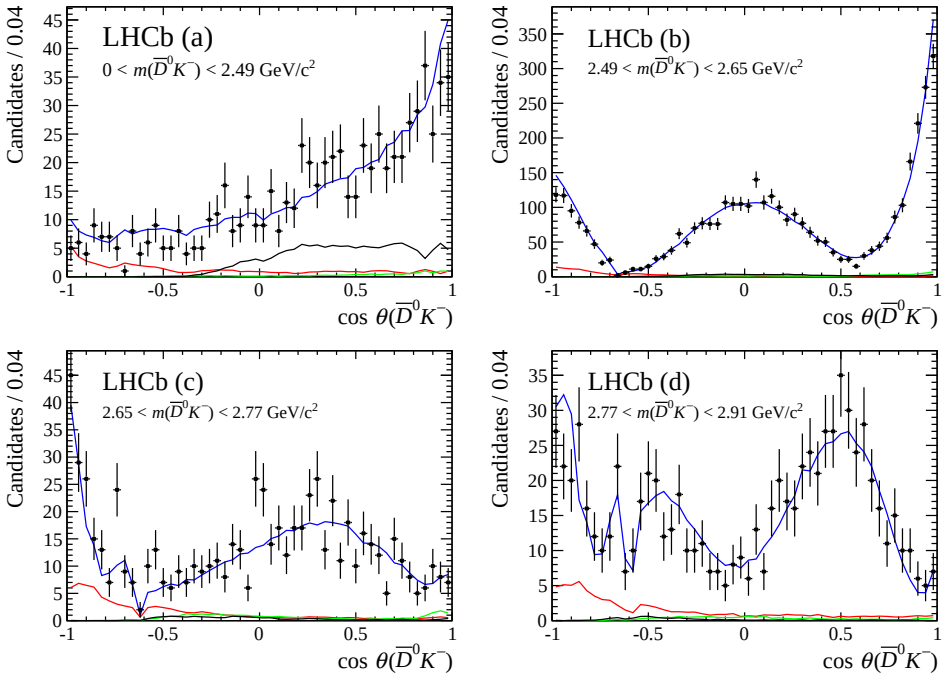

Figure 6.16: Projections of the data and DP fit results onto the cosine of the $\overline{D}^0K^-$ helicity angle, $\cos\theta(\overline{D}^0K^-)$, for slices in $m(\overline{D}^0K^-)$ of (a) 0–2.49 GeV/c^2, (b) 2.49–2.65 GeV/c^2, (c) 2.65–2.77 GeV/c^2 and (d) 2.77–2.91 GeV/c^2. The full fit result is shown as a blue line, and the contributions from combinatorial background, $B^0 \to \overline{D}^0\pi^+\pi^-$ and $\overline{\Lambda}_b^0 \to \overline{D}^0\overline{p}\pi^+$ as red, green and black lines respectively. The data are shown as black points.

resonance at high $m(\overline{D}^0\pi^+)$. This is unlikely to be due to a physical resonance and is probably an artefact of the data-fit disagreement seen in the helicity distribution of the $D^*_{s2}(2573)^-$ resonance, which dominates this region of the phase space. Smaller improvements are also seen for the addition of a spin-0 or spin-3 resonance in this region of $m(\overline{D}^0\pi^+)$.

The strongest hints for a new resonance are seen in the $m(\overline{D}^0K^-) \sim 3100\,\text{MeV}/c^2$ region of the phase space. This region is interesting as a $D_{sJ}(3040)$ state has previously been observed, although this state is believed to have unnatural spin-parity and therefore, should not decay to $\overline{D}^0K^-$. The $D_{sJ}(3040)$ state is thought to be part of either the 2P or 1F family, either of which would also contain natural parity states of even spin. While the largest improvement in the likelihood in this region corresponds to a spin-1 resonance, this is most likely an artefact of the presence of two broad overlapping spin-1 states, $D^*_{s1}(2700)^-$ and $D^*_{s1}(2860)^-$, in this region of the phase space. The hint of a spin-2 resonance is intriguing but such a state could not be conclusively observed with the available dataset. In summary, this study highlights known issues with the fit model but does not identify any resonances

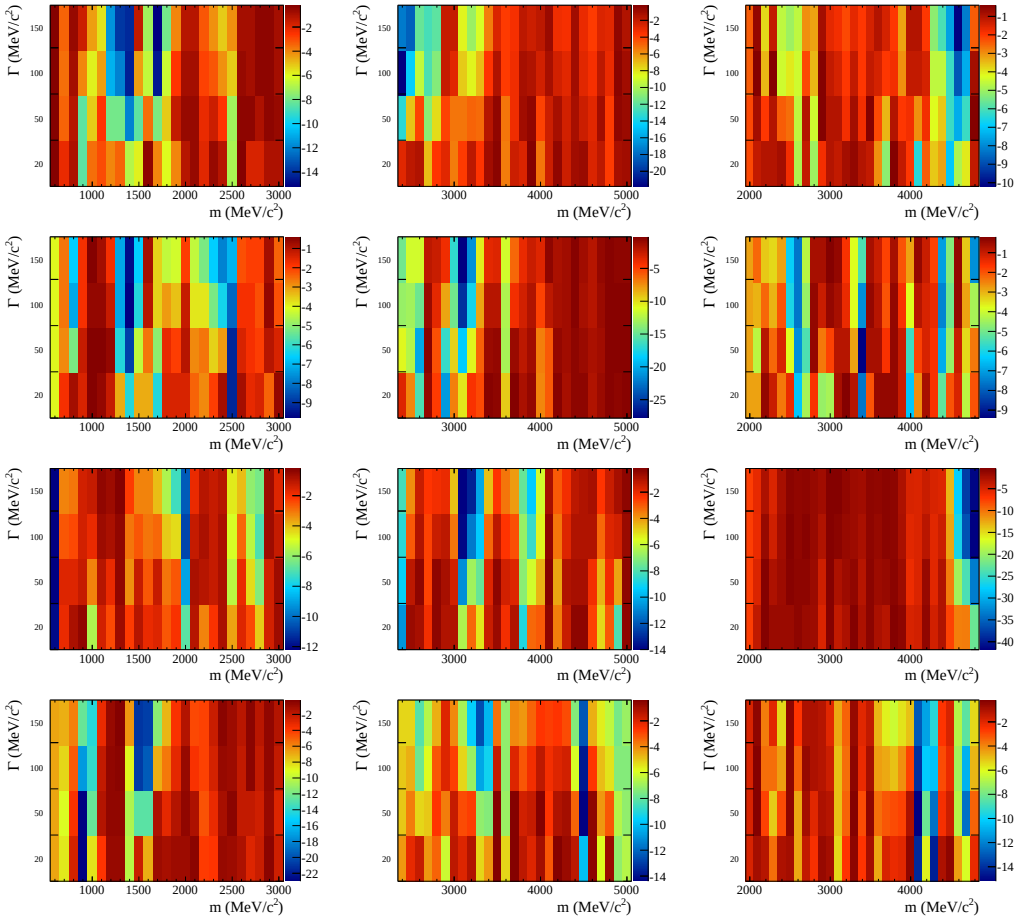

Figure 6.17: Variation of 2ΔNLL as a function of the mass and width of the additional (left) $K^-\pi^+$, (centre) $\overline{D}^0K^-$ or (right) $\overline{D}^0\pi^+$ resonance of spin (top – bottom) 0, 1, 2 or 3.

that should be added to the model.

6.6 Systematic uncertainties

Two sources of systematic uncertainty are considered: experimental and model uncertainties. Experimental uncertainties are due to imperfect knowledge of: the yields of signal and background in the selected events; the background distributions across the phase space; the efficiency variation across the phase space; any bias introduced by the fit; the momentum calibration; the fixed masses of the B_s^0 and $\overline{D}^0$ mesons. Model uncertainties arise from: parameters that are fixed in the DP model; whether marginal components are included in the fit or not; the choice of models for the $K^-\pi^+$ S-wave and the $\overline{D}^0K^-$ S- and P-waves. Two main methods are used to extract the uncertainties on measured quantities. For systematic effects caused by a

Gaussian uncertainty on an input parameter to the fit, the input parameter is varied within its uncertainties 100 times and the fit is repeated. For each measured quantity, a Gaussian function is used to fit the distribution of the 100 values obtained. As with the statistical uncertainties, the width of this Gaussian is taken as the uncertainty on that quantity. For systematic uncertainties caused by a discrete change to the fit, the uncertainty on each quantity is taken as the difference between the nominal fit result and the value returned by the modified fit. Uncertainties from all of these sources are combined in quadrature for each measured parameter.

6.6.1 Experimental uncertainties

The experimental uncertainties on the components of the complex amplitudes and on the fit fractions are given in Table 6.10 and a breakdown by source is given for the fit fractions in Table 6.11. A breakdown of the experimental uncertainties on the mass and width measurements is given in Table 6.12. The various sources of experimental uncertainty are described in more detail below.

Uncertainties due to yields

The signal and background yields used in the fit to the DP distribution were obtained from the fit to the B_s^0 candidate invariant mass. In addition to the statistical uncertainties on these yields, systematic uncertainties due to the sources discussed in Sec. 5.2 are also considered. The statistical uncertainties on the yields are propagated into the DP fit by varying the fixed yields within uncertainties, accounting for correlations, while for the systematic uncertainties, uncertainties are simply taken from the difference between the fit using the nominal yields and the fit using the systematically varied yields.

Uncertainties due to background distributions

The histograms that describe the distribution of each background across the phase space are each varied within uncertainties. The uncertainty in each bin of each histogram is varied independently.

Uncertainties due to efficiency variation

Similarly to the background distributions, the various sources of efficiency variation across the DP are described by histograms which are then converted into splines. Systematic uncertainties due to uncorrelated uncertainties in the bins of the histograms could be determined using the same procedure as for the backgrounds.

However, of more concern is the possibility of a systematic bias where the efficiencies in neighbouring bins vary in a correlated fashion. To account for such an effect, the bins are grouped into square cells of nine bins. The central bin in each cell is varied independently and the variations of the neighbouring bins are determined by linear interpolation. An additional systematic uncertainty is considered due to PIDCalib. An alternative binning scheme is used to determine the PID efficiency as a function of a track's kinematics.

Uncertainties due to fit bias

A systematic bias may arise from the DP fitting procedure. This bias is determined from the same study used to evaluate the statistical uncertainties in Sec. 6.5. The uncertainty for each parameter is taken as quadratic sum of the difference between the generated value and fitted values with the uncertainty from the Gaussian fit.

Uncertainties due to momentum calibration

To obtain precise mass measurements, the momenta of the tracks are scaled by a factor obtained from calibration using $J/\psi \to \mu^+\mu^-$ decays. The uncertainty due to this momentum calibration is estimated by changing the calibration factor by one standard deviation [111, 112].

Uncertainties due to masses of the B_s^0 and $\overline{D}^0$ mesons

The masses of the B_s^0 and $\overline{D}^0$ mesons are fixed to their known values [3] when the DP coordinates are calculated. The analysis is repeated after varying the B_s^0 and $\overline{D}^0$ meson masses up and down by one standard deviation independently, to obtain systematic uncertainties on the measured parameters.

6.6.2 Model uncertainties

The model uncertainties on the components of the complex amplitudes and on the fit fractions are given in Table 6.13 and a breakdown by source is given for the fit fractions in Table 6.14. A breakdown of the model uncertainties on the mass and width measurements is given in Table 6.15. The various sources of model uncertainty are described in more detail below.

Uncertainties due to fixed parameters

The masses and widths listed in Table 6.6 and the Blatt–Weisskopf radius parameters investigated in Sec. 6.5 are fixed in the B_s^0 DP fit. Uncertainties due to the masses and

Table 6.10: Experimental systematic uncertainties on the fit fractions and complex amplitudes.

Resonance	Fit fraction (%)	Real part	Imaginary part	Magnitude	Phase (radians)
$\overline{K}^*(892)^0$	0.74	0.16	0.13	0.03	0.20
$\overline{K}^*(1410)^0$	0.16	0.02	0.12	0.02	0.50
LASS nonresonant	1.52	0.16	0.06	0.05	0.26
$\overline{K}_0^*(1430)^0$	0.72	0.22	0.07	0.03	0.25
LASS total	0.95	—	—	—	—
$\overline{K}_2^*(1430)^0$	0.39	0.08	0.02	0.02	0.20
$\overline{K}^*(1680)^0$	0.26	0.06	0.02	0.04	0.32
$\overline{K}_0^*(1950)^0$	0.13	0.03	0.04	0.03	0.32
$D_{s2}^*(2573)^-$	0.78	—	—	—	—
$D_{s1}^*(2700)^-$	0.44	0.02	0.06	0.03	0.18
$D_{s1}^*(2860)^-$	0.65	0.05	0.05	0.03	0.12
$D_{s3}^*(2860)^-$	0.28	0.03	0.02	0.02	0.10
Nonresonant	4.30	0.25	0.04	0.15	0.36
$D_{s\,v}^{*-}$	1.09	0.04	0.05	0.05	0.08
$D_{s0\,v}^*(2317)^-$	1.94	0.22	0.05	0.16	0.72
B_v^{*+}	1.07	0.08	0.11	0.06	0.34

Table 6.11: Breakdown of experimental systematic uncertainties on the fit fractions (%). The columns give the contributions from the different sources described in the text.

Resonance	S/B frac.	Eff.	Bkgd SDP	Fit bias	p scale	$\overline{D}^0, B_s^0$ mass	Total
$\overline{K}^*(892)^0$	0.24	0.61	0.09	0.13	0.10	0.29	0.74
$\overline{K}^*(1410)^0$	0.06	0.11	0.06	0.07	0.00	0.04	0.16
LASS nonresonant	0.37	0.68	0.72	0.93	0.15	0.55	1.52
$\overline{K}_0^*(1430)^0$	0.50	0.33	0.18	0.21	0.15	0.24	0.72
LASS total	0.49	0.54	0.43	0.36	0.05	0.24	0.95
$\overline{K}_2^*(1430)^0$	0.22	0.18	0.13	0.22	0.01	0.09	0.39
$\overline{K}^*(1680)^0$	0.18	0.10	0.05	0.05	0.00	0.14	0.26
$\overline{K}_0^*(1950)^0$	0.06	0.03	0.03	0.03	0.03	0.10	0.13
$D_{s2}^*(2573)^-$	0.50	0.53	0.08	0.20	0.16	0.13	0.78
$D_{s1}^*(2700)^-$	0.41	0.07	0.14	0.05	0.04	0.02	0.44
$D_{s1}^*(2860)^-$	0.42	0.25	0.36	0.19	0.00	0.10	0.65
$D_{s3}^*(2860)^-$	0.03	0.07	0.05	0.15	0.02	0.21	0.28
Nonresonant	3.53	1.06	1.13	1.05	0.45	1.51	4.30
$D_{s\,v}^{*-}$	0.63	0.48	0.44	0.24	0.08	0.55	1.09
$D_{s0\,v}^*(2317)^-$	1.79	0.37	0.46	0.28	0.10	0.37	1.94
B_v^{*+}	0.54	0.54	0.68	0.19	0.00	0.27	1.07

widths are determined by simultaneously varying all parameters within uncertainties. The radius parameters of the parent and resonance Blatt–Weisskopf form factors are independently varied to 3 and 5 GeV^{-1}.

Uncertainties due to marginal components

The least significant components in the signal model are the $\overline{K}^*(1680)$, $\overline{K}_0^*(1950)$, $D_{s0\,v}^*(2317)^-$ and B_v^{*+} terms. Furthermore, the $\overline{K}_3^*(1780)^0$ and $\overline{K}_4^*(2045)^0$ resonances

Table 6.12: Breakdown of experimental systematic uncertainties on the masses and widths. Units of MeV/c^2 are implied. The columns give the contributions from the different sources described in the text.

Resonance				Mass			
	S/B frac.	Eff.	Bkgd SDP	Fit bias	p scale	$\overline{D}^0, B_s^0$ mass	Total
$D_{s2}^*(2573)^-$	0.10	0.04	0.02	0.05	0.02	0.14	0.19
$D_{s1}^*(2860)^-$	2.7	0.8	1.1	3.6	0.5	2.8	5.5
$D_{s3}^*(2860)^-$	1.2	0.8	0.4	0.4	0.03	1.8	2.5
Resonance				Width			
	S/B frac.	Eff.	Bkgd SDP	Fit bias	p scale	$\overline{D}^0, B_s^0$ mass	Total
$D_{s2}^*(2573)^-$	0.18	0.03	0.04	0.32	0.02	0.09	0.4
$D_{s1}^*(2860)^-$	22	7	6	4	1.9	4	27
$D_{s3}^*(2860)^-$	2.5	1.2	0.8	1.2	1.0	0.9	3.6

may be expected to contribute to the DP but these terms are not included in the baseline model. The effects on the other parameters, of excluding or including these six components, are assigned as systematic uncertainties. As well as determining uncertainties, these fits are used to set upper limits on the branching fractions corresponding to these six components, as discussed in Sec. 6.7.

Uncertainties due to model variations

The models used to describe the $K^-\pi^+$ S-wave and the $\overline{D}^0K^-$ S- and P-waves are known to be approximate forms and alternative parameterisations are available to describe these components. The effects on the other measured quantities when these parameterisations are changed are therefore assigned as systematic uncertainties. The LASS shape, describing the $K^-\pi^+$ S-wave, is replaced with a Flatté shape [113] for the $\overline{K}_0^*(1430)$ and a resonant term with a modified mass-dependent width for the κ resonance at low $m(K^-\pi^+)$ [114]. Additionally, the form for the $K^-\pi^+$ S-wave given in Ref. [115] is used as a second alternative. For each measured quantity, the larger variation from these two alternatives is assigned as the systematic uncertainty. A power-law dependent term is used as an alternative to the exponential form factor for the $\overline{D}^0K^-$ S-wave. The broad spin-1 $\overline{D}^0K^-$ resonances, $D_{s1}^*(2700)^-$ and $D_{s1}^*(2860)^-$, are modelled using a modified version of the Gounaris–Sakurai lineshape [116] as an alternative to the nominal relativistic Breit–Wigner functions.

In addition to these changes, a systematic is assigned to account for the dependence of the fit results on the effective pole mass description of virtual resonances, introduced in Eq. 2.48. The mass-dependent width (Eq. 2.47) of each virtual component is replaced with the constant width, Γ_0, of the resonance.

Table 6.13: Model uncertainties on the fit fractions and complex amplitudes.

Resonance	Fit fraction (%)	Real part	Imaginary part	Magnitude	Phase (radians)
$\overline{K}^*(892)^0$	0.88	0.72	0.33	0.03	0.76
$\overline{K}^*(1410)^0$	1.37	0.15	0.22	0.14	1.09
LASS nonresonant	4.09	0.14	0.18	0.11	0.26
$\overline{K}_0^*(1430)^0$	3.32	0.14	0.08	0.07	0.16
LASS total	4.69	—	—	—	—
$\overline{K}_2^*(1430)^0$	1.06	0.26	0.03	0.05	0.65
$\overline{K}^*(1680)^0$	0.80	0.14	0.20	0.11	2.66
$\overline{K}_0^*(1950)^0$	2.42	0.21	0.23	0.22	1.71
$D_{s2}^*(2573)^-$	1.05	—	—	—	—
$D_{s1}^*(2700)^-$	0.54	0.06	0.13	0.04	0.53
$D_{s1}^*(2860)^-$	3.28	0.24	0.09	0.17	0.52
$D_{s3}^*(2860)^-$	0.42	0.05	0.04	0.03	0.18
Nonresonant	7.64	0.28	0.28	0.19	0.48
$D_{s\,v}^{*-}$	4.02	0.18	0.17	0.16	0.43
$D_{s0\,v}^*(2317)^-$	2.30	0.18	0.09	0.13	0.43
B_v^{*+}	1.83	0.25	0.31	0.13	1.53

Table 6.14: Breakdown of model uncertainties on the fit fractions (%). The columns give the contributions from the different sources described in the text.

Resonance	Fixed parameters	Marginal components	Alternative models	Total
$\overline{K}^*(892)^0$	0.63	0.43	0.43	0.88
$\overline{K}^*(1410)^0$	0.37	0.47	1.23	1.37
LASS nonresonant	0.85	3.78	1.32	4.09
$\overline{K}_0^*(1430)^0$	0.90	3.19	0.26	3.32
LASS total	0.73	2.62	3.82	4.69
$\overline{K}_2^*(1430)^0$	0.21	0.21	1.01	1.06
$\overline{K}^*(1680)^0$	0.63	0.26	0.42	0.80
$\overline{K}_0^*(1950)^0$	0.14	0.22	2.40	2.42
$D_{s2}^*(2573)^-$	0.50	0.26	0.88	1.05
$D_{s1}^*(2700)^-$	0.26	0.31	0.36	0.54
$D_{s1}^*(2860)^-$	0.57	1.80	2.67	3.28
$D_{s3}^*(2860)^-$	0.12	0.29	0.28	0.42
Nonresonant	0.72	5.55	5.20	7.64
$D_{s\,v}^{*-}$	1.35	2.04	3.19	4.02
$D_{s0\,v}^*(2317)^-$	0.55	1.38	1.76	2.30
B_v^{*+}	0.40	1.53	0.91	1.83

6.6.3 Summary of systematic uncertainties

The largest experimental uncertainties on the fit fractions are, generally, due to the efficiency variation across the phase space, the relative signal and background yields and the distributions of background events across the phase space. Of the model

Table 6.15: Breakdown of model uncertainties on the masses and widths. Units of MeV/c^2 are implied. The columns give the contributions from the different sources described in the text.

Mass Resonance	Fixed parameters	Marginal components	Alternative models	Total
$D^*_{s2}(2573)^-$	0.03	0.10	0.15	0.18
$D^*_{s1}(2860)^-$	4	4	23	23
$D^*_{s3}(2860)^-$	0.9	1.5	5.7	6.0
Width Resonance	**Fixed parameters**	**Marginal components**	**Alternative models**	**Total**
$D^*_{s2}(2573)^-$	0.16	0.18	0.4	0.4
$D^*_{s1}(2860)^-$	19	43	54	72
$D^*_{s3}(2860)^-$	0.8	3.3	5.5	6.5

uncertainties on the fit fractions, the largest uncertainties, in general, come from the description of the $K^-\pi^+$ S-wave and from removing the $\overline{K}^*(1680)^0$ and B_v^{*+} components from the model. The systematic uncertainties on the mass and width measurements are also dominated by these sources.

6.6.4 Crosschecks

A number of crosschecks are performed to test the stability of the results. The dataset is divided based on: the year of data-taking; the polarity of the magnet; the flavour (B_s^0 or $\overline{B}_s^0$) of the decaying meson; the hardware level trigger category. The fit is repeated for each subset individually, and no significant discrepancies are seen in the measured quantities. Additionally, the analysis is repeated using larger and smaller mass windows to select candidates.

6.7 Results

As discussed in Sec. 6.5, both a spin-1 and a spin-3 resonance are required in the $m(\overline{D}^0K^-) \approx 2.86\,\text{GeV}/c^2$ region to describe the data. The result of the baseline fit is shown in Figure 6.18, compared to alternative models containing only a single resonance, either spin-1 or spin-3, in this region. The angular distributions expected for each spin hypothesis were introduced in Eqs 2.42-2.45, although efficiency effects modify the underlying distributions. Removing the spin-1 or spin-3 components from the fit model leads to changes in the NLL relative to the baseline fit of 156.8 and 136.5, respectively. Of the 576 bins used to calculate the χ^2 value in Sec. 6.5, 70 bins cover this region of the phase space. Within these 70 bins, the χ^2 value obtained

from the baseline model is 56, while values of 233 and 139 are obtained for the spin-1 only and spin-3 only models, respectively.

The significance of both states being present is determined from ensembles of simulated pseudoexperiments, generated with parameters corresponding to the best fits: with the baseline model; with a spin-1 only model; with a spin-3 only model. Figure 6.19 shows the distributions of twice the difference in NLL (2ΔNLL) obtained when these latter two ensembles are fitted either with both resonances included or with the model used to generate the pseudoexperiment. A χ^2 function, with the number of degrees of freedom floated, is used to fit each distribution and the tails are extrapolated to obtain the p-values to observe 2ΔNLL values at least as large as those seen in data. These p-values correspond to statistical significances of 16 and 15 standard deviations for the spin-3 and spin-1 resonances, respectively. The pseudoexperiments generated from the baseline model are also fitted using either one or both resonances. The values of 2ΔNLL observed in data are seen to lie well within the bulk of the distributions with p-values of 24 % and 4 % for retaining the $D^*_{s1}(2860)^-$ and $D^*_{s3}(2860)^-$ resonances, respectively.

To incorporate the effects of systematic uncertainties on these significances, the procedure is repeated with the model variations that give the largest uncertainties on the parameters of the $D^*_{sJ}(2860)^-$ states. For the spin-1 only model, the effect of using the κ model to describe the $K^-\pi^+$ S-wave is evaluated. For the spin-3 only model, the κ description of the $K^-\pi^+$ S-wave, the addition of the $\overline{K}^*_4(2045)^0$ resonance to the model and the variation of the $\overline{D}^0$ mass are considered. Two states are found to be required in this region with significance in excess of 10 standard deviations in all of these models.

While the $D^*_{s2}(2573)^-$ resonance has been universally assumed to have a spin of two, this has not previously been experimentally determined [3]. Figure 6.20 compares the fit to the helicity distribution from the baseline spin-2 assignment with the best alternative, a spin-0 hypothesis. This alternative gives a $\sqrt{2\Delta\text{NLL}}$ value in excess of 40. It is clear that no alternative spin hypothesis can describe this resonance.

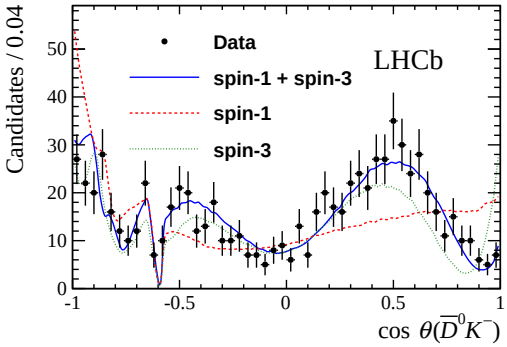

Figure 6.18: Projections of the data and DP fit results with alternative models onto the cosine of the $\overline{D}^0 K^-$ helicity angle, $\cos\theta(\overline{D}^0 K^-)$, for $2.77 < m(\overline{D}^0 K^-) < 2.91\,\text{GeV}/c^2$. The data are shown as black points, the result of the baseline fit with both spin-1 and spin-3 resonances is given as a solid blue curve, and results of fits from the best models with only either a spin-1 or a spin-3 resonance are shown as dashed red and dotted green lines, respectively. The dip at $\cos\theta(\overline{D}^0 K^-) \approx -0.6$ is due to the $\overline{D}^0$ veto. Comparison of the data and the different fit results in the 50 bins of this projection gives χ^2 values of 47.3, 214.0 and 150.0 for the default, spin-1 only and spin-3 only models, respectively.

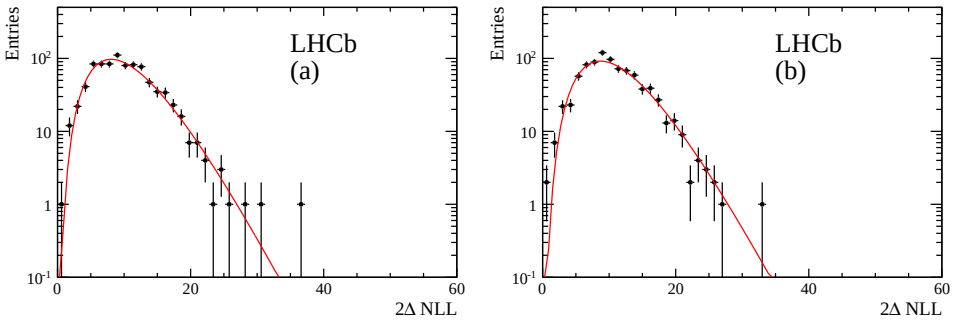

Figure 6.19: Fits of χ^2 functions to the 2ΔNLL distributions obtained from fits to pseudoexperiments generated with (left) no $D^*_{s1}(2860)^-$ and (right) no $D^*_{s3}(2860)^-$ component. The corresponding 2ΔNLL values observed in data are 273 and 314, respectively.

The measured masses and widths are determined to be

$$
\begin{aligned}
m(D^*_{s2}(2573)^-) &= 2568.39 \pm 0.29 \pm 0.19 \pm 0.18\,\text{MeV}/c^2\,, \\
\Gamma(D^*_{s2}(2573)^-) &= 16.9 \pm 0.5 \pm 0.4 \pm 0.4\,\text{MeV}/c^2\,, \\
m(D^*_{s1}(2860)^-) &= 2859 \pm 12 \pm 6 \pm 23\,\text{MeV}/c^2\,, \\
\Gamma(D^*_{s1}(2860)^-) &= 159 \pm 23 \pm 27 \pm 72\,\text{MeV}/c^2\,, \\
m(D^*_{s3}(2860)^-) &= 2860.5 \pm 2.6 \pm 2.5 \pm 6.0\,\text{MeV}/c^2\,, \\
\Gamma(D^*_{s3}(2860)^-) &= 53 \pm 7 \pm 4 \pm 6\,\text{MeV}/c^2\,,
\end{aligned}
$$

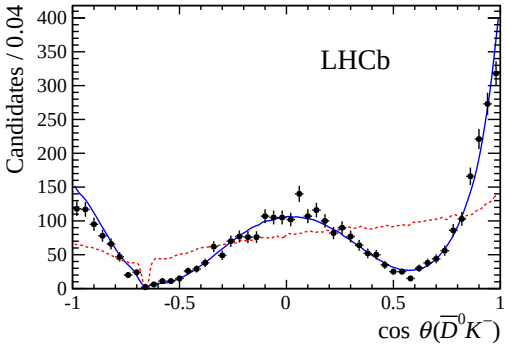

Figure 6.20: Projections of the data and DP fit results with alternative models onto the cosine of the helicity angle of the $\overline{D}^0 K^-$ system, $\cos\theta(\overline{D}^0 K^-)$, for $2.49 < m(\overline{D}^0 K^-) < 2.65\,\text{GeV}/c^2$. The data are shown as black points, the result of the baseline fit with a spin-2 resonance is given as a solid blue curve, and the result of the fit from the best model with a spin-0 resonance is shown as a dashed red line.

where the first uncertainty is statistical, the second is from experimental systematic effects and the third is due to model variations. Table 6.16 lists the results for the complex amplitudes, expressed as both real and imaginary parts and as magnitudes and phases, while Table 6.17 gives the results for the fit fractions. For components that do not have a significant signal, upper limits are established. A likelihood profile is constructed as a function of each component's fit fraction and this function is integrated to obtain upper limits at 90 % and 95 % confidence levels. This process is applied for the $\overline{K}^*(1680)^0$, $\overline{K}_0^*(1950)^0$, $D_{s0\,v}^*(2317)^-$ and B_v^{*+} components of the default model, as well as for the $\overline{K}_3^*(1780)^0$ and $\overline{K}_4^*(2045)^0$ states.

Quasi-two-body branching fractions are constructed from the fit fractions by multiplying them by the three-body branching fraction measured in Sec. 5.3, $\mathcal{B}(B_s^0 \to \overline{D}^0 K^- \pi^+) = (1.00 \pm 0.04\,(\text{stat}) \pm 0.10\,(\text{syst}) \pm 0.10\,(\mathcal{B})) \times 10^{-3}$ [84]. Where the branching fraction of the subsequent resonance decay is known, the product branching fraction is converted into the B_s^0 decay branching fraction. These results are given in Table 6.18.

Table 6.16: Results for the complex amplitudes and their uncertainties. The three quoted errors are statistical, experimental systematic and model uncertainties, respectively. The central values and statistical uncertainties are as reported in Table 6.7, while the experimental and model systematic uncertainties are as reported in Tables 6.10 and 6.13.

Resonance	Real part	Imaginary part
$\overline{K}^*(892)^0$	$-0.75 \pm 0.08 \pm 0.16 \pm 0.72$	$0.74 \pm 0.08 \pm 0.13 \pm 0.33$
$\overline{K}^*(1410)^0$	$-0.25 \pm 0.03 \pm 0.02 \pm 0.15$	$-0.04 \pm 0.05 \pm 0.12 \pm 0.22$
LASS nonresonant	$-0.43 \pm 0.09 \pm 0.16 \pm 0.14$	$0.59 \pm 0.06 \pm 0.06 \pm 0.18$
$\overline{K}_0^*(1430)^0$	$-0.49 \pm 0.10 \pm 0.22 \pm 0.14$	$0.73 \pm 0.07 \pm 0.07 \pm 0.08$
$\overline{K}_2^*(1430)^0$	$0.09 \pm 0.05 \pm 0.08 \pm 0.26$	$-0.37 \pm 0.03 \pm 0.02 \pm 0.03$
$\overline{K}^*(1680)^0$	$-0.08 \pm 0.04 \pm 0.06 \pm 0.14$	$0.12 \pm 0.04 \pm 0.02 \pm 0.20$
$\overline{K}_0^*(1950)^0$	$0.11 \pm 0.03 \pm 0.03 \pm 0.21$	$-0.01 \pm 0.04 \pm 0.04 \pm 0.23$
$D_{s2}^*(2573)^-$	1.00	0.00
$D_{s1}^*(2700)^-$	$-0.22 \pm 0.04 \pm 0.02 \pm 0.06$	$-0.13 \pm 0.04 \pm 0.06 \pm 0.13$
$D_{s1}^*(2860)^-$	$-0.41 \pm 0.05 \pm 0.05 \pm 0.24$	$0.16 \pm 0.06 \pm 0.05 \pm 0.09$
$D_{s3}^*(2860)^-$	$0.27 \pm 0.02 \pm 0.03 \pm 0.05$	$-0.12 \pm 0.03 \pm 0.02 \pm 0.04$
Nonresonant	$0.58 \pm 0.07 \pm 0.25 \pm 0.28$	$-0.39 \pm 0.06 \pm 0.04 \pm 0.28$
$D_{s\,v}^{*-}$	$0.36 \pm 0.04 \pm 0.04 \pm 0.18$	$0.23 \pm 0.05 \pm 0.05 \pm 0.17$
$D_{s0\,v}^*(2317)^-$	$0.18 \pm 0.08 \pm 0.22 \pm 0.18$	$0.24 \pm 0.04 \pm 0.05 \pm 0.09$
B_v^{*+}	$-0.09 \pm 0.10 \pm 0.08 \pm 0.25$	$-0.26 \pm 0.05 \pm 0.11 \pm 0.31$

Resonance	Magnitude	Phase
$\overline{K}^*(892)^0$	$1.06 \pm 0.02 \pm 0.03 \pm 0.03$	$2.36 \pm 0.13 \pm 0.20 \pm 0.76$
$\overline{K}^*(1410)^0$	$0.25 \pm 0.04 \pm 0.02 \pm 0.14$	$-2.96 \pm 0.21 \pm 0.50 \pm 1.09$
LASS nonresonant	$0.73 \pm 0.06 \pm 0.05 \pm 0.11$	$2.19 \pm 0.16 \pm 0.26 \pm 0.26$
$\overline{K}_0^*(1430)^0$	$0.88 \pm 0.04 \pm 0.03 \pm 0.07$	$2.16 \pm 0.20 \pm 0.25 \pm 0.16$
$\overline{K}_2^*(1430)^0$	$0.38 \pm 0.03 \pm 0.02 \pm 0.05$	$-1.34 \pm 0.10 \pm 0.20 \pm 0.65$
$\overline{K}^*(1680)^0$	$0.14 \pm 0.06 \pm 0.04 \pm 0.11$	$2.16 \pm 0.26 \pm 0.32 \pm 2.66$
$\overline{K}_0^*(1950)^0$	$0.11 \pm 0.04 \pm 0.03 \pm 0.22$	$-0.09 \pm 0.41 \pm 0.32 \pm 1.71$
$D_{s2}^*(2573)^-$	1.00	0.00
$D_{s1}^*(2700)^-$	$0.25 \pm 0.04 \pm 0.03 \pm 0.04$	$-2.61 \pm 0.17 \pm 0.18 \pm 0.53$
$D_{s1}^*(2860)^-$	$0.44 \pm 0.05 \pm 0.03 \pm 0.17$	$2.78 \pm 0.20 \pm 0.12 \pm 0.52$
$D_{s3}^*(2860)^-$	$0.29 \pm 0.02 \pm 0.02 \pm 0.03$	$-0.42 \pm 0.07 \pm 0.10 \pm 0.18$
Nonresonant	$0.58 \pm 0.07 \pm 0.25 \pm 0.28$	$-0.39 \pm 0.06 \pm 0.04 \pm 0.28$
$D_{s\,v}^{*-}$	$0.36 \pm 0.04 \pm 0.04 \pm 0.18$	$0.23 \pm 0.05 \pm 0.05 \pm 0.17$
$D_{s0\,v}^*(2317)^-$	$0.18 \pm 0.08 \pm 0.22 \pm 0.18$	$0.24 \pm 0.04 \pm 0.05 \pm 0.09$
B_v^{*+}	$-0.09 \pm 0.10 \pm 0.08 \pm 0.25$	$-0.26 \pm 0.05 \pm 0.11 \pm 0.31$

Table 6.17: Results for the fit fractions and their uncertainties (%). The three quoted errors are statistical, experimental systematic and model uncertainties, respectively. Upper limits at both 90 % and 95 % confidence level (CL) are given for components that are not significant. The central values and statistical uncertainties are as reported in Table 6.7, while the experimental and model systematic uncertainties are as reported in Tables 6.10 and 6.13.

Resonance	Fit fraction	Upper limits	
		90 % CL	95 % CL
$\overline{K}^*(892)^0$	$28.6 \pm 0.6 \pm 0.7 \pm 0.9$		
$\overline{K}^*(1410)^0$	$1.7 \pm 0.5 \pm 0.2 \pm 1.4$		
LASS nonresonant	$13.7 \pm 2.5 \pm 1.5 \pm 4.1$		
$\overline{K}_0^*(1430)^0$	$20.0 \pm 1.6 \pm 0.7 \pm 3.3$		
LASS total	$21.4 \pm 1.4 \pm 1.0 \pm 4.7$		
$\overline{K}_2^*(1430)^0$	$3.7 \pm 0.6 \pm 0.4 \pm 1.1$		
$\overline{K}^*(1680)^0$	$0.5 \pm 0.4 \pm 0.3 \pm 0.8$	< 2.0	< 2.4
$\overline{K}_0^*(1950)^0$	$0.3 \pm 0.2 \pm 0.1 \pm 2.4$	< 3.7	< 4.1
$\overline{K}_3^*(1780)^0$	—	< 0.33	< 0.38
$\overline{K}_4^*(2045)^0$	—	< 0.21	< 0.24
$D_{s2}^*(2573)^-$	$25.7 \pm 0.7 \pm 0.8 \pm 1.1$		
$D_{s1}^*(2700)^-$	$1.6 \pm 0.4 \pm 0.4 \pm 0.5$		
$D_{s1}^*(2860)^-$	$5.0 \pm 1.2 \pm 0.7 \pm 3.3$		
$D_{s3}^*(2860)^-$	$2.2 \pm 0.1 \pm 0.3 \pm 0.4$		
Nonresonant	$12.4 \pm 2.7 \pm 4.3 \pm 7.6$		
$D_{s\,v}^{*-}$	$4.7 \pm 1.4 \pm 1.1 \pm 4.0$		
$D_{s0\,v}^*(2317)^-$	$2.3 \pm 1.1 \pm 1.9 \pm 2.3$	< 7.2	< 8.4
B_v^{*+}	$1.9 \pm 1.2 \pm 1.1 \pm 1.8$	< 7.7	< 8.7

Table 6.18: Results for the product branching fractions (top) $\mathcal{B}(B_s^0 \to \overline{D}^0 \overline{K}^{**0}) \times \mathcal{B}(\overline{K}^{**0} \to K^-\pi^+)$ and (bottom) $\mathcal{B}(B_s^0 \to D_s^{**-}\pi^+) \times \mathcal{B}(D_s^{**-} \to \overline{D}^0 K^-)$, for each $\overline{K}^{**0}$ and D_s^{**-} resonance. For the $\overline{K}^{**0}$ resonances, where $\mathcal{B}(\overline{K}^{**0} \to K^-\pi^+)$ is known [3], the B_s^0 decay branching fraction is also given. The four quoted uncertainties are statistical, experimental systematic, model and PDG uncertainties, respectively. Upper limits are given at 90 % (95 %) confidence level.

Resonance	Product branching fraction (10^{-5})	Branching fraction (10^{-4})
$\overline{K}^*(892)^0$	$28.6 \pm 0.6 \pm 0.7 \pm 0.9 \pm 4.2$	$4.29 \pm 0.09 \pm 0.11 \pm 0.14 \pm 0.63$
$\overline{K}^*(1410)^0$	$1.7 \pm 0.5 \pm 0.2 \pm 1.4 \pm 0.2$	$3.86 \pm 1.14 \pm 0.45 \pm 3.18 \pm 0.89$
LASS nonresonant	$13.7 \pm 2.5 \pm 1.5 \pm 4.1 \pm 2.0$	$2.06 \pm 0.38 \pm 0.23 \pm 0.62 \pm 0.30$
$\overline{K}_0^*(1430)^0$	$20.0 \pm 1.6 \pm 0.7 \pm 3.3 \pm 2.9$	$3.00 \pm 0.24 \pm 0.11 \pm 0.50 \pm 0.44$
LASS total	$21.4 \pm 1.4 \pm 1.0 \pm 4.7 \pm 3.1$	$3.21 \pm 0.21 \pm 0.15 \pm 0.71 \pm 0.47$
$\overline{K}_2^*(1430)^0$	$3.7 \pm 0.6 \pm 0.4 \pm 1.1 \pm 0.5$	$1.11 \pm 0.18 \pm 0.12 \pm 0.33 \pm 0.15$
$\overline{K}^*(1680)^0$	< 2.0 (2.4)	< 0.78 (0.93)
$\overline{K}_0^*(1950)^0$	< 3.7 (4.1)	< 1.1 (1.2)
$\overline{K}_3^*(1780)^0$	< 0.33 (0.38)	< 0.26 (0.30)
$\overline{K}_4^*(2045)^0$	< 0.21 (0.24)	< 0.31 (0.36)
$D_{s2}^*(2573)^-$	$25.7 \pm 0.7 \pm 0.8 \pm 1.1 \pm 3.8$	
$D_{s1}^*(2700)^-$	$1.6 \pm 0.4 \pm 0.4 \pm 0.5 \pm 0.2$	
$D_{s1}^*(2860)^-$	$5.0 \pm 1.2 \pm 0.7 \pm 3.3 \pm 0.7$	
$D_{s3}^*(2860)^-$	$2.2 \pm 0.1 \pm 0.3 \pm 0.4 \pm 0.3$	

Chapter 7

Dalitz plot analysis of $B^0 \to \overline{D}^0 K^+ \pi^-$ decays

This chapter describes the DP analysis of $B^0 \to \overline{D}^0 K^+ \pi^-$ decays based on the full $3\,\text{fb}^{-1}$ of data recorded by LHCb during run 1 of the LHC. Results are reported for the masses, widths and spins of some D^{**} resonances, and for the branching fractions of the quasi-two-body decays that contribute to the DP.

7.1 Selection modifications

In contrast to the B_s^0 decay, the final state of the dominant B^0 decay features two kaons with the same charge. Requiring this combination of charges halves the number of combinatorial candidates selected and removes the peaks due to $B_s^0 \to \overline{D}^{(*)0} K^- \pi^+$ decays. For this analysis, invariant mass vetoes are employed to remove peaking backgrounds from $B^0 \to D^- K^+$ decays (1850–1890 MeV/c^2 in $m(\overline{D}^0(\pi)K\pi)$) and from signal decays where the $\overline{D}^0$ candidate has been reconstructed from the wrong pair of tracks (1850–1885 MeV/c^2 in $m(\overline{D}^0(\pi)K)$ and 1835–1890 MeV/c^2 in $m(K\pi)$).

The NN used in this analysis has been trained on a $B^0 \to \overline{D}^0 \pi^+ \pi^-$ dataset where a peaking background due to $B^+ \to \overline{D}^0 \pi^+$ decays has been removed. This leads to slight differences in the ranking of the input variables and the distribution of the NN output variable compared with the NN used in the B_s^0 DP analysis, however, the requirement on the output variable is optimised using the same process detailed in Sec. 6.1.

7.2 Mass fit

As described in Chapter 6 for the B_s^0 DP analysis, the mass window, and signal and background yields are obtained from a fit to the B^0 candidate mass distribution. The fit model used to describe the data contains the following components.

- B^0 signal;
- B_s^0 signal;
- combinatorial background;
- partially reconstructed background from $B^0 \to \overline{D}^{*0} K^+ \pi^-$;
- peaking (and partially reconstructed) background from $B^0 \to \overline{D}^{(*)0} \pi^+ \pi^-$;
- peaking (and partially reconstructed) background from $\overline{\Lambda}_b^0 \to \overline{D}^{(*)0} K^+ \overline{p}$;
- peaking (and partially reconstructed) background from $B^0 \to \overline{D}^{(*)0} K^+ K^-$;
- peaking (and partially reconstructed) background from $B_s^0 \to \overline{D}^{(*)0} K^+ K^-$;

Compared to the B_s^0 DP analysis, the mass range of the fit is expanded to 5100 – 5900 MeV/c^2 to provide a sufficient region to understand the background from $B^0 \to \overline{D}^{*0} K^+ \pi^-$ decays at masses below the signal peak. The functional forms of the signal and peaking background components are the same as described previously in Sec. 6.2 so these are not described in detail here. One change to the partially reconstructed background shape is the introduction of a "shift" parameter that offsets the component shape in the fit. This parameter is left free in the fit to data to account for resonant contributions to the partially reconstructed background and potential polarisation of the $\overline{D}^{*0}$ meson, which may alter the mass distribution. Additionally, an exponential shape was found to give a better description of the combinatorial background in this mass fit than the previously-used linear function. The fixed parameters of the signal shape, obtained from fits to simulated signal decays and $B^0 \to \overline{D}^0 \pi^+ \pi^-$ data, are listed in Table 7.1, while the reweighted shapes used to model the four peaking background contributions are shown in Fig. 7.1.

Most of the peaking backgrounds are reweighted to match the PID response of data and the DP distribution of the $\overline{D}^0 hh'$ part as described in Sec. 6.2.1. However, for the $\overline{D}^{(*)0} \pi^+ \pi^-$ background an improved treatment is used to also account for the DP distribution of the $\overline{D}^{*0} \pi^+ \pi^-$ component. The $\overline{D}^0 \pi^+ \pi^-$ decays are reweighted to match the DP model obtained from a previous analysis [103]. The DP model used for the $\overline{D}^{*0} \pi^+ \pi^-$ component is constructed by modifying the $\overline{D}^0 \pi^+ \pi^-$ model as follows.

Table 7.1: Parameters obtained from fits to (top) simulated decays and (bottom) $B^0 \to \overline{D}^0\pi^+\pi^-$ data.

Parameter	Value
a_1	1.85 ± 0.34
n_1	1.30 ± 0.22
a_2	-2.2 ± 0.5
n_2	3.5 ± 2.3
Width ratio (σ_2/σ_1)	1.756 ± 0.048
Relative fraction (f)	0.796 ± 0.018

- The narrow $D_2^*(2460)^-$ resonance, which is significantly shifted by the $\overline{D}^{*0}$ – $\overline{D}^0$ mass difference, and the $D_0^*(2400)^-$ and D^{*-} resonances, which do not decay to the $\overline{D}^{*0}\pi^-$ final state, are removed from the model.

- Simulated $B^0 \to D_2^*(2460)^-\pi^+$ and $B^0 \to D_1(2420)^-\pi^+$ decays, where the D^{**} resonances decay to the $\overline{D}^{*0}\pi^-$ channel, are produced separately.

- The distributions of these two resonant contributions are combined with the distribution from the modified $\overline{D}^0\pi^+\pi^-$ model according to the fit fractions previously obtained by Belle [98].

The mass distributions from $B^0 \to \overline{D}^0\pi^+\pi^-$ and $B^0 \to \overline{D}^{*0}\pi^+\pi^-$ decays are then combined according to the relative branching fractions and efficiencies within the range of the mass fit.

Due to the large number of components in the mass fit, the yields of the four peaking background components are constrained within uncertainties relative to the B^0 signal yield. The ratios of the yields for the $\overline{D}^0hh'$ backgrounds are determined as the ratio of efficiencies (determined using simulated data and PIDCalib) multiplied by the ratio of the branching fractions and fragmentation fractions. These ratios are then corrected to account for the $\overline{D}^{*0}hh'$ backgrounds based on the relative efficiencies and branching fractions of the two components. Table 7.2 details these constrained ratios and their respective uncertainties.

The fit to $m(\overline{D}^0K^+\pi^-)$ is shown in Fig. 7.2 and the values of the free parameters are given in Table 7.3. The fit is found to be stable and unbiased following a study identical to the one described in Sec. 5.1.2 and yields a χ^2/ndf of 1.25.

Candidates are retained for the DP fit if they fall into a mass window of 5248.6 – 5309.1 MeV/c^2, which corresponds to $\mu_{B^0} \pm 2.5\sigma_1$. A zoom of this region is shown in Fig. 7.3, while the yields of the signal and background components within

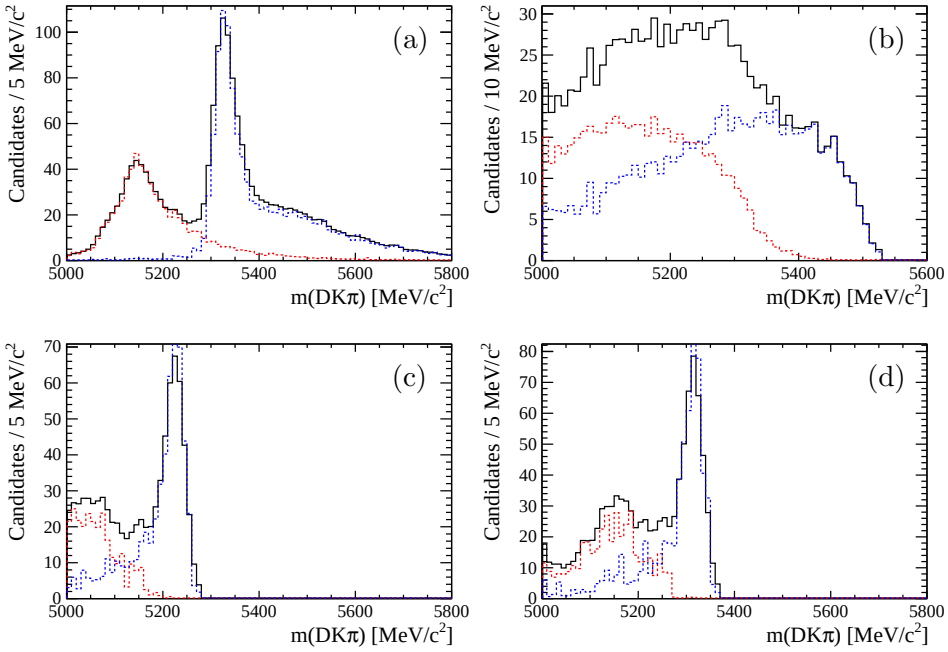

Figure 7.1: PDFs for (a) $B^0 \to \overline{D}^{(*)0}\pi^+\pi^-$, (b) $\overline{\Lambda}_b^0 \to \overline{D}^{(*)0}K^+\overline{p}$, (c) $B^0 \to \overline{D}^{(*)0}K^+K^-$ and (d) $B_s^0 \to \overline{D}^{(*)0}K^+K^-$ backgrounds, including (red) the $\overline{D}^{*0}hh'$ contribution and (blue) the $\overline{D}^0hh'$ contribution.

this window (and two alternative windows used for systematic crosschecks) are given in Table 7.4.

7.3 Dalitz plot fit

7.3.1 Efficiency variation and background distributions

The efficiency with which signal decays can be reconstructed and selected is described as a function of the DP following the same procedure outlined in Sec. 6.3. The total

Table 7.2: Determination of the four peaking background yields as fractions of the signal decay yield. Inputs to the branching fraction (BF) and fragmentation fraction (FF) calculations are taken from Refs. [3, 93, 97, 117], while efficiencies are evaluated using simulated decays and PIDCalib.

Mode	$B^0 \to \overline{D}^0\pi^+\pi^-$	$\overline{\Lambda}_b^0 \to \overline{D}^0\overline{p}K^+$	$B^0 \to \overline{D}^0K^+K^-$	$B_s^0 \to \overline{D}^0K^+K^-$
Ratio of BF $\times$ FF	9.4 ± 0.9	0.19 ± 0.05	0.54 ± 0.13	0.13 ± 0.06
Eff. ratio (%)	1.16 ± 0.01	12.2 ± 0.2	7.4 ± 0.2	8.3 ± 0.2
$N_{\overline{D}^{(*)0}hh'}/N_{\overline{D}^0hh'}$	1.615	1.595	1.126	1.507
$N_{\overline{D}^{(*)0}hh'}/N_{\overline{D}^0K^+\pi^-}$	0.176 ± 0.018	0.037 ± 0.010	0.045 ± 0.011	0.017 ± 0.007

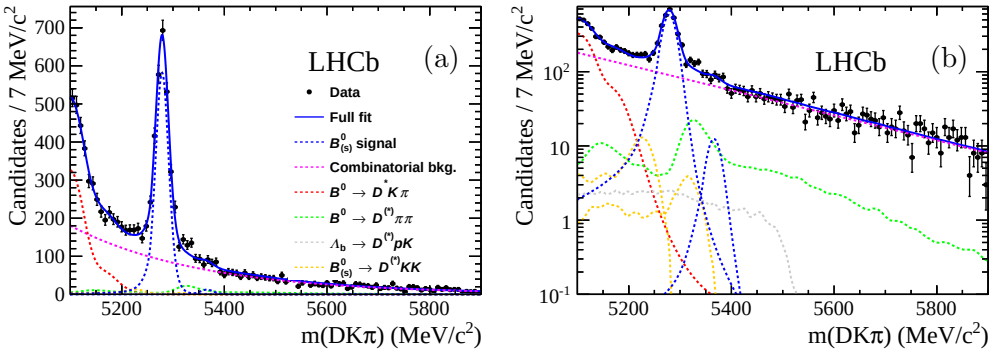

Figure 7.2: Fit to the B^0 candidate invariant mass distribution on (a) linear and (b) logarithmic scales. The components are as described in the legend.

Table 7.3: Parameters from the fit to the $\overline{D}^0 K^+\pi^-$ mass distribution.

Parameter	Value
μ_{B^0}	$5278.8 \pm 0.4\,\text{MeV}/c^2$
σ_1	$12.1 \pm 0.4\,\text{MeV}/c^2$
σ_2	$\sigma_1 \times 1.77 \pm 0.05$
Relative fraction (f)	0.794 ± 0.018
Exponential slope	-0.000388 ± 0.00012
PR offset	$-12.6 \pm 2.6\,\text{MeV}/c^2$
$N(B^0 \to \overline{D}^0 K^+\pi^-)$	2576 ± 72 events
$N(B^0_s \to D^0 K^-\pi^+)$	55 ± 27 events
N(comb. bkg)	5540 ± 187 events
$N(B^0 \to \overline{D}^{*0} K^-\pi^+)$	1750 ± 99 events
$N(B^0 \to \overline{D}^{(*)0}\pi^+\pi^-)$	485 ± 47 events
$N(\overline{\Lambda}^0_b \to \overline{D}^{(*)0}\overline{p}\pi^+)$	95 ± 26 events
$N(B^0 \to \overline{D}^{(*)0} K^+K^-)$	127 ± 27 events
$N(B^0_s \to \overline{D}^{(*)0} K^+K^-)$	54 ± 18 events

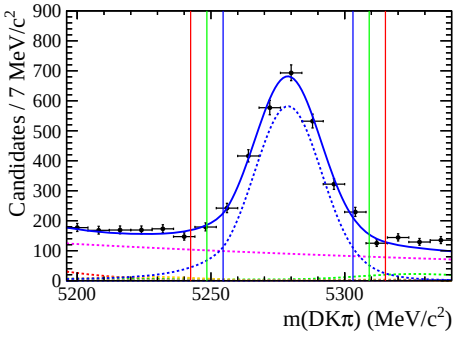

Figure 7.3: The signal region of the fit to the B^0 candidate invariant mass distribution showing the (blue) $\pm 2\sigma$, (green) $\pm 2.5\sigma$ and (red) $\pm 3\sigma$ regions.

Table 7.4: Yields of the fit components within $\pm 2\sigma$, $\pm 2.5\sigma$ and $\pm 3\sigma$ of the fitted B^0 candidate mass distribution.

Component	Yield		
	$\pm 2\sigma$	$\pm 2.5\sigma$	$\pm 3\sigma$
$B^0 \to \overline{D}^0 K^+\pi^-$	2220	2344	2413
$B_s^0 \to D^0 K^-\pi^+$	1	1	1
comb. bkg	547	684	822
$B^0 \to \overline{D}^{*0} K^+\pi^-$	4	6	8
$B^0 \to \overline{D}^{(*)0}\pi^+\pi^-$	37	51	68
$\overline{\Lambda}_b^0 \to \overline{D}^{(*)0}\overline{p}\pi^+$	14	18	21
$B^0 \to \overline{D}^{(*)0}\pi^+\pi^-$	6	10	17
$B^0 \to \overline{D}^{(*)0}\pi^+\pi^-$	11	14	18

efficiencies for signal decays triggered by the `TOS` and `!TOS` trigger paths are shown in Fig. 7.4.

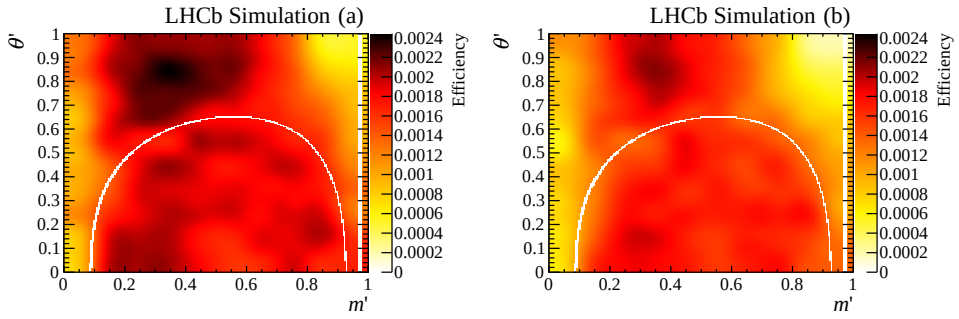

Figure 7.4: Efficiency variation across the SDP for (a) TOS and (b) !TOS candidates. The effect of the D^0 veto can be seen as a curved band running across the SDP, while the D^* veto appears as a vertical stripe.

Of the backgrounds listed in Table 7.4, only combinatorial background (21.9 %) and $B^0 \to \overline{D}^{(*)0}\pi^+\pi^-$ (1.6 %) decays have significant yields within the defined mass window. The Dalitz plot distributions of these backgrounds are shown in Fig. 7.5. The other background categories all yield less than 1 % of the selected candidates and are neglected in the DP fit. The distribution of the combinatorial background is modelled as described in Sec. 6.4.1, while the description of the $B^0 \to \overline{D}^{(*)0}\pi^+\pi^-$ background has been improved for this analysis. The distributions of $\overline{D}^0\pi^+\pi^-$ and $\overline{D}^{*0}\pi^+\pi^-$ background decays are obtained from simulated decays reweighted to match the PID response and DP distribution of data using the procedure outlined in Sec. 7.2. These distributions are combined according to the relative yields of the two components within the signal window of the mass fit.

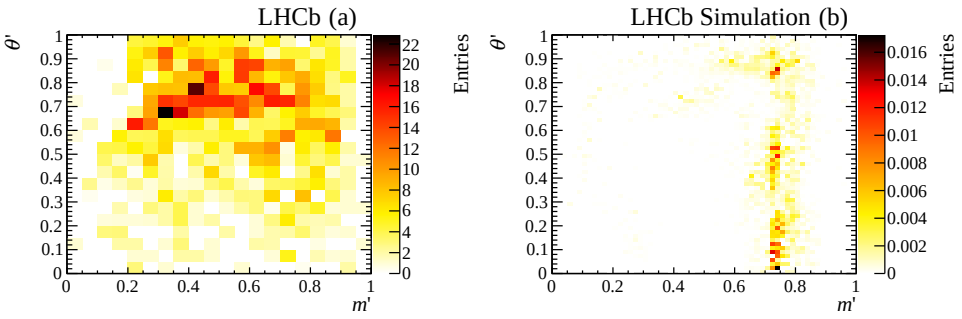

Figure 7.5: Distribution of the (a) combinatorial and (b) $B^0 \to \overline{D}^{(*)0}\pi^+\pi^-$ backgrounds in the SDP variables.

7.3.2 Signal DP model

As was the case in the fit to the DP of the B_s^0 decay, the $B^0 \to \overline{D}^0 K^+\pi^-$ DP is described using the isobar model and fitted using the LAURA^{++} DP fitting package. The resonances included in the fit model are listed in Table 7.5 and are mostly described by the previously introduced RBW, LASS and EFF mass terms. In addition, the "dabba" lineshape, described below, is used to describe the $\overline{D}^0\pi^-$ nonresonant S-wave component and a Gaussian lineshape is used to describe the residual contribution due to $B^0 \to D^{*-}\pi^+$ decays. While most such decays are removed by the invariant mass veto introduced in Sec. 4.2.4, the large branching fraction of this decay combined with a finite mass resolution causes a significant contribution to enter the signal sample. As resolution effects are much broader than the natural width of the D^{*-} resonance, this component is well described by a Gaussian term. Furthermore, the small width of the D^{*-} resonance means that this component does not interfere with other resonances so the corresponding amplitude is summed incoherently with those of the other components. While this component is included in the signal model for convenience, for the purposes of this DP fit it is considered a peaking background. The masses and widths of resonances are floated in the fit if competitive measurements are possible. In this case the parameters of the $D_0^*(2400)^-$ and $D_2^*(2460)^-$ resonances are floated.

Dabba

The dabba lineshape [118], used to describe the nonresonant $\overline{D}^0\pi^-$ S-wave component, is defined by

$$T(m) = \frac{B'(m^2)(m^2 - s_A)\rho}{1 - \beta(m^2 - m_{\min}^2) - iB'(m^2)(m^2 - s_A)\rho}\,, \tag{7.1}$$

Table 7.5: Resonances included in the fit to the $\overline{D}^0 K^+\pi^-$ data sample. Parameters (and uncertainties) are taken from the PDG [3] unless stated otherwise.

Resonance	Spin	DP axis	Model	Parameters
$K^*(892)^0$	1	$m^2(K^+\pi^-)$	RBW	$m = 895.81 \pm 0.19\,\text{MeV}/c^2$, $\Gamma = 47.4 \pm 0.6\,\text{MeV}$
$K^*(1410)^0$	1	$m^2(K^+\pi^-)$	RBW	$m = 1414 \pm 15\,\text{MeV}/c^2$, $\Gamma = 232 \pm 21\,\text{MeV}$
$K_0^*(1430)^0$	0	$m^2(K^+\pi^-)$	LASS	Floated
$K_2^*(1430)^0$	2	$m^2(K^+\pi^-)$	RBW	$m = 1432.4 \pm 1.3\,\text{MeV}/c^2$, $\Gamma = 109 \pm 5\,\text{MeV}$
$D_0^*(2400)^-$	2	$m^2(\overline{D}^0\pi^-)$	RBW	Floated
$D_2^*(2460)^-$	1	$m^2(\overline{D}^0\pi^-)$	RBW	Floated
Nonresonant S-wave	0	$m^2(\overline{D}^0\pi^-)$	Dabba	See text
Nonresonant P-wave	1	$m^2(\overline{D}^0\pi^-)$	EFF	Floated
D^{*-}	1	$m^2(\overline{D}^0\pi^-)$	Gauss	$m = 2010.26 \pm 0.07\,\text{MeV}/c^2$, Γ floated

where

$$B'(m^2) = b\exp[-\alpha(m^2 - m^2_{\text{min}})]\,. \tag{7.2}$$

Here $m_{\text{min}} = m(\overline{D}^0) + m(\pi^-)$, s_A is the Adler zero at $m^2(\overline{D}^0) - 0.5m^2(\pi^-)$, ρ is a phasespace factor, defined for $m > m_{\text{min}}$ by

$$\rho = \sqrt{1 - \frac{m^2_{\text{min}}}{m^2}}\,, \tag{7.3}$$

and b, α and β are parameters which take values of $24.49\,\text{GeV}^{-2}$, $0.1\,\text{GeV}^{-2}$ and $0.1\,\text{GeV}^{-2}$, respectively [118].

7.3.3 The fit to data

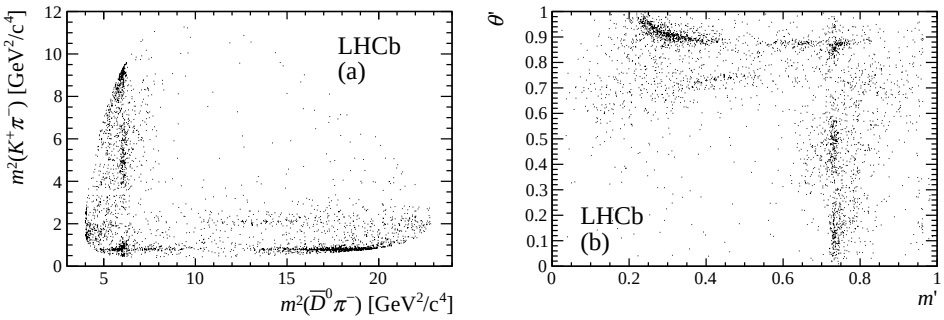

Figure 7.6: The distribution of data candidates in the (a) DP and (b) SDP variables.

The distributions across the DP and SDP phase spaces, of candidates from the mass window of 5248.6 – 5309.1 MeV/c^2, are shown in Fig. 7.6. The fit to these data yields the complex amplitudes and fit fractions given in Table 7.6, as well as the shape parameters given in Tables 7.7 and 7.8. Statistical uncertainties are determined for all derived quantities from an ensemble of independent pseudoexperiments generated

using the fit model. For consistency, in this analysis, this method is also used to determine the statistical uncertainties on the real and imaginary parts of the coefficients. As in the previous analysis, fit fractions are reported both for the total LASS shape and for the resonant and nonresonant parts.

Table 7.6: Fit fractions and complex coefficients determined from the B^0 DP fit. Uncertainties are statistical only and are determined as described in the text. Note that the sum of the fit fractions need not be 100% due to interference effects.

		Isobar model coefficients			
Resonance	Fit fraction (%)	Real part	Imaginary part	Magnitude	Phase
$K^*(892)^0$	36.0 ± 1.4	-0.00 ± 0.15	-1.27 ± 0.06	1.27 ± 0.06	-1.57 ± 0.11
$K^*(1410)^0$	0.7 ± 0.3	0.15 ± 0.06	-0.09 ± 0.09	0.18 ± 0.07	-0.54 ± 0.21
$K_0^*(1430)^0$	4.9 ± 1.9	0.14 ± 0.38	0.45 ± 0.15	0.47 ± 0.09	1.27 ± 0.95
LASS nonresonant	4.6 ± 3.6	-0.10 ± 0.24	0.44 ± 0.14	0.46 ± 0.14	1.79 ± 0.65
LASS total	6.4 ± 2.6				
$K_2^*(1430)^0$	7.2 ± 1.6	-0.32 ± 0.09	-0.47 ± 0.07	0.57 ± 0.05	-2.16 ± 0.19
$D_0^*(2400)^-$	18.6 ± 2.7	-0.80 ± 0.08	-0.44 ± 0.14	0.91 ± 0.07	-2.64 ± 0.15
$D_2^*(2460)^-$	22.3 ± 1.1	1.00	0.00	1.00	0.00
$D\pi$ S-wave (dabba)	6.3 ± 1.4	-0.39 ± 0.09	0.36 ± 0.17	0.53 ± 0.07	2.40 ± 0.27
$D\pi$ P-wave (EFF)	8.5 ± 1.6	-0.62 ± 0.06	-0.03 ± 0.06	0.62 ± 0.06	-3.09 ± 0.10
D^{*-} (incoh.)	3.7 ± 0.9				
Total fit fraction	112.9				

Table 7.7: Parameters of the $D_0^*(2400)^-$ and $D_2^*(2460)^-$ resonances from the B^0 DP fit. Uncertainties are statistical only.

Resonance	Mass (MeV/c^2)	Width (MeV/c^2)
$D_0^*(2400)^-$	2360 ± 15	255 ± 26
$D_2^*(2460)^-$	2465.6 ± 1.8	46.0 ± 3.4

Table 7.8: Floated shape parameters from the LASS and EFF shapes in the fit to data (statistical uncertainties only).

Parameter	Value
a	$3.2 \pm 1.8\,\mathrm{GeV}/c^2$
r	$0.9 \pm 1.1\,\mathrm{GeV}/c^2$
m_0	$1450 \pm 80\,\mathrm{MeV}/c^2$
Γ_0	$400 \pm 230\,\mathrm{MeV}/c^2$
α	$0.88 \pm 0.10\ (\mathrm{GeV}/c^2)^{-2}$

The distributions of data and the fit model across the SDP phase space are shown in Fig. 7.7 (top). Compared in 144 equally populated bins these distributions yield a χ^2/ndf between $141.2/116 = 1.22$ and $141.2/143 = 0.99$, where, as in the previous analysis, the value of ndf is bounded by $n_{\mathrm{bins}} - n_{\mathrm{par}} - 1$ and $n_{\mathrm{bins}} - 1$. Here

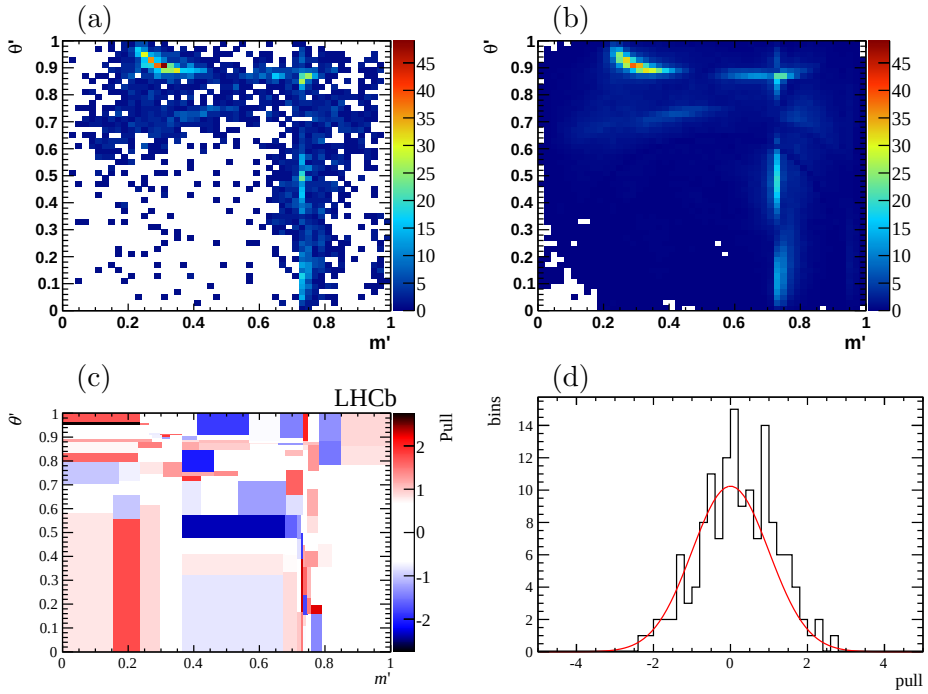

Figure 7.7: The distribution across the SDP of (a) data and (b) the fit model, and (c) the pull between the two distributions in equally populated bins. Also shown (d) is the distribution of these pulls — a Gaussian of mean zero and width one is superimposed.

the number of free parameters in the fit, n_{par}, is 27. These values are evaluated with a minimum bin content of 20 entries. The pulls between data and the fit model in these bins are shown in Fig. 7.7 (bottom). These are seen to follow a distribution that is consistent with a unit Gaussian. The three invariant mass projections of the data are shown in Fig. 7.8 with the fit model superimposed, while Fig. 7.9 shows zooms of these projections in the low $m(K^-\pi^+)$ region and around the $D_2^*(2460)^-$ resonance. Figures 7.10 and 7.11 show the angular distributions in slices of $m(K^-\pi^+)$ and $m(\overline{D}^0\pi^-)$. As in the previous analysis, these projections show good agreement between data and the fit model suggesting that the resonant composition of the DP model is correct.

As described in Sec. 6.5.1, secondary minima are common in DP fits. Of 100 fits with randomised initial values, a single fit finds a minimum other than the global minimum, however, the parameters of interest do not differ significantly from the global minimum. The only significant difference between these two minima is the values of the LASS shape parameters, which take unreasonable values in the secondary minimum. This minimum is not considered further.

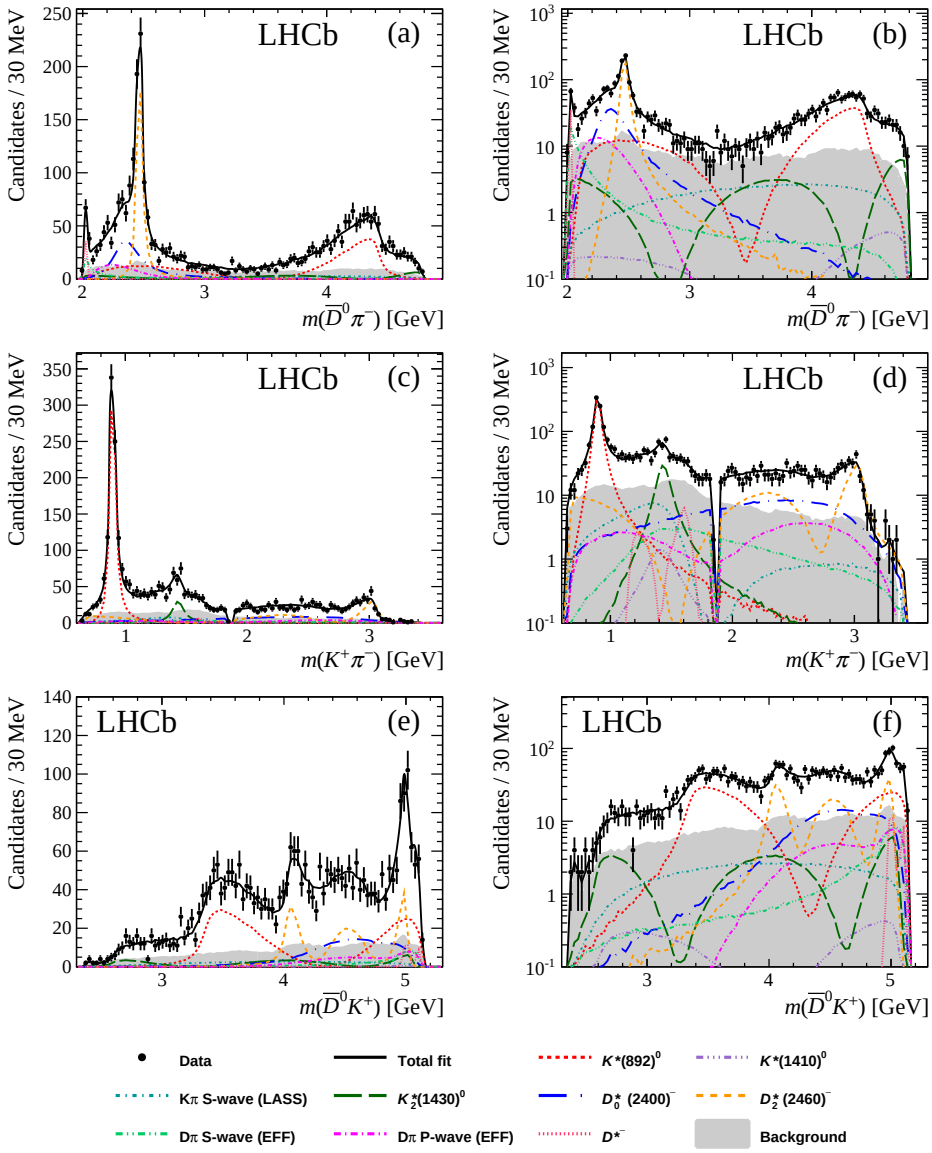

Figure 7.8: Invariant mass projections of the data and the DP fit result onto (a) $m(\overline{D}^0\pi^-)$, (c) $m(K^+\pi^-)$ and (e) $m(\overline{D}^0K^+)$. The same projections are shown on a logarithmic y-scale in (b), (d) and (f). The fit components are shown as described in the legend.

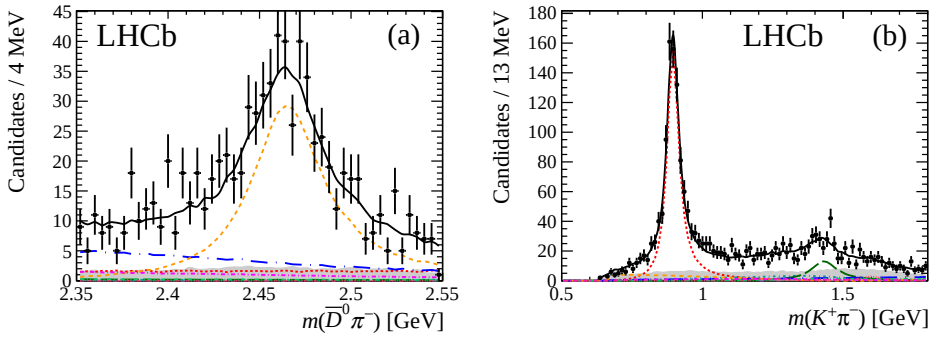

Figure 7.9: Invariant mass projections of the data and the DP fit result onto (a) $m(\overline{D}^0\pi^-)$ around the $D_2^*(2460)^-$ resonance and (b) $m(K^-\pi^+)$ in the range 0.5–1.8 GeV/c^2. The components are as described in the legend for Fig. 7.8.

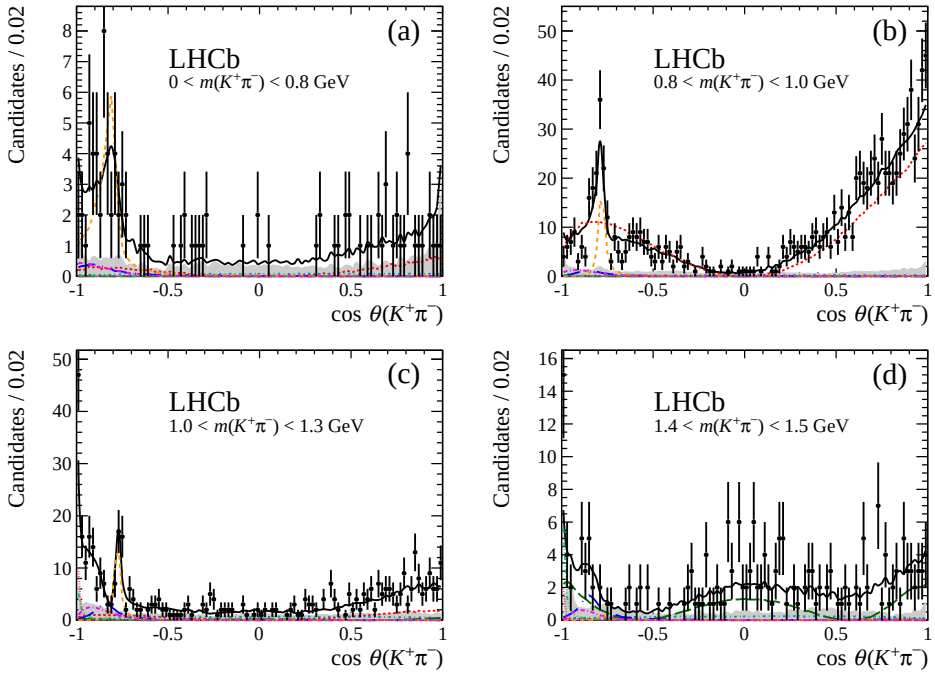

Figure 7.10: Projections of the data and DP fit results onto the cosine of the $K^-\pi^+$ helicity angle, $\cos\theta(K^-\pi^+)$, for slices in $m(K^-\pi^+)$ of (a) 0–0.8 GeV/c^2, (b) 0.8–1.0 GeV/c^2, (c) 1.0–1.3 GeV/c^2 and (d) 1.4–1.5 GeV/c^2. The components are as described in the legend for Fig. 7.8.

7.3.4 Testing the baseline model

An additional resonance study similar to the one detailed in Sec. 6.5.2 was also performed for this DP analysis. Resonances of spin 0, 1, 2 and 3 are added in the three pairs of resonance daughters: $\overline{D}^0\pi^-$, $K^+\pi^-$ and $\overline{D}^0K^+$. In each case the mass of the resonance is allowed to float within the kinematically allowed range while the

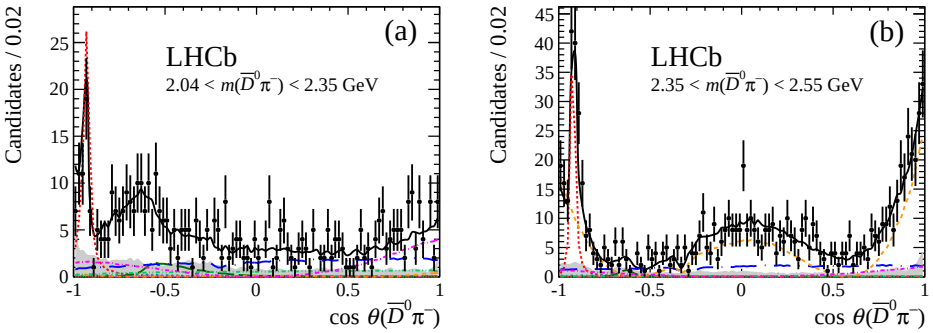

Figure 7.11: Projections of the data and DP fit results onto the cosine of the $\overline{D}^0\pi^-$ helicity angle, $\cos\theta(\overline{D}^0\pi^-)$, for slices in $m(\overline{D}^0\pi^-)$ of (a) 2.04–2.35 GeV/c^2 and (b) 2.35–2.55 GeV/c^2. The components are as described in the legend for Fig. 7.8.

width can be in the range 5 MeV/c^2–1.2 GeV/c^2. Each fit is repeated 25 times with a randomised initial mass and width to explore the full available phase space. The best fit for each additional resonance is tabulated in Table 7.9. None of these resonances are found to be statistically significant, although it is worth noting that the preferred spin-3 $\overline{D}^0\pi^-$ resonance is seen at a similar mass to the $D_3^*(2760)^-$ meson seen in the analysis of the $B^0 \to \overline{D}^0\pi^+\pi^-$ DP [103].

Table 7.9: The changes in the NLL and the total fit fraction (TFF) due to adding arbitrary resonances to the fit model. The fit fraction, mass (MeV/c^2) and width (MeV/c^2) of the additional resonance are also listed.

Daughter pair	Spin	ΔNLL	ΔTFF (%)	FF (%)	Mass	Width
$K^+\pi^-$	0	8.0	−1.6	5.2	1324	507
	1	8.6	−2.4	0.9	2472	347
	2	6.6	−6.7	0.8	2726	311
	3	6.9	−1.0	0.5	1075	23
$\overline{D}^0\pi^-$	0	9.7	3.4	1.0	2507	16
	1	6.7	−0.3	1.5	4653	193
	2	5.3	1.2	0.3	4168	15
	3	11.2	0.2	0.8	2725	53
$\overline{D}^0K^+$	0	7.1	3.6	2.5	4892	312
	1	5.0	7.7	0.9	3136	447
	2	4.6	−0.7	0.5	4624	36
	3	4.8	0.9	0.2	3313	10

Table 7.10: Experimental systematic uncertainties on the fit fractions and complex amplitudes.

Resonance	Fit fraction (%)	Real part	Imaginary part	Magnitude	Phase
$K^*(892)^0$	1.1	0.24	0.03	0.03	0.16
$K^*(1410)^0$	0.8	0.04	0.18	0.10	0.55
$K_0^*(1430)^0$	2.3	0.48	0.37	0.10	1.04
LASS Non. Res.	3.6	0.16	0.17	0.16	0.35
LASS total	2.6	—	—	—	—
$K_2^*(1430)^0$	1.0	0.15	0.14	0.04	0.43
$D_0^*(2400)^-$	2.0	0.07	0.12	0.06	0.14
$D_2^*(2460)^-$	1.1	—	—	—	—
Nonresonant S-wave	1.1	0.09	0.14	0.04	0.24
Nonresonant P-wave	2.1	0.03	0.05	0.04	0.07

7.4 Systematic uncertainties

The sources of systematic uncertainty considered are divided into experimental and model uncertainties as described in Sec. 6.6. Aside from the uncertainties due to momentum resolution and the fixed parent and $\overline{D}^0$ masses, which were found to be negligible, all of the previously considered uncertainties are also considered for this analysis. Most of these uncertainties are determined in the same way as described in Sec. 6.6, however, any changes relative to the B_s^0 DP analysis are detailed below.

7.4.1 Experimental uncertainties

The experimental uncertainties on the components of the complex amplitudes and on the fit fractions are given in Table 7.10 and a breakdown by source is given for the fit fractions in Table 7.11. A breakdown of the experimental uncertainties on the mass and width measurements is given in Table 7.12. Only the method to determine the experimental systematic uncertainty due to efficiency variations differs from the previous analysis. The new process is outlined below.

7.4.2 Uncertainties due to efficiency variations

Both correlated and uncorrelated variations of the efficiency histograms are considered and the uncertainty on each parameter is given by the larger of the two values. In this analysis, correlations are introduced into the efficiency histograms by defining a correlation matrix that drops off as a Gaussian with the distance between bin centres.

Table 7.11: Breakdown of experimental systematic uncertainties on the fit fractions (%). The columns give the contributions from the different sources described in the text.

Resonance	Value ± stat.	S/B frac.	Eff.	Bkgd SDP	Fit bias	Total syst.
$K^*(892)^0$	36.0 ± 1.4	0.57	0.80	0.48	0.30	1.13
$K^*(1410)^0$	0.7 ± 0.3	0.06	0.38	0.66	0.05	0.77
$K_0^*(1430)^0$	4.9 ± 1.9	0.27	1.43	1.78	0.32	2.32
LASS Non. Res.	4.6 ± 3.6	0.49	2.17	2.75	0.83	3.63
LASS total	6.4 ± 2.6	0.25	1.79	1.54	0.99	2.57
$K_2^*(1430)^0$	7.2 ± 1.6	0.22	0.69	0.51	0.52	1.03
$D_0^*(2400)^-$	18.6 ± 2.7	0.20	1.34	1.38	0.39	1.97
$D_2^*(2460)^-$	22.3 ± 1.1	0.67	0.67	0.47	0.15	1.07
Nonresonant S-wave	6.3 ± 1.4	0.03	0.78	0.57	0.55	1.11
Nonresonant P-wave	8.5 ± 1.6	0.83	1.84	0.50	0.36	2.11

Table 7.12: Breakdown of experimental systematic uncertainties on the masses and widths. Units of MeV/c^2 are implied. The columns give the contributions from the different sources described in the text.

Resonance	Mass					
	Value ± stat.	S/B frac.	Eff.	Bkgd SDP	Fit bias	Total syst.
$D_0^*(2400)^-$	2360 ± 15	4.60	8.08	7.02	3.67	12.21
$D_2^*(2460)^-$	2465.6 ± 1.8	0.01	0.37	0.22	0.29	0.51
Resonance	Width					
	Value ± stat.	S/B frac.	Eff.	Bkgd SDP	Fit bias	Total syst.
$D_0^*(2400)^-$	255 ± 26	2.79	13.08	13.93	4.79	19.90
$D_2^*(2460)^-$	46.0 ± 3.4	0.48	0.86	0.92	0.49	1.43

7.4.3 Model uncertainties

The model uncertainties on the components of the complex amplitudes and on the fit fractions are given in Table 7.13 and a breakdown by source is given for the fit fractions in Table 7.14. A breakdown of the model uncertainties on the mass and width measurements is given in Table 7.15. The uncertainty due to fixed parameters is determined using the method described in Sec. 6.6 except that the Blatt–Weisskopf radius parameters are varied for D^{**} resonances, K^{**} resonances and the parent barrier factor separately. The model variations due to marginal components and due to alternative models of the S- and P-wave components are detailed below.

7.4.4 Uncertainties due to marginal components

The marginal components considered in this analysis are the $K^*(1410)^0$ resonance, which is removed from the fit model, and the $K^*(1680)^0$, $D_3^*(2760)^-$, $D_1^*(2760)^-$ and $B_v^*(5325)^+$ resonances, which are added to the fit model. The mass and width of the $D_3^*(2760)^-$ state are fixed to those obtained in a DP analysis of $B^0 \to \overline{D}^0\pi^+\pi^-$ [103],

Table 7.13: Model uncertainties on the fit fractions and complex amplitudes.

Resonance	Fit fraction (%)	Real part	Imaginary part	Magnitude	Phase
$K^*(892)^0$	1.68	0.344	0.062	0.046	0.272
$K^*(1410)^0$	0.73	0.086	0.182	0.107	1.037
$K_0^*(1430)^0$	3.27	0.377	0.167	0.142	0.809
LASS Non. Res.	6.40	0.416	0.234	0.287	0.689
LASS total	5.23	—	—	—	—
$K_2^*(1430)^0$	1.91	0.227	0.146	0.076	0.430
$D_0^*(2400)^-$	7.13	0.224	0.176	0.173	0.230
$D_2^*(2460)^-$	1.20	—	—	—	—
Nonresonant S-wave	3.60	0.137	0.232	0.142	0.438
Nonresonant P-wave	2.84	0.105	0.102	0.105	0.166

Table 7.14: Breakdown of model uncertainties on the fit fractions (%). The columns give the contributions from the different sources described in the text.

Resonance	Value $\pm$ stat.	Fixed params	Add/rem	Alt. models	Total syst.
$K^*(892)^0$	36.0 ± 1.4	0.72	1.10	1.05	1.68
$K^*(1410)^0$	0.7 ± 0.3	0.18	0.68	0.21	0.73
$K_0^*(1430)^0$	4.9 ± 1.9	0.76	3.18	0.22	3.27
LASS Non. Res.	4.6 ± 3.6	1.06	3.84	5.01	6.40
LASS total	6.4 ± 2.6	0.51	1.36	5.02	5.23
$K_2^*(1430)^0$	7.2 ± 1.6	0.35	1.80	0.54	1.91
$D_0^*(2400)^-$	18.6 ± 2.7	0.53	1.88	6.85	7.13
$D_2^*(2460)^-$	22.3 ± 1.1	0.17	0.70	0.95	1.20
Nonresonant S-wave	6.3 ± 1.4	0.26	1.35	3.33	3.60
Nonresonant P-wave	8.5 ± 1.6	0.30	1.92	2.07	2.84

while the parameters of the $D_1^*(2760)^-$ resonance are fixed to those seen for $D_1^*(2760)^0$ in an analysis of $B^+ \to D^- K^+ \pi^+$ decays [119], assuming isospin symmetry. The masses and widths of the other states are taken from the PDG [3].

7.4.5 Uncertainties due to model variations

Alternative parameterisations are used to describe the $K^+\pi^-$ S-wave and the $\overline{D}^0\pi^-$ S- and P-waves. The LASS shape, describing the $K^+\pi^-$ S-wave, is replaced with a Flatté shape [113] for the $\overline{K}_0^*(1430)$ and a resonant term with a modified mass-dependent width for the κ resonance at low $m(K^-\pi^+)$ [114]. A model-independent treatment of the S-wave, where the magnitude and phase variation are each described by a spline, is also used as an alternative. The larger variation is assigned as the systematic uncertainty for each measured quantity. The dabba shape describing the $\overline{D}^0\pi^-$ S-wave is replaced with an EFF term, while a power-law dependent term is used as an alternative to the EFF shape for the $\overline{D}^0\pi^-$ P-wave.

Table 7.15: Breakdown of model uncertainties on the masses and widths. Units of MeV/c^2 are implied. The columns give the contributions from the different sources described in the text.

Resonance			Mass		
	Value ± stat.	Fixed params	Add/rem	Alt. models	Total syst.
$D_0^*(2400)^-$	2360 ± 15	6.15	9.31	25.58	27.90
$D_2^*(2460)^-$	2465.6 ± 1.8	0.09	1.05	0.48	1.15
Resonance			Width		
	Value ± stat.	Fixed params	Add/rem	Alt. models	Total syst.
$D_0^*(2400)^-$	255 ± 26	3.98	18.00	43.49	47.23
$D_2^*(2460)^-$	46.0 ± 3.4	1.41	0.52	2.44	2.87

7.4.6 Summary of systematic uncertainties

The largest experimental uncertainty on most parameters is due to either the efficiency or background histograms, while model uncertainties are generally dominated by model variations. For the parameters of narrow resonances, the statistical, experimental and model uncertainties are all of a similar magnitude, while model uncertainties tend to dominate for the parameters of broader components.

7.4.7 Crosschecks

Crosschecks are performed to test the stability of the results. The dataset is divided into the same categories as used in Sec. 6.6.4 and the fit is repeated for each subset individually. No significant discrepancies are seen in the measured quantities.

7.5 Results

The measured masses and widths are determined to be

$$\begin{aligned} m(D_0^*(2400)^-) &= (2360 \pm 15\,(\text{stat}) \pm 12\,(\text{syst}) \pm 28\,(\text{model}))\,\text{MeV}/c^2 \\ \Gamma(D_0^*(2400)^-) &= (255 \pm 26\,(\text{stat}) \pm 20\,(\text{syst}) \pm 47\,(\text{model}))\,\text{MeV}/c^2 \\ m(D_2^*(2460)^-) &= (2465.6 \pm 1.8\,(\text{stat}) \pm 0.5\,(\text{syst}) \pm 1.2\,(\text{model}))\,\text{MeV}/c^2 \\ \Gamma(D_2^*(2460)^-) &= (46.0 \pm 3.4\,(\text{stat}) \pm 1.4\,(\text{syst}) \pm 2.9\,(\text{model}))\,\text{MeV}/c^2 \end{aligned}$$

where the first uncertainty is statistical, the second is from experimental systematic effects and the third is due to model variations. These results are in good agreement with independent measurements determined from a DP analysis of $B^0 \to \overline{D}^0\pi^+\pi^-$ decays [103] and with the previous averages for these quantities, as reported by the PDG [3]. Comparisons of these measurements are shown in Fig. 7.12.

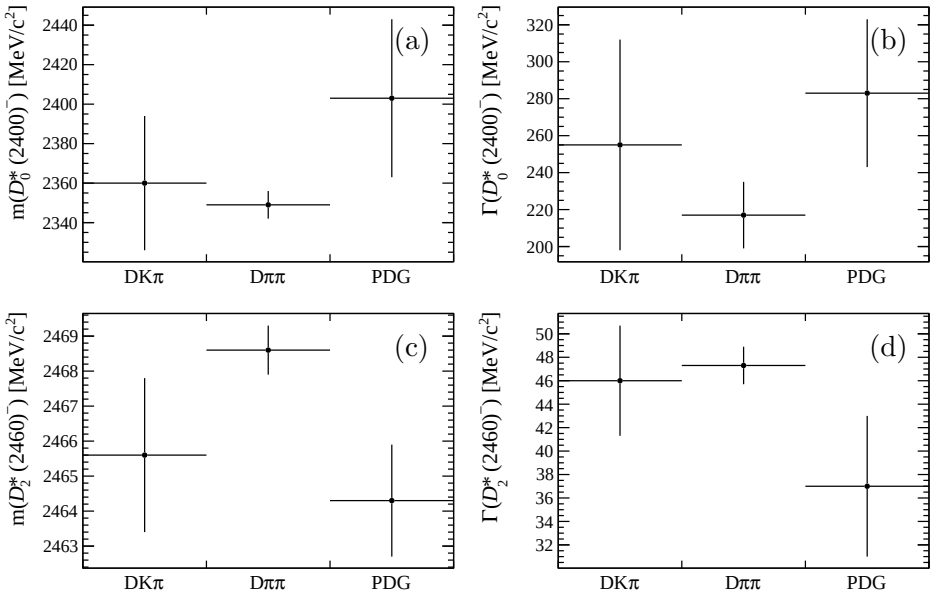

Figure 7.12: Comparisons of different measurements of the masses and widths of the (a and b) $D_0^*(2400)^-$ and (c and d) $D_2^*(2460)^-$ resonances.

The results for the complex amplitudes and fit fractions are given in Tables 7.16 and 7.17, respectively. Upper limits are established, at 90 % and 95 % confidence levels, for the fit fractions of components that do not make a significant contribution to the DP model.

The fit fractions are multiplied by the three body branching fraction to obtain the product branching fraction for each resonance. In Sec. 5.3, the total branching fraction [84] was measured relative to the branching fraction of the $B^0 \to \overline{D}^0\pi^+\pi^-$ decay mode as

$$\frac{\mathcal{B}\left(B^0 \to \overline{D}^0 K^+\pi^-\right)}{\mathcal{B}\left(B^0 \to \overline{D}^0\pi^+\pi^-\right)} = 0.106 \pm 0.007 \pm 0.008\,. \tag{7.4}$$

The $B^0 \to \overline{D}^0\pi^+\pi^-$ branching fraction has since been measured as $(8.46\pm0.14\pm0.29\pm 0.40)\times 10^{-4}$ [103] for $m(\overline{D}^0\pi^-) > 2.1\,\mathrm{GeV}/c^2$. This can be translated to the same region of phase space used in Sec. 5 by scaling by a factor of $1/0.945$ [103], yielding a total branching fraction of $\mathcal{B}(B^0 \to \overline{D}^0 K^+\pi^-) = (9.5 \pm 0.6\,(\mathrm{stat}) \pm 0.7\,(\mathrm{syst}) \pm 0.6\,(\mathcal{B}))\times 10^{-5}$, where the third uncertainty is from the updated $B^0 \to \overline{D}^0\pi^+\pi^-$ branching fraction.

Where the branching fraction of the subsequent resonance decay is known, the product branching fraction is converted into the B^0 decay branching fraction. These results are given in Table 7.18.

Table 7.16: Results for the complex amplitudes and their uncertainties. The three quoted errors are statistical, experimental systematic and model uncertainties, respectively. The central values and statistical uncertainties are as reported in Table 7.6, while the experimental and model systematic uncertainties are as reported in Tables 7.10 and 7.13.

Resonance	Real part	Imaginary part
$K^*(892)^0$	$-0.00 \pm 0.15 \pm 0.24 \pm 0.34$	$-1.27 \pm 0.06 \pm 0.03 \pm 0.06$
$K^*(1410)^0$	$0.15 \pm 0.06 \pm 0.04 \pm 0.09$	$-0.09 \pm 0.09 \pm 0.18 \pm 0.18$
$K_0^*(1430)^0$	$0.14 \pm 0.38 \pm 0.48 \pm 0.38$	$0.45 \pm 0.15 \pm 0.37 \pm 0.17$
LASS nonresonant	$-0.10 \pm 0.24 \pm 0.16 \pm 0.42$	$0.44 \pm 0.14 \pm 0.17 \pm 0.23$
$K_2^*(1430)^0$	$-0.32 \pm 0.09 \pm 0.15 \pm 0.23$	$-0.47 \pm 0.07 \pm 0.14 \pm 0.15$
$D_0^*(2400)^-$	$-0.80 \pm 0.08 \pm 0.07 \pm 0.22$	$-0.44 \pm 0.14 \pm 0.12 \pm 0.18$
$D_2^*(2460)^-$	1.00	0.00
$D\pi$ S-wave (dabba)	$-0.39 \pm 0.09 \pm 0.09 \pm 0.14$	$0.36 \pm 0.17 \pm 0.14 \pm 0.23$
$D\pi$ P-wave (EFF)	$-0.62 \pm 0.06 \pm 0.03 \pm 0.11$	$-0.03 \pm 0.06 \pm 0.05 \pm 0.10$

Resonance	Magnitude	Phase
$K^*(892)^0$	$1.27 \pm 0.06 \pm 0.03 \pm 0.05$	$-1.57 \pm 0.11 \pm 0.16 \pm 0.27$
$K^*(1410)^0$	$0.18 \pm 0.07 \pm 0.10 \pm 0.11$	$-0.54 \pm 0.21 \pm 0.55 \pm 1.04$
$K_0^*(1430)^0$	$0.47 \pm 0.09 \pm 0.10 \pm 0.14$	$1.27 \pm 0.95 \pm 1.04 \pm 0.81$
LASS nonresonant	$0.46 \pm 0.14 \pm 0.16 \pm 0.29$	$1.79 \pm 0.65 \pm 0.35 \pm 0.69$
$K_2^*(1430)^0$	$0.57 \pm 0.05 \pm 0.04 \pm 0.08$	$-2.16 \pm 0.19 \pm 0.43 \pm 0.43$
$D_0^*(2400)^-$	$0.91 \pm 0.07 \pm 0.06 \pm 0.17$	$-2.64 \pm 0.15 \pm 0.14 \pm 0.23$
$D_2^*(2460)^-$	1.00	0.00
$D\pi$ S-wave (dabba)	$0.53 \pm 0.07 \pm 0.04 \pm 0.14$	$2.40 \pm 0.27 \pm 0.24 \pm 0.44$
$D\pi$ P-wave (EFF)	$0.62 \pm 0.06 \pm 0.04 \pm 0.11$	$-3.09 \pm 0.10 \pm 0.07 \pm 0.17$

Table 7.17: Results for the fit fractions and their uncertainties (%). The three quoted errors are statistical, experimental systematic and model uncertainties, respectively. Upper limits at both 90 % and 95 % confidence level (CL) are given for components that are not significant. The central values and statistical uncertainties are as reported in Table 7.6, while the experimental and model systematic uncertainties are as reported in Tables 7.10 and 7.13.

Resonance	Fit fraction	Upper limits	
		90 % CL	95 % CL
$K^*(892)^0$	$36.0 \pm 1.4 \pm 1.1 \pm 1.7$		
$K^*(1410)^0$	$0.7 \pm 0.3 \pm 0.8 \pm 0.7$	< 3.1	< 3.6
$K_0^*(1430)^0$	$4.9 \pm 1.9 \pm 2.3 \pm 3.3$		
LASS nonresonant	$4.6 \pm 3.6 \pm 3.6 \pm 6.4$		
LASS total	$6.4 \pm 2.6 \pm 2.6 \pm 5.2$		
$K_2^*(1430)^0$	$7.2 \pm 1.6 \pm 1.0 \pm 1.9$		
$D_0^*(2400)^-$	$18.6 \pm 2.7 \pm 2.0 \pm 7.1$		
$D_2^*(2460)^-$	$22.3 \pm 1.1 \pm 1.1 \pm 1.2$		
$D_3^*(2760)$	—	< 1.0	< 1.1
$D\pi$ S-wave (dabba)	$6.3 \pm 1.4 \pm 1.1 \pm 3.6$		
$D\pi$ P-wave (EFF)	$8.5 \pm 1.6 \pm 2.1 \pm 2.8$		

Table 7.18: Results for the product branching fractions (top) $\mathcal{B}(B^0 \to \overline{D}^0 K^{**0}) \times \mathcal{B}(K^{**0} \to K^+\pi^-)$ and (bottom) $\mathcal{B}(B^0 \to D^{**-}K^+) \times \mathcal{B}(D^{**-} \to \overline{D}^0\pi^-)$, for each K^{**0} and D^{**-} resonance. For the K^{**0} resonances, where $\mathcal{B}(K^{**0} \to K^-\pi^+)$ is known [3], the B^0 decay branching fraction is also given. The four quoted uncertainties are statistical, experimental systematic, model and PDG uncertainties, respectively. Upper limits are given at 90 % (95 %) confidence level.

Resonance	Product branching fraction (10^{-5})	Branching fraction (10^{-5})
$K^*(892)^0$	$3.42 \pm 0.13 \pm 0.10 \pm 0.16 \pm 0.40$	$5.13 \pm 0.20 \pm 0.15 \pm 0.24 \pm 0.60$
$K^*(1410)^0$	$0.07 \pm 0.03 \pm 0.08 \pm 0.07 \pm 0.01$	$1.59 \pm 0.68 \pm 1.81 \pm 1.59 \pm 0.36$
$K_0^*(1430)^0$	$0.47 \pm 0.18 \pm 0.22 \pm 0.31 \pm 0.05$	$0.71 \pm 0.27 \pm 0.33 \pm 0.47 \pm 0.08$
LASS nonresonant	$0.44 \pm 0.34 \pm 0.34 \pm 0.61 \pm 0.05$	$0.66 \pm 0.51 \pm 0.51 \pm 0.92 \pm 0.08$
LASS total	$0.61 \pm 0.25 \pm 0.25 \pm 0.49 \pm 0.07$	$0.92 \pm 0.38 \pm 0.38 \pm 0.74 \pm 0.11$
$K_2^*(1430)^0$	$0.68 \pm 0.15 \pm 0.10 \pm 0.18 \pm 0.08$	$2.04 \pm 0.45 \pm 0.30 \pm 0.54 \pm 0.25$
$K^*(1410)^0$	< 0.29 (0.34)	< 6.7 (7.8)
$D_0^*(2400)^-$	$1.77 \pm 0.26 \pm 0.19 \pm 0.67 \pm 0.20$	
$D_2^*(2460)^-$	$2.12 \pm 0.10 \pm 0.11 \pm 0.11 \pm 0.25$	
$D_3^*(2760)^-$	< 0.10 (0.11)	
$D\pi$ S-wave (dabba)	$0.60 \pm 0.13 \pm 0.11 \pm 0.34 \pm 0.07$	
$D\pi$ P-wave (EFF)	$0.81 \pm 0.15 \pm 0.20 \pm 0.27 \pm 0.09$	

Chapter 8

Measurement of γ from $B^0 \to DK^+\pi^-$ decays

This chapter details the determination of the CKM angle γ from $B^0 \to DK\pi$ decays. Preliminary results are reported for the Cartesian parameters

$$x_\pm = r_B \cos(\delta_B \pm \gamma) , \tag{8.1}$$

$$y_\pm = r_B \sin(\delta_B \pm \gamma) , \tag{8.2}$$

for the $K^*(892)^0$ and $K_2^*(1430)^0$ resonances. Throughout the analysis, an offset was applied to the reported central value of each of these parameters to avoid inadvertently biasing the results, while allowing the statistical and systematic uncertainties to be extracted. Only after the analysis was completed were the offsets removed.

8.1 Datasets and selection modifications

For the determination of γ, decays of B^0 mesons to the $DK^+\pi^-$ final state are analysed with the D meson decaying to both the quasi-flavour-specific final state, $K^+\pi^-$, and the *CP* eigenstates, K^+K^- and $\pi^+\pi^-$, henceforth denoted $K\pi$, KK and $\pi\pi$, respectively. As in Chapter 7, the more abundant B_s^0 decay is removed from the $K\pi$ dataset by requiring the two kaons in the final state to have the same charge. Candidates with oppositely charged kaons are retained in a separate dataset, denoted πK, to allow the fitting procedure to be validated using $B_s^0 \to DK^-\pi^+$ decays.

The selection requirements for all four datasets are based on those used in the previous DP analyses, although separate BDTs are used to identify the D decay to each final state. Furthermore, as the output of the D BDT is an input to the NN,

separate NNs are trained for the KK and $\pi\pi$ datasets — in each case trained on $B^0 \to D\pi^+\pi^-$ decays with the same D decay. The NN used previously in Chapter 7 is used again for the $K\pi$ and πK datasets. In addition, several minor changes have been made to the selection requirements to reduce the level of charmless background in the KK and $\pi\pi$ datasets. In particular, the D decay vertex is required to be downstream of the B decay vertex; the D mass window is tightened (to the ranges listed in Table 8.1); and the daughters of the D meson are required to have a total momentum of less than $100\,\text{GeV}/c$ (in line with requirements on the bachelor tracks to allow PID differentiation between kaons and pions). The cumulative effect of these modifications is that the overlap between the $K\pi$ dataset and the dataset used previously in Chapter 7 is only around 60 %.

Table 8.1: D mass windows applied to the $DK\pi$ data samples, determined from fits to the corresponding D mass spectra.

D decay	signal mass window
$K\pi$, πK	$1846 - 1887\,\text{MeV}/c^2$
KK	$1849 - 1884\,\text{MeV}/c^2$
$\pi\pi$	$1845 - 1889\,\text{MeV}/c^2$

8.2 Mass fits

As the precision of the γ measurement is expected to be statistically limited, the sensitivity to γ is maximised as follows. Instead of a single requirement on the NN output variable, multiple thresholds are defined to divide each dataset into five bins of increasing signal purity and roughly equal signal yields. In each decay channel, a simultaneous fit is performed to the B mass spectra allowing for varying ratios of signal to background in each subset.[1] The signal and background yields determined from these fits are then used as inputs to the simultaneous DP fit. The following components are included in the fit models where needed.

- B^0 signal;
- B_s^0 signal;
- combinatoric background;
  - general combinatorial background;
  - partial combinatorial background: $B^+ \to D^*K^+$ and $B^0 \to DK^+\pi^-$;

[1] A similar approach was applied in a search for the $B_s^0 \to \overline{D}^0 f_0(980)$ decay mode [120].

- partially reconstructed backgrounds;
  - $B^0 \to D^* K^+ \pi^-$ with $D^* \to D\pi^0$ and $D^* \to D\gamma$;
  - $B^0_s \to D^* K^- \pi^+$ with $D^* \to D\pi^0$ and $D^* \to D\gamma$;
- peaking backgrounds;
  - $B^0 \to D^{(*)} \pi^+ \pi^-$;
  - $B^0 \to D^{(*)} K^+ K^-$;
  - $B^0_s \to D^{(*)} K^+ K^-$;
  - $\overline{\Lambda}^0_b \to D^{(*)} \overline{p} \pi^+$;
  - $\overline{\Lambda}^0_b \to D^{(*)} \overline{p} K^+$;

The majority of these components are modelled as described in previous chapters so are not discussed further here. In each fit, the fractions of the B^0 and B^0_s signal components and the peaking backgrounds within each NN bin were assumed to be the same. Separate fractions are used for the combinatorial and peaking background components as, in each case, the distribution of candidates in the NN output variable is expected to differ from that of signal decays. The partial combinatorial background and the background due to $B^0_s \to D^* K^- \pi^+$ decays were not included in the model described in Chapter 7 so are covered below.

8.2.1 Partial combinatorial background

The inclusion of low purity bins in the mass fit necessitates a more complete understanding of the sources of combinatorial background. While random combinations of a D meson with two charged tracks are still best described by a functional form, a significant background is seen from candidates where a DK^+ combination from a real B decay is combined with a random pion. The simplest background of this form is due to $B^+ \to DK^+$ decays but these can be removed by requiring the DK^+ invariant mass to lie within the DP — *i.e.* $m(DK^+) < m_B - m_\pi$. Backgrounds are, therefore, considered where a pion has been missed from the final state hence allowing the candidate to fall within the DP. Backgrounds due to $B^+ \to D^* K^+$ with $D^* \to D\pi^0$ and $B^0 \to DK^+\pi^-$ are considered where in both cases the pion in the final state is replaced by a random track. Note that this second contribution is due to mis-reconstructed signal decays.[2] These backgrounds are combined according to their relative branching fractions and efficiencies, and are modelled using a single PDF derived from simulation, as shown in Fig. 8.1.

[2] This is similar to the self-cross-feed category used in some previous DP analyses [121–123].

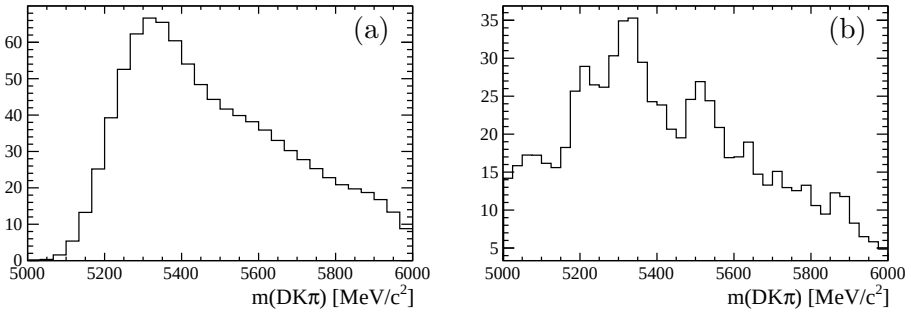

Figure 8.1: Invariant mass distributions of the partially combinatorial (a) $B^+ \to \overline{D}^{*0}K^+$ and (b) $B^0 \to \overline{D}^0 K^+\pi^-$ backgrounds as determined from simulation.

8.2.2 Background due to $B_s^0 \to D^*K^-\pi^+$ decays

As $B_s^0 \to D^*K^-\pi^+$ decays form important backgrounds to the KK and $\pi\pi$ datasets, it is necessary to construct a more faithful DP model of this decay than has been used previously. While the DP distribution of $B_s^0 \to D^*K^-\pi^+$ decays is unknown, a reasonable model is constructed based on the related decays $B_s^0 \to \overline{D}^0 K^-\pi^+$ and $B^0 \to \overline{D}^{*0}\pi^+\pi^-$. Simulated candidates are weighted to match the DP distribution of $B_s^0 \to \overline{D}^0 K^-\pi^+$ decays [52, 86] reported in Chapter 6 but with the D_{sv}^{*-}, and $D_{s2}^*(2573)^-$ resonances removed. The narrow $D_{s1}(2536)^-$ and $D_{s2}^*(2573)^-$ resonances are then added to the model according to the fit fractions observed for the $D_1(2420)^-$ and $D_2^*(2460)^-$ resonances in $B^0 \to \overline{D}^{*0}\pi^+\pi^-$ decays [98]. Both S-wave and D-wave decays of the $D_{s1}(2536)^-$ resonance are included in the model according to the fractions observed in $D_{s1}(2536)^- \to D^{*-}\overline{K}^0$ decays [124].

8.2.3 Fit results

The results of the fits to all four datasets are summarised in Table 8.2. The fits to the $K\pi$, KK and $\pi\pi$ datasets are shown on linear and logarithmic scales in Figs 8.2 and 8.3, respectively, where the NN bins have been weighted according to signal purity and combined. The individual bins from the fit to the $K\pi$ dataset are shown in Fig. 8.4, while equivalent plots for the πK, KK and $\pi\pi$ datasets are presented in Figs 8.6, 8.8 and 8.10, respectively. The same fits are shown on logarithmic scales in Figs 8.5, 8.7, 8.9 and 8.11. The χ^2/ndf value for each fit is also reported in Table 8.2. In total, $\chi^2/\text{ndf} = 836.3/891 = 0.94$. Some discrepancies are seen in the fit to the πK dataset, however, as this dataset is not used to extract γ, the fit quality is sufficient for validating the DP fitting method.

The signal window is defined in each fit as $m(B^0) \pm 2.5 \times \sigma_1$. This cor-

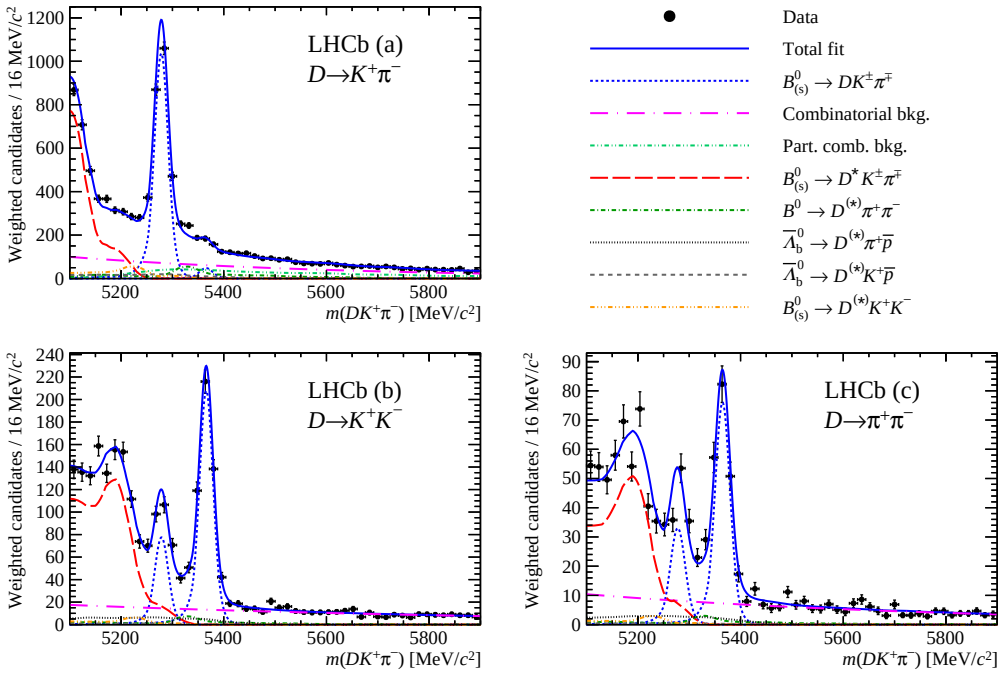

Figure 8.2: Results of fits to $DK^+\pi^-$ candidates in the (a) $D\to K^+\pi^-$, (b) $D\to K^+K^-$ and (c) $D\to\pi^+\pi^-$ samples. The data and the fit results in each NN output bin have been weighted according to signal purity and combined.

responds to windows of 5246.6–5309.9 MeV/c^2, 5246.9–5310.5 MeV/c^2 and 5243.1–5312.3 MeV/c^2 in the $K\pi$, KK and $\pi\pi$ samples. Equivalent B^0_s signal windows are defined by shifting the signal window by the known $B^0_s - B^0$ mass difference. Table 8.3 gives the yields and purities within these windows for the four datasets.

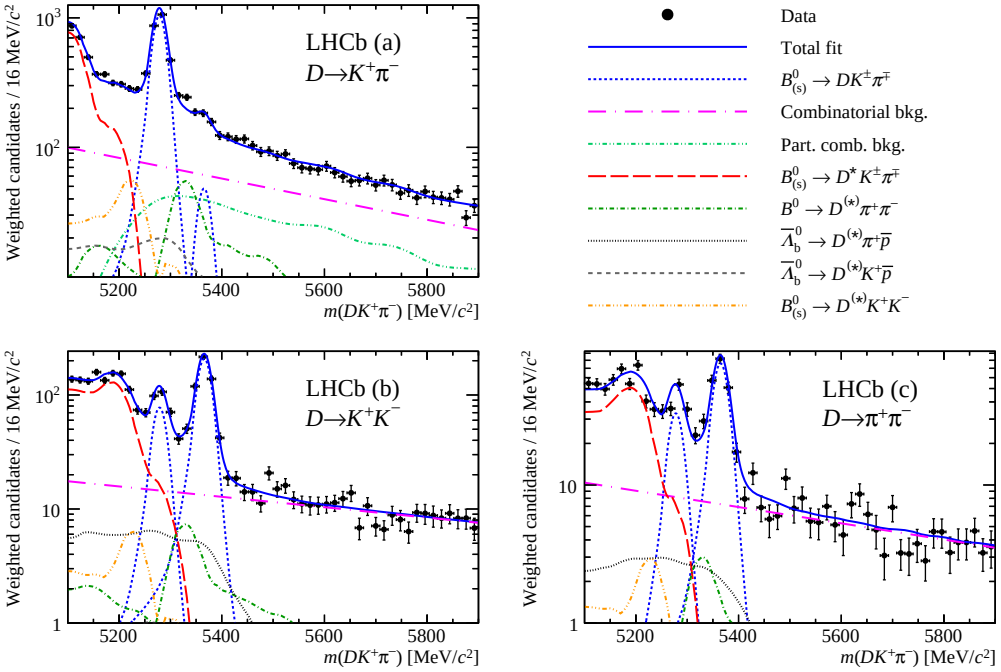

Figure 8.3: Results of fits to $DK^+\pi^-$ candidates in the (a) $D\to K^+\pi^-$, (b) $D\to K^+K^-$ and (c) $D\to\pi^+\pi^-$ samples. The data and the fit results in each NN output bin have been weighted according to signal purity and combined.

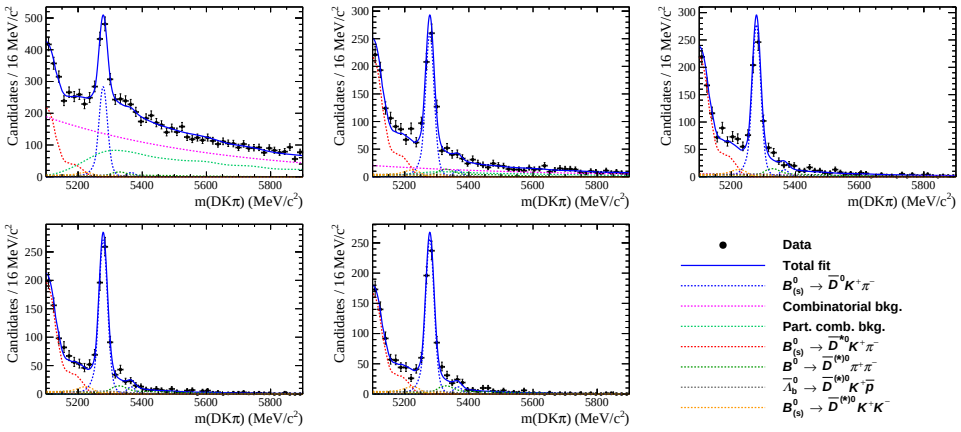

Figure 8.4: Fit to $D(K^+\pi^-)K^+\pi^-$ data in the 5 bins of the neural network output variable. They are (a) $[-0.80, 0.00]$, (b) $[0.00, 0.50]$, (c) $[0.50, 0.72]$, (d) $[0.72, 0.81]$, (e) $[0.81, 1.00]$.

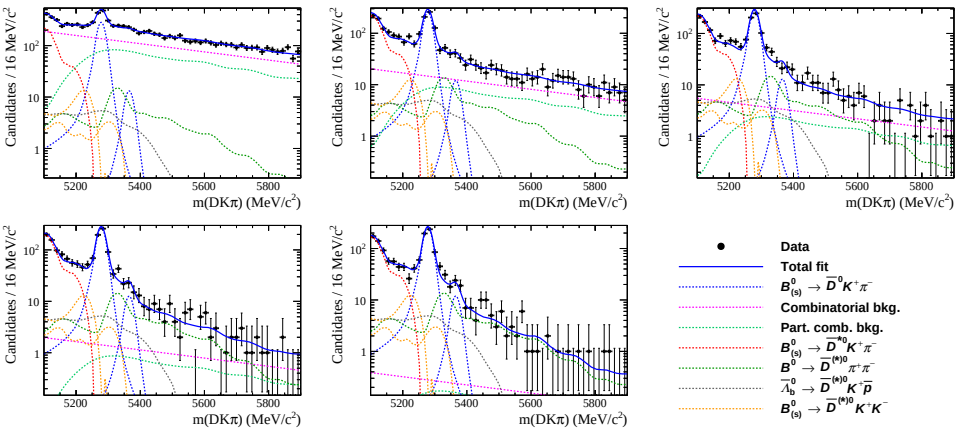

Figure 8.5: Fit to $D(K^+\pi^-)K^+\pi^-$ data in the 5 bins of the neural network output variable. They are (a) $[-0.80, 0.00]$, (b) $[0.00, 0.50]$, (c) $[0.50, 0.72]$, (d) $[0.72, 0.81]$, (e) $[0.81, 1.00]$.

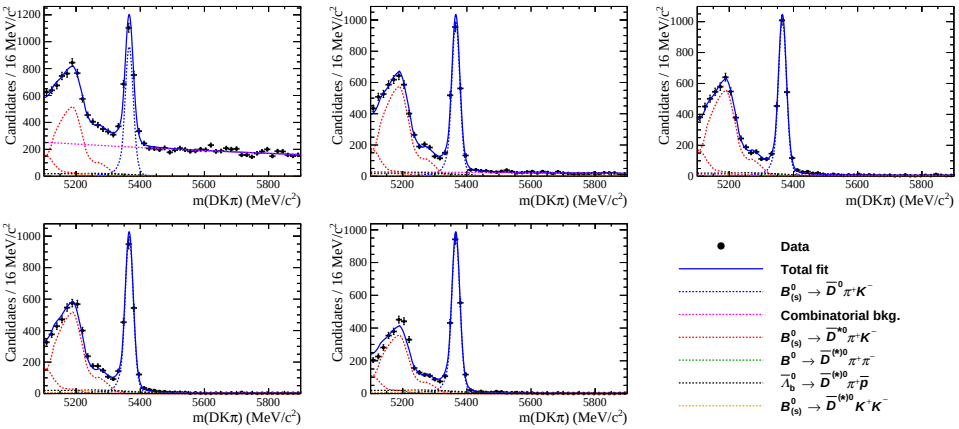

Figure 8.6: Fit to $D(\pi^+K^-)K^+\pi^-$ data in the 5 bins of the neural network output variable. They are (a) $[-0.80, 0.00]$, (b) $[0.00, 0.50]$, (c) $[0.50, 0.72]$, (d) $[0.72, 0.81]$, (e) $[0.81, 1.00]$.

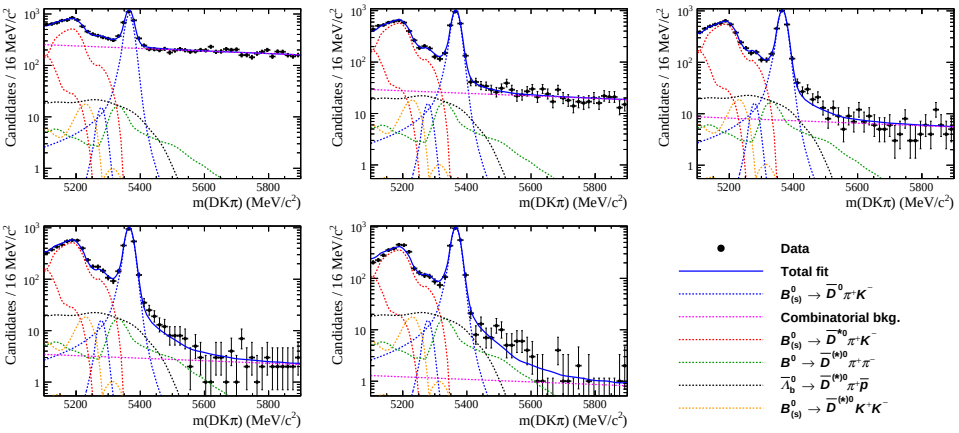

Figure 8.7: Fit to $D(\pi^+K^-)K^+\pi^-$ data in the 5 bins of the neural network output variable. They are (a) $[-0.80, 0.00]$, (b) $[0.00, 0.50]$, (c) $[0.50, 0.72]$, (d) $[0.72, 0.81]$, (e) $[0.81, 1.00]$.

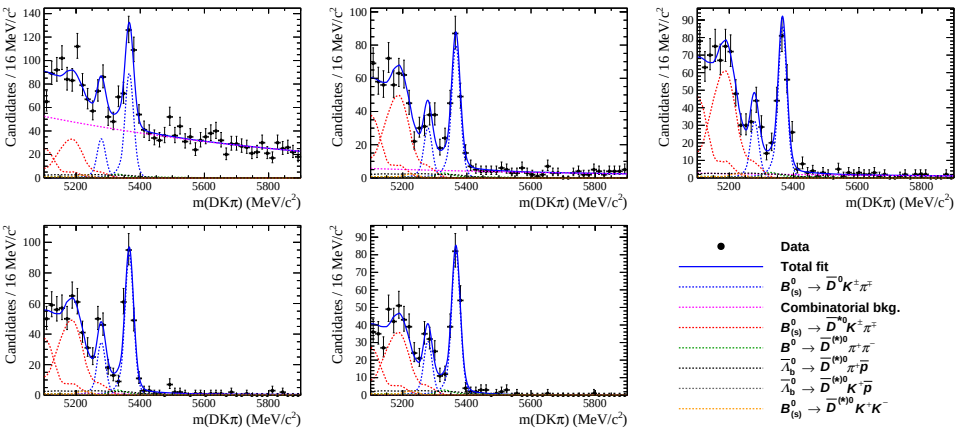

Figure 8.8: Fit to $D(K^+K^-)K^+\pi^-$ data in the 5 bins of the neural network output variable. They are (a) $[-0.80, -0.08]$, (b) $[-0.08, 0.43]$, (c) $[0.43, 0.59]$, (d) $[0.59, 0.67]$, (e) $[0.67, 1.00]$.

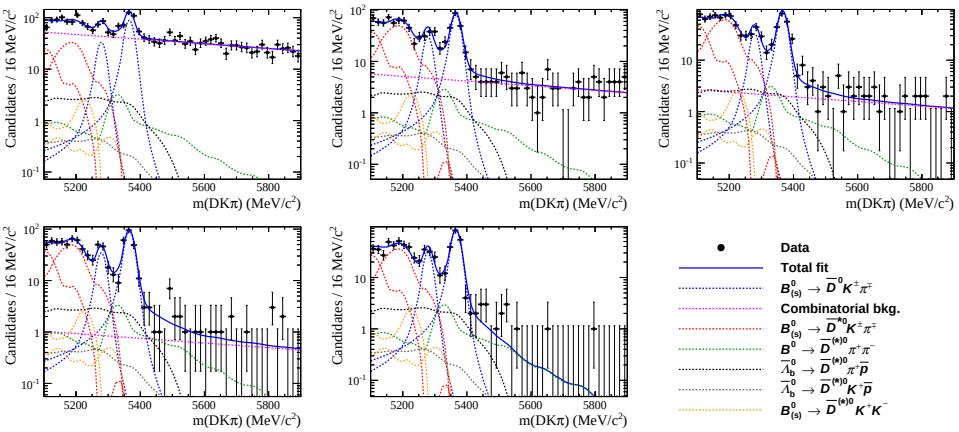

Figure 8.9: Fit to $D(K^+K^-)K^+\pi^-$ data in the 5 bins of the neural network output variable. They are (a) $[-0.80, -0.08]$, (b) $[-0.08, 0.43]$, (c) $[0.43, 0.59]$, (d) $[0.59, 0.67]$, (e) $[0.67, 1.00]$.

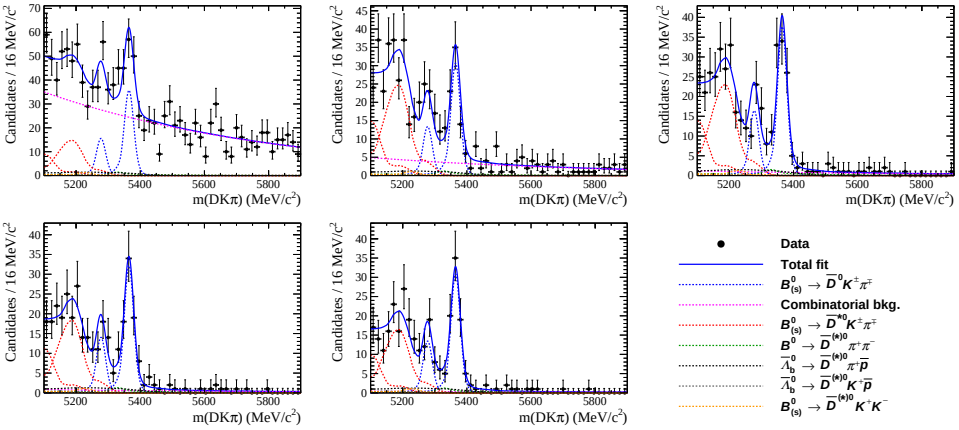

Figure 8.10: Fit to $D(\pi^+\pi^-)K^+\pi^-$ data in the 5 bins of the neural network output variable. They are (a) $[-0.80, -0.25]$, (b) $[-0.25, 0.23]$, (c) $[0.23, 0.57]$, (d) $[0.57, 0.74]$, (e) $[0.74, 1.00]$.

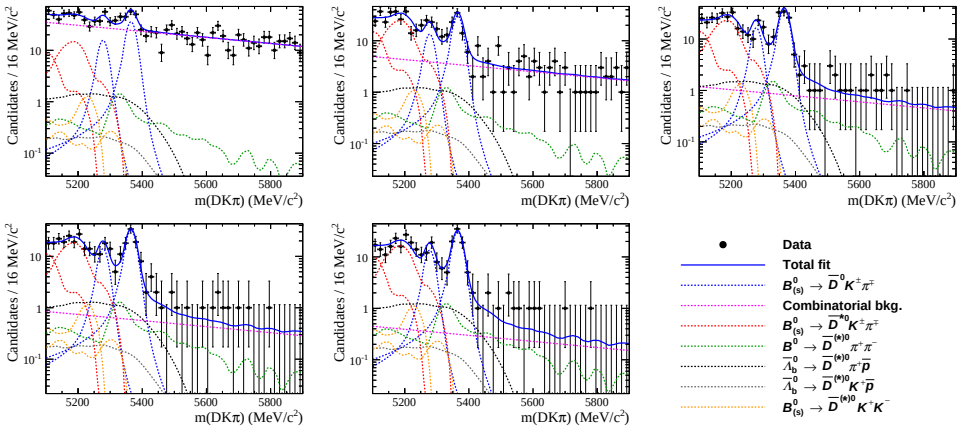

Figure 8.11: Fit to $D(\pi^+\pi^-)K^+\pi^-$ data in the 5 bins of the neural network output variable. They are (a) $[-0.80, -0.25]$, (b) $[-0.25, 0.23]$, (c) $[0.23, 0.57]$, (d) $[0.57, 0.74]$, (e) $[0.74, 1.00]$.

Table 8.2: Fit parameters from the fits to the four datasets. The fraction marked (*) is not a floated parameter but is calculated as the difference between 1 and the sum of the other fractions. The total χ^2/ndf values are also reported for the four fits.

Parameter	Value			
	$K\pi$	πK	KK	$\pi\pi$
$m(B)$	5278.3 ± 0.4	5278.3 ± 0.2	5278.7 ± 0.5	5277.7 ± 1.0
σ_1	12.7 ± 0.4	11.9 ± 0.2	12.7 ± 0.5	13.9 ± 0.8
f	0.787 ± 0.017	0.787 ± 0.017	0.798 ± 0.018	0.797 ± 0.018
σ_2/σ_1	1.80 ± 0.05	1.72 ± 0.04	1.75 ± 0.05	1.76 ± 0.05
Exp. slope (10^{-3})	-1.84 ± 0.13	-0.57 ± 0.07	-1.05 ± 0.19	-1.35 ± 0.26
$N(B^0 \to DK\pi)$	3125 ± 79	171 ± 64	418 ± 27	185 ± 21
$N(B_s^0 \to DK\pi)$	146 ± 27	$10\,969 \pm 128$	1014 ± 41	429 ± 28
N(Comb. bkg.)	5694 ± 529	$11\,887 \pm 222$	2092 ± 95	1288 ± 86
$N(B^0 \to D^*K\pi)$	3028 ± 115	2294 ± 120	543 ± 48	183 ± 33
$N(B_s^0 \to D^*K\pi)$	—	$17\,030 \pm 229$	1493 ± 77	639 ± 52
$N(B^0 \to D^{(*)}\pi\pi)$	783 ± 67	833 ± 132	146 ± 17	72 ± 11
$N(\Lambda_b^0 \to D^{(*)}p\pi)$	—	1895 ± 274	241 ± 47	118 ± 26
$N(\Lambda_b^0 \to D^{(*)}pK)$	416 ± 64	—	34 ± 9	17 ± 5
$N(B^0 \to D^{(*)}KK)$	371 ± 51	479 ± 84	64 ± 15	33 ± 8
$N(B_s^0 \to D^{(*)}KK)$	171 ± 47	39 ± 52	25 ± 11	14 ± 6
$N(B^+ \to D^*K)$	2648 ± 454	—	—	—
$f_{\rm sig}^1$	0.210 ± 0.012	0.195 ± 0.005	0.187 ± 0.017	0.214 ± 0.029
$f_{\rm sig}^2$	0.192 ± 0.008	0.200 ± 0.004	0.186 ± 0.011	0.184 ± 0.019
$f_{\rm sig}^3$	0.206 ± 0.008	0.206 ± 0.004	0.201 ± 0.012	0.225 ± 0.019
$f_{\rm sig}^4$	0.201 ± 0.007	0.203 ± 0.004	0.215 ± 0.012	0.193 ± 0.018
$f_{\rm sig}^5$ *	0.190 ± 0.007	0.196 ± 0.004	0.211 ± 0.011	0.184 ± 0.017
$f_{\rm part}^1$	0.214 ± 0.023	0.205 ± 0.005	0.145 ± 0.020	0.152 ± 0.042
$f_{\rm part}^2$	0.214 ± 0.010	0.228 ± 0.003	0.217 ± 0.011	0.254 ± 0.021
$f_{\rm part}^3$	0.215 ± 0.011	0.220 ± 0.003	0.267 ± 0.013	0.237 ± 0.021
$f_{\rm part}^4$	0.193 ± 0.010	0.205 ± 0.003	0.215 ± 0.012	0.189 ± 0.019
$f_{\rm part}^5$ *	0.164 ± 0.009	0.142 ± 0.003	0.156 ± 0.010	0.169 ± 0.018
$f_{\rm comb}^1$	0.870 ± 0.013	0.856 ± 0.015	0.849 ± 0.012	0.828 ± 0.018
$f_{\rm comb}^2$	0.094 ± 0.008	0.099 ± 0.010	0.092 ± 0.009	0.116 ± 0.014
$f_{\rm comb}^3$	0.025 ± 0.004	0.029 ± 0.004	0.043 ± 0.007	0.027 ± 0.008
$f_{\rm comb}^4$	0.009 ± 0.003	0.012 ± 0.002	0.017 ± 0.005	0.019 ± 0.007
$f_{\rm comb}^5$ *	0.002 ± 0.002	0.004 ± 0.002	0.000 ± 0.000	0.010 ± 0.006
χ^2	171.5	299.6	188.2	169.1
ndf	223	223	223	222
χ^2/ndf	0.77	1.34	0.84	0.76

Table 8.3: Signal yields and purities within B^0 and B_s^0 signal windows for candidates in the five NN bins of each dataset.

$D \to K\pi$					
	Bin 1	Bin 2	Bin 3	Bin 4	Bin 5
B^0 in window	596.8 ± 41.9	545.8 ± 27.7	585.1 ± 24.7	570.7 ± 22.8	540.0 ± 21.4
B^0 window purity	39.8 %	79.0 %	87.6 %	89.7 %	90.7 %
B_s^0 in window	27.7 ± 5.6	25.4 ± 4.9	27.2 ± 5.1	26.5 ± 4.9	25.1 ± 4.6
B_s^0 window purity	3.3 %	16.7 %	28.2 %	33.1 %	35.9 %
$D \to \pi K$					
	Bin 1	Bin 2	Bin 3	Bin 4	Bin 5
B^0 in window	30.0 ± 11.4	30.8 ± 11.6	31.7 ± 12.0	31.3 ± 11.8	30.1 ± 11.4
B^0 window purity	2.2 %	4.7 %	5.5 %	5.9 %	7.3 %
B_s^0 in window	1911.6 ± 52.9	1961.7 ± 44.7	2017.4 ± 42.9	1990.9 ± 42.7	1916.8 ± 42.6
B_s^0 window purity	67.9 %	91.4 %	94.3 %	95.0 %	95.4 %
$D \to KK$					
	Bin 1	Bin 2	Bin 3	Bin 4	Bin 5
B^0 in window	70.2 ± 8.5	63.2 ± 5.9	68.2 ± 6.1	72.7 ± 6.2	64.5 ± 5.4
B^0 window purity	24.5 %	47.8 %	50.3 %	56.2 %	60.2 %
B_s^0 in window	187.7 ± 18.7	169.0 ± 12.2	182.3 ± 12.3	194.5 ± 12.4	172.7 ± 11.4
B_s^0 window purity	51.9 %	84.2 %	88.4 %	90.7 %	92.1 %
$D \to \pi\pi$					
	Bin 1	Bin 2	Bin 3	Bin 4	Bin 5
B^0 in window	35.8 ± 7.5	30.7 ± 4.7	37.7 ± 4.7	32.3 ± 4.2	30.9 ± 4.0
B^0 window purity	20.1 %	41.0 %	53.3 %	54.6 %	56.5 %
B_s^0 in window	82.1 ± 14.2	70.5 ± 8.4	86.6 ± 8.5	74.0 ± 7.7	70.9 ± 7.4
B_s^0 window purity	41.7 %	75.7 %	87.0 %	87.5 %	88.7 %

8.3 Dalitz plot fit strategy

The DP model for the $b \to c$ amplitude was determined in Chapter 7 and includes the resonant and nonresonant components listed in Table 7.5. The simultaneous fit to the $K\pi$, KK and $\pi\pi$ datasets is used to determine the $b \to u$ contribution to the K^* resonances. For a given resonance, the $b \to u$ and $b \to c$ amplitudes are related by Eq. 2.20. The complex coefficients associated with a K^* resonance in the $B^0 \to \overline{D}^0 K^+\pi^-$ and $B^0 \to D_{CP}K^+\pi^-$ DPs are, therefore, given by Eqs 2.34 and 2.35, respectively. While this parameterisation offers a direct determination of γ, the fitted parameters are not statistically well-behaved. This is because the uncertainty on γ is dependent on the central value of r_B, which in turn must be constrained to be positive. To facilitate combinations with other measurements, a parameterisation is preferred where the uncertainty on each parameter does not depend on the central value of any parameter. To address this issue, an alternative parametrisation is used

$$c_j \left[1 + r_{B,j} \exp\left\{i\left(\delta_{B,j} \pm \gamma\right)\right\}\right] \longrightarrow c_j \left[1 + x_{\pm,j} + i y_{\pm,j}\right] , \tag{8.3}$$

where c_j is the complex coefficient associated with resonance j in the $B^0 \to \overline{D}^0 K^+\pi^-$ DP. This parameterisation was inspired by the GGSZ analyses described in Sec. 2.4.1, and is, henceforth, labelled the "nominal Cartesian" parameterisation.

Another parameterisation of interest is

$$c_j \left[1 + x_{\pm,j} + i y_{\pm,j}\right] \longrightarrow c_j \left[1 + \left(\bar{x}_j \pm \Delta x_j\right) + i\left(\bar{y}_j \pm \Delta y_j\right)\right] . \tag{8.4}$$

This allows the significance of *CP* violation to be determined based on the change in NLL when Δx_j and Δy_j are fixed to zero. This is termed the "alternative Cartesian" parameterisation. Finally, the polar "γ" parameterisation may be modified by allowing each resonance to use a separate value of γ. This is identified as the "local γ" parameterisation.

While a $b \to u$ contribution may be present in any of the $K^+\pi^-$ components, these parameterisations are only used for the $K^*(892)^0$ and $K_2^*(1430)^0$ resonances. For the $K\pi$ S-wave, there is no reason to expect the associated values of r_B and δ_B to be invariant with $m(K\pi)$. This renders these parameterisations potentially meaningless so *CP* violation in the $K\pi$ S-wave is treated separately from the other resonances. The *CP* parameters are shared between the resonant and nonresonant parts of the S-wave in the baseline fit. Separate parameters are introduced as a systematic variation. Since the $K^*(1410)$ component is not significant, it is treated

as CP conserving.

Additional contributions may also enter the $B^0 \to D_{CP}K^+\pi^-$ DP due to DK^+ resonances, for example from the $D_{s1}^*(2700)^+$ resonance. As these components are mediated purely by the $b \to u$ amplitude, they do not contribute to the $B^0 \to \overline{D}^0 K^+\pi^-$ DP. These are added to the model as necessary with complex coefficients parameterised by real and imaginary parts. CP violation in these components is considered as a source of systematic uncertainty by parameterising the B^0 and $\overline{B}^0$ coefficients independently as

$$c_{\pm,j} = X_{\pm,j} + iY_{\pm,j}\,. \tag{8.5}$$

In the baseline fit model, a $D_{s1}^*(2700)$ component is included, while the possible effects from a $D_{s2}^*(2573)$ amplitude are considered among the sources of systematic uncertainty. To reduce the risk of the $D_{s1}^*(2700)$ amplitude absorbing mismodelled $\overline{B}_s^0 \to D^{*0}K^+\pi^-$ background decays, a constraint is applied to the magnitude of this amplitude assuming:

$$\frac{\mathcal{B}(B^0 \to D_{s1}^*(2700)^+\pi^-) \times \mathcal{B}(D_{s1}^*(2700)^+ \to D^0K^+)}{\mathcal{B}(B^0 \to D_{s1}^*(2700)^+D^-) \times \mathcal{B}(D_{s1}^*(2700)^+ \to D^0K^+)} = \left(\frac{|V_{ub}|}{|V_{cb}|}\right)^2 \left(\frac{f_\pi}{f_D}\right)^2 \left(\frac{p_\pi}{p_D}\right)^2 \tag{8.6}$$

where $|V_{ub}| = 0.00355 \pm 0.00015$ and $|V_{cb}| = 0.0414 \pm 0.0012$ [3] are the CKM elements, $f_\pi = 130.2 \pm 1.4\,\text{MeV}$ and $f_D = 208 \pm 7\,\text{MeV}$ [125] are hadronic form factors, and the phase-space factor is given by the ratio of the momenta of the particles in the rest frame of the B: $p_\pi = 1942.0 \pm 2.0\,\text{MeV}$ and $p_D = 1298.4 \pm 3.4\,\text{MeV}$. Using the previously measured product branching fraction, $\mathcal{B}(B^0 \to D_{s1}^*(2700)^+D^-) \times \mathcal{B}(D_{s1}^*(2700)^+ \to D^0K^+) = (7.14 \pm 0.96 \pm 0.69) \times 10^{-4}$ [126], this leads to

$$\mathcal{B}(B^0 \to D_{s1}^*(2700)^+\pi^-) \times \mathcal{B}(D_{s1}^*(2700)^+ \to D^0K^+) = (4.6 \pm 1.0) \times 10^{-6}\,. \tag{8.7}$$

An additional 30 % uncertainty is assigned due to the assumptions made in Eq. (8.6) giving $(4.6 \pm 1.7) \times 10^{-6}$, or relative to the $D_2^*(2460)^-$ contribution determined in Chapter 7,

$$\frac{\mathcal{B}(B^0 \to D_{s1}^*(2700)^+\pi^-) \times \mathcal{B}(D_{s1}^*(2700)^+ \to D^0K^+)}{\mathcal{B}(B^0 \to D_2^*(2460)^-K^+) \times \mathcal{B}(D_2^*(2460)^- \to \overline{D}^0\pi^-)} = 0.217 \pm 0.085\,. \tag{8.8}$$

This constraint is applied in the fit. A similar constraint is evaluated for the ratio of the $D_{s2}^*(2573)^+$ contribution to the $D_{s1}^*(2700)^+$ component, which is applied when the $D_{s2}^*(2573)^+$ resonance is included.

8.4 Fit to the $B_s^0 \to DK^-\pi^+$ control sample

The larger samples of $B_s^0 \to DK^-\pi^+$ decays relative to the B^0 decay mode allow a validation of the γ fitting procedure to be performed on real data. Due to significantly larger suppression of the $b \to u$ amplitudes and a lack of overlap between the narrow $\overline{K}^*(892)^0$ and $D_{s2}^*(2573)^-$ resonances (see Fig. 6.11),[3] an analysis of the B_s^0 decay is expected to have very little sensitivity to γ.

The fit is performed simultaneously to the datasets obtained from the 15 signal regions of the πK, KK and $\pi\pi$ mass fits. These correspond to mass windows of 5335.7–5395.2 MeV/c^2, 5333.9–5397.4 MeV/c^2 and 5330.4–5398.9 MeV/c^2 for the πK, KK and $\pi\pi$ datasets, respectively. The amplitudes listed in Table 6.6 are included in the signal model for all three datasets but, for the KK and $\pi\pi$ datasets, the $\overline{K}^*(892)^0$ and $\overline{K}_2^*(1430)^0$ coefficients are parameterised as in Eq. 8.3. The background contributions and efficiency variation in each DP are modelled by histograms as in the previous analyses. For brevity, these models are not presented here. The signal and background yields determined from the mass fits are presented in Tables 8.4, 8.5 and 8.6.

Table 8.4: Yields of the fit components within $\pm 2.5\sigma$ of the fitted B_s^0 mass in the five MVA output bins for the $D \to \pi K$ dataset. Note that only the backgrounds due to comb. bkg, $B^0 \to D^{(*)}\pi\pi$ and $\overline{\Lambda}_b^0 \to D^{(*)}p\pi$ are included in the fit model.

Component	Yield					Included?
	bin 1	bin 2	bin 3	bin 4	bin 5	
$B_s^0 \to DK\pi$	1912	1962	2017	1991	1917	✓
$B^0 \to DK\pi$	0	0	0	0	0	✗
comb. bkg	813	94	28	11	4	✓
$B^0 \to D^*K\pi$	0	0	0	0	0	✗
$B_s^0 \to D^*K\pi$	3	3	3	3	2	✗
$B^0 \to D^{(*)}\pi\pi$	36	37	38	37	36	✓
$\overline{\Lambda}_b^0 \to D^{(*)}p\pi$	50	51	53	52	50	✓
$B^0 \to D^{(*)}KK$	0	0	0	0	0	✗
$B_s^0 \to D^{(*)}KK$	1	1	1	1	1	✗

The fit is repeated with the $\overline{K}^*(892)^0$ and $\overline{K}_2^*(1430)^0$ components described by each of the four parameterisations given in Section 8.3. The numerical results for the amplitude coefficients from these four fits are presented in Tables 8.7, 8.8, 8.9 and 8.10, while the values of the *CP* parameters (and various derived quantities) are

[3] As the $\overline{K}^*(892)^0$ and $D_{s2}^*(2573)^-$ resonances do not overlap in the $B_s^0 \to DK^-\pi^+$ DP, their relative phase is determined less precisely, relying on their mutual interference with other broader amplitudes.

Table 8.5: Yields of the fit components within $\pm 2.5\sigma$ of the fitted B_s^0 mass in the five MVA output bins for the $D \to KK$ dataset. Note that only the backgrounds due to comb. bkg, $B^0 \to D^{(*)}\pi\pi$ and $\overline{\Lambda}_b^0 \to D^{(*)}p\pi$ are included in the fit model.

Component	Yield					Included?
	bin 1	bin 2	bin 3	bin 4	bin 5	
$B_s^0 \to DK\pi$	189	169	182	195	174	✓
$B^0 \to DK\pi$	0	0	0	0	0	✗
comb. bkg	157	17	8	3	0	✓
$B^0 \to D^*K\pi$	0	0	0	0	0	✗
$B_s^0 \to D^*K\pi$	0	0	1	1	0	✗
$B^0 \to D^{(*)}\pi\pi$	6	6	6	6	6	✓
$\overline{\Lambda}_b^0 \to D^{(*)}p\pi$	7	7	7	8	7	✓
$\overline{\Lambda}_b^0 \to D^{(*)}pK$	1	1	1	1	1	✗
$B^0 \to D^{(*)}KK$	0	0	0	0	0	✗
$B_s^0 \to D^{(*)}KK$	0	0	0	0	0	✗

Table 8.6: Yields of the fit components within $\pm 2.5\sigma$ of the fitted B_s^0 mass in the five MVA output bins for the $D \to \pi\pi$ dataset. Note that only the backgrounds due to comb. bkg, $B^0 \to D^{(*)}\pi\pi$ and $\overline{\Lambda}_b^0 \to D^{(*)}p\pi$ are included in the fit model.

Component	Yield					Included?
	bin 1	bin 2	bin 3	bin 4	bin 5	
$B_s^0 \to DK\pi$	82	70	86	74	71	✓
$B^0 \to DK\pi$	0	0	0	0	0	✗
comb. bkg	105	15	4	3	1	✓
$B^0 \to D^*K\pi$	0	0	0	0	0	✗
$B_s^0 \to D^*K\pi$	0	1	0	0	0	✗
$B^0 \to D^{(*)}\pi\pi$	3	3	3	3	3	✓
$\overline{\Lambda}_b^0 \to D^{(*)}p\pi$	4	3	4	4	3	✓
$\overline{\Lambda}_b^0 \to D^{(*)}pK$	1	0	1	1	1	✗
$B^0 \to D^{(*)}KK$	0	0	0	0	0	✗
$B_s^0 \to D^{(*)}KK$	0	0	0	0	0	✗

given in Table 8.11 for all four fits. The four alternative parameterisations appear to give consistent results although a detailed toy study is not performed. The values obtained for the Δx_i and Δy_i parameters are consistent with zero as was expected for this decay mode.

Figure 8.12 shows mass projections of the "nominal Cartesian" fit compared to the data for the πK dataset and for the KK and $\pi\pi$ datasets combined. The NN bins have been weighted according to signal purity and combined. While some discrepancies are seen, particularly in the region of the $\overline{K}_0^*(1430)^0$ resonance, the fit

Table 8.7: Results of the "nominal Cartesian" fit to B_s^0 validation data.

	Isobar model coefficients			
Resonance	Real part	Imaginary part	Magnitude	Phase
$\overline{K}^*(892)^0$	0.22 ± 0.10	-0.86 ± 0.03	0.89	-1.32
$\overline{K}^*(1410)^0$	0.06 ± 0.04	-0.27 ± 0.03	0.28	-1.35
$\overline{K}_0^*(1430)^0$	0.26 ± 0.05	0.45 ± 0.04	0.52	1.04
LASS Non. Res.	-0.42 ± 0.07	0.64 ± 0.04	0.77	2.15
$\overline{K}_2^*(1430)^0$	-0.18 ± 0.03	-0.26 ± 0.02	0.32	-2.18
$\overline{K}^*(1680)^0$	0.13 ± 0.03	0.06 ± 0.03	0.15	0.45
$\overline{K}_0^*(1950)^0$	0.14 ± 0.03	0.15 ± 0.03	0.21	0.82
$D_{s2}^*(2573)^-$	1.00 ± 0.00	0.00 ± 0.00	1.00	0.00
$D_{s1}^*(2700)^-$	-0.06 ± 0.02	0.09 ± 0.02	0.11	2.14
$D_{s1}^*(2860)^-$	0.02 ± 0.03	-0.08 ± 0.03	0.08	-1.30
$D_{s3}^*(2860)^-$	0.17 ± 0.03	-0.15 ± 0.03	0.23	-0.75
Nonresonant	0.97 ± 0.06	-1.10 ± 0.06	1.46	-0.85
D_{sv}^{*-}	0.64 ± 0.03	0.54 ± 0.03	0.84	0.70
$D_{s0v}^*(2317)^-$	0.45 ± 0.06	-0.94 ± 0.04	1.04	-1.13
B_v^{*+}	-0.37 ± 0.05	-0.48 ± 0.06	0.61	-2.23

Table 8.8: Results of the "alternative Cartesian" fit to B_s^0 validation data.

	Isobar model coefficients			
Resonance	Real part	Imaginary part	Magnitude	Phase
$\overline{K}^*(892)^0$	0.22 ± 0.09	-0.86 ± 0.03	0.89	-1.32
$\overline{K}^*(1410)^0$	0.06 ± 0.04	-0.27 ± 0.03	0.28	-1.35
$\overline{K}_0^*(1430)^0$	0.26 ± 0.05	0.45 ± 0.04	0.52	1.04
LASS Non. Res.	-0.42 ± 0.07	0.64 ± 0.04	0.77	2.15
$\overline{K}_2^*(1430)^0$	-0.18 ± 0.03	-0.26 ± 0.02	0.32	-2.18
$\overline{K}^*(1680)^0$	0.13 ± 0.03	0.06 ± 0.03	0.15	0.45
$\overline{K}_0^*(1950)^0$	0.14 ± 0.03	0.15 ± 0.03	0.21	0.82
$D_{s2}^*(2573)^-$	1.00 ± 0.00	0.00 ± 0.00	1.00	0.00
$D_{s1}^*(2700)^-$	-0.06 ± 0.02	0.09 ± 0.02	0.11	2.14
$D_{s1}^*(2860)^-$	0.02 ± 0.03	-0.08 ± 0.03	0.08	-1.30
$D_{s3}^*(2860)^-$	0.17 ± 0.03	-0.15 ± 0.03	0.23	-0.75
Nonresonant	0.97 ± 0.06	-1.10 ± 0.06	1.46	-0.85
D_{sv}^{*-}	0.64 ± 0.03	0.54 ± 0.03	0.84	0.70
$D_{s0v}^*(2317)^-$	0.45 ± 0.06	-0.94 ± 0.04	1.04	-1.13
B_v^{*+}	-0.37 ± 0.05	-0.48 ± 0.06	0.61	-2.23

quality is sufficient to confirm that the framework to obtain γ from a simultaneous fit to 15 DPs is working as expected. The amplitudes of the *CP* parameters obtained from this fit are visualised in Fig. 8.13 and compared to the values determined from the other three parameterisations in Fig. 8.14.

Table 8.9: Results of the "γ" fit to B_s^0 validation data.

	Isobar model coefficients			
Resonance	Real part	Imaginary part	Magnitude	Phase
$\overline{K}^*(892)^0$	0.22 ± 0.09	-0.86 ± 0.03	0.89	-1.32
$\overline{K}^*(1410)^0$	0.06 ± 0.04	-0.27 ± 0.03	0.28	-1.34
$\overline{K}_0^*(1430)^0$	0.26 ± 0.05	0.45 ± 0.04	0.52	1.04
LASS Non. Res.	-0.42 ± 0.07	0.64 ± 0.04	0.77	2.15
$\overline{K}_2^*(1430)^0$	-0.18 ± 0.03	-0.26 ± 0.02	0.32	-2.18
$\overline{K}^*(1680)^0$	0.13 ± 0.03	0.06 ± 0.03	0.15	0.46
$\overline{K}_0^*(1950)^0$	0.14 ± 0.03	0.15 ± 0.03	0.21	0.82
$D_{s2}^*(2573)^-$	1.00 ± 0.00	0.00 ± 0.00	1.00	0.00
$D_{s1}^*(2700)^-$	-0.06 ± 0.02	0.09 ± 0.02	0.11	2.14
$D_{s1}^*(2860)^-$	0.02 ± 0.03	-0.08 ± 0.03	0.08	-1.30
$D_{s3}^*(2860)^-$	0.17 ± 0.03	-0.15 ± 0.03	0.23	-0.75
Nonresonant	0.97 ± 0.06	-1.10 ± 0.06	1.47	-0.84
D_{sv}^{*-}	0.64 ± 0.03	0.54 ± 0.03	0.84	0.70
$D_{s0v}^*(2317)^-$	0.45 ± 0.06	-0.94 ± 0.04	1.04	-1.13
B_v^{*+}	-0.37 ± 0.05	-0.48 ± 0.06	0.61	-2.23

Table 8.10: Results of the "local γ" fit to B_s^0 validation data.

	Isobar model coefficients			
Resonance	Real part	Imaginary part	Magnitude	Phase
$\overline{K}^*(892)^0$	0.23 ± 0.10	-0.86 ± 0.03	0.89	-1.31
$\overline{K}^*(1410)^0$	0.06 ± 0.04	-0.27 ± 0.03	0.28	-1.34
$\overline{K}_0^*(1430)^0$	0.26 ± 0.05	0.45 ± 0.04	0.52	1.05
LASS Non. Res.	-0.42 ± 0.07	0.64 ± 0.04	0.77	2.15
$\overline{K}_2^*(1430)^0$	-0.18 ± 0.03	-0.26 ± 0.02	0.32	-2.18
$\overline{K}^*(1680)^0$	0.13 ± 0.03	0.06 ± 0.03	0.15	0.45
$\overline{K}_0^*(1950)^0$	0.14 ± 0.03	0.15 ± 0.03	0.21	0.82
$D_{s2}^*(2573)^-$	1.00 ± 0.00	0.00 ± 0.00	1.00	0.00
$D_{s1}^*(2700)^-$	-0.06 ± 0.02	0.09 ± 0.02	0.11	2.14
$D_{s1}^*(2860)^-$	0.02 ± 0.03	-0.08 ± 0.03	0.08	-1.30
$D_{s3}^*(2860)^-$	0.17 ± 0.03	-0.15 ± 0.03	0.23	-0.74
Nonresonant	0.98 ± 0.06	-1.10 ± 0.06	1.47	-0.84
D_{sv}^{*-}	0.64 ± 0.03	0.54 ± 0.03	0.84	0.70
$D_{s0v}^*(2317)^-$	0.45 ± 0.06	-0.94 ± 0.04	1.04	-1.13
B_v^{*+}	-0.37 ± 0.05	-0.48 ± 0.06	0.61	-2.23

All four parameterisations yield NLL values that differ by less than one unit, further suggesting that the same results have been obtained with all four fits. The two Cartesian parameterisations produce identical results. This is expected as the possible values of the parameters cover the same phase space. The best secondary

Table 8.11: *CP* parameters obtained with each of the four alternative parameterisations. Uncertainties are from the fit. Quantities without uncertainties have been derived for comparison. $\phi_\pm = \delta_B \pm \gamma$. All phases are measured in radians.

	Value			
Quantity	Nominal Cartesian fit	Alternative Cartesian fit	γ fit	Local γ fit
		$\overline{K}^*(892)^0$		
γ	0.17	0.17	0.38 ± 0.40	0.21 ± 0.21
δ_B	-1.24	-1.24	-1.17 ± 0.67	-1.27 ± 0.54
r_B	0.09	0.09	0.07 ± 0.07	0.09 ± 0.08
x_{+i}	0.05 ± 0.05	0.05	0.05	0.04
x_{-i}	0.01 ± 0.05	0.01	0.00	0.01
y_{+i}	-0.08 ± 0.11	-0.08	-0.05	-0.08
y_{-i}	-0.08 ± 0.12	-0.08	-0.07	-0.09
$\bar{x}_i$	0.03	0.03 ± 0.04	0.03	0.03
Δx_i	0.02	0.02 ± 0.03	0.03	0.02
$\bar{y}_i$	-0.08	-0.08 ± 0.08	-0.06	-0.08
Δy_i	-0.00	-0.00 ± 0.08	0.01	0.01
ϕ_+	-1.07	-1.07	-0.79	-1.06
ϕ_-	-1.41	-1.41	-1.56	-1.47
		$\overline{K}_2^*(1430)^0$		
γ	0.42	0.42	0.38 ± 0.40	0.49 ± 0.49
δ_B	-1.97	-1.97	-2.00 ± 0.45	-2.05 ± 0.43
r_B	0.39	0.39	0.38 ± 0.14	0.38 ± 0.14
x_{+i}	0.01 ± 0.21	0.01	-0.02	0.00
x_{-i}	-0.18 ± 0.22	-0.18	-0.27	-0.32
y_{+i}	-0.52 ± 0.20	-0.52	-0.38	-0.38
y_{-i}	-0.17 ± 0.19	-0.17	-0.26	-0.22
$\bar{x}_i$	-0.08	-0.08 ± 0.15	-0.15	-0.16
Δx_i	0.10	0.10 ± 0.14	0.13	0.16
$\bar{y}_i$	-0.35	-0.35 ± 0.14	-0.32	-0.30
Δy_i	-0.18	-0.18 ± 0.13	-0.06	-0.08
ϕ_+	-1.55	-1.55	-1.61	-1.56
ϕ_-	-2.39	-2.39	-2.38	-2.55

minimum in each case has a 2ΔLL of around 18 units. As these minima are well separated we do not consider them further.

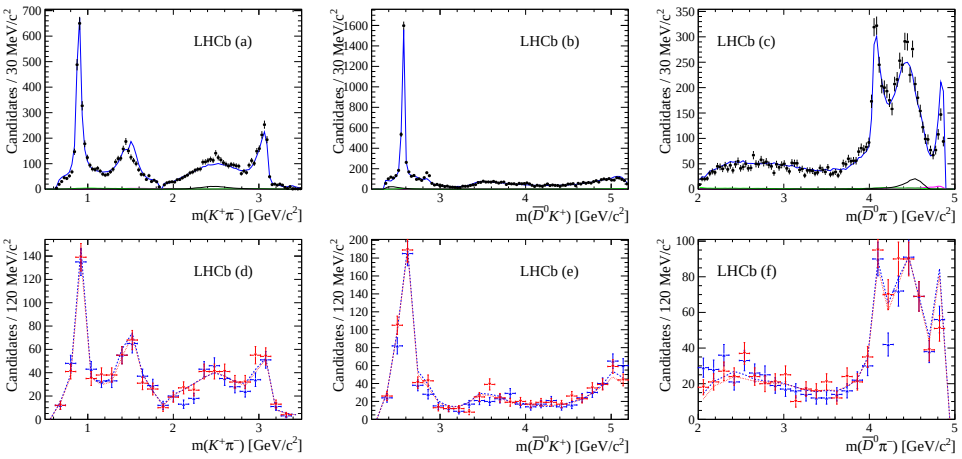

Figure 8.12: Invariant mass projections of the B_s^0, $D \to \pi K$ dataset and the DP fit result onto (a) $m(K^+\pi^-)$, (b) $m(\overline{D}^0 K^+)$ and (c) $m(\overline{D}^0\pi^-)$. The same projections are shown for the combined KK and $\pi\pi$ datasets in (d), (e) and (f). The NN bins have been weighted according to signal purity and combined. For the $K\pi$ dataset, the full fit is shown in blue, background from combinatorics, $B^0 \to D\pi\pi$ and $\Lambda_b^0 \to D\overline{p}\pi^+$ in magenta, green and black, respectively, and the data are shown as black points. For the combined KK and $\pi\pi$ datasets, separate distributions for (blue) B_s^0 and (red) $\overline{B}_s^0$ decays are shown.

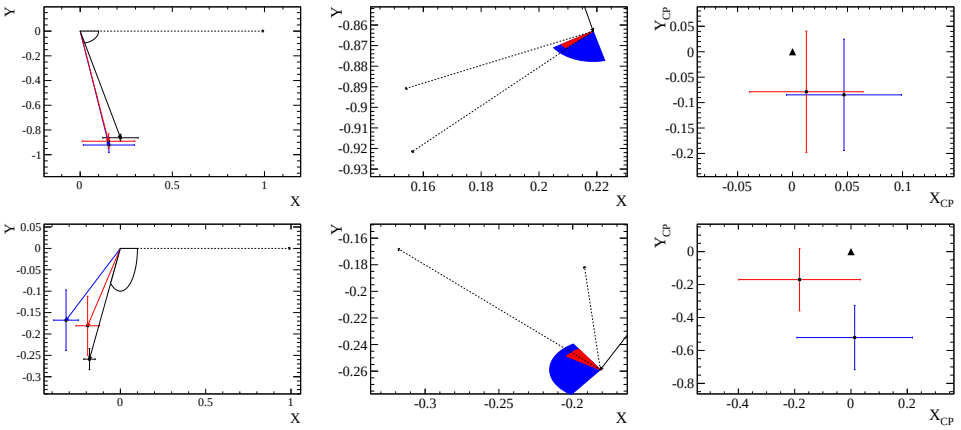

Figure 8.13: (Left) Amplitudes of (black) $B_s^0 \to \overline{D}^0\overline{K}^{*0}$, (blue) $B_s^0 \to D\overline{K}^{*0}$ and (red) $\overline{B}_s^0 \to DK^{*0}$ decays relative to the reference $B_s^0 \to D_{s2}^*(2573)^-\pi^+$ amplitude, showing the relative phase Δ. (Middle) zoom showing the additional CP-violating amplitudes of $B_s^0 \to D\overline{K}^{*0}$ and $\overline{B}_s^0 \to DK^{*0}$ decays relative to the $B_s^0 \to \overline{D}^0\overline{K}^{*0}$ amplitude. Also shown are the strong and weak phases (blue) δ and (red) γ as determined from these amplitudes. (Right) the Cartesian CP parameters (blue) (x_+, y_+) and (red) (x_-, y_-). Plots show the parameters of the (top) $\overline{K}^*(892)^0$ and (bottom) $\overline{K}_2^*(1430)^0$ resonances.

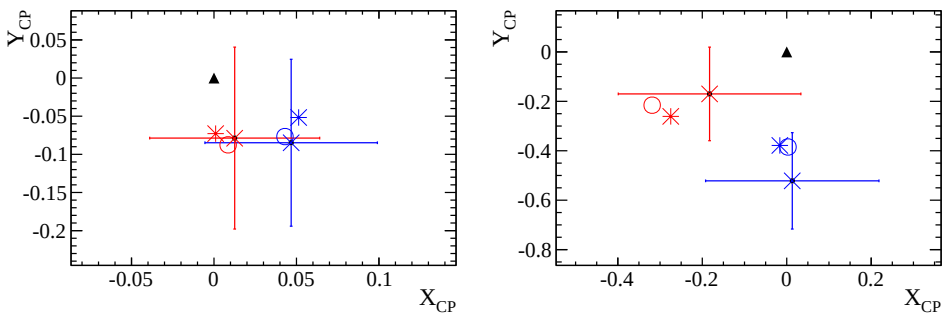

Figure 8.14: The Cartesian *CP* parameters, (blue) (x_+, y_+) and (red) (x_-, y_-), from the nominal B_s^0 fit relative to those derived from the results of the ($\times$) "alternative Cartesian", ($*$) "γ" and ($\circ$) "local γ" parameterisations.

8.5 Fit to determine γ

8.5.1 Efficiency variation and background distributions

The efficiency with which signal decays can be reconstructed and selected across the phase space is described following the same procedure introduced in Sec. 6.3. Each component of the efficiency is evaluated separately for each of the three decay channels. All efficiency components are shared between the five NN bins — in principle selection and PID efficiencies may vary between bins but the differences are seen to be negligible compared to the statistical fluctuations introduced by the reduced statistics.

Of the backgrounds included in the mass fits, only those with significant contributions within the signal window are included in the fit to the DPs. Summaries of the included components are given for each of the decay channels in Tables 8.13, 8.14 and 8.15. As the NNs are trained to remove combinatorial background candidates, the distribution of the combinatorial and partial combinatorial backgrounds may vary between MVA bins. Due to limited statistics, only two distributions are used — one for the least pure bin and another for the remaining four bins. The distributions of the remaining backgrounds are found to be independent of the MVA bin so a single distribution is used for each background. The most critical background in the fit is due to $B_s^0 \to D^* K^- \pi^+$ decays, which enters the signal region in the KK and $\pi\pi$ mass fits and is not discriminated against by the NNs. The procedure for modelling this background is described in Sec. 8.2.2 and the distributions used to model this background in the signal regions of the KK and $\pi\pi$ datasets are shown in Fig. 8.15.

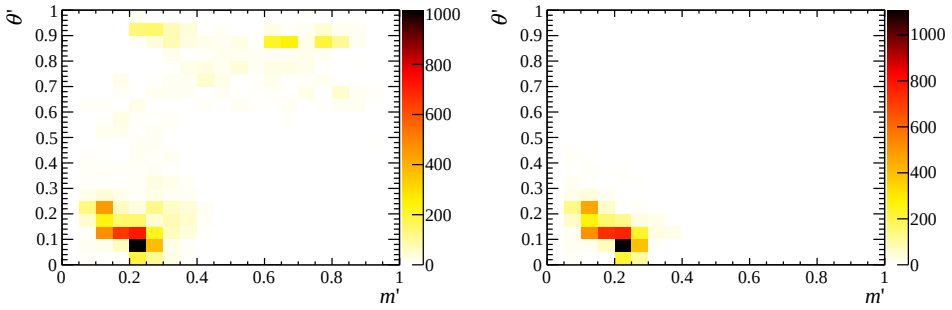

Figure 8.15: Distribution of the $B_s^0 \to D^* K^- \pi^+$ background to the (a) KK and (b) $\pi\pi$ datasets in the SDP variables.

8.5.2 The fit to data

The signal and background yields within the signal regions defined by the mass fits are listed for each dataset in Tables 8.13, 8.14 and 8.15. These samples correspond to mass windows of 5246.6–5309.9 MeV/c^2, 5246.9–5310.5 MeV/c^2 and 5243.1–5312.3 MeV/c^2 for the $K\pi$, KK and $\pi\pi$ datasets, respectively. The fit to data is performed using all five bins of the KK and $\pi\pi$ datasets and the four purest bins of the $K\pi$ dataset. In preliminary fits to 15 DPs, the large combinatoric backgrounds in bin 1 of the $K\pi$ dataset were found to be inadequately modelled. As this DP does not significantly contribute to the precision with which γ can be measured, fits are instead performed to the 14 other DPs.

As with the previous DP fits, the signal and background yields in this fit are fixed, while the parameters of the complex coefficients are determined from the fit. The shape parameters of the LASS and EFF components are floated again, while the masses and widths of the $D\pi^-$ resonances that were previously floated in Chapter 7 are constrained to the averages listed in Table 8.12.

Table 8.12: Measurements of the masses and widths of charmed resonances used to determine the constraints on these quantities. Units of MeV are implied.

$D_2^*(2460)$ mass	$D_2^*(2460)$ width	$D_0^*(2400)$ mass	$D_0^*(2400)$ width	Reference
2464.3 ± 1.6	37 ± 6	2403 ± 40	283 ± 40	[3]
2463.1 ± 0.6	48.6 ± 2.3			[127]
2468.6 ± 0.7	47.3 ± 1.6	2349 ± 7	217 ± 18	[103]
2465.6 ± 2.2	46.0 ± 4.7	2360 ± 34	255 ± 57	[87]
2465.4 ± 0.4	47.1 ± 1.2	2351.0 ± 6.8	230.2 ± 15.8	

Due to the large number of free parameters in the fit, it is necessary to perform a two-stage fit. The shape parameters of the LASS and EFF components are floated in the first stage, while the *CP* violation in the $K\pi$ S-wave is fixed to zero. In the second stage of the fit, the *CP* parameters of the $K\pi$ S-wave are free parameters but the shape parameters are fixed to the values obtained in the first stage.

The "nominal Cartesian" parameters are used to describe *CP* violation in the $K^*(892)^0$ and $K_2^*(1430)^0$ resonances. As described previously, the fitter reports the values of these parameters after applying an offset — termed blinding. Each parameter is blinded using a separate "blinding string". The string is used to produce a hash, which in turn is used to seed a random number generator. A random number is then sampled from a Gaussian distribution to act as the offset, where the half-width of the distribution is chosen to be $\sim 10\,\%$ of the parameters allowed range in the

Table 8.13: Yields of the fit components within $\pm 2.5\sigma$ of the fitted B^0 mass in the five MVA output bins for the $D \to K\pi$ dataset. Note that only the backgrounds due to comb. bkg, $B^+ \to D^*K$, $B^0 \to D^{(*)}\pi\pi$ and $\overline{\Lambda}_b^0 \to D^{(*)}pK$ are included in the fit model.

Component	Yield					Included?
	bin 1	bin 2	bin 3	bin 4	bin 5	
$B^0 \to DK\pi$	597	546	585	571	540	✓
$B_s^0 \to DK\pi$	1	1	1	1	1	✗
comb. bkg	540	58	16	6	1	✓
part. comb. bkg	305	33	9	3	1	✓
$B^0 \to D^*K\pi$	1	1	1	1	1	✗
$B^0 \to D^{(*)}\pi\pi$	20	18	20	19	18	✓
$\Lambda_b^0 \to D^{(*)}pK$	21	19	21	20	19	✓
$B^0 \to D^{(*)}KK$	8	7	8	7	7	✗
$B_s^0 \to D^{(*)}KK$	10	9	10	10	9	✗

Table 8.14: Yields of the fit components within $\pm 2.5\sigma$ of the fitted B^0 mass in the five MVA output bins for the $D \to KK$ dataset. Note that only the backgrounds due to comb. bkg, $B_s^0 \to D^*K\pi$, $B^0 \to D^{(*)}\pi\pi$ and $\overline{\Lambda}_b^0 \to D^{(*)}p\pi$ are included in the fit model.

Component	Yield					Included?
	bin 1	bin 2	bin 3	bin 4	bin 5	
$B^0 \to DK\pi$	70	63	68	73	65	✓
$B_s^0 \to DK\pi$	5	5	5	6	5	✓
comb. bkg	173	19	9	3	0	✓
$B^0 \to D^*K\pi$	0	1	1	1	0	✗
$B_s^0 \to D^*K\pi$	19	28	34	28	20	✓
$B^0 \to D^{(*)}\pi\pi$	4	3	4	4	3	✓
$\Lambda_b^0 \to D^{(*)}p\pi$	11	10	10	11	10	✓
$\Lambda_b^0 \to D^{(*)}pK$	2	1	2	2	2	✗
$B^0 \to D^{(*)}KK$	2	1	2	2	1	✗
$B_s^0 \to D^{(*)}KK$	1	1	1	2	1	✗

fit. These quantities were only "unblinded" once the fit model had been finalised and all systematic uncertainties had been evaluated. Furthermore, the B^0 and $\overline{B}^0$ components of the mass fit were not observed separately until the fit model had been finalised.

The values obtained for the complex coefficients, the unblinded *CP* parameters and the shape parameters are shown in Tables 8.16, 8.17 and 8.18, respectively. The results are generally consistent with those in Table 7.16, obtained from the dedicated DP analysis of $B^0 \to \overline{D}^0 K^+\pi^-$ decays, however, some small discrepancies are seen — primarily in the fit fractions for the $K^*(892)^0$, $K_0^*(1430)^0$ and $D_0^*(2400)^-$ components.

Table 8.15: Yields of the fit components within $\pm 2.5\sigma$ of the fitted B^0 mass in the five MVA output bins for the $D \to \pi\pi$ dataset. Note that only the backgrounds due to comb. bkg, $B^0_s \to D^* K\pi$, $B^0 \to D^{(*)}\pi\pi$ and $\overline{\Lambda}^0_b \to D^{(*)} p\pi$ are included in the fit model.

Component	Yield					Included?
	bin 1	bin 2	bin 3	bin 4	bin 5	
$B^0 \to DK\pi$	36	31	38	32	31	✓
$B^0_s \to DK\pi$	3	2	3	3	2	✓
comb. bkg	119	17	4	3	2	✓
$B^0 \to D^* K\pi$	0	0	0	0	0	✗
$B^0_s \to D^* K\pi$	9	16	15	12	10	✓
$B^0 \to D^{(*)}\pi\pi$	2	2	2	2	2	✓
$\overline{\Lambda}^0_b \to D^{(*)} p\pi$	6	5	6	5	5	✓
$\overline{\Lambda}^0_b \to D^{(*)} pK$	1	1	1	1	1	✗
$B^0 \to D^{(*)} KK$	1	1	1	1	1	✗
$B^0_s \to D^{(*)} KK$	1	1	1	1	1	✗

These differences are understood and are due to changes in the selection, which are required for the D_{CP} datasets and detailed in Sec. 8.1. These additional requirements lead to a relatively low overlap between the old and new datasets of around 60 %. Furthermore, the different selection results in changes to the result of the mass fit, which in particular gives changes in the amount of combinatorial background in the signal window. This feeds into the S-wave components, and has a knock-on effect on the other components, as their fit fractions tend to reduce when the S-wave fit fractions increase (in the absence of any new interference effects); this is most visible for the $K^*(892)^0$. These differences do not have a significant effect on the parameters of interest for a measurement of γ.

Projections of the fit PDF and data into the two-body invariant masses are shown in Fig. 8.16 for the $K\pi$ dataset and Fig. 8.17 for the combined KK and $\pi\pi$ datasets. The NN bins have been weighted according to signal purity and combined. The projections of the KK and $\pi\pi$ datasets are also shown separately for B^0 and $\overline{B}^0$ decays in Fig. 8.18. A discrepancy between the fit model and the data is seen in the low $m(\overline{D}^0 K^+)$ region KK and $\pi\pi$ datasets. This is due to a limited understanding of the DP distribution of the background from $B^0_s \to D^* K\pi$ decays. As this region of the DP dos not overlap with the K^{**} resonances, the effect of this mis-modelling on the determination of γ is small. Nevertheless, a systematic uncertainty is assigned to account for this effect. The central values and statistical uncertainties of the Cartesian *CP* parameters are shown in Fig. 8.19.

Table 8.16: Results for the complex coefficients from the fit to data. Uncertainties are statistical only.

		Isobar model coefficients			
Resonance	Fit frac. ($K\pi$)	Real part	Imaginary part	Magnitude	Phase
$K^*(892)^0$	31.0	-0.07 ± 0.10	-1.19 ± 0.04	1.19	-1.63
$K^*(1410)^0$	1.5	0.16 ± 0.04	0.21 ± 0.06	0.26	0.90
$K_0^*(1430)^0$	13.2	0.40 ± 0.08	0.67 ± 0.06	0.78	1.03
LASS Non. Res.	13.3	0.37 ± 0.07	0.69 ± 0.07	0.78	1.08
$K_2^*(1430)^0$	5.1	-0.01 ± 0.06	-0.48 ± 0.04	0.48	-1.60
$D_0^*(2400)^-$	27.3	-1.10 ± 0.05	-0.18 ± 0.07	1.12	-2.98
$D_2^*(2460)^-$	21.9	1.00	0.00	1.00	0.00
Nonresonant $D\pi$ S-wave	4.2	-0.44 ± 0.06	0.02 ± 0.07	0.44	3.09
Nonresonant $D\pi$ P-wave	8.2	-0.61 ± 0.05	-0.08 ± 0.06	0.61	-3.00
$D_{s1}^*(2700)^+$		0.57 ± 0.05	-0.09 ± 0.19	0.58	-0.16

Table 8.17: Results for the *CP* parameters from the fit to data. Uncertainties are statistical only.

Quantity	Value
$K^*(892)^0$	
x_{+i}	0.05 ± 0.16
x_{-i}	-0.01 ± 0.13
y_{+i}	-0.48 ± 0.28
y_{-i}	-0.30 ± 0.26
$K_2^*(1430)^0$	
x_{+i}	-0.27 ± 0.36
x_{-i}	-0.90 ± 0.49
y_{+i}	-0.38 ± 0.35
y_{-i}	0.35 ± 0.28

Table 8.18: Results for the shape parameters from the fit to data. Uncertainties are statistical only.

Component	Parameter	Value
LASS	m	1.487 ± 0.020
	Γ	0.337 ± 0.067
	a	3.1 ± 0.7
	r	0.0 ± 0.1
EFF	α	0.50 ± 0.06

8.5.3 Validation of the fit for Cartesian parameters

To establish statistical uncertainties and search for any fit biases, an ensemble of toy datasets are generated based on the fit model. These datasets are generated directly by the fitter so are based on the true blinded values of the *CP* parameters.

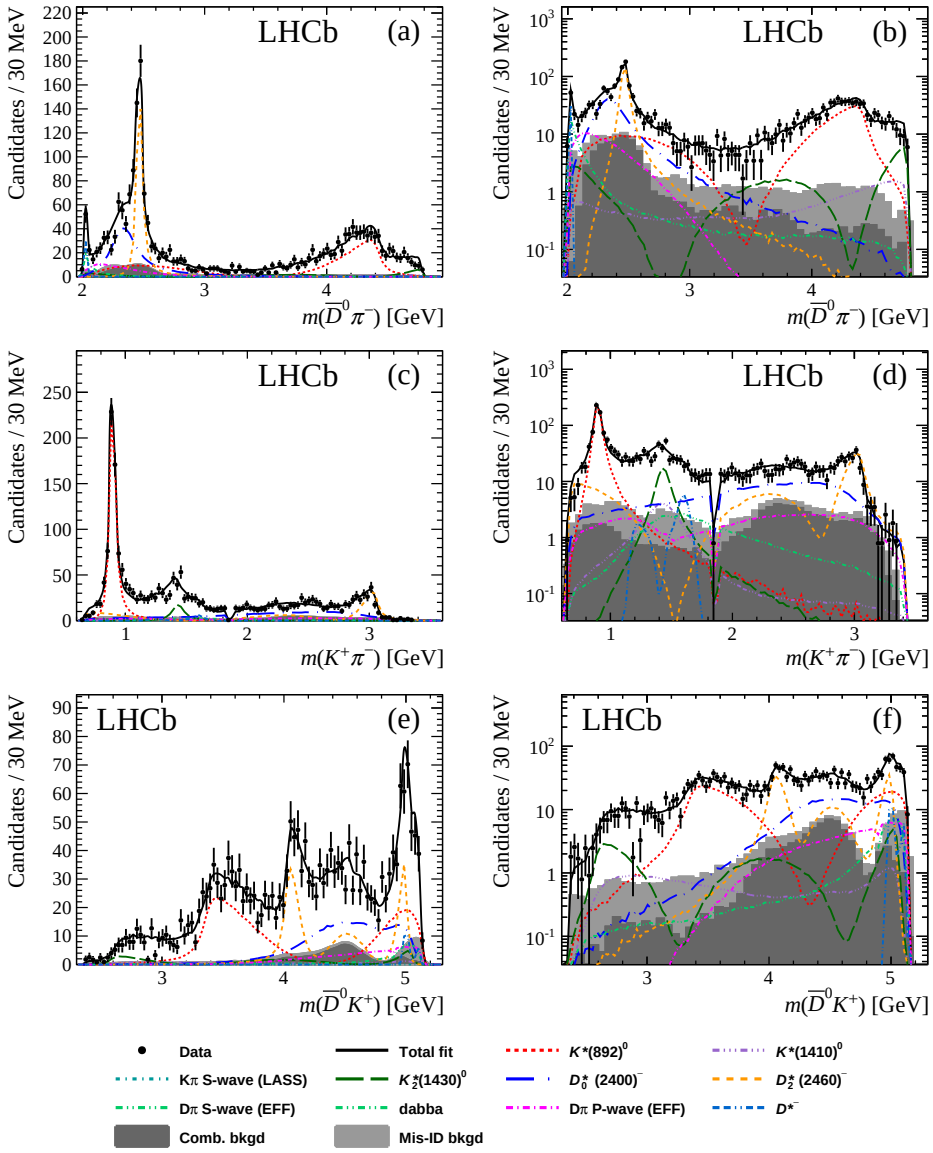

Figure 8.16: Invariant mass projections of the $K\pi$ dataset and the DP fit result onto (a) $m(\overline{D}^0\pi^-)$, (c) $m(K^+\pi^-)$ and (e) $m(\overline{D}^0K^+)$. The same projections are shown on a logarithmic y-scale in (b), (d) and (f). The NN bins have been weighted according to signal purity and combined. The fit components are shown as described in the legend.

Each toy is fit using the same fit model and the same blinding strings to enable fit biases to be determined prior to unblinding. For each parameter, the distribution of values returned by the toys is fitted with a Gaussian function and the width of the Gaussian is taken as the statistical uncertainty on that parameter. The fit bias is determined as the difference between the generated and fitted central values, while the systematic uncertainty assigned due to fit bias is obtained as the quadratic sum

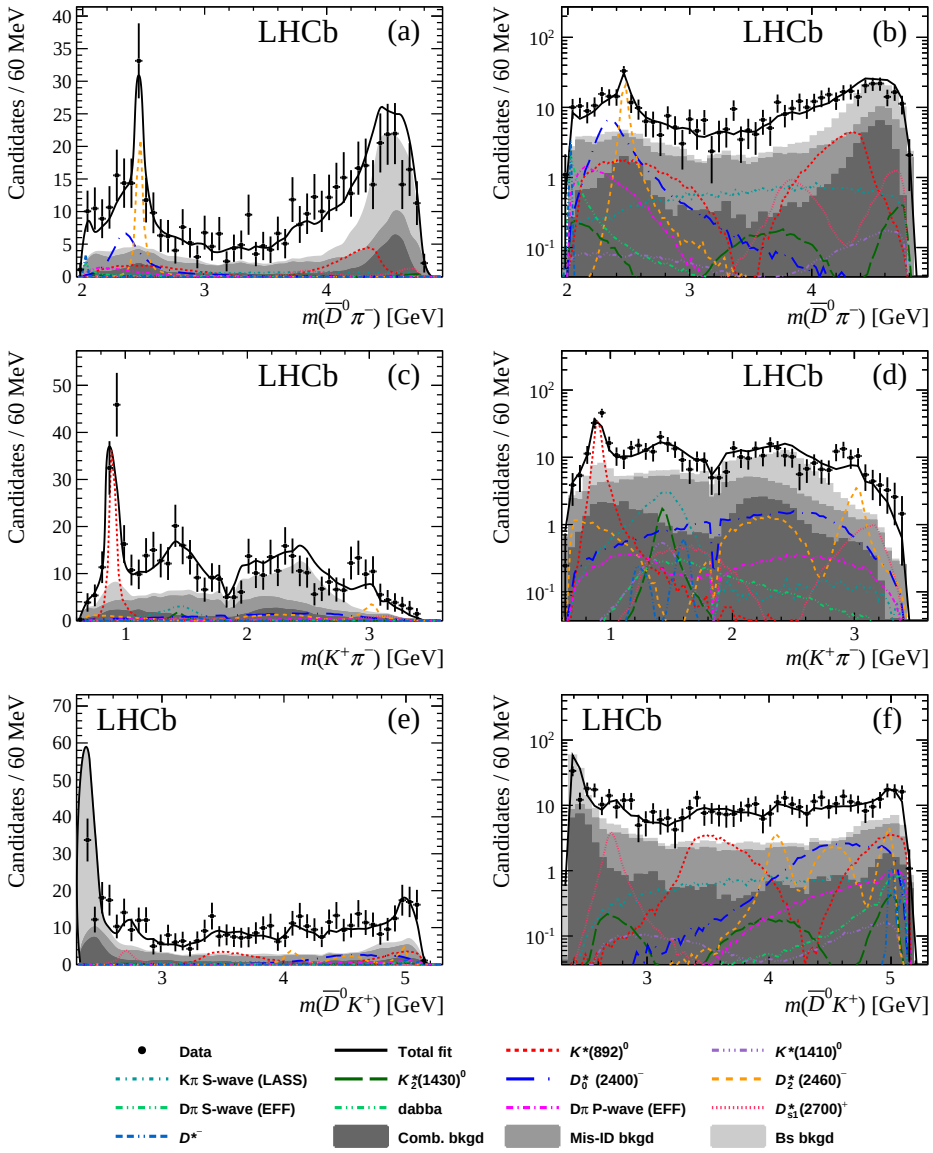

Figure 8.17: Invariant mass projections of the KK and $\pi\pi$ datasets and the DP fit result onto (a) $m(\overline{D}^0\pi^-)$, (c) $m(K^+\pi^-)$ and (e) $m(\overline{D}^0K^+)$. The same projections are shown on a logarithmic y-scale in (b), (d) and (f). The NN bins have been weighted according to signal purity and combined. The fit components are shown as described in the legend.

of the measured bias with the uncertainty on the central value from the Gaussian fit. Note that these are the same procedures introduced in Chapter 6.

Both the central values and uncertainties obtained for the *CP* parameters from data and the toy study are compared in Table 8.19. Also shown is the fit bias on each parameter including its uncertainty. No significant bias is seen on any of the *CP* parameters; moreover, the central values of the obtained biases are all small

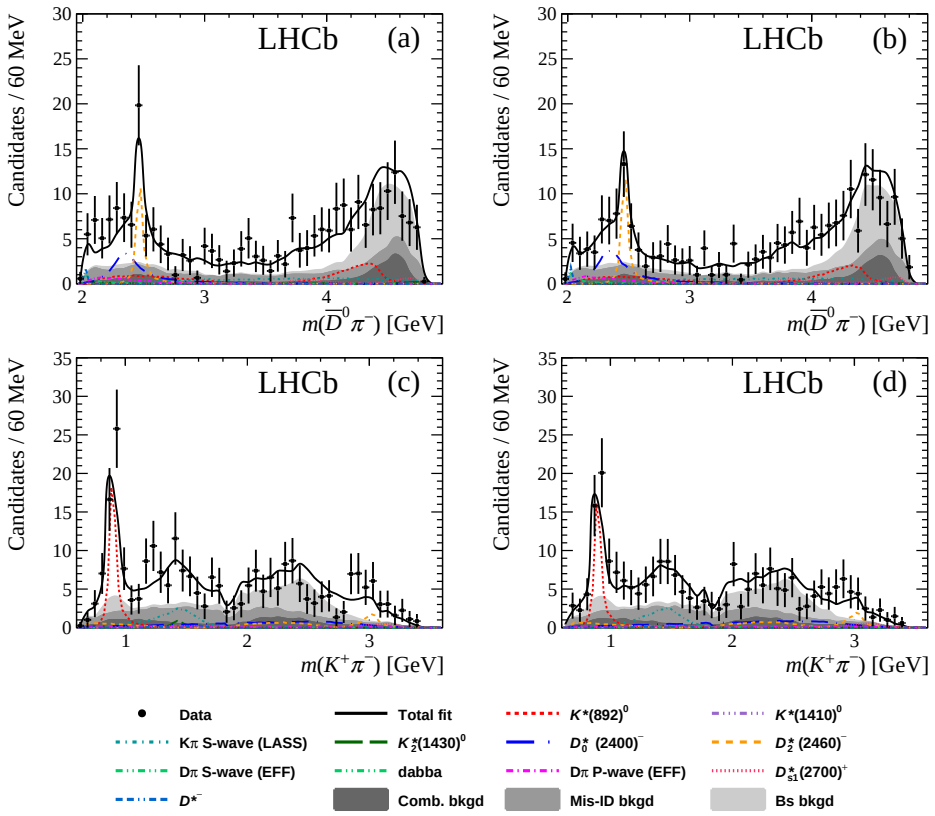

Figure 8.18: Invariant mass projections for (a and c) B^0 and (b and d) $\overline{B}^0$ decays from the KK and $\pi\pi$ datasets. The NN bins have been weighted according to signal purity and combined. The fit components are shown as described in the legend.

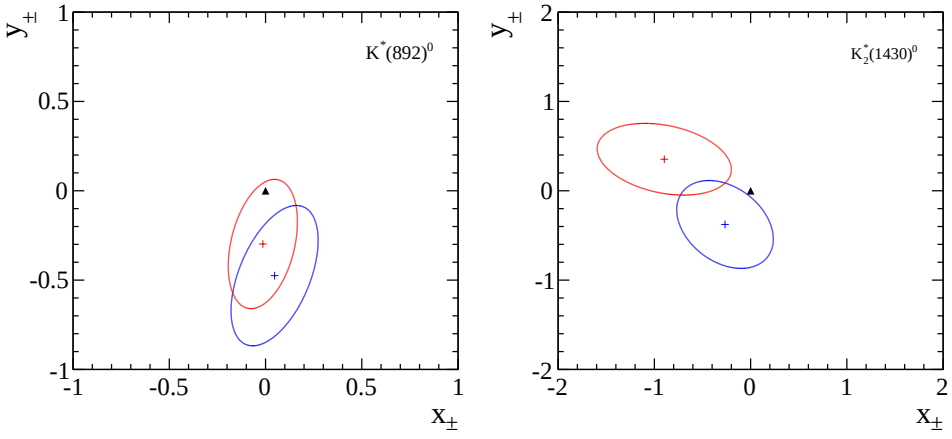

Figure 8.19: The Cartesian CP parameters, (blue) (x_+, y_+) and (red) (x_-, y_-), for the (left) $K^*(892)^0$ and (right) $K_2^*(1430)^0$ resonances determined from the fit to data. The statistical uncertainties and their correlations are shown as ellipses.

compared to the statistical uncertainties. While the uncertainties obtained from the fit are generally in good agreement with those determined from the toy study, as in previous chapters, the values from the toy study will be used when quoting the final results.

Table 8.19: Comparison of the values of the *CP* parameters obtained from data and the values obtained by fitting a Gaussian to the results of an ensemble of toy datasets. Also shown is the fit bias which is determined as the difference between the two central values. Note that the central values shown have been blinded.

Parameter	Data result (blind)	Toy result (blind)	Difference
		$K^*(892)^0$	
x_{+i}	-0.74 ± 0.15	-0.70 ± 0.20	0.034 ± 0.024
x_{-i}	0.70 ± 0.20	0.68 ± 0.27	-0.022 ± 0.036
y_{+i}	-1.60 ± 0.29	-1.65 ± 0.41	-0.043 ± 0.060
y_{-i}	-1.62 ± 0.21	-1.68 ± 0.27	-0.056 ± 0.032
		$K_2^*(1430)^0$	
x_{+i}	-0.90 ± 0.39	-0.91 ± 0.43	-0.010 ± 0.057
x_{-i}	-1.15 ± 0.36	-1.22 ± 0.46	-0.078 ± 0.059
y_{+i}	0.79 ± 0.45	0.81 ± 0.54	0.013 ± 0.066
y_{-i}	-1.69 ± 0.46	-1.76 ± 0.61	-0.072 ± 0.098

8.6 Systematic uncertainties

Systematic uncertainties on the γ-sensitive quantities are classified as follows. As the previous chapters, it is convenient to consider experimental systematics and model uncertainties separately. Additionally, it is useful to further distinguish between *CP*-conserving sources of uncertainty and sources that may lead to *CP* asymmetries. The *CP*-conserving sources of uncertainty evaluated are the same as those in Sections 6.6 and 7.4 so these are not described in detail here. One additional uncertainty that was not considered in the previous chapters is due to the lack of a reliable model of the DP distribution of $B_s^0 \to D^* K \pi$ decays. To account for this, the sizes of the $D_{s1}(2536)^-$ and $D_{s2}^*(2573)^-$ contributions to the model are varied according to the uncertainties from the $B^0 \to \overline{D}^{*0}\pi^+\pi^-$ model [98]. The uncertainties on the *CP* parameters due to *CP*-conserving sources are given in Tables 8.20 and 8.21 for experimental and model uncertainties, respectively.

Table 8.20: *CP*-conserving experimental systematic uncertainties on the *CP* parameters.

Parameter	Uncertainty				
	S/B frac.	Eff.	Bkgd	Fit bias	Total
		$K^*(892)^0$			
x_{+i}	0.010	0.035	0.046	0.021	0.062
x_{-i}	0.026	0.028	0.063	0.019	0.076
y_{+i}	0.019	0.042	0.122	0.066	0.146
y_{-i}	0.024	0.022	0.054	0.035	0.072
		$K_2^*(1430)^0$			
x_{+i}	0.026	0.040	0.174	0.116	0.215
x_{-i}	0.038	0.029	0.172	0.189	0.260
y_{+i}	0.034	0.057	0.135	0.043	0.157
y_{-i}	0.055	0.059	0.123	0.059	0.159

Table 8.21: *CP*-conserving model uncertainties on the *CP* parameters.

Parameter	Uncertainty			
	Fixed params	Add/remove	Alt. models	Total
		$K^*(892)^0$		
x_{+i}	0.027	0.028	0.068	0.078
x_{-i}	0.030	0.034	0.076	0.089
y_{+i}	0.075	0.061	0.131	0.163
y_{-i}	0.040	0.066	0.255	0.267
		$K_2^*(1430)^0$		
x_{+i}	0.043	0.054	0.032	0.076
x_{-i}	0.031	0.296	1.856	1.880
y_{+i}	0.029	0.039	0.096	0.108
y_{-i}	0.052	0.452	0.724	0.855

8.6.1 *CP*-violating experimental systematic uncertainties

The *CP*-violating experimental systematic uncertainties on the *CP* parameters are listed in Table 8.22. The various sources of these uncertainties are detailed in the following sections.

Asymmetries in the background yields

The mass fits used to extract signal and background yields do not account for possible asymmetries between B^0 and $\overline{B}^0$ decays. Separate fits are performed to the mass spectra of B^0 and $\overline{B}^0$ candidates to evaluate the level of asymmetry seen in each component. These are then propagated into the DP fit to establish systematic uncertainties. No significant asymmetry is expected in the dominant backgrounds so

Table 8.22: *CP*-violating experimental systematic uncertainties on the *CP* parameters.

Parameter	Uncertainty			
	Bkgd yield asym.	Bkgd shape asym.	Eff. asym.	Total
		$K^*(892)^0$		
x_{+i}	0.007	0.049	0.000	0.049
x_{-i}	0.010	0.045	0.001	0.046
y_{+i}	0.017	0.027	0.000	0.032
y_{-i}	0.018	0.071	0.000	0.073
		$K_2^*(1430)^0$		
x_{+i}	0.004	0.091	0.001	0.091
x_{-i}	0.016	0.046	0.000	0.049
y_{+i}	0.018	0.120	0.001	0.121
y_{-i}	0.029	0.015	0.000	0.033

this uncertainty is expected to be small.

The effect of asymmetry in the combinatorial background shape is evaluated by determining separate SDP distributions from B^0 and $\overline{B}^0$ candidates in the high-mass regions of the B mass spectra. To obtain the systematic uncertainty due to a potential *CP* asymmetry in the $\overline{\Lambda}_b^0 \to \overline{D}^{(*)}K^+\overline{p}$ background to the $K\pi$ dataset the background distribution is reweighted according to a model including a conservative 30 % asymmetry in the low $m(K^+\overline{p})$ region.

Asymmetries in the efficiency maps

The efficiency histograms used in the baseline fit to data do not account for possible sources of detection and reconstruction asymmetry. Previous analyses have investigated the K–π detection asymmetry [128, 129] and found it to be at the percent level. The precise size of the asymmetry is dependent on the kinematics of the tracks involved but any effect will be negligible at the current level of precision.

A second source of asymmetry comes from the PID requirements placed on the bachelor tracks. The systematic uncertainty due to this source is evaluated by determining the PID efficiency maps separately for positively- and negatively-charged tracks.

Asymmetries in the background SDP distributions

The SDP distributions of combinatoric background and the background due to $\overline{\Lambda}_b^0 \to \overline{D}^{(*)}K^+\overline{p}$ decays may, in principle, be sources of *CP* violation. All other non-negligible backgrounds are due to decays of b-hadrons dominated by Cabibbo-

favoured $b \to c$ amplitudes. *CP* conservation in such transitions is fundamental to the extraction of γ and the effects of doubly-Cabibbo-suppressed $b \to u$ transitions in these backgrounds are negligible at the current level of precision.

8.6.2 *CP*-violating model uncertainties

Table 8.23 gives the *CP*-violating model uncertainties on the *CP* parameters. The sources of these uncertainties are discussed below.

Table 8.23: *CP*-violating model uncertainties on the *CP* parameters.

Parameter	Value		
	D_s^{**} *CPV*	$K\pi$ S-wave *CPV*	Total
	$K^*(892)^0$		
x_{+i}	0.008	0.003	0.009
x_{-i}	0.056	0.022	0.060
y_{+i}	0.012	0.047	0.049
y_{-i}	0.286	0.064	0.293
	$K_2^*(1430)^0$		
x_{+i}	0.004	0.014	0.015
x_{-i}	0.640	0.035	0.641
y_{+i}	0.104	0.071	0.126
y_{-i}	0.147	0.046	0.154

Contributions from D_s^{**} resonances

As discussed in Sec. 8.3, $b \to u$ mediated $B^0 \to D_s^{**+}\pi^-$ decays may contribute to the DP model in the KK and $\pi\pi$ datasets. A contribution due to the $D_{s1}^*(2700)^+$ resonance is included in the baseline model but assumed to be *CP*-conserving. A systematic uncertainty is evaluated by allowing for *CP* violation in this component.

Asymmetries in the $K\pi$ S-wave

As discussed in Sec. 8.3, the values of r_B and δ_B associated with the $K\pi$ S-wave component may not be invariant with $m(K\pi)$. In the baseline fit a single set of Cartesian *CP* parameters are used for the full S-wave contribution. To evaluate the systematic uncertainty associated with this choice, the fit is repeated with separate *CP* parameters for the resonant and nonresonant parts of the S-wave.

CP violation in the $D \to K^+K^-$ and $D \to \pi^+\pi^-$ decays

The levels of CP-asymmetry[4] observed in $D \to K^+K^-$ and $D \to \pi^+\pi^-$ decays are -0.0016 ± 0.0012 and $+0.0005 \pm 0.0015$, respectively [130]. These asymmetries are negligible at the current level of precision so no systematic uncertainties are assigned.

8.6.3 Crosschecks

Various crosschecks are performed to test the stability of the fit results. Separate fits are performed for: 2011 and 2012 datasets; candidates identified as either TIS or TOS in the L0 trigger; data recorded with each magnet polarity; and the $D \to \pi^+\pi^-$ or the $D \to K^+K^-$ samples. In addition, fits are performed: with the least pure NN bins removed; with a more stringent PID requirement on the bachelor kaon; and using wider and narrower signal windows. In all cases, the blinded CP parameters are found to be consistent with the baseline results. Finally, a fit is performed that allows for an explicit production asymmetry between B^0 and $\overline{B}^0$ decays. In the baseline fit, the constraint that the reference amplitude is the same in all cases allows for any asymmetry to be absorbed but asymmetry can be allowed for by introducing a Δx parameter into the $D_2^*(2460)^-$ coefficient. The value obtained for this additional parameter is found to be small and consistent with zero (0.020 ± 0.025), while no shifts were seen in the other fit parameters. Figure 8.20 shows a comparison of the values obtained for the CP parameters from each of the cross checks with the baseline fit. No significant discrepancies are seen.

8.7 Results and extraction of γ

The results for the Cartesian CP parameters are given in Table 8.24. The large systematic uncertainties on the CP parameters associated to the $K_2^*(1430)^0$ resonance indicate that this resonance cannot currently be used to extract useful constraints on γ.

8.7.1 Determination of γ

The Cartesian parameters are used as inputs to likelihood scans of γ, δ_B and r_B. Scans are performed using the GammaCombo framework [131], which constructs a

[4] CP asymmetries defined as $\frac{\Gamma(D^0 \to h^+h^-) - \Gamma(\overline{D}^0 \to h^+h^-)}{\Gamma(D^0 \to h^+h^-) + \Gamma(\overline{D}^0 \to h^+h^-)}$.

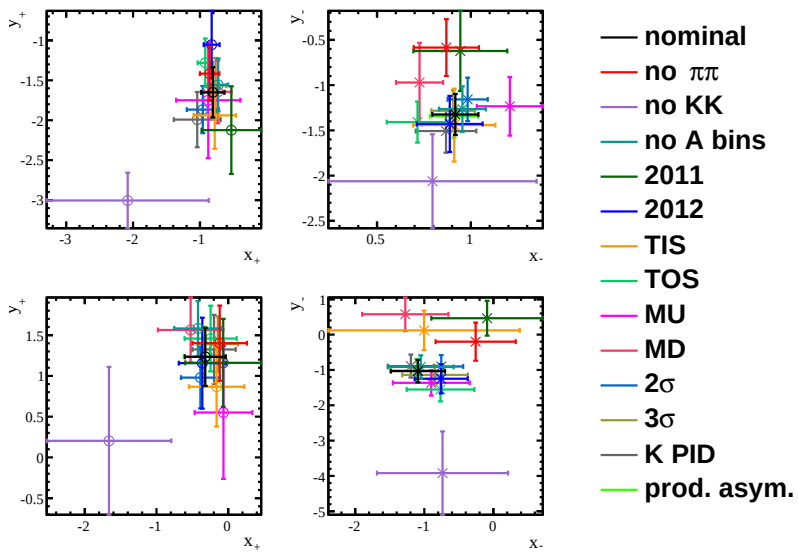

Figure 8.20: Values of the *CP* parameters for the (top) $K^*(892)^0$ and (bottom) $K_2^*(1430)^0$ resonances obtained from the cross-check fits. Where multiple minima exist with similar NLLs, the minimum that is most similar to the result of the nominal fit is shown.

Table 8.24: Results for the *CP* parameters from the fit to data. Uncertainties are statistical, *CP*-conserving experimental, *CP*-conserving model, *CP*-violating experimental and *CP*-violating model, respectively.

Quantity	Value
	$K^*(892)^0$
x_{+i}	$0.05 \pm 0.16 \pm 0.06 \pm 0.08 \pm 0.05 \pm 0.01$
x_{-i}	$-0.01 \pm 0.13 \pm 0.08 \pm 0.09 \pm 0.05 \pm 0.06$
y_{+i}	$-0.48 \pm 0.28 \pm 0.15 \pm 0.16 \pm 0.03 \pm 0.05$
y_{-i}	$-0.30 \pm 0.26 \pm 0.07 \pm 0.27 \pm 0.07 \pm 0.29$
	$K_2^*(1430)^0$
x_{+i}	$-0.27 \pm 0.36 \pm 0.22 \pm 0.08 \pm 0.09 \pm 0.02$
x_{-i}	$-0.90 \pm 0.49 \pm 0.26 \pm 1.88 \pm 0.05 \pm 0.64$
y_{+i}	$-0.38 \pm 0.35 \pm 0.16 \pm 0.11 \pm 0.12 \pm 0.13$
y_{-i}	$0.35 \pm 0.28 \pm 0.16 \pm 0.86 \pm 0.03 \pm 0.15$

multidimensional likelihood function

$$\mathcal{L}\left(\vec{\alpha}\right) = \prod_i f_i\left(\vec{A_i}^{\,\mathrm{obs}} | \vec{\alpha}\right) , \tag{8.9}$$

where f_i are the PDFs associated with the observables $\vec{A_i}^{\,\mathrm{obs}}$, and $\vec{\alpha}$ are the set of physical parameters. The total PDF is assumed to be a multidimensional Gaussian

with the likelihood profile defined entirely by the central values of the observables and the statistical and systematic covariance matrices. The likelihood profile is then determined as a function of the physical parameters by scanning the phase space. Figures 8.21 and 8.22 show 1D and 2D profiles of $1 - \mathrm{CL}$ for γ, δ_B and r_B, where CL is the confidence level at which a point in the phase space can be rejected. The best-fit values and 68 % CL confidence intervals (CIs) obtained are listed in Table 8.25. At the current levels of uncertainty, no constraints may be determined for any of the parameters at the 95 % CL.

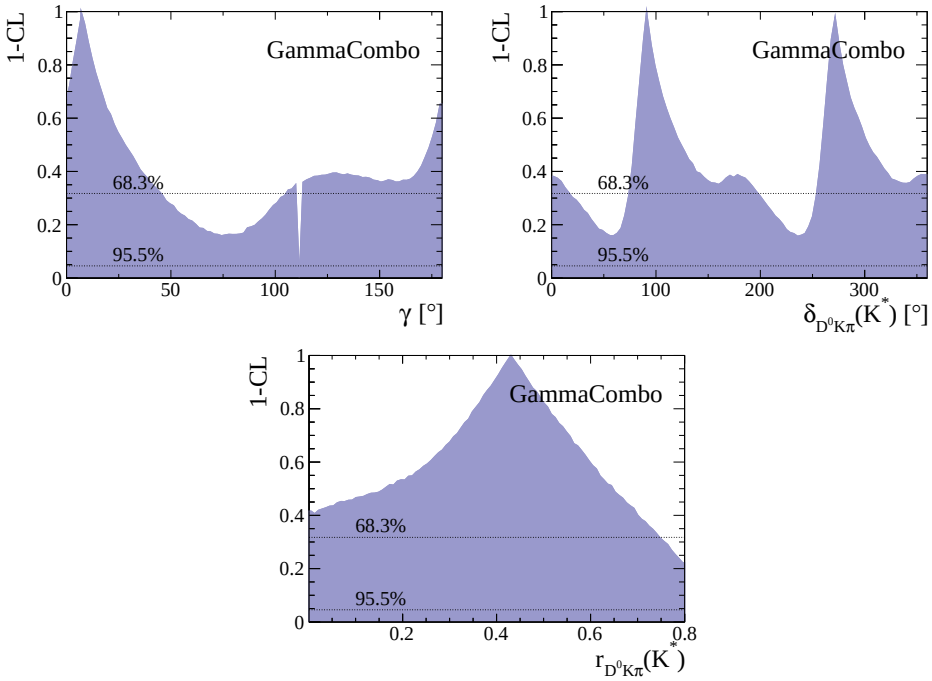

Figure 8.21: Plots of $1 - \mathrm{CL}$ as a function of (left) γ, (right) δ_B and (bottom) r_B.

Table 8.25: Central values and confidence intervals determined from the likelihood scan.

Quantity	Best-fit value	68 % CI
γ	7°	$[0, 45]^\circ \cup [106, 180]^\circ$
δ_B	271°	$[0, 18]^\circ \cup [74, 198]^\circ \cup [254, 360]^\circ$
r_B	0.43	[0.00, 0.75]

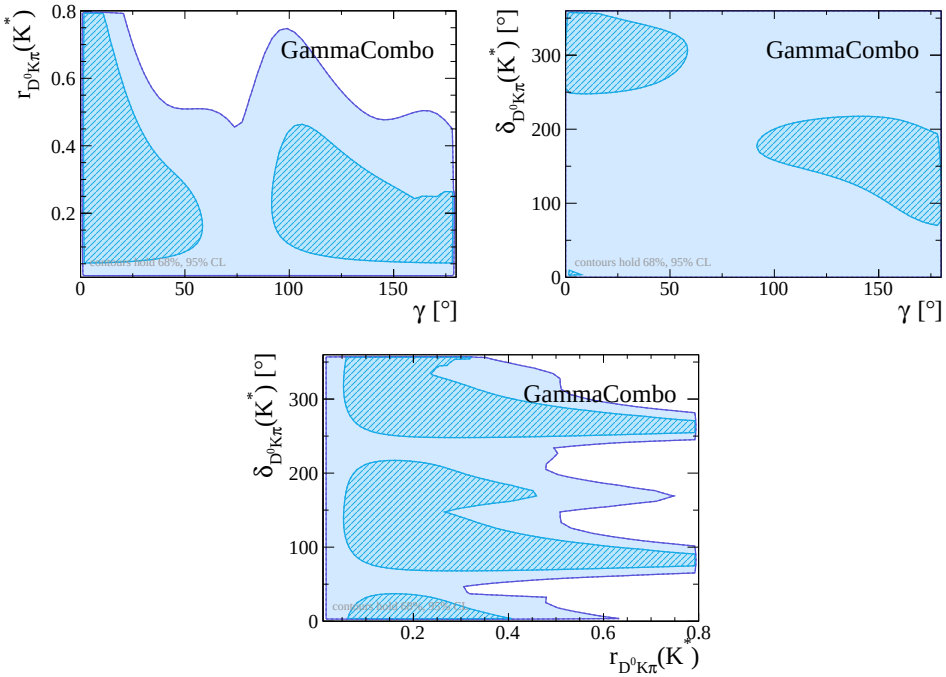

Figure 8.22: Likelihood profiles as a function of (left) γ and r_B, (right) γ and δ_B and (bottom) r_B and δ_B.

8.7.2 Comparison with direct fits for γ and *CP* violation

A direct fit to γ is also performed by changing the parameterisation of the *CP* parameters associated with the $K^*(892)^0$ resonance. This fit yields results of

$$\begin{aligned} \gamma &= (8 \pm 10)^\circ\,, \\ \delta_B &= (273 \pm 17)^\circ\,, \\ r_B &= 0.40 \pm 0.20\,, \end{aligned}$$

where the uncertainties are statistical only. This minimum is consistent with the results obtained from the likelihood scans. Additionally, the "alternative Cartesian" parameterisation is used to establish the significance of the *CP* violation in the $K^*(892)^0$ component. Both Δx and Δy are found to be consistent with zero, thus clearly there is no significant *CP*-violating effect.

Chapter 9

Summary

A range of quantities have been determined from analyses of $B^0_{(s)} \to DK\pi$ decays using data collected during Run 1 of the LHC. These include branching fraction and product branching fraction measurements of the decays and their resonant components, spectroscopic measurements of the D^{**} and D^{**}_s systems, and a determination of the CKM angle γ.

9.1 Branching fractions

The branching fraction ratios of $B^0_{(s)} \to \overline{D}{}^0 K\pi$ decays relative to $B^0 \to \overline{D}{}^0\pi^+\pi^-$ decays were measured based on 1.0 fb^{-1} of data and found to be

$$\frac{\mathcal{B}\left(B^0 \to \overline{D}{}^0 K^+\pi^-\right)}{\mathcal{B}\left(B^0 \to \overline{D}{}^0\pi^+\pi^-\right)} = 0.106 \pm 0.007 \pm 0.008\,, \tag{9.1}$$

$$\frac{\mathcal{B}\left(B^0_s \to \overline{D}{}^0 K^-\pi^+\right)}{\mathcal{B}\left(B^0 \to \overline{D}{}^0\pi^+\pi^-\right)} = 1.18 \pm 0.05 \pm 0.12\,, \tag{9.2}$$

where the uncertainties are statistical and systematic. In addition the fractions of these decays that proceed via various resonant and nonresonant components were determined from Dalitz plot analyses based on 3.0 fb^{-1} of data and are listed in Tables 9.1 and 9.2. The branching fractions and product branching fractions obtained by combining these results with the latest measurement of $\mathcal{B}\left(B^0 \to \overline{D}{}^0\pi^+\pi^-\right)$ [103] are given in Table 9.3.

Table 9.1: Results for the fit fractions of the $B^0 \to \overline{D}^0 K^+\pi^-$ DP and their uncertainties (%). The three quoted errors are statistical, experimental systematic and model uncertainties, respectively. Upper limits at both 90 % and 95 % confidence level (CL) are given for components that are not significant.

Resonance	Fit fraction	Upper limits	
		90 % CL	95 % CL
$K^*(892)^0$	$36.0 \pm 1.4 \pm 1.1 \pm 1.7$		
$K^*(1410)^0$	$0.7 \pm 0.3 \pm 0.8 \pm 0.7$	< 3.1	< 3.6
$K_0^*(1430)^0$	$4.9 \pm 1.9 \pm 2.3 \pm 3.3$		
LASS nonresonant	$4.6 \pm 3.6 \pm 3.6 \pm 6.4$		
LASS total	$6.4 \pm 2.6 \pm 2.6 \pm 5.2$		
$K_2^*(1430)^0$	$7.2 \pm 1.6 \pm 1.0 \pm 1.9$		
$D_0^*(2400)^-$	$18.6 \pm 2.7 \pm 2.0 \pm 7.1$		
$D_2^*(2460)^-$	$22.3 \pm 1.1 \pm 1.1 \pm 1.2$		
$D_3^*(2760)$	—	< 1.0	< 1.1
$D\pi$ S-wave (dabba)	$6.3 \pm 1.4 \pm 1.1 \pm 3.6$		
$D\pi$ P-wave (EFF)	$8.5 \pm 1.6 \pm 2.1 \pm 2.8$		

Table 9.2: Results for the fit fractions of the $B_s^0 \to \overline{D}^0 K^-\pi^+$ DP and their uncertainties (%). The three quoted errors are statistical, experimental systematic and model uncertainties, respectively. Upper limits at both 90 % and 95 % confidence level (CL) are given for components that are not significant.

Resonance	Fit fraction	Upper limits	
		90 % CL	95 % CL
$\overline{K}^*(892)^0$	$28.6 \pm 0.6 \pm 0.7 \pm 0.9$		
$\overline{K}^*(1410)^0$	$1.7 \pm 0.5 \pm 0.2 \pm 1.4$		
LASS nonresonant	$13.7 \pm 2.5 \pm 1.5 \pm 4.1$		
$\overline{K}_0^*(1430)^0$	$20.0 \pm 1.6 \pm 0.7 \pm 3.3$		
LASS total	$21.4 \pm 1.4 \pm 1.0 \pm 4.7$		
$\overline{K}_2^*(1430)^0$	$3.7 \pm 0.6 \pm 0.4 \pm 1.1$		
$\overline{K}^*(1680)^0$	$0.5 \pm 0.4 \pm 0.3 \pm 0.8$	< 2.0	< 2.4
$\overline{K}_0^*(1950)^0$	$0.3 \pm 0.2 \pm 0.1 \pm 2.4$	< 3.7	< 4.1
$\overline{K}_3^*(1780)^0$	—	< 0.33	< 0.38
$\overline{K}_4^*(2045)^0$	—	< 0.21	< 0.24
$D_{s2}^*(2573)^-$	$25.7 \pm 0.7 \pm 0.8 \pm 1.1$		
$D_{s1}^*(2700)^-$	$1.6 \pm 0.4 \pm 0.4 \pm 0.5$		
$D_{s1}^*(2860)^-$	$5.0 \pm 1.2 \pm 0.7 \pm 3.3$		
$D_{s3}^*(2860)^-$	$2.2 \pm 0.1 \pm 0.3 \pm 0.4$		
Nonresonant	$12.4 \pm 2.7 \pm 4.3 \pm 7.6$		
$D_{s\,v}^{*-}$	$4.7 \pm 1.4 \pm 1.1 \pm 4.0$		
$D_{s0\,v}^*(2317)^-$	$2.3 \pm 1.1 \pm 1.9 \pm 2.3$	< 7.2	< 8.4
B_v^{*+}	$1.9 \pm 1.2 \pm 1.1 \pm 1.8$	< 7.7	< 8.7

Table 9.3: Branching fractions and product branching fractions determined for B^0 and B_s^0 decays. Uncertainties are the combined statistical and systematic uncertainties.

Branching fraction	Value (10^{-4})
$B^0 \to \overline{D}^0 K^+\pi^-$	0.95 ± 0.11
$B^0 \to \overline{D}^0 K^*(892)^0$, $K^*(892)^0 \to K^+\pi^-$	0.34 ± 0.05
$B^0 \to \overline{D}^0 K^*(1410)^0$, $K^*(1410)^0 \to K^+\pi^-$	0.07 ± 0.11
$B^0 \to \overline{D}^0 K_0^*(1430)^0$, $K_0^*(1430)^0 \to K^+\pi^-$	0.47 ± 0.42
$B^0 \to \overline{D}^0 (K\pi)^0_{\text{S-wave NR}}$, $(K\pi)^0_{\text{S-wave NR}} \to K^+\pi^-$	0.4 ± 0.9
$B^0 \to \overline{D}^0 K_2^*(1430)^0$, $K_2^*(1430)^0 \to K^+\pi^-$	0.68 ± 0.27
$B^0 \to D_0^*(2400)^- K^+$, $D_0^*(2400)^- \to \overline{D}^0\pi^-$	1.8 ± 0.8
$B^0 \to D_2^*(2460)^- K^+$, $D_2^*(2460)^- \to \overline{D}^0\pi^-$	2.12 ± 0.31
$B^0 \to (D\pi)^-_{\text{S-wave NR}} K^+$, $(D\pi)^-_{\text{S-wave NR}} \to \overline{D}^0\pi^-$	0.6 ± 0.4
$B^0 \to (D\pi)^-_{\text{P-wave NR}} K^+$, $(D\pi)^-_{\text{P-wave NR}} \to \overline{D}^0\pi^-$	0.8 ± 0.4
$B^0 \to \overline{D}^0 K^*(892)^0$	0.51 ± 0.07
$B^0 \to \overline{D}^0 K^*(1410)^0$	0.16 ± 0.25
$B^0 \to \overline{D}^0 K_0^*(1430)^0$	0.07 ± 0.06
$B^0 \to \overline{D}^0 (K\pi)^0_{\text{S-wave NR}}$	0.07 ± 0.12
$B^0 \to \overline{D}^0 K_2^*(1430)^0$	0.20 ± 0.08
$B_s^0 \to \overline{D}^0 K^-\pi^+$	10.0 ± 1.5
$B_s^0 \to \overline{D}^0 \overline{K}^*(892)^0$, $\overline{K}^*(892)^0 \to K^-\pi^+$	2.9 ± 0.4
$B_s^0 \to \overline{D}^0 \overline{K}^*(1410)^0$, $\overline{K}^*(1410)^0 \to K^-\pi^+$	0.17 ± 0.15
$B_s^0 \to \overline{D}^0 \overline{K}_0^*(1430)^0$, $\overline{K}_0^*(1430)^0 \to K^-\pi^+$	2.0 ± 0.5
$B_s^0 \to \overline{D}^0 (K\pi)^0_{\text{S-wave NR}}$, $(K\pi)^0_{\text{S-wave NR}} \to K^-\pi^+$	1.4 ± 0.5
$B_s^0 \to \overline{D}^0 \overline{K}_2^*(1430)^0$, $\overline{K}_2^*(1430)^0 \to K^-\pi^+$	0.37 ± 0.14
$B_s^0 \to D_{s2}^*(2573)^-\pi^+$, $D_{s2}^*(2573)^- \to \overline{D}^0 K^-$	2.6 ± 0.4
$B_s^0 \to D_{s1}^*(2700)^-\pi^+$, $D_{s1}^*(2700)^- \to \overline{D}^0 K^-$	0.16 ± 0.08
$B_s^0 \to D_{s1}^*(2860)^-\pi^+$, $D_{s1}^*(2860)^- \to \overline{D}^0 K^-$	0.5 ± 0.4
$B_s^0 \to D_{s3}^*(2860)^-\pi^+$, $D_{s3}^*(2860)^- \to \overline{D}^0 K^-$	0.22 ± 0.06
$B_s^0 \to \overline{D}^0 \overline{K}^*(892)^0$	4.3 ± 0.7
$B_s^0 \to \overline{D}^0 \overline{K}^*(1410)^0$	3.9 ± 3.5
$B_s^0 \to \overline{D}^0 \overline{K}_0^*(1430)^0$	3.0 ± 0.7
$B_s^0 \to \overline{D}^0 (K\pi)^0_{\text{S-wave NR}}$	2.1 ± 0.8
$B_s^0 \to \overline{D}^0 \overline{K}_2^*(1430)^0$	1.1 ± 0.4

9.2 Spectroscopy

The Dalitz plot analyses of $B_s^0 \to \overline{D}^0 K^-\pi^+$ and $B^0 \to \overline{D}^0 K^+\pi^-$ decays also included measurements of the masses and widths of D_s^{**} and D^{**} resonances, respectively. The determined masses and widths of these resonances are listed in Table 9.4. In addition, it was found that both a spin-1 and a spin-3 resonance were required to describe the $m(\overline{D}^0 K^-) \sim 2.86\,\text{GeV}/c^2$ region, with significances in excess of 10σ and the $D_{s2}^*(2573)^-$ resonance was confirmed to be spin-2 with a statistical significance

in excess of 40σ.

Table 9.4: Masses and widths determined from the DP analyses of $B^0 \to \overline{D}^0 K^+\pi^-$ and $B_s^0 \to \overline{D}^0 K^-\pi^+$ decays. Uncertainties are the combined statistical and systematic uncertainties.

Resonance	Mass (MeV/c^2)	Width (MeV/c^2)
$D_0^*(2400)^-$	2360 ± 34	260 ± 60
$D_2^*(2460)^-$	2465.6 ± 2.2	46 ± 5
$D_{s2}^*(2573)^-$	2568.4 ± 0.4	16.9 ± 0.8
$D_{s1}^*(2860)^-$	2859 ± 27	160 ± 8
$D_{s3}^*(2860)^-$	2861 ± 7	53 ± 10

9.3 *CP* violation

The CKM angle γ has been extracted from an amplitude analysis of $B^0 \to DK^+\pi^-$ decays for the first time. As expected, negligible *CP* violation was seen in the $B_s^0 \to DK^-\pi^+$ DP. The Cartesian *CP* parameters associated with the $K^*(892)^0$ and $K_2^*(1430)^0$ resonances in the $B^0 \to DK^+\pi^-$ DP have been measured as listed in Table 9.5, and the level of *CP* violation is also seen to be neglible. While the $K_2^*(1430)^0$ *CP* parameters were found to be too poorly determined to give a useful constraint on γ, the parameters associated with the $K^*(892)^0$ were used to extract best-fit values and 68 % CL confidence intervals for γ, r_B and δ_B, which are shown in Table 9.6. At the current levels of uncertainty is was not possible to constrain any of these parameters at the 95 % CL. Nevertheless, this analysis demonstrates the use of this method, which will give more precise constraints on γ in the future.

9.4 Conclusion

The analyses detailed within this thesis highlight the key strengths of a DP analysis, both in making unambiguous spectroscopic measurements and in searching for *CP* violation. A key future measurement would be a study of the $B_s^0 \to \overline{D}^{*0} K^-\pi^+$ decay mode. Such an analysis would both build on the D_s^{**} spectroscopy performed in the study of the $B_s^0 \to \overline{D}^0 K^-\pi^+$ DP and provide a more robust model for a key background in the $B^0 \to DK^+\pi^-$ DP in preparation for future measurements of γ using this decay mode. While the soft photon or neutral pion from the $\overline{D}^{*0}$ decay makes this decay mode difficult to study with LHCb, an analysis of the related decays $B_s^0 \to D^- K^-\pi^+\pi^+$ and $B_s^0 \to D^{*-} K_S^0\pi^+$ would also yield some information about the background and allow further study of the D_s^{**} spectrum.

Table 9.5: Results for the Cartesian *CP* parameters from the fit to data. Uncertainties are statistical, *CP*-conserving experimental, *CP*-conserving model, *CP*-violating experimental and *CP*-violating model, respectively.

Quantity	Value
	$K^*(892)^0$
x_{+i}	$0.05 \pm 0.16 \pm 0.06 \pm 0.08 \pm 0.05 \pm 0.01$
x_{-i}	$-0.01 \pm 0.13 \pm 0.08 \pm 0.09 \pm 0.05 \pm 0.06$
y_{+i}	$-0.48 \pm 0.28 \pm 0.15 \pm 0.16 \pm 0.03 \pm 0.05$
y_{-i}	$-0.30 \pm 0.26 \pm 0.07 \pm 0.27 \pm 0.07 \pm 0.29$
	$K_2^*(1430)^0$
x_{+i}	$-0.27 \pm 0.36 \pm 0.22 \pm 0.08 \pm 0.09 \pm 0.02$
x_{-i}	$-0.90 \pm 0.49 \pm 0.26 \pm 1.88 \pm 0.05 \pm 0.64$
y_{+i}	$-0.38 \pm 0.35 \pm 0.16 \pm 0.11 \pm 0.12 \pm 0.13$
y_{-i}	$0.35 \pm 0.28 \pm 0.16 \pm 0.86 \pm 0.03 \pm 0.15$

Table 9.6: Best fit values and 68 % CL confidence interval for γ, δ_B and r_B.

Quantity	Best-fit value	68 % CI
γ	7°	$[0, 45]^\circ \cup [106, 180]^\circ$
δ_B	271°	$[0, 18]^\circ \cup [74, 198]^\circ \cup [254, 360]^\circ$
r_B	0.43	[0.00, 0.75]

Furthermore, the recent start of run 2 at the LHC and the upcoming Belle2 experiment will both provide large new datasets to allow a more precise measurement of γ from $B^0 \to \overline{D}^0 K^+\pi^-$ decays. Further gains in sensitivity to γ could also be made with the inclusion of D decay modes to other final states as has been successfully achieved in studies of $B^\pm \to DK^\pm$ decays. Of particular interest are the suppressed πK final state [44], which would first require a more detailed understanding of the large backgrounds from B_s^0 decays; the $\pi^+\pi^-\pi^0$ final state, which may be treated as a quasi-*CP* eigenstate [132,133]; and the $K^0_S\pi^+\pi^-$ final state, which may be exploited via a double-DP analysis [134].

Appendix A

Alternative lineshapes

The most commonly used resonance mass terms are introduced in Sec. 2.5.1. This appendix defines additional lineshapes, which are primarily used as systematic variations of the DP models used to describe $B^0_{(s)} \to DK\pi$ decays.

A.1 Flatté

For resonances with a mass close to the kinematic threshold of one of their decay channels, the Flatté lineshape [113] may be used. In this thesis, the Flatté lineshape is used as an alternative parameterisation for the $K_0^*(1430)^0$ resonance. In addition to the $K\pi$ channel, this state may also decay into the $K\eta'$ channel which is close to threshold at the pole mass of the resonance. The functional form is identical to that of the RBW (Eq. 2.46) except that the mass-dependent width is given by

$$\Gamma(m) = \left(\frac{m^2 - s_A}{m_0^2 - s_A}\right)\left(g_1\rho_{K\pi}(m) + g_2\rho_{K\eta'}(m)\right) \tag{A.1}$$

where $\rho_{K\pi}$ and $\rho_{K\eta'}$ are phase-space factors associated with the two channels, $g_{1,2}$ parameterise the couplings to these two channels and s_A is the Adler zero. The values used for these constants are

$$\begin{aligned} m_0 &= 1.515\,\text{GeV}/c^2\,, \\ g_1 &= 0.304\,\text{GeV}/c^2\,, \\ g_2 &= 0.380\,\text{GeV}/c^2\,, \\ s_A &= 0.234\,\text{GeV}^2/c^4\,. \end{aligned}$$

These values are taken from BES data [114], with the exception of the Adler zero which is calculated as $m_K^2 - 0.5m_\pi^2$.

A.2 Gounaris–Sakurai

Another alternative lineshape for resonant amplitudes is the Gounaris–Sakurai parameterisation [116]. This is usually used to describe the decays of broad ρ resonances to two pions and is given by

$$R_j(m) = \frac{1 + D \cdot \Gamma_0/m_0}{(m_0^2 - m^2) + f(m) - i\, m_0 \Gamma(m)}\,, \tag{A.2}$$

where

$$f(m) = \Gamma_0 \frac{m_0^2}{q_0^3} \left[q^2 \left(h(m) - h(m_0)\right) + \left(m_0^2 - m^2\right) q_0^2 \left.\frac{dh}{dm}\right|_{m_0} \right], \tag{A.3}$$

and the function $h(m)$ is defined as

$$h(m) = \frac{2}{\pi} \frac{q}{m} \ln\left(\frac{m + 2q}{2m_\pi}\right), \tag{A.4}$$

with

$$\left.\frac{dh}{dm}\right|_{m_0} = h(m_0)\left[(8q_0^2)^{-1} - (2m_0^2)^{-1}\right] + (2\pi m_0^2)^{-1}. \tag{A.5}$$

Here, q is the magnitude of the momentum of one of the daughter particles in the rest frame of the resonance, and the subscript 0 denotes the value of a quantity evaluated at the pole mass, m_0, of the resonance. The normalization condition at $R_j(0)$ fixes the parameter $D = f(0)/(\Gamma_0 m_0)$. It is found to be

$$D = \frac{3}{\pi} \frac{m_\pi^2}{q_0^2} \ln\left(\frac{m_0 + 2q_0}{2m_\pi}\right) + \frac{m_0}{2\pi\, q_0} - \frac{m_\pi^2 m_0}{\pi\, q_0^3}\,. \tag{A.6}$$

These equations can be altered for the more general case that a given resonance does not decay to two pions. Factors of $2m_\pi$ must be replaced with $m_i + m_j$ and m_π^2 terms are changed to $(m_i + m_j)^2/4$.

A.3 kappa and dabba

The nonresonant component of the $K\pi$ S-wave is nominally included in the LASS component in this thesis. An alternative is to include the broad κ resonance in the

DP model [114]. As the lineshape is extremely broad, a modified mass-dependent width term is used. This is defined by

$$\Gamma(m) = \rho\left(\frac{m^2 - s_A}{m_0^2 - s_A}\right) f(m)\exp\left(\frac{-\left(m^2 - m_0^2\right)}{A}\right) . \tag{A.7}$$

Here $\rho = 2q/m$ is a phase-space factor, $f(m) = b_2 m^2 + b_1$, where b_1 and b_2 are constants, A is a constant and s_A is the Adler zero. The values used for these constants, once again taken from BES data [114], are

$$\begin{aligned} b_1 &= 24.49\,\text{GeV}/c\,, \\ b_2 &= 0.0\,\text{GeV}/c\,, \\ A &= 2.5\,\text{GeV}^2/c^4\,, \\ m_0 &= 3.3\,\text{GeV}/c^2\,, \\ s_A &= 0.234\,\text{GeV}^2/c^4\,. \end{aligned}$$

A similar broad contribution is expected near threshold in the $D\pi$ channel. A similar functional form, called "dabba" [118], may be used to describe this. This parameterisation is detailed in Sec. 7.3.2.

A.4 EFKLLM

Another alternative model for the $K\pi$ S-wave was introduced in Ref. [115]. The total S-wave contribution is parameterised as

$$R(m) = F(m)\left(\frac{c_0}{m^2} + c_1\right) , \tag{A.8}$$

where $F(m)$ is a mass-dependent complex form factor whose value is determined from a table provided by the authors of Ref. [115] and the coefficients $c_{0,1}$ are complex numbers to be determined by the fit.

A.5 Model-independent partial wave

Any partial wave may be described in a model-independent way, by defining splines to model the variation of either the magnitude and phase, or the real and imaginary parts of the amplitude as a function of invariant mass. Each spline is defined by a series of "knots" at fixed x values and is parameterised between a pair of knots, i

and $i+1$, as

$$y_i(t) = (1-t) \times y_i + t \times y_{i+1} + t(1-t) \times (a_i(1-t) + b_i \times t) \tag{A.9}$$

where t is the normalised mass $(m - m_i)/(m_{i+1} - m_i)$, a_i and b_i are coefficients determined by constraints, and the y value at each knot is a free parameter of the fit (except for one knot, where the amplitude is fixed to unity as a reference). For a spline with n knots, $2n$ constraints are required to define the values of a_i and b_i in each cell. $2n-2$ constraints are obtained by requiring $y_i'(m_{i+1}) = y_{i+1}'(m_{i+1})$ and $y_i''(m_{i+1}) = y_{i+1}''(m_{i+1})$, where $y' = \frac{dy}{dx}$ and $y'' = \frac{d^2y}{dx^2}$, at each internal knot $1 < i < n-1$. Various alternative boundary conditions are available to define the final two constraints. In this thesis, the "not-a-knot" boundary conditions are imposed, which also require the third derivative to be continuous at knots $i = 1$ and $i = n-1$.

Appendix B

EvtGen developments

My main contributions to the EvtGen package are an XML interface for configuring decays and a decay model to describe a generic Dalitz plot. These developments are detailed in Sec. B.1 and Sec. B.2, respectively.

B.1 XML interface

The XML interface is intended as a more user-friendly alternative to the standard "DECAY.DEC" decay configuration file, which is primarily used to configure the branching fractions and phasespace distributions of decays. The primary advantage of an XML format is that the datafile is self-documenting, while understanding a standard decay file requires the user to know the syntax and the correct order of parameters. An XML file may also be combined with a compatible XSL stylesheet to provide additional documentation. Furthermore the use of a common syntax throughout the file makes the format more flexible for future extensions, while extending the standard format would, in many cases, require significant modifications to the parser. An XML configuration file follows a standard XML syntax, using "tags" and "attributes" *e.g.*

```
<parentTag>
  <tag1 attribute1="value1" attribute2="value2">
    <subtag attribute="value" />
  </tag1>
  <tag2 attribute="value" />
</parentTag>
```

A summary of the tags recognised by EvtGen is given in Table B.1, while the attributes associated with each tag are listed in Tables B.2, B.3, B.4 and B.5. Most

of these tags control existing features within EvtGen and correspond directly to "DECAY.DEC" commands — the functionality of these tags is not described further. The tags relating to the generic Dalitz decay model are described further in Sec. B.2.

One significant improvement of the existing functionality is the introduction of named parameters for decay models. In the standard decay file format, model parameters are inserted as a space-separated list, following the model name and terminated by a semicolon. This format requires the user to know the number of arguments required by each model as well as the correct order of those arguments. The existing functionality is replicated in XML using the `params` attribute but parameters may also be configured individually using attributes defined by the specific decay model. This functionality is provided by the virtual methods `EvtDecayBase::getParamName` and `EvtDecayBase::getParamDefault`, which may be overridden by a derived class to assign a name or default value to each of the model's parameters.

Table B.1: Summary of tags recognised by EvtGen XML parser.

Tag	Parent	Usage	Attributes
		General	
`data`	none	Top level tag	none
`alias`	`data`	Define an alias for a particle	See Table B.2
`modelAlias`	`data`	Define an alias for a decay model	
`chargeConj`	`data`	Set two aliases as charge conjugates	
`conjDecay`	`data`	Get decay from particle's conjugate	
`define`	`data`	Define a constant	
`particle`	`data`	Update properties of a particle	
`lineShapePW`	`data`	Set partial wave of a decay	
		External generators	
`photos`	`data`	Turn photos on or off	See Table B.3
`pythiaParam`	`data`	Configure Pythia	
`pythia6Param`	`data`	Configure Pythia	
		Decay models	
`decay`	`data`	Define the decays of a particle	See Table B.4
`copyDecay`	`data`	Copy other particle's decays	
`removeDecay`	`data`	Remove channels from a decay	
`channel`	`decay`, `removeDecay`	Define a single decay channel	
		Dalitz plot models	
`dalitzDecay`	`data`	Define a Dalitz model	See Table B.5
`resonance`	`dalitzDecay`	Component of a Dalitz model	
`copyDalitz`	`data`	Copy other particle's Dalitz model	

Table B.2: Summary of attributes for general tags.

Attribute	Usage
	`alias`
`name`	the name of the alias
`particle`	the name of the particle
	`modelAlias`
`name`	the name of the alias
`model`	the name of the model
`params`	parameters to use for the model
	`chargeConj`
`particle`	the name of the particle
`conjugate`	the name of the conjugate particle
	`conjDecay`
`particle`	the name of the particle
	`define`
`name`	the name of the constant
`value`	the value of the constant
	`particle`
`name`	the name of the particle
`mass`	the mass of the particle
`width`	the width of the particle
`massMin`	the minimum allowed mass for the particle
`massMax`	the maximum allowed mass for the particle
`includeBirthFactor`	whether to include a birth barrier factor for the particle
`includeDecayFactor`	whether to include a decay barrier factor for the particle
`lineShape`	the shape of the resonance
`blattWeisskopfFactor`	the radius of the particle's Blatt–Weisskopf barrier factor
	`lineShapePW`
`parent`	the name of the decaying particle
`daug1`	the name of the first daughter
`daug2`	the name of the second daughter
`pw`	the partial wave to be used in this decay

Table B.3: Summary of attributes for external generator tags.

Attribute	Usage
	`photos`
`usage`	whether photos should be used for all decays
	`pythiaParam`
`generator`	the generator to be configured — `Generic`, `Alias` or `Both`
`module`	the PYTHIA 8 module containing the parameter to be configured
`param`	the PYTHIA 8 parameter to be configured
`value`	the value to be set
	`pythia6Param`
`generator`	the generator to be configured — `Generic`, `Alias` or `Both`
`module`	the PYTHIA 6 module containing the parameter to be configured
`param`	the PYTHIA 6 parameter to be configured
`value`	the value to be set

Table B.4: Summary of attributes for decay model tags.

Attribute	Usage
	`decay`
`name`	the name of the decaying particle
	`copyDecay`
`particle`	the name of the decaying particle
`copy`	the particle to copy
	`removeDecay`
`particle`	the name of the decaying particle
	`channel`
`br`	the branching fraction for the channel
`daughters`	the daughters of the decay channel
`model`	the phasespace model for the decay
`params`	parameters to configure the decay model
`photos`	whether to turn photos on for this decay
`verbose`	whether to display verbose output for this decay
`summary`	whether to give a summary for this decay

Table B.5: Summary of attributes for Dalitz plot model tags.

Attribute	Usage
	`dalitzDecay`
`particle`	the name of the decaying particle
`daughters`	the daughters of the decay channel
`probMax`	the maximum probability for accept/reject generation
	`resonance`
`mag`	magnitude of the isobar coefficient
`phase`	phase of the isobar coefficient
`real`	real part of the isobar coefficient
`imag`	imaginary part of the isobar coefficient
`particle`	the name of the resonance
`mass`	the mass of the resonance
`width`	the width of the resonance
`spin`	the spin of the resonance
`shape`	the lineshape of the resonance
`resDaughters`	the pair of daughters in the resonance
`normalise`	whether to normalise symmetric resonances
`BlattWeisskopfFactorParent`	the radius of the parent's barrier factor
`BlattWeisskopfFactorResonance`	the radius of the resonance's barrier factor
	`copyDalitz`
`particle`	the name of the decaying particle
`daughters`	the daughters of the decay channel
`copy`	the decaying particle in the model to be copied
`copyDaughters`	the daughters in the model to be copied

B.2 Generic Dalitz model

The generic Dalitz model allows for spinless three-body decays to be generated according to a DP model defined at run time, while previous models only defined a hardcoded amplitude model at compile time. This development allows the user to define and modify a DP model through the XML interface described in Sec. B.1. Each DP decay model is defined in XML by a `dalitzDecay` tag containing a number of `resonance` tags, which correspond to the resonant and nonresonant components of the model. The `dalitzDecay` tag has two mandatory attributes, `name` and `daughters`, which take the name of the decaying particle and a space separated list of the daughters, respectively. Additionally a third attribute, `probMax`, may be defined. This attribute defines the maximum allowed value of the squared amplitude across the phase space, which is used to convert amplitudes into probabilities when generating decays using the accept/reject method. This value must be larger than the square of the total amplitude obtained at any point in the phase space to avoid probabilities larger than unity but should otherwise be as small as possible to speed up generation. If `probMax` is not defined then a special run is performed to determine a safe value based on a million random points in the phase space. This value is determined as the square of the maximum amplitude found plus 10 %. If a value larger than `probMax` is found during generation then a warning message is produced to inform the user that the generated events are invalid.

Each component of the model has an associated complex coefficient expressed as either real and imaginary parts or as a magnitude and phase. These are stored in the `real`, `imag`, `mag` and `phase` attributes, respectively. In addition, the phasespace distribution of each resonance is defined by the `resDaughters` and `shape` attributes. The `resDaughters` attribute must be given the names of two of the daughter particles separated by a space, while the `shape` attribute describes the lineshape of the resonance and takes one of the values listed in Table B.6. Also listed, in Table B.7 are the additional attributes corresponding to each lineshape, which are used to define any shape parameters. The lineshape of each component is also dependent on spin and, in the case of resonant contributions, the mass and width of the resonance. For many particles, these quantities are available using the `particle` attribute, which obtains values from the main EvtGen particle list. Where a particle is not known to EvtGen or different values are needed, the attributes `mass`, `width` and `spin` may be defined. Finally, the radii of the production and decay Blatt–Weisskopf barrier factors may be specified using the attributes `BlattWeisskopfFactorParent` and `BlattWeisskopfFactorResonance`.

Table B.6: Summary of lineshapes available for resonances.

Lineshape	Description
RBW_CLEO_ZEMACH	Relativistic Breit–Wigner (Zemach tensor spin formalism)
RBW	Relativistic Breit–Wigner (helicity spin formalism)
GS_CLEO_ZEMACH	Gounaris–Sakurai (Zemach tensor spin formalism)
GS	Gounaris–Sakurai (helicity spin formalism)
GAUSS_CLEO_ZEMACH	Gaussian (Zemach tensor spin formalism)
GAUSS	Gaussian (helicity spin formalism)
Flatte	Flatté lineshape
LASS	LASS parameterisation for $K\pi$ S-wave
NonRes	Flat nonresonant term
NonRes_Lin	Nonresonant term with a linear form factor
NonRes_Exp	Nonresonant term with an exponetial form factor

Table B.7: Summary of attributes available for resonance lineshapes.

Attribute	Description
LASS	
a	LASS scattering length
r	LASS effective range
R	Resonant-part magnitude
phiR	Resonant-part phase
B	Nonresonant-part magnitude
phiB	Nonresonant-part phase
cutoff	Cutoff for the nonresonant part
NonRes_Exp	
alpha	Exponential coefficient

An example DP generated using this generic model is shown in Fig. B.1, while the XML used to define this DP is given below.

```
<dalitzDecay particle="D+" daughters="K- pi+ pi+" probMax="2500.">
  <resonance real="-7.02168" imag="2.33580" shape="NonRes"/>
  <resonance mag="1.0" phase="0.0" particle="K*0"
             resDaughters="pi+ K-" shape="RBW_CLEO_ZEMACH"
             BlattWeisskopfFactorParent="5.0"/>
  <resonance mag="3.0" phase="-130.3"
             width="0.164" mass="1.463" spin="0"
             resDaughters="K- pi+" shape="RBW"
             BlattWeisskopfFactorParent="5.0"/>
  <resonance mag="0.96" phase="150.1" particle="K_2*0"
             resDaughters="K- pi+" shape="RBW_CLEO_ZEMACH"
             BlattWeisskopfFactorParent="5.0"/>
  <resonance mag="6.5" phase="29" particle="K''*0"
             resDaughters="pi+ K-" shape="RBW_CLEO_ZEMACH"
             BlattWeisskopfFactorParent="5.0"/>
  <resonance mag="5.01" phase="16.3"
             width="0.470" mass="0.809" spin="0"
             resDaughters="K- pi+" shape="RBW"
             BlattWeisskopfFactorParent="5.0"/>
</dalitzDecay>
```

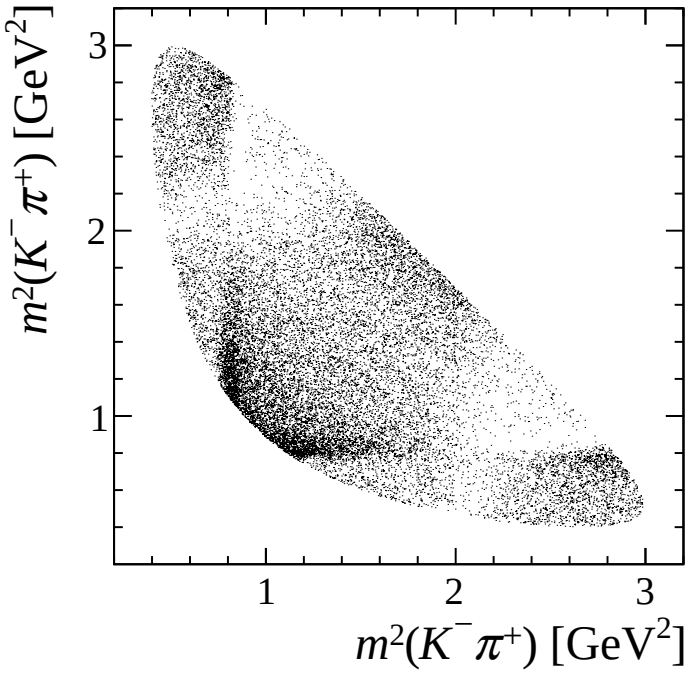

Figure B.1: The Dalitz plot distribution of $D^+ \to K^-\pi^+\pi^+$ decays as generated by EvtGen.

Appendix C

Laura^{++} developments

This appendix details my main contributions to the Laura^{++} package — these are

- cubic spline interpolation of 2D histograms;
- new isobar coefficients for the determination of γ;
- a model-independent description of partial waves;
- a parameteric description of narrow peaking backgrounds

C.1 2D spline interpolation

The signal efficiency across the DP and background contributions are both described using 2D histograms in the SDP co-ordinates m' and θ'. Interpolation is used to determine the value of the efficiency term between bin centres of the input histogram. While it is simple to perform a linear interpolation of the input histogram in the "cell" between four bin centres (as offered by the pre-existing `Lau2DHistDP` class), this results in discontinuities in the derivatives of the efficiency function between cells. As described in Sec. 6.3.3, a cubic function,

$$f(x,y) = \sum_{i=0}^{3}\sum_{j=0}^{3} a_{ij}x^i y^j \,, \tag{C.1}$$

may be defined in each cell, where x and y run from 0 to 1 and the coefficients a_{ij} are chosen to ensure that the efficiency, ϵ, and its derivatives $\frac{d\epsilon}{dm'}$, $\frac{d\epsilon}{d\theta'}$ and $\frac{d^2\epsilon}{dm'd\theta'}$ are continuous between cells.

This functionality is provided by the `Lau2DCubicSpline` class, which receives a 2D histogram in its constructor and precalculates the coefficients in each cell

and provides an `evaluate` method to evaluate the spline at a given point. The `Lau2DSplineDP` class acts as a wrapper for a `Lau2DCubicSpline` object and implements the `Lau2DAbsHistDP` abstract base class, which is also implemented by the `Lau2DHistDP` class allowing the two models to be used interchangeably.

A further development is the ability to separate the efficiency model out into separate components each described by an implementation of the `Lau2DAbsHistDP` class. The full efficiency model is provided by the `LauEffModel` class, which has been updated to contain an array of pointers to `Lau2DAbsHistDP` objects. Existing functionality is preserved by the methods `setEffHisto` and `setEffSpline`, which initialise an efficiency model based on a single histogram or spline, while subsequent calls to the new methods `addEffHisto` and `addEffSpline` allow the efficiency to be determined as the product of an arbitrary number of splines and histograms.

Furthermore, an alternative efficiency model, `LauWeightedSumEffModel`, has been developed to allow multiple efficiency models to be summed together. This functionality is useful, *e.g.*, to combine multiple trigger pathways with different efficiency maps.

C.2 Coefficients for γ

As introduced in Sec. 2.4.3, the determination of the CKM angle γ from the $B^0 \to DK^+\pi^-$ DP requires a comparison of the amplitudes of a K^{**} resonance in three DPs. It is useful to use a single set of parameters to describe these three amplitudes and to parameterise the amplitudes in terms of γ. The possible parameterisations for the K^{**} resonances, detailed in Sec. 8.3, are implemented by the classes `LauPolarGammaCP`, `LauRealImagGammaCP` and `LauCartesianGammaCP`. In all three of these parameterisations, the *CP*-violating parameters must be fixed to zero for the $\overline{D}^0 K\pi$ DP and free parameters in the $D_{CP}K\pi$ DPs. This is achieved by a modification to the `getParameters` methods of these classes so that the parameters are only shared between simultaneous fits when their values are not fixed. Furthermore, the parameterisation implemented by `LauPolarGammaCP` allows a single γ parameter to be shared between multiple resonances. The class includes a static parameter, which is used for γ in all instances where the parameter is shared.

C.3 Model independent partial wave

As described in Sec. A.5, an alternative to the usual isobar model is to describe an entire partial wave in a model-independent way. In Laura^{++}, this functionality

is implemented by the classes derived from `LauAbsModIndPartWave`. The complex amplitude as a function of mass is determined by a pair of `Lau1DCubicSpline` objects that relate to either the magnitude and phase or the real and imaginary parts.

C.4 Peaking backgrounds

The default method of modelling backgrounds, using 2D histograms, does not work well for narrow peaking backgrounds. In such backgrounds, events are clustered in a small region of the phase space so a very large number of bins would be required to give a reasonable description of the distribution. An alternative approach is to include parametric descriptions of such backgrounds and combine them incoherently with the signal model. This functionality has been added to `LauIsobarDynamics` and a `addIncoherentResonance` method has been introduced to add incoherent components to the signal model. Incoherent components are described by classes derived from `LauAbsIncohRes`, which in turn implements `LauAbsResonance`. A simple Gaussian lineshape is provided by the class `LauGaussIncohRes`.

Note that this background model requires that the background has a similar efficiency distribution to signal so that the same efficiency model can be used. The yield of the background component must also be included in the signal yield so fit fractions need to be rescaled to remove the contribution from the background.

Bibliography

[1] ATLAS collaboration, G. Aad *et al.*, *Observation of a new particle in the search for the Standard Model Higgs boson with the ATLAS detector at the LHC*, Phys. Lett. **B716** (2012) 1, arXiv:1207.7214.

[2] CMS collaboration, S. Chatrchyan *et al.*, *Observation of a new boson at a mass of 125 GeV with the CMS experiment at the LHC*, Phys. Lett. **B716** (2012) 30, arXiv:1207.7235.

[3] Particle Data Group, K. A. Olive *et al.*, *Review of particle physics*, Chin. Phys. C **38** (2014) 090001.

[4] Belle collaboration, S.-K. Choi *et al.*, *Observation of a resonance-like structure in the $\pi^{\pm}\psi'$ mass distribution in exclusive $B \to K\pi^{\pm}\psi'$ decays*, Phys. Rev. Lett. **100** (2008) 142001.

[5] Belle collaboration, K. Chilikin *et al.*, *Experimental constraints on the spin and parity of the $Z(4430)^{+}$*, Phys. Rev. D **88** (2013) 074026.

[6] LHCb collaboration, R. Aaij *et al.*, *Observation of the resonant character of the $Z(4430)^{-}$ state*, Phys. Rev. Lett. **112** (2014) 222002, arXiv:1404.1903.

[7] LHCb collaboration, R. Aaij *et al.*, *Evidence for pentaquark-charmonium states in $\Lambda_b^0 \to J/\psi p K^{-}$ decays*, Phys. Rev. Lett. **115** (2015) 07201, arXiv:1507.03414.

[8] S. Godfrey and I. T. Jardine, *Comment on the nature of the $D_{s1}^{*}(2710)$ and $D_{sJ}^{*}(2860)$ mesons*, Phys. Rev. **D89** (2014) 074023, arXiv:1312.6181.

[9] S. L. Glashow, J. Iliopoulos, and L. Maiani, *Weak interactions with lepton-hadron symmetry*, Phys. Rev. D **2** (1970) 1285.

[10] M. Kobayashi and T. Maskawa, *CP-violation in the renormalizable theory of weak interaction*, Progress of Theoretical Physics **49** (1973) 652.

[11] S. Weinberg, *A model of leptons*, Phys. Rev. Lett. **19** (1967) 1264.

[12] A. Salam, *Weak and electromagnetic interactions*, in *Elementary particle theory* (N. Svartholm, ed.), pp. 367–377, Almquist & Wiksell.

[13] M. Gell-Mann, *Symmetries of baryons and mesons*, Phys. Rev. **125** (1962) 1067.

[14] F. Englert and R. Brout, *Broken symmetry and the mass of gauge vector mesons*, Phys. Rev. Lett. **13** (1964) 321.

[15] P. W. Higgs, *Broken symmetries and the masses of gauge bosons*, Phys. Rev. Lett. **13** (1964) 508.

[16] G. S. Guralnik, C. R. Hagen, and T. W. B. Kibble, *Global conservation laws and massless particles*, Phys. Rev. Lett. **13** (1964) 585.

[17] A. D. Sakharov, *Violation of CP invariance, C asymmetry, and baryon asymmetry of the universe*, Soviet Physics Uspekhi **34** (1991) 392.

[18] J. S. Bell, *i. Time reversal in field theory, ii. Some functional methods in field theory*, PhD thesis, University of Birmingham, 1956.

[19] W. Pauli, ed., *Niels Bohr and the development of physics; essays dedicated to Niels Bohr on the occasion of his seventieth birthday*, Pergamon Press, London, 1955.

[20] G. Lüders, *On the equivalence of invariance under time reversal and under particle-antiparticle conjugation for relativistic Field Theories*, Kong. Dan. Vid. Sel. Mat. Fys. Med. **28N5** (1954) 1.

[21] J. H. Christenson, J. W. Cronin, V. L. Fitch, and R. Turlay, *Evidence for the 2π decay of the K_2^0 meson*, Phys. Rev. Lett. **13** (1964) 138.

[22] L. Wolfenstein, *Violation of CP invariance and the possibility of very weak interactions*, Phys. Rev. Lett. **13** (1964) 562.

[23] N. Cabibbo, *Unitary symmetry and leptonic decays*, Phys. Rev. Lett. **10** (1963) 531.

[24] L.-L. Chau and W.-Y. Keung, *Comments on the parametrization of the Kobayashi-Maskawa matrix*, Phys. Rev. Lett. **53** (1984) 1802.

[25] L. Wolfenstein, *Parametrization of the Kobayashi-Maskawa matrix*, Phys. Rev. Lett. **51** (1983) 1945.

[26] A. J. Buras, M. E. Lautenbacher, and G. Ostermaier, *Waiting for the top quark mass, $K^+ \to \pi^+ \nu\overline{\nu}$, $B^0_{(s)} - \overline{B}^0_{(s)}$ mixing and CP asymmetries in B decays*, Phys. Rev. **D50** (1994) 3433, arXiv:hep-ph/9403384.

[27] CKMfitter Group, J. Charles *et al.*, *CP violation and the CKM matrix: Assessing the impact of the asymmetric B factories*, Eur. Phys. J. **C41** (2005) 1, arXiv:hep-ph/0406184, http://ckmfitter.in2p3.fr/.

[28] C. Jarlskog, *Commutator of the quark mass matrices in the standard electroweak model and a measure of maximal CP nonconservation*, Phys. Rev. Lett. **55** (1985) 1039.

[29] M. Gronau, J. L. Rosner, and D. London, *Weak coupling phase from decays of charged B mesons to πK and $\pi\pi$*, Phys. Rev. Lett. **73** (1994) 21, arXiv:hep-ph/9404282.

[30] D. Atwood, I. Dunietz, and A. Soni, *Enhanced CP violation with $B \to K D^0(\overline{D}^0)$ modes and extraction of the Cabibbo-Kobayashi-Maskawa angle γ*, Phys. Rev. Lett. **78** (1997) 3257.

[31] A. Giri, Y. Grossman, A. Soffer, and J. Zupan, *Determining γ using $B^\pm \to DK^\pm$ with multibody D decays*, Phys. Rev. D **68** (2003) 054018.

[32] LHCb collaboration, R. Aaij *et al.*, *Observation of CP violation in $B^\pm \to DK^\pm$ decays*, Phys. Lett. **B712** (2012) 203, Erratum ibid. **B713** (2012) 351, arXiv:1203.3662.

[33] LHCb collaboration, R. Aaij *et al.*, *Measurement of CP violation parameters in $B^0 \to DK^{*0}$ decays*, Phys. Rev. **D90** (2014) 112002, arXiv:1407.8136.

[34] LHCb collaboration, R. Aaij *et al.*, *Study of $B^- \to DK^-\pi^+\pi^-$ and $B^- \to D\pi^-\pi^+\pi^-$ decays and determination of the CKM angle γ*, arXiv:1505.07044, submitted to Phys. Rev. D.

[35] LHCb collaboration, R. Aaij *et al.*, *Observation of the suppressed ADS modes $B^\pm \to [\pi^\pm K^\mp \pi^+\pi^-]_D K^\pm$ and $B^\pm \to [\pi^\pm K^\mp \pi^+\pi^-]_D \pi^\pm$*, Phys. Lett. **B723** (2013) 44, arXiv:1303.4646.

[36] LHCb collaboration, R. Aaij *et al.*, *A model-independent Dalitz plot analysis of $B^\pm \to DK^\pm$ with $D \to K^0_S h^+h^-$ ($h = \pi, K$) decays and constraints on the CKM angle γ*, Phys. Lett. **B718** (2012) 43, arXiv:1209.5869.

[37] LHCb collaboration, R. Aaij *et al.*, *Measurement of the CKM angle γ using $B^\pm \to DK^\pm$ with $D \to K^0_S\pi^+\pi^-$, $K^0_S K^+K^-$ decays*, JHEP **10** (2014) 097, arXiv:1408.2748.

[38] BaBar collaboration, B. Aubert *et al.*, *Improved measurement of the CKM angle γ in $B^\mp \to D^{(*)}K^{(*)\mp}$ decays with a Dalitz plot analysis of D decays to $K^0_S\pi^+\pi^-$ and $K^0_S K^+K^-$*, Phys. Rev. **D78** (2008) 034023, arXiv:0804.2089.

[39] BaBar collaboration, P. del Amo Sanchez *et al.*, *Evidence for direct CP violation in the measurement of the Cabibbo-Kobayashi-Maskawa angle gamma with $B^\mp \to D^{(*)}K^{(*)\mp}$ decays*, Phys. Rev. Lett. **105** (2010) 121801, arXiv:1005.1096.

[40] CLEO collaboration, J. Libby *et al.*, *Model-independent determination of the strong-phase difference between D^0 and $\overline{D}^0 \to K^0_{S,L} h^+h^-$ ($h = \pi, K$) and its impact on the measurement of the CKM angle γ/ϕ_3*, Phys. Rev. **D82** (2010) 112006, arXiv:1010.2817.

[41] LHCb collaboration, R. Aaij *et al.*, *Measurement of CP violation and constraints on the CKM angle γ in $B^\pm \to DK^\pm$ with $D \to K^0_S\pi^+\pi^-$ decays*, Nucl. Phys. **B888** (2014) 169, arXiv:1407.6211.

[42] LHCb collaboration, R. Aaij *et al.*, *Measurement of CP asymmetry in $B^0_s \to D^\mp_s K^\pm$ decays*, JHEP **11** (2014) 060, arXiv:1407.6127.

[43] T. Gershon, *On the measurement of the Unitarity Triangle angle γ from $B^0 \to DK^{*0}$ decays*, Phys. Rev. **D79** (2009) 051301, arXiv:0810.2706.

[44] T. Gershon and M. Williams, *Prospects for the measurement of the Unitarity Triangle angle γ from $B^0 \to DK^+\pi-$ decays*, Phys. Rev. **D80** (2009) 092002, arXiv:0909.1495.

[45] R. H. Dalitz, *On the analysis of tau-meson data and the nature of the tau-meson*, Phil. Mag. **44** (1953) 1068.

[46] G. N. Fleming, *Recoupling effects in the isobar model. 1. General formalism for three-pion scattering*, Phys. Rev. **135** (1964) B551.

[47] D. Morgan, *Phenomenological analysis of $I = \frac{1}{2}$ single-pion production processes in the energy range 500 to 700 MeV*, Phys. Rev. **166** (1968) 1731.

[48] D. Herndon, P. Soding, and R. J. Cashmore, *Generalised isobar model formalism*, Phys. Rev. **D11** (1975) 3165.

[49] J. Blatt and V. E. Weisskopf, *Theoretical nuclear physics*, J. Wiley (New York), 1952.

[50] C. Zemach, *Three-pion decays of unstable particles*, Phys. Rev. **133** (1964) B1201.

[51] C. Zemach, *Use of angular-momentum tensors*, Phys. Rev. **140** (1965) B97.

[52] LHCb collaboration, R. Aaij *et al.*, *Dalitz plot analysis of $B_s^0 \to \overline{D}^0 K^- \pi^+$ decays*, Phys. Rev. **D90** (2014) 072003, arXiv:1407.7712.

[53] Belle collaboration, A. Garmash *et al.*, *Dalitz analysis of the three-body charmless decays $B^+ \to K^+\pi^+\pi^-$ and $B^+ \to K^+K^+K^-$*, Phys. Rev. **D71** (2005) 092003, arXiv:hep-ex/0412066.

[54] LASS collaboration, D. Aston *et al.*, *A study of $K^-\pi^+$ scattering in the reaction $K^-p \to K^-\pi^+n$ at 11 GeV/c*, Nucl. Phys. **B296** (1988) 493.

[55] L. Evans and P. Bryant, *LHC Machine*, JINST **3 S08001** (2008).

[56] ATLAS collaboration, G. Aad *et al.*, *The ATLAS Experiment at the CERN Large Hadron Collider*, JINST **3** (2008) S08003.

[57] CMS collaboration, S. Chatrchyan *et al.*, *The CMS experiment at the CERN LHC*, JINST **3** (2008) S08004.

[58] ALICE collaboration, K. Aamodt *et al.*, *The ALICE experiment at the CERN LHC*, JINST **3** (2008) S08002.

[59] EPC Group, CERN Technology Department, *http://te-dep-epc.web.cern.ch/te-dep-epc/machines*, October 2014.

[60] M. Lamont, *Status of the LHC*, Journal of Physics: Conference Series **455** (2013) 012001.

[61] LHCb collaboration, A. A. Alves, Jr *et al.*, *The LHCb Detector at the LHC*, JINST **3** (2008) S08005.

[62] LHCb collaboration, *LHCb magnet: Technical Design Report*, CERN-LHCC-2000-007. LHCb-TDR-001.

[63] LHCb collaboration, *LHCb VELO (VErtex LOcator): Technical Design Report*, CERN-LHCC-2001-011. LHCb-TDR-005.

[64] R. Aaij *et al.*, *Performance of the LHCb Vertex Locator*, JINST **9** (2014) P09007, arXiv:1405.7808.

[65] LHCb collaboration, *LHCb inner tracker: Technical Design Report*, CERN-LHCC-2002-029. LHCb-TDR-008.

[66] LHCb collaboration, *LHCb outer tracker: Technical Design Report*, CERN-LHCC-2001-024. LHCb-TDR-006.

[67] R. Arink *et al.*, *Performance of the LHCb Outer Tracker*, JINST **9** (2014) P01002, arXiv:1311.3893.

[68] LHCb collaboration, *LHCb RICH: Technical Design Report*, CERN-LHCC-2000-037. LHCb-TDR-003.

[69] M. Adinolfi *et al.*, *Performance of the LHCb RICH detector at the LHC*, Eur. Phys. J. **C73** (2013) 2431, arXiv:1211.6759.

[70] LHCb collaboration, *LHCb calorimeters: Technical Design Report*, CERN-LHCC-2000-036. LHCb-TDR-002.

[71] R. Aaij *et al.*, *Performance of the LHCb calorimeters*, LHCb-DP-2013-004, in preparation.

[72] LHCb collaboration, *LHCb muon system: Technical Design Report*, CERN-LHCC-2001-010. LHCb-TDR-004.

[73] F. Archilli *et al.*, *Performance of the muon identification at LHCb*, JINST **8** (2013) P10020, arXiv:1306.0249.

[74] A. A. Alves Jr. *et al.*, *Performance of the LHCb muon system*, JINST **8** (2013) P02022, arXiv:1211.1346.

[75] LHCb collaboration, *LHCb trigger system: Technical Design Report*, CERN-LHCC-2003-031. LHCb-TDR-010.

[76] R. Aaij *et al.*, *The LHCb trigger and its performance in 2011*, JINST **8** (2013) P04022, arXiv:1211.3055.

[77] V. V. Gligorov and M. Williams, *Efficient, reliable and fast high-level triggering using a bonsai boosted decision tree*, JINST **8** (2013) P02013, arXiv:1210.6861.

[78] LHCb collaboration, *LHCb online system, data acquisition and experiment control: Technical Design Report*, CERN-LHCC-2001-040. LHCb-TDR-007.

[79] T. Sjöstrand *et al.*, *An Introduction to PYTHIA 8.2*, arXiv:1410.3012.

[80] D. J. Lange, *The EvtGen particle decay simulation package*, Nucl. Instrum. Meth. **A462** (2001) 152.

[81] Warwick EvtGen group, http://evtgen.warwick.ac.uk/, October 2014.

[82] GEANT4 collaboration, S. Agostinelli *et al.*, *GEANT4: A Simulation toolkit*, Nucl. Instrum. Meth. **A506** (2003) 250.

[83] T. Latham *et al.*, October 2014. Laura++ Dalitz plot fitting package, http://laura.hepforge.org/.

[84] LHCb collaboration, R. Aaij *et al.*, *Measurements of the branching fractions of the decays* $B_s^0 \to \overline{D}^0 K^- \pi^+$ *and* $B^0 \to \overline{D}^0 K^+ \pi^-$, Phys. Rev. **D87** (2013) 112009, arXiv:1304.6317.

[85] LHCb collaboration, R. Aaij *et al.*, *First observation of the decay* $\overline{B}_s^0 \to D^0 K^{*0}$ *and a measurement of the ratio of branching fractions* $\frac{\mathcal{B}(\overline{B}_s^0 \to D^0 K^{*0})}{\mathcal{B}(\overline{B}^0 \to D^0 \rho^0)}$, Phys. Lett. **B706** (2011) 32, arXiv:1110.3676.

[86] LHCb collaboration, R. Aaij *et al.*, *Observation of overlapping spin-*1 *and spin-*3 $\overline{D}^0 K^-$ *resonances at mass* 2.86 GeV/c^2, Phys. Rev. Lett. **113** (2014) 162001, arXiv:1407.7574.

[87] LHCb collaboration, R. Aaij *et al.*, *Amplitude analysis of* $B^0 \to \overline{D}^0 K^+ \pi^-$ *decays*, Phys. Rev. **D92** (2015) 012012, arXiv:1505.01505.

[88] V. V. Gligorov and M. Williams, *Efficient, reliable and fast high-level triggering using a bonsai boosted decision tree*, arXiv:1210.6861.

[89] LHCb collaboration, R. Aaij *et al.*, *Observation of* $B^0 \to \overline{D}^0 K^+ K^-$ *and evidence for* $B_s^0 \to \overline{D}^0 K^+ K^-$, Phys. Rev. Lett. **109** (2012) 131801, arXiv:1207.5991.

[90] LHCb collaboration, R. Aaij *et al.*, *First observations of* $\overline{B}_s^0 \to D^+ D^-$, $D_s^+ D^-$ *and* $D^0 \overline{D}^0$ *decays*, Phys. Rev. **D87** (2013) 092007, arXiv:1302.5854.

[91] M. Feindt and U. Kerzel, *The NeuroBayes neural network package*, Nucl. Instrum. Meth. A **559** (2006) 190.

[92] M. Pivk and F. R. Le Diberder, *sPlot: a statistical tool to unfold data distributions*, Nucl. Instrum. Meth. **A555** (2005) 356, arXiv:physics/0402083.

[93] LHCb collaboration, R. Aaij *et al.*, *Measurement of b hadron production fractions in 7 TeV pp collisions*, Phys. Rev. **D85** (2012) 032008, arXiv:1111.2357.

[94] LHCb collaboration, R. Aaij *et al.*, *Measurement of the fragmentation fraction ratio f_s/f_d and its dependence on B meson kinematics*, JHEP **04** (2013) 001, arXiv:1301.5286.

[95] LHCb collaboration, R. Aaij *et al.*, *Study of the kinematic dependences of Λ_b^0 production in pp collisions and a measurement of the $\Lambda_b^0 \to \Lambda_c^+\pi^-$ branching fraction*, JHEP **08** (2014) 143, arXiv:1405.6842.

[96] BaBar collaboration, B. Aubert *et al.*, *Measurement of branching fractions and resonance contributions for $B^0 \to \overline{D}^0 K^+\pi^-$ and search for $B^0 \to D^0 K^+\pi^-$ decays*, Phys. Rev. Lett. **96** (2006) 011803.

[97] LHCb collaboration, R. Aaij *et al.*, *Study of beauty baryon decays to $D^0 ph^-$ and $\Lambda_c^+ h^-$ final states*, Phys. Rev. **D89** (2014) 032001, arXiv:1311.4823.

[98] Belle collaboration, K. Abe *et al.*, *Study of $B^0 \to \bar{D}^{(*)0}\pi^+\pi^-$ decays*, arXiv:hep-ex/0412072.

[99] T. Skwarnicki, *A study of the radiative cascade transitions between the Upsilon-prime and Upsilon resonances*, PhD thesis, Institute of Nuclear Physics, Krakow, 1986, DESY-F31-86-02.

[100] LHCb collaboration, R. Aaij *et al.*, *Measurements of the branching fractions of the decays $B_s^0 \to D_s^\mp K^\pm$ and $B_s^0 \to D_s^- \pi^+$*, JHEP **06** (2012) 115, arXiv:1204.1237.

[101] LHCb collaboration, R. Aaij *et al.*, *Determination of f_s/f_d for 7 TeV pp collisions and measurement of the $B^0 \to D^- K^+$ branching fraction*, Phys. Rev. Lett. **107** (2011) 211801, arXiv:1106.4435.

[102] Belle collaboration, A. Kuzmin *et al.*, *Study of $\bar{B}^0 \to D^0\pi^+\pi^-$ decays*, Phys. Rev. **D76** (2007) 012006, arXiv:hep-ex/0611054.

[103] LHCb collaboration, R. Aaij *et al.*, *Dalitz plot analysis of $B^0 \to \overline{D}^0\pi^+\pi^-$ decays*, Phys. Rev. **D92** (2015) 032002, arXiv:1505.01710.

[104] A. Martín Sánchez, P. Robbe, and M.-H. Schune, *A single track HLT1 trigger*, LHCb-PUB-2011-003.

[105] LHCb collaboration, R. Aaij *et al.*, *Measurement of the track reconstruction efficiency at LHCb*, JINST **10** (2015) P02007, arXiv:1408.1251.

[106] BaBar collaboration, B. Aubert *et al.*, *Study of D_{sJ} decays to D^*K in inclusive e^+e^- interactions*, Phys. Rev. **D80** (2009) 092003, arXiv:0908.0806.

[107] LHCb collaboration, R. Aaij *et al.*, *Study of D_{sJ} decays to $D^+K^0_S$ and D^0K^+ final states in pp collisions*, JHEP **10** (2012) 151, arXiv:1207.6016.

[108] Belle collaboration, K. Abe *et al.*, *Study of $B^- \to D^{**0}\pi^-$ ($D^{**0} \to D^{(*)+}\pi^-$) decays*, Phys. Rev. **D69** (2004) 112002, arXiv:hep-ex/0307021.

[109] BaBar collaboration, B. Aubert *et al.*, *Dalitz plot analysis of $B^- \to D^+\pi^-\pi^-$*, Phys. Rev. **D79** (2009) 112004, arXiv:0901.1291.

[110] M. Williams, *How good are your fits? Unbinned multivariate goodness-of-fit tests in high energy physics*, JINST **5** (2010) P09004, arXiv:1006.3019.

[111] LHCb collaboration, R. Aaij *et al.*, *Measurements of the Λ_b^0, Ξ_b^-, and Ω_b^- baryon masses*, Phys. Rev. Lett. **110** (2013) 182001, arXiv:1302.1072.

[112] LHCb collaboration, R. Aaij *et al.*, *Precision measurement of D meson mass differences*, JHEP **06** (2013) 065, arXiv:1304.6865.

[113] S. M. Flatté, *Coupled-channel analysis of the $\pi\eta$ and $K\overline{K}$ systems near $K\overline{K}$ threshold*, Phys. Lett. **B63** (1976) 224.

[114] D. V. Bugg, *Comments on the sigma and kappa*, Phys. Lett. **B572** (2003) 1.

[115] B. El-Bennich *et al.*, *CP violation and kaon-pion interactions in $B \to K\pi^+\pi^-$ decays*, Phys. Rev. **D79** (2009) 094005, Erratum ibid. **D83** (2011) 039903, arXiv:0902.3645.

[116] G. J. Gounaris and J. J. Sakurai, *Finite-width corrections to the vector-meson-dominance prediction for $\rho \to e^+e^-$*, Phys. Rev. Lett. **21** (1968) 244.

[117] CDF collaboration, A. Abulencia *et al.*, *Measurement of $\sigma(\Lambda_b^0)/\sigma(\bar{B}^0) \times \mathrm{BR}(\Lambda_b^0 \to \Lambda_c^+\pi^-)/\mathrm{BR}(\bar{B}^0 \to D^+\pi^-)$ in $p\bar{p}$ collisions at $\sqrt{s} = 1.96$-TeV.*, Phys. Rev. Lett. **98** (2007) 122002, arXiv:hep-ex/0601003.

[118] D. V. Bugg, *The $D\pi$ S-wave*, J. Phys. **G36** (2009) 075003, arXiv:0901.2217.

[119] LHCb collaboration, R. Aaij *et al.*, *First observation and amplitude analysis of the $B^- \to D^+K^-\pi^-$ decay*, Phys. Rev. **D91** (2015) 092002, arXiv:1503.02995.

[120] LHCb collaboration, R. Aaij *et al.*, *Search for the decay $B_s^0 \to \overline{D}^0 f_0(980)$*, JHEP **08** (2015) 005, arXiv:1505.01654.

[121] Belle collaboration, A. Kusaka *et al.*, *Measurement of CP asymmetry in a time-dependent Dalitz analysis of $B^0 \to (\rho\pi)^0$ and a constraint on the CKM angle ϕ_2*, Phys. Rev. Lett. **98** (2007) 221602, arXiv:hep-ex/0701015.

[122] BaBar collaboration, J. P. Lees *et al.*, *Measurement of CP-violating asymmetries in $B^0 \to (\rho\pi)^0$ decays using a time-dependent Dalitz plot analysis*, Phys. Rev. **D88** (2013) 012003, arXiv:1304.3503.

[123] BaBar collaboration, J. P. Lees *et al.*, *Evidence for CP violation in $B^+ \to K^*(892)^+\pi^0$ from a Dalitz plot analysis of $B^+ \to K^0_S\pi^+\pi^0$ decays*, arXiv:1501.00705.

[124] Belle collaboration, V. Balagura *et al.*, *Observation of $D_{s1}(2536)^+ \to D^+\pi^-K^+$ and angular decomposition of $D_{s1}(2536)^+ \to D^{*+}K^0_S$*, Phys. Rev. D **77** (2008) 032001.

[125] Flavour lattice averaging group (FLAG), S. Aoki *et al.*, *Review of lattice results concerning low-energy particle physics*, Eur. Phys. J. **C74** (2014) 2890, arXiv:1310.8555.

[126] BaBar collaboration, J. P. Lees *et al.*, *Dalitz plot analyses of $B^0 \to D^-D^0K^+$ and $B^+ \to \overline{D}^0D^0K^+$ decays*, Phys. Rev. **D91** (2015) 052002, arXiv:1412.6751.

[127] LHCb collaboration, R. Aaij *et al.*, *Study of D_J meson decays to $D^+\pi^-$, $D^0\pi^+$ and $D^{*+}\pi^-$ final states in pp collisions*, JHEP **09** (2013) 145, arXiv:1307.4556.

[128] LHCb collaboration, R. Aaij *et al.*, *Measurement of CP asymmetry in $D^0 \to K^-K^+$ and $D^0 \to \pi^-\pi^+$ decays*, JHEP **07** (2014) 041, arXiv:1405.2797.

[129] LHCb collaboration, R. Aaij *et al.*, *Measurement of the semileptonic CP asymmetry in B^0–$\overline{B}^0$ mixing*, Phys. Rev. Lett. **114** (2015) 041601, arXiv:1409.8586.

[130] Heavy Flavor Averaging Group (HFAG), Y. Amhis *et al.*, *Averages of b-hadron, c-hadron, and τ-lepton properties as of summer 2014*, arXiv:1412.7515.

[131] LHCb collaboration, R. Aaij *et al.*, *A measurement of the CKM angle γ from a combination of $B^{\pm} \to Dh^{\pm}$ analyses*, Phys. Lett. **B726** (2013) 151, arXiv:1305.2050.

[132] M. Nayak *et al.*, *First determination of the CP content of $D \to \pi^+\pi^-\pi^0$ and $D \to K^+K^-\pi^0$*, Phys. Lett. **B740** (2015) 1, arXiv:1410.3964.

[133] S. Malde *et al.*, *First determination of the CP content of $D \to \pi^+\pi^-\pi^+\pi^-$ and updated determination of the CP contents of $D \to \pi^+\pi^-\pi^0$ and $D \to K^+K^-\pi^0$*, Phys. Lett. **B747** (2015) 9, arXiv:1504.05878.

[134] T. Gershon and A. Poluektov, *Double Dalitz plot analysis of the decay $B^0 \to DK^+\pi^-$, $D \to K^0_S\pi^+\pi^-$*, Phys. Rev. **D81** (2010) 014025, arXiv:0910.5437.